

International
Journal of 3D Printing
Technologies and Digital Industry

IJ3DPTDI



Uluslararası 3B Yazıcı Teknolojileri
ve Dijital Endüstri
Dergisi

Vol:8

Issue:3

2024

Cilt:8

Sayı:3

Sayın Yazarlar;

Dergimize 4 dilde (Türkçe Tr, İngilizce En, Rusça Ru ve Ukraynaca Ua) yazı kabul etmekteyiz. Türkçe, Rusça ve Ukraynaca yazılarda İngilizce özet yazılması zorunludur.

ULUSLARARASI 3B YAZICI TEKNOLOJİLERİ VE DİJİTAL ENDÜSTRİ dergisi,

IJ3DPTDI, Endüstri 4.0 – dijital endüstri teknolojileri, 3B yazıcı teknolojileri, katmanlı-eklemeli imalat teknolojileri ve uygulamaları yani mühendislik, bilim, teknoloji gibi tüm disiplinlerle ilgili araştırmaların sonuçlarını yaymak için açık, hakemli, disiplinlerarası, uluslararası, bilimsel, akademik, online bir dergidir. ij3dptdi, Mühendislik, Teknoloji ve Bilimin Endüstri 4.0 daki uygulamaları, tüm araştırmaları, gözden geçirme makalelerini, kısa bilgi paylaşımlarını ve önemli ilerlemeleri sunan teknik notları online yayınlamak için yazarları davet eder.

Endüstri 4.0, Dijital Endüstri, 3B Yazıcılar üzerine tüm bilimsel mühendislik araştırma ve teknoloji alanı konuları;

3B baskı için tıbbi uygulamalar; dokuların ve organların biyografik baskıları, 3B vaskülarize organların oluşturulmasında karşılaşılan zorluklar, özelleştirilmiş implantlar ve protezler, düşük maliyetli protez parçaları, cerrahi hazırlık için anatomik modeller, sentetik cilt, kafatası değişimi, tıbbi donatımı, kemik, özel üretilen sensörler, kişiselleştirilmiş ilaç dozu, benzersiz dozaj şekilleri, kompleks ilaç salınım profilleri v.d.

3B yazıcı uygulama alanları; tıbbi ve diş hekimliği uygulamaları, diş hekimliği uygulamaları ve materyalleri, yumuşak robotik sistemleri, robot tutucu sistemler, bina uygulamaları, kalıp / kalıp uygulamaları, mimarlık uygulamaları, model uygulamaları, hızlı prototip uygulamaları, görsel sanat uygulamaları, tekstil uygulamaları, dijital fabrikalar, mimari model uygulamaları ve malzemeleri, endüstriyel uygulamalar ve malzemeler, gıda uygulamaları ve malzemeleri, sanatsal uygulamalar ve malzemeler, tarama yöntemleri ve modelleme v.d.

Endüstri 4.0 ve dijital sanayi; büyük veri, yapay zeka, dijital yaşam döngüsü, sensör motorları, artırılmış gerçeklik, görselleştirme, sistem simülasyonu, kablosuz iletişim, BİT güvenlik, dijital iş, blok zinciri, veri Güvenliği, özerk robotlar, sistem entegrasyonu, nesnelerin interneti (IoTs), siber güvenlik, bulut bilişim, dijital fabrika v.d.

3B yazıcı tasarım, modelleme ve analiz; 3D yazıcı tasarımı, ekstruder tasarımı, 3B baskı için ürün geliştirme, seramik sistemleri tasarımı, gıda sistemleri tasarımı, elektronik bileşenleri, mekanik parçalar, standart bileşenler v.d.

3B yazıcı malzeme ve mekanik özellikleri; polimer malzemeler, esnek malzemeler, biyo malzemeler, metalik malzemeler, toz malzeme üretim yöntemleri, ağaç malzemeler, kompozit malzemeler v.d.

3B yazıcı program kontrol teknolojileri; kontrol programları, tasarım programları, 3D tarama teknolojileri, DMLS teknolojileri, SLA teknolojileri, SLS teknolojileri, FDM teknolojileri, dijital üretim teknolojileri, diğer 3B yazıcı teknolojileri v.d.

ij3dptdi, online yayınlanan bir dergidir ve yılda 3 defa yayınlanır.

- 1.peryot Ocak-Nisan
- 2.peryot Mayıs-Ağustos
- 3.peryot Eylül-Aralık

ISSN 2602-3350

web-site : <http://dergipark.gov.tr/ij3dptdi>

e-mail : korayozsoy32@gmail.com

Dear author,

Our Journal accepts articles in 4 languages (Turkish Tr, English En, Russian Ru and Ukrainian Ua). Articles in Turkish, Russian and Ukrainian must have an abstract in English.

International Journal of 3D Printing Technologies and Digital Industry

ij3dptdi, is an open access peer-reviewed, interdisciplinary international platform for disseminating results of relevant research related to all the disciplines of engineering, science, technology etc on Industry 4.0 - digital industry technologies, 3D printer technologies, additive manufacturing technologies and applications . ij3dptdi, invites all research, review articles, short communications & technical notes that describe significant advances research in the areas of Engineering, Technology, Science on Industry 4.0, Digital Industry, 3D Printers, additive manufacturing;

All scientific engineering research & technology area on Industry 4.0, Digital Industry and 3D printers;

Medical applications for 3D printing; bioprinting tissues and organs, challenges in building 3D vascularized organs, customized implants and prostheses, low-cost prosthetic parts, anatomical models for surgical preparation, synthetic skin, cranium replacement, medical equipment, bone, tailor-made sensors, personalized drug dosing, unique dosage forms, complex drug-release profiles ect.

Application fields; medical and dental applications, dental practices and materials, soft robotics systems, robot gripper systems, building applications, die/mold applications, architecture applications, models applications, rapid prototype applications, visual arts applications, textile applications, digital factories, architectural-model applications and materials, industrial applications and materials, food applications and materials, artistic practices and materials, scanning methods and modeling ect.

Digital industry; big data, artificial intelligence, digital life cycles, sensors actuators, augmented reality, visualization, system simulation, wireless communication, ICT security, digital business, block chain, data safety, autonomous robots, system integration, internet of things (IT's), cyber security, cloud computing, digital factory ect.

Design, modelling and analysis; 3D printer design, extruder design, product development, ceramic systems design, food systems design, table system design, electronics components, mechanic components, standard components ect.

Mechanical properties of filaments; polymer materials, flexible materials, bio materials, metallic materials, wood materials, composite materials ect.

Program – control technologies; control programs, design programs, 3D scanning technologies, DMLS technologies, SLA technologies, SLS technologies, FDM technologies, Digital production technologies, other 3D printer technologies ect.

ij3dptdi, Its publication frequency is 3 issues per year.

- 1.Period January-April
- 2.period May-August
- 3.period September-December

ISSN 2602-3350
Web-site: <http://dergipark.gov.tr/ij3dptdi>
E-mail: korayozsoy32@gmail.com

Уважаемый автор,

наш журнал принимает статьи на 4-х языках (турецком, английском, русском и украинском). Статьи на турецком, русском и украинском языках должны сопровождаться аннотацией на английском языке.

Международный журнал технологий 3D-печати и цифровой индустрии

IJ3DPTDI – это рецензируемое издание с открытым доступом, междисциплинарная международная платформа для обмена результатами исследований по инженерно-конструкторским разработкам, теоретическим исследованиям, усовершенствованию технологий Индустрии 4.0, в том числе – технологий цифровой промышленности, 3D-печати, аддитивного производства и разработки приложений. **IJ3DPTDI** принимает исследовательские статьи, обзорные статьи, краткие сообщения и технические заметки, которые описывают значимые результаты исследований в области машиностроения, технологии, теоретической основы индустрии 4.0, цифровой промышленности, 3D печати, производства многокомпонентных материалов.

Тематика журнала включает все научно-технические исследования и обзор технологий Индустрии 4.0, цифровой промышленности и 3D печати.

Медицинские технологии 3D-печати: биопринтинг – воспроизведение объемных моделей тканей и органов, создание трехмерных васкуляризованных органов, индивидуализированных имплантатов и протезов, синтетической кожи, костей, замены частей черепа; удешевление технологии протезирования, разработка анатомических моделей для подготовки хирургов, тестовых хирургических операций, медицинского оборудования; изготовление датчиков с заданным набором характеристик, создание уникальных лекарственных препаратов с индивидуальными дозировками, сложных многокомпонентных лекарственных средств.

Области применения: материалы и оборудование для медицины и стоматологии, роботизированные системы на основе биологических прототипов, роботизированные захватные устройства, строительные материалы, пресс-формы, модели и прототипы в архитектуре, моделирование реальных объектов, прототипирование, сфера визуального искусства, текстильная промышленность, цифровые заводы, приложения и материалы для архитектурного моделирования, промышленные образцы и материалы, создание пищевых продуктов, технологии художественной обработки материалов, методы моделирования и сканирования и т.п.

Цифровая индустрия: большие данные, искусственный интеллект, жизненный цикл цифровых технологий, приводные механизмы датчиков, расширенная реальность, визуализация, моделирование систем, беспроводная связь, ИТ-безопасность, электронная коммерция, блокчейн технологии, безопасность данных, автономные роботы, системная интеграция, интернет вещей, кибербезопасность, облачные вычисления, цифровое производство.

Дизайн, моделирование и анализ: моделирование для 3D печати, экструдера; разработка разнообразных продуктов, проектирование систем керамического производства, усовершенствование технологии производства пищевых продуктов, проектирование предметов мебели, электронных компонентов, механических деталей, стандартных компонентов и т.п.

Механические свойства нитей: полимерные материалы, гибкие материалы, биоматериалы, изделия из металла и древесины, композиционные материалы.

Технологии управления приложениями: контрольные программы, проектные программы, технологии 3D-сканирования, технологии DMLS, SLA, SLS, FDM, цифровые технологии производства, другие технологии 3D-печати и т.п.

Периодичность выхода журнала – 3 раза в год:

1-й выпуск – январь-апрель;

2-й выпуск – май-август;

3-й выпуск – сентябрь-декабрь.

ISSN 2602-3350

Сайт журнала: <http://dergipark.gov.tr/ij3dptdi>

Электронная почта: korayozsoy32@gmail.com

Шановний авторе,

наш журнал приймає статті на 4-х мовах (турецькою, англійською, російською та українською). Статті турецькою, російською та українською мовою повинні супроводжуватися анотацією англійською мовою.

Міжнародний журнал технологій 3D-друку і цифрової індустрії

IJ3DPTDI – це рецензоване видання з відкритим доступом, міждисциплінарна міжнародна платформа для обміну результатами досліджень з інженерно-конструкторських розробок, теоретичних досліджень, удосконалення технологій Індустрії 4.0, в тому числі – технологій цифрової промисловості, 3D-друку, адитивного виробництва і розробки додатків. IJ3DPTDI приймає дослідні статті, оглядові статті, короткі повідомлення і технічні записки, які містять значущі результати досліджень в галузі машинобудування, технології, теоретичній основі індустрії 4.0, цифровій промисловості, 3D друку, виробництва багатокomпонентних матеріалів.

Тематика журналу охоплює всі науково-технічні дослідження та огляд технологій Індустрії 4.0, цифрової промисловості і 3D друку.

Медичні технології 3D-друку: біопрінтинг – відтворення об'ємних моделей тканин і органів, створення тривимірних васкуляризованих органів, індивідуалізованих імплантатів і протезів, синтетичної шкіри, кісток, заміни частин черепа; здешевлення технології протезування, розроблення анатомічних моделей для підготовки хірургів, тестових хірургічних операцій, медичного обладнання; виготовлення датчиків із заданим набором характеристик, створення унікальних лікарських препаратів із індивідуальними дозуваннями; складних багатокomпонентних лікарських засобів.

Сфери застосування: матеріали та обладнання для медицини і стоматології, роботизовані системи на основі біологічних прототипів, роботизовані захватні пристрої, будівельні матеріали, прес-форми, моделі і прототипи в архітектурі, моделювання реальних об'єктів, прототипування, сфера візуального мистецтва, текстильна промисловість, цифрові заводи, додатки та матеріали для архітектурного моделювання, промислові зразки і матеріали, створення харчових продуктів, технології художньої обробки матеріалів, методи моделювання та сканування і т.п.

Цифрова індустрія: великі дані, штучний інтелект, життєвий цикл цифрових технологій, приводні механізми датчиків, розширена реальність, візуалізація, моделювання систем, бездротовий зв'язок, IT-безпека, електронна комерція, блокчейн технології, безпека даних, автономні роботи, системна інтеграція, інтернет речей, кібербезпека, хмарні обчислення, цифрове виробництво.

Дизайн, моделювання і аналіз: моделювання для 3D друку, екструдера; розробка різноманітних продуктів, проектування систем керамічного виробництва, удосконалення технології виробництва харчових продуктів, проектування предметів меблів, електронних компонентів, механічних деталей, стандартних компонентів і т.п.

Механічні властивості ниток: полімерні матеріали, гнучкі матеріали, біоматеріали, вироби з металу і деревини, композиційні матеріали.

Технології управління додатками: контрольні програми, проектні програми, технології 3D-сканування, технології DMLS, SLA, SLS, FDM, цифрові технології виробництва, інші технології 3D-друку і т.п.

Періодичність виходу журналу – 3 рази на рік:

1-й випуск – січень-квітень;

2-й випуск – травень-серпень;

3-й випуск – вересень-грудень.

ISSN 2602-3350
Web-site: <http://dergipark.gov.tr/ij3dptdi>
E-mail: korayozsoy32@gmail.com

ULUSLARARASI 3B YAZICI TEKNOLOJİLERİ VE DİJİTAL ENDÜSTRİ DERGİSİ

Cilt:8 Sayı: 3 Yıl: 2024

INTERNATIONAL JOURNAL OF 3D PRINTING TECHNOLOGIES AND DIGITAL INDUSTRY

Volume:8 Number: 3 Year: 2024

ISSN: 2602-3350

Yazıların tüm bilimsel sorumluluğu yazar(lar)a aittir. Editör, yardımcı editör ve yayıncı dergide yayımlanan yazılar için herhangi bir sorumluluk kabul etmez. Bu dergi, aşağıda listelenen veri tabanları tarafından taranmaktadır. All the scientific responsibilities of the manuscripts belong to the authors (s). The editor, assistant editor and publisher accept no responsibility for the articles published in the journal. The Journal is indexed by the following abstracting and indexing databases.

TR Dizin, Google Scholar, ResearchBib, Index Copernicus, Asos indeks



<http://dergipark.gov.tr/ij3dptdi>

**Uluslararası 3B Yazıcı Teknolojileri ve Dijital Endüstri Dergisi /
International Journal of 3D Printing Technologies and Digital
Industry**

Vol: 8, No:3 (2024)

Cilt: 8, Sayı:3 (2024)

Editörler ve Kurullar / Editors and Boards

Yayın Kurulu Başkanı / Publication Board Manager

Dr. Kerim ÇETİNKAYA, Antalya BELEK Üniversitesi, Sanat ve Tasarım Fakültesi, TÜRKİYE

Baş Editörler / Editor(s)-in-Chief

Dr. Kerim ÇETİNKAYA, Antalya BELEK Üniversitesi, Sanat ve Tasarım Fakültesi, TÜRKİYE

Dr. Koray ÖZSOY, Isparta Uygulamalı Bilimler Üniversitesi, Isparta OSB MYO, Makine ve Metal Teknolojileri Bölümü, TÜRKİYE

Editörler Kurulu / Editorial Board

Dr. Burhan DUMAN, Isparta Uygulamalı Bilimler Üniversitesi, Teknoloji Fakültesi, Bilgisayar Mühendisliği Bölümü, TÜRKİYE

Dr. Ahu ÇELEBİ, Celal Bayar Üniversitesi, Mühendislik Fakültesi, Malzeme Mühendisliği Bölümü, TÜRKİYE

Dr. Hatice EVLEN, Karabük Üniversitesi, Teknoloji Fakültesi, Endüstriyel Tasarım Mühendisliği Bölümü, TÜRKİYE

Dr. Murat Aydın, Karabük Üniversitesi, Teknoloji Fakültesi, Endüstriyel Tasarım Mühendisliği Bölümü, TÜRKİYE

Dr. Hanane ZERMANE, Batna 2 Üniversitesi, Endüstri Mühendisliği Bölümü, CEZAYİR

Dr. Serhii Yevseiev, Simon Kuznets Kharkiv Ulusal Ekonomi Üniversitesi, Siber Güvenlik ve Bilgi Teknolojileri Bölümü, UKRAYNA

Dr. Pınar DEMİRCİOĞLU, Aydın Adnan Menderes Üniversitesi, Mühendislik Fakültesi, Makine Mühendisliği Bölümü, TÜRKİYE

Dr. Bekir AKSOY, Isparta Uygulamalı Bilimler Üniversitesi, Teknoloji Fakültesi, Mekatronik Mühendisliği Bölümü, TÜRKİYE

Dr. İshak ERTUĞRUL, Muş Alparslan Üniversitesi, Teknik Bilimler MYO, Mekatronik Programı, TÜRKİYE

Dr. Levent AYDIN, Kocaeli Üniversitesi, Sağlık Hizmetleri MYO, Sağlık Bakım Hizmetleri Bölümü, TÜRKİYE

Dr. Kıyas KAYAALP, Isparta Uygulamalı Bilimler Üniversitesi, Teknoloji Fakültesi, Bilgisayar Mühendisliği Bölümü, TÜRKİYE

Dr. Senai YALÇINKAYA, Marmara Üniversitesi, Teknoloji Fakültesi, Makine Mühendisliği Bölümü, TÜRKİYE

Dr. İbrahim KARAAĞAÇ, İmalat Mühendisliği, Teknoloji Fakültesi, Gazi Üniversitesi, TÜRKİYE

Dr. Yasin HAMARAT, Biyoteknoloji, Kaunas University Of Technology, LİTVANYA

Dr. Binnur SAĞBAŞ, Yıldız Teknik Üniversitesi, Makine Fakültesi, Makine Mühendisliği Bölümü, TÜRKİYE

Dr. Hesham A. Hegazi, Tasarım ve Üretim Mühendisliği, German Üniversitesi, KAHİRE, MISIR

Mizanpaj Editörü/ Layout Editor

Mehmet YÜCEL, Isparta Uygulamalı Bilimler Üniversitesi, Teknoloji Fakültesi, Mekatronik Mühendisliği Bölümü, TÜRKİYE

Arda PAZARCIKCI, Isparta Uygulamalı Bilimler Üniversitesi, Teknoloji Fakültesi, Mekatronik Mühendisliği Bölümü, TÜRKİYE

Danışma Kurulu / Advisory Board

Dr. Hüseyin Rıza BÖRKLÜ, GAZİ ÜNİVERSİTESİ, TR
Dr. Mustafa BOZDEMİR KIRIKKALE ÜNİVERSİTESİ, TR
Dr. Savaş DİLİBAL, İSTANBUL GEDİK ÜNİVERSİTESİ, TR
Dr. Cem Bülent ÜSTÜNDAĞ, YILDIZ TEKNİK ÜNİVERSİTESİ, TR
Dr. Ahmet CAN, NECMETTİN ERBAKAN ÜNİVERSİTESİ, TR
Dr. Fuat KARTAL, KASTAMONU ÜNİVERSİTESİ, TR
Dr. İhsan TOKTAŞ, YILDIRIM BEYAZIT ÜNİVERSİTESİ, TR
Dr. Okan ORAL, AKDENİZ ÜNİVERSİTESİ, TR
Dr. Mustafa Aydın, KÜTAHYA DUMLUPINAR ÜNİVERSİTESİ, TR
Dr. Serap ÇELEN, EGE ÜNİVERSİTESİ, TR
Dr. İsmail BÖĞREKÇİ, AYDIN ADNAN MENDERES ÜNİVERSİTESİ, TR
Dr. Samsun M. BAŞARICI, AYDIN ADNAN MENDERES ÜNİVERSİTESİ, TR
Dr. Serkan ŞENDAĞ, MERSİN ÜNİVERSİTESİ, TR

ISSN 2602-3350

| İçindekiler /Table of Contents | Sayfa /Pages |
|---|---------------------|
| Araştırma Makaleleri/Research Articles | |
| DESIGN AND FINITE ELEMENT ASSESSMENT OF FUNCTIONALLY GRADED AUXETIC STRUCTURES | 303-315 |
| Mert Özen ^a  , Hamit Kenan ^b  , Cumhuriyet Oktay Azeloğlu ^a  | |
| AN INDUSTRIAL APPLICATION OF DIGITAL TWIN FOR A SMART FACTORY MODEL USING COPPELIASIM | 316-325 |
| Cüneyt KILIÇ ^a  , Kamil ÇETİN ^{a,b}  , Mehmet Erdal ÖZBEK ^{a,b}  | |
| TENSILE BEHAVIOUR OF Ti6Al4V LATTICE STRUCTURES PRODUCED BY LASER POWDER BED FUSION AND DESIGN CRITERIA | 326-336 |
| Doruk Gürkan ^{a*}  , Binnur Sagbas ^b  , Kadir Kiran ^{c,d}  | |
| REDESIGN AND FABRICATION OF STENT DESIGNS PRODUCED BY COMMON METHODS BY OPTİMİZING FOR MELT ELECTRO WRITING (MEW) METHOD | 337-351 |
| Fatih KÖSE ^a  , Alper TEZCAN ^a  | |
| EKLEMELİ İMALAT TEKNOLOJİSİYLE ÜRETİLMİŞ DÜZ VE KAVİSLİ KARBON FİBER TAKVİYELİ POLİMER MATRİSLİ KOMPOZİTLERİN KISA-KIRIŞ MUKAVEMETLERİNİN KARŞILAŞTIRILMASI | 352-360 |
| Sedat Süsler ^a  | |
| EXAMINING THE RELATIONSHIP BETWEEN SUSTAINABLE MATERIAL AND BUILDING DESIGN IN BUILDING CONSTRUCTION WITH ADDITIVE MANUFACTURING | 361-369 |
| Kübra SÜMER HAYDARASLAN ^a  | |
| COMPARATIVE STUDY OF MATERIAL EXTRUSION AND VAT PHOTOPOLYMERIZATION ADDITIVE MANUFACTURING TECHNIQUE USING SQUARE BASE PYRAMID AS AN ARTIFACT AND APPLICATIONS | 370-386 |
| Bhanu Prakash BISHT ^{a,b}  , Vijaykumar TOUTAM ^{a,b*}  , Sanjay R. DHAKATE ^{a,b}  | |
| KOMPOZİT CYSZ KAPLAMANIN DEĞİŞEN YÜKLER ALTINDA AŞINMA DAVRANIŞININ İNCELENMESİ | 387-398 |
| Ali AVCI ^{a*}  , Muhammet KARABAŞ ^b  | |
| ERGİYİK BİRİKTİRME YÖNTEMİYLE ÜRETİLEN PVA NUMUNELERİN BASMA DAYANIMININ BULANIK MANTIKLA TAHMİNİ | 399-406 |
| Ebru Kuruoğlu ^a  , Osman Saltık ^b  , Koray Özsoy ^b  | |
| EXAMINATION OF MECHANICAL PROPERTIES OF FASTENERS PRODUCED WITH PET AND PLA MATERIALS IN EXTRUSION-BASED ADDITIVE MANUFACTURING METHOD | 407-415 |
| Alperen DOĞRU ^a  , Muazzez KAÇAK ^b  , M.Özgür SEYDİBEYOĞLU ^b  | |
| THE ADVANTAGES AND IMPLEMENTATION CHALLENGES WITHIN THE SCOPE OF THE BASIC PRINCIPLES OF TRANSITION TO ZERO TRUST ARCHITECTURE | 416-427 |
| Ahmet Ali SÜZEN ^a  , Osman CEYLAN ^b  | |

| | |
|---|----------------|
| A NEW SPECIFIC CARBON FOOTPRINT (SCF) THEORY OF FLOW RATE AND ENERGY CONSUMPTION VARIATIONS OF AN INDUSTRIAL INTERNAL GEAR PUMP | 428-436 |
| Osman ÖZDAMAR ^a  , Burak ÖZTÜRK ^b  | |
| OPTIMIZATION OF ENERGY CONSUMPTION IN CNC MARBLE PROCESSING: STATISTICAL AND MACHINE LEARNING APPROACHES | 437-450 |
| Gencay Sarıışık ^a  , Ahmet Sabri Ögütü ^a  | |
| CONTROL OF SEAT BELTS OF VEHICLE DRIVERS WHILE DRIVING WITH AN UNMANNED AERIAL VEHICLE WITH ARTIFICIAL INTELLIGENCE | 451-458 |
| Mustafa Melikşah ÖZMEN ^a  , Muzaffer EYLENCE ^a  , Bekir AKSOY ^a  | |
| EKLEMELİ İMALAT İLE DEMİR KATKILI FİLAMAN ÜRETİMİ İÇİN EKSTRÜZYON CİHAZININ TASARIMI, İMALATI VE CİHAZIN TERMAL ANALİZİ | 459-467 |
| Barış Güneç ^a  , Ertutuğrul Durak ^a  | |



ULUSLARARASI 3B YAZICI TEKNOLOJİLERİ
VE DİJİTAL ENDÜSTRİ DERGİSİ

INTERNATIONAL JOURNAL OF 3D PRINTING
TECHNOLOGIES AND DIGITAL INDUSTRY

ISSN:2602-3350 (Online)

URL: <https://dergipark.org.tr/ij3dptdi>

DESIGN AND FINITE ELEMENT ASSESSMENT OF FUNCTIONALLY GRADED AUXETIC STRUCTURES

Yazarlar (Authors): Mert Özen , Hamit Kenan , Cumhuriyet Oktay Azeloğlu 

Bu makaleye şu şekilde atıfta bulunabilirsiniz (To cite to this article): Özen M., Kenan H., Azeloğlu C. O. "Design and Finite Element Assessment of Functionally Graded Auxetic Structures" *Int. J. of 3D Printing Tech. Dig. Ind.*, 8(3): 303-315, (2024).

DOI: 10.46519/ij3dptdi.1418791

Araştırma Makale/ Research Article

Erişim Linki: (To link to this article): <https://dergipark.org.tr/en/pub/ij3dptdi/archive>

DESIGN AND FINITE ELEMENT ASSESSMENT OF FUNCTIONALLY GRADED AUXETIC STRUCTURES

Mert Özen^a, Hamit Kenan^b, Cumhuri Oktay Azeloğlu^a

^aYildiz Technical University, Mechanical Engineering Department, İstanbul, Türkiye

^bAntalya Bilim University, Mechanical Engineering Department, Antalya, Türkiye

*Corresponding Author: hamit.kenan@antalya.edu.tr

(Received: 12.01.2024; Revised: 28.08.2024; Accepted: 12.09.2024)

ABSTRACT

The development of lightweight structures that utilize minimal material while maintaining desired mechanical properties has become increasingly significant with advancements in manufacturing technologies, attracting the attention of researchers. Additive manufacturing methods have enabled the rapid production and testing of new design prototypes, thereby accelerating research in this domain. This study aims to investigate new designs through the functional grading approach applied to auxetic structures. Drawing on established structural patterns from the literature, three patterns were selected for this study. These patterns were modeled with varying wall thicknesses in line with the functional grading approach, and static analyses were conducted using the Ansys Workbench program. For the static analysis, a uniform deformation value was applied to each structure, and the reaction forces at the fixed end were used as the comparison criterion. When the re-entrant, rcw-honeycomb, and elliptical patterns were redesigned using the functional grading approach, their weights increased by 13%, 9%, and 12%, respectively. However, the reaction forces, which serve as an indicator of the structures' load-carrying capacity, showed increases of 68%, 56%, and 43%, respectively. These results underscore the effectiveness of the functional grading approach in enhancing the load capacity of auxetic structures.

Keyword: Auxetic Structure, Functionally Graded Structure, Static Analysis

1. INTRODUCTION

One of the main topics of research and development (R&D) activities is developing structures that offer a lightweight design with minimal material use while meeting the desired mechanical properties. One sub-topic in this context is "auxetic" materials or structures. The term auxetic comes from the Greek word "auxetikos," meaning "that which tends to increase" [1]. Auxetic refers to materials or structures exhibiting a negative Poisson's ratio. They expand under tensile stress and contract under compressive stress. These structures typically consist of repeating units designed to deform in a specific way when subjected to external forces. This unique property makes auxetic materials useful in applications such as protective clothing, biomedical implants, and textiles.

The advantages of using auxetic materials in engineering applications are:

- Enhanced energy damping: Auxetic materials expand laterally under stress, absorbing impacts and shocks more effectively than conventional materials.
- Increased flexibility and range of motion: Useful in applications like sports equipment, auxetic materials provide increased flexibility and range of motion.
- Improved mechanical properties: Auxetic materials exhibit greater stiffness, strength, and toughness, making them useful in structural applications.
- Better fit and comfort: Conforming to the shape of the body or object they contact, auxetic materials provide a better fit and improved comfort, useful in medical devices or wearable technology.

- Improved filtration and insulation: Auxetic materials can be designed with unique pore structures that enhance filtration and insulation properties, useful in applications like air filters or thermal insulation.

The properties of auxetic structures and their advantages largely depend on their geometry. Various geometric unit structures have been presented in the literature and continue to be developed.

Uzun [2] emphasized the need for smart materials today, pointing out that materials with new and varied properties are being developed. This study examines the new properties obtained when conventional materials have a negative Poisson's ratio and their advantageous properties during use. In B. Öztürk's [3] thesis, compression and flexure tests were performed on sandwich structures with different cell shapes. Horizontal honeycomb, vertical honeycomb, cubic, horizontal truss, vertical truss, skeleton, and gyroid geometries were used, each with fixed dimensions of 5mm×5mm×5mm. The samples, made using PLA and CFR-PLA, showed that vertical truss, vertical honeycomb, and cubic geometries had the best compressive strength and modulus of elasticity. Increased relative density slightly improved mechanical properties. A.T. Özen [4] produced "re-entrant" auxetic structures using additive manufacturing. He also created a similar "curved geometry" structure. Tensile, compression, and microhardness tests showed that adding boron nitride to PLA improved mechanical properties. Reducing the angle between branches increased the negative Poisson's ratio to -0.30. B. Ergene and B. Yalçın [5] compared traditional honeycomb structures with negative Poisson's ratio auxetic re-entrant, hybrid re-entrant, honeycomb, and chiral structures. Honeycomb structures showed a positive Poisson's ratio depending on deformation rate. Cell orientation and beam thickness affected energy absorption, with increased wall thickness improving compressive and tensile strengths. H.Y. Sarvestani et al. [6] tested three core structures using PLA and found that the re-entrant structure absorbed 33% more energy. Quasi-static uniaxial tensile tests showed that the RCA structure had higher tensile properties and auxetic effect compared to re-entrant honeycomb when loaded in the X direction. A. Alomarah et al. [7] proposed the re-entrant

chiral auxetic (RCA) structure, combining hexagonal re-entrant and anti-tetrachiral honeycombs. Six samples made of photopolymer and aluminum alloy were fabricated by additive manufacturing and conventional methods. X. Liv [8] noted that improving mechanical properties of auxetic structures often compromises their negative Poisson's ratio. His study proposed two new auxetic cellular structures that maintained negative Poisson's ratios while improving Young's modulus and yield strength. C. Li [9] designed three functionally graded 3D auxetic structures, finding that they reduced dynamic deflections compared to structures with positive Poisson's ratios. Functional grading affected natural frequencies and dynamic displacement. A. Alomarah et al. [10] found that the RCA structure outperformed other honeycombs in strength and specific energy absorption when loaded in the Y direction. Only tetrachiral honeycombs outperformed the RCA in the X direction. Y. Zhou [11] focused on improving metamaterial performance through unit cell innovations. His study developed a re-entrant combined-wall (RCW) honeycomb structure, which increased Young's modulus by 120% and decreased Poisson's ratio by 43%. İ.K. Türkoğlu [12] noted that additive manufacturing advancements allow for printing auxetic structures with negative Poisson's ratios, enhancing energy absorption and durability. A. Yousefi et al. [13] investigated 3D printed auxetic structures using soft and hard polymers under various loads, showing that additive manufacturing is suitable for fabricating auxetic structures with high energy absorption and Young's modulus. Y. Zhang et al. [14] investigated the hardness of re-entrant structures, predicting that factors like entrance angles and wall thicknesses will guide future studies. O. Gülcan et al. [15] discussed functionally graded structures (FGS) and their applications in industry, noting that additive manufacturing allows for optimizing mechanical properties. A.A. Karaca [16] compared finite element analysis and experiments on stainless steel auxetic structures, showing close results and proving accuracy for auxetic structures. C. Kaboğlu [17] studied a sandwich composite with a PA 12 core and glass fiber reinforced Polypropylene for automotive bumpers, emphasizing its negative Poisson's ratio and suitability for aircraft and automotive industries. M.D. Demirbas et al.

[18] analyzed static behavior of structures with negative Poisson's ratio using ABS and PLA cores, noting their potential in high-force, low-temperature applications. F. Murat et al. [19] proposed integrating functionally graded structures into implants for better mechanical performance in biomedical applications. Y. Zhu et al. [20] developed a new tetra-incomplete chiral honeycomb structure, showing improved Poisson's ratios, elastic and shear moduli. D. Han et al. [21] investigated elliptical perforated plate-based structures, finding that specific energy absorption can be increased by reducing mass while maintaining auxetic behavior. H. Jian et al. [22] designed a lightweight structure combining elliptical perforated plates and re-entrant structures, demonstrating improved mechanical properties and utility performance. Páscoa et al. [23] Proposed a new method to

investigate the effect of functionally graded structures through experimental and theoretical studies. Hu et al. focused on novel types of arc-shaped auxetic pattern by carrying out experimental and theoretical studies [24] and 3D auxetic textile structures [25].

Some common examples of auxetic structures include auxetic foams, auxetic honeycombs and auxetic lattices can be seen in Table 1. The table generally shows the preferred patterns for 2- and 3-dimensional auxetic structures and the test samples designed with these patterns. Considering the patterns in this list, the sample patterns to be discussed in this study were decided and those suitable for the functional rating approach were determined.

Table 1. 2D and 3D Auxetic Structure Patterns

| Name | Patterns | Test Specimen | Ref. | Name | Patterns | Test Specimen | Ref. |
|----------------------|----------|---------------|------|-------------------------------------|----------|---------------|-----------|
| Sinusoidal Slotted | | | [12] | Hexagonal Honeycom b | - | | [5] |
| Hexagonal Honeycom b | | | [12] | Anti-tetra Chiral | | | [10] |
| Re-entrant | | | [12] | Oval Core Strutral-Auxetic Elliptic | | | [21] |
| Double Arrowhead | | | [12] | Elliptical | | | [21] |
| Tetrachiral | | | [12] | Re-entrant Elliptical | | - | [22] |
| Re-entrant | | | [3] | Re-entrant Chiral Auxetic (RCA) | | | [7], [10] |
| Hexagonal Honeycom b | | | [3] | Tetra Chiral Honeybom b | | | [22],[10] |
| Star Shaped | | | [3] | Tetra-missing Rib Honeycom b | | | [22] |
| Triangular | - | | [3] | Origami | | | [26] |
| Re-entrant | | | [6] | RCW Honeycom b | | | [11] |
| Rectangula r | | | [6] | Star-Triangular Auxetic Honeycom b | | | [13] |
| Hexagonal Honeycom b | | | [6] | Gyroid | | | [13] |
| Re-entrant | - | | [5] | Chiral 3 Dimension Truss | | | [27] [28] |
| Chiral | - | | [5] | | | | |

When the studies in the literature are examined, it is seen that it is generally aimed to improve mechanical properties with new elements added to existing patterns. In this study, it is aimed to approach the subject from a different perspective. It is planned to obtain new auxetic structures by reorganizing existing structures with a functionally graded approach. A functionally graded structure (FGS) describes a material system whose mechanical, thermal or electrical properties change gradually and continuously in a controlled manner throughout the volume of the structure. In other words, a FGS is a composite material consisting of multiple layers with different material properties arranged to provide a specific performance or function. The concept of functionally graded was first introduced in the 1980s to address the limitations of traditional homogeneous materials in certain applications [29]. By varying the properties of a material in a controlled manner, FGS can offer better performance in terms of strength, stiffness, toughness and other mechanical properties and can be tailored to specific applications. FGS have a wide range of potential applications, including in the aerospace, automotive, biomedical and energy industries. For example, FGS can be used in aircraft and spacecraft components to reduce weight while maintaining strength and stiffness. In biomedical engineering, FGS can be used in implantable devices to improve biocompatibility and reduce the risk of implant failure. Overall, functional graded structures are an important area of research and development in materials science and engineering and are being studied and optimized for various applications.

Limited manufacturing possibilities, which is one of the existing disadvantages of eutectic structures, have been overcome to a great extent with the rapidly developing manufacturing technologies in recent years. The production of both auxetic and FGS with 3D printers has become very popular in recent years. With this technology, it is possible to use different materials with different properties in the same structure. In this way, the design of structures according to the desired properties of the materials has been made possible by using different 3D printer technologies such as stereolithography (SLA) or fused deposition modeling (FDM).

In the studies conducted in the literature on eutectic structures, polymer-based materials have been preferred more than metal-based materials. Polymers are engineering materials that are becoming more and more widely used in our country and in the world. The main reasons for this are ease of production, cost and obtaining lighter structures. In addition to such advantages, while high temperature and energy are required to produce metal-based materials, this need is less in polymers.

One of the disadvantages of polymers is that their operating temperature range is slightly more limited than metal-based materials. Nevertheless, it is a great advantage that polymer-based materials do not need support structures in additive manufacturing compared to metal-based materials. Within the scope of the advantages mentioned above, polymer-based materials are frequently preferred in additive manufacturing methods. Looking at additive manufacturing applications, it is seen that PLA (polylactic acid) is more widely used than other material types.

PLA is a material that is generally classified as a biodegradable thermoplastic polymer. It is derived from sugar beets, corn starch or slow-release plant materials. Therefore, it is considered an environmentally friendly material. PLA is often used in 3D printers because it has a low melting point (usually in the range of 180-220 degrees) and can thus be easily printed. It is non-toxic and offers a high print quality despite having a low tensile strength. The mechanical properties of PLA are relatively low compared to other polymer materials. For example, the tensile strength of PLA is usually 60-70 MPa [30], while the elongation at break is in the range of about 5-10%. However, it has a high hardness (usually around Shore D80), the decay or degradation time can vary depending on environmental conditions, and is available in many colors and options [31]. In conclusion, PLA was chosen for its excellent stiffness, tensile strength, and gas permeability, which are comparable to those of synthetic polymers, making it one of the most promising materials to replace petroleum-based polymers [30].

In this study, some patterns from the literature on auxetic structures were selected as examples. Previous studies have generally focused on the design of patterns with auxetic properties, their mechanical performance, testing with different materials, or using various manufacturing methods. In this study, patterns that can be easily produced with 3D printers using the FDM method were modeled with different wall thicknesses under a functional grading approach. As future manufacturing studies and experimental tests are expected to use FDM-based methods, PLA, a material suitable for this method, was selected. Although the existing process in the literature was followed regarding the method, material, and pattern, the use of the functional grading approach in the design makes this study distinct from previous ones. The selected patterns were designed in 3D and their static analyses were performed using the Ansys program. The analysis results were then used to compare the static performance of the functionally graded patterns with normal patterns, and the findings were discussed.

2. METHOD

2.1 Functionally Graded Structures

Functionally graded structures (FGS) result in property changes that gradually increase or decrease when applied to structures. Such changes can be achieved by gradual variations in material, thickness or density. Due to these characteristics, functionally graded structures offer significant advantages through their mechanical properties that vary based on their location. A functional grading method will be applied to geometries available in this study, and their wall thickness will be gradually increased.

2.2 Auxetic Structures

Auxetic structures behave unusually due to their negative Poisson's ratio. Owing to this property, when a compressive force is applied to the structure, it starts to contract instead of expanding. Likewise, when they are subjected to tension, they begin to expand instead of contract.

The mechanical properties of PLA used for parts to be used in the analyses are shown in Table 2.

Table 2. Mechanical Properties of PLA [32]

| | |
|--------------------------------|--------------------|
| Density (kg/m^3) | 1300 |
| Young modulus (Pa) | $2,34 \times 10^9$ |
| Poisson ratio | 0,33 |
| Bulk modulus (Pa) | $2,29 \times 10^9$ |
| Shear modulus (Pa) | $8,79 \times 10^8$ |
| Tensile yield strength (Pa) | $4,19 \times 10^7$ |
| Tensile ultimate strength (Pa) | $5,95 \times 10^7$ |

2.3 Modelling and Analysis of Auxetic Structures

The parts chosen for analysis were created using the SolidWorks computer-aided design program. Functional graded structures were designed alongside the given geometries using this program. Afterwards, the solid modelled parts were transferred to Ansys Workbench, one of the finite element method programs, for analysis. As a result, the structures will be analyzed, and the results will be evaluated. A size of 75x75x75 mm was chosen to ensure each designed geometry could achieve 3 complete core structures, facilitating comparisons. The bottom and top layers of the models were designed to be 3 mm thick, with wall thickness set at 1 mm. All functional graded parts were designed to gradually increase in thickness, from 1 mm at the bottom to 1,2 mm and 1,4 mm at the top core structures. These dimensions were selected to avoid exceeding the manufacturing constraints of fused deposition modeling (FDM) and to ensure clear geometry. The project has focused on the theoretical aspect so far. These values have been adopted to provide guidance for future experimental studies.

Figure 1a. displays the re-entrant structure, which is the most commonly encountered geometry of auxetic structures among the parts to be solid modelled and analyzed. The computer-aided design program Solidworks was used to create a model measuring 75x75x75x75 mm through solid modelling creation and cutting via extrusion. Figure 1b. shows the newly developed model with functional grading. The wall thickness of the model was gradually increased from 1 mm to 1,2 mm and finally to 1,4 mm from the bottom to the top. The second geometry in Figure 1c. was selected due to the RCW honeycomb structure's features, such as effective Young's modulus and high resistance to compression (increase of 120% and 140%) in comparison to

classical re-entrant structures. The RCW honeycomb structure with functional grading also can be seen in Figure 1d. The third type of geometry, the elliptical structure, is given in Figure 1e. The literature review led to the

selection of this structure due to its energy absorption feature [21]. Figure 1f. shows the elliptical structure with functional grading applied.

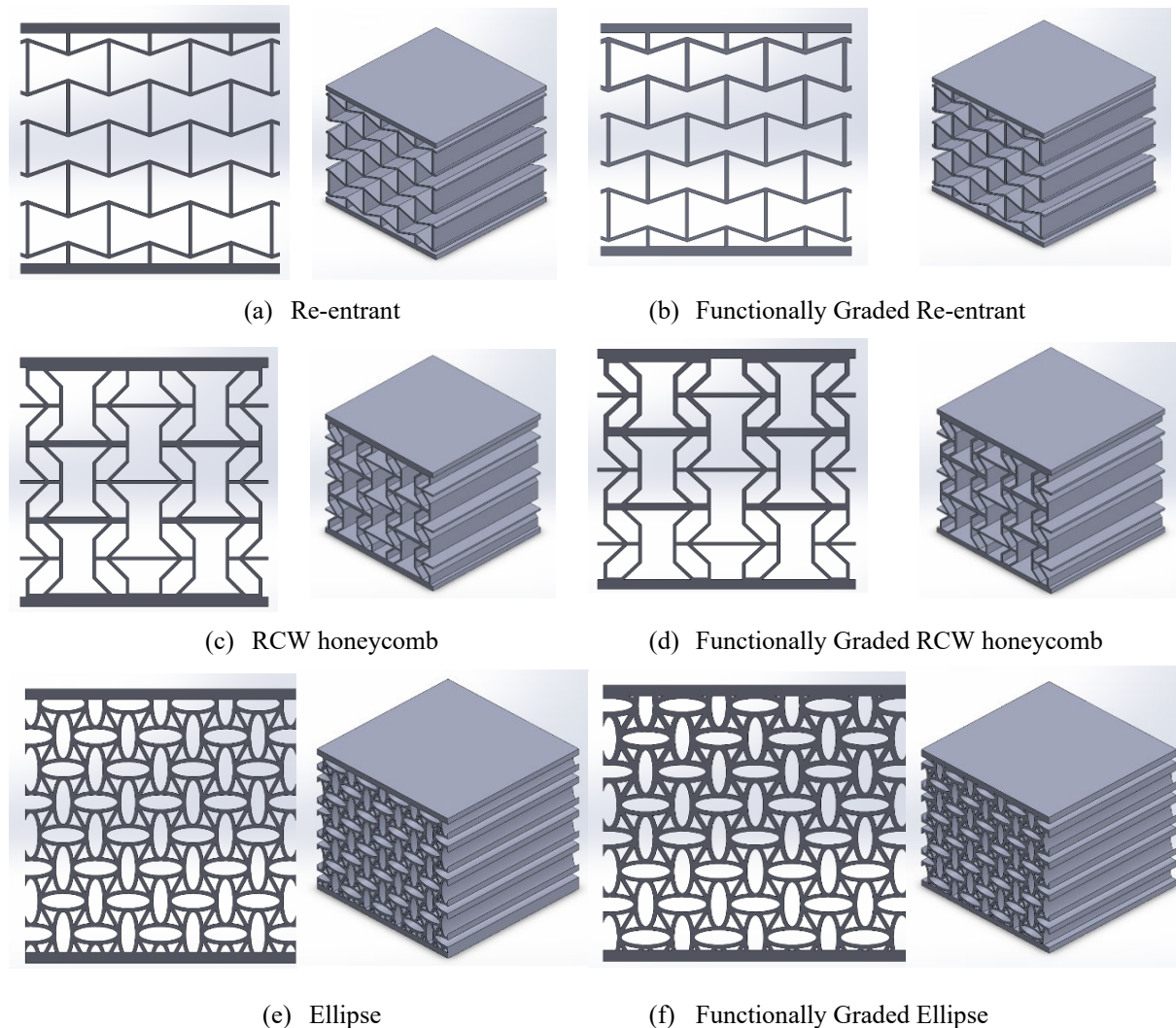


Figure 1. Selected auxetic structures

2.4 Finite Element Analysis of the Auxetic Structures

The static analysis of the structures modelled in the SolidWorks computer-aided design program was carried out in the Ansys Workbench finite element method program. Prior to conducting static analysis, the PLA material's properties listed in Table 2 were defined in the Ansys engineering data library. To perform static analysis, the SolidWorks parts saved with SLDPRT extension were transferred to the Ansys Workbench Design Modeler module. Each defined part was meshed using

equal element sizing. Therefore, each experimental part was meshed with an element size of 0,8 mm. The bottom surface of each analyzed geometry was fixed and 0,5 mm displacement was defined from the top surface towards the part. Following the analysis, the structures' total deformation (mm), equivalent stress (MPa) and reaction forces (N) were obtained and evaluated. To reveal the negative Poisson's ratio of the parts more distinctly, the analysis results of the parts were scaled up by a factor of 12. This helps to better understand how the geometry will behave when compressed.

3. RESULTS AND DISCUSSIONS

In this study, the basic mechanical behaviors of auxetic structures when they were redesigned with the functional grading approach were investigated. Using 3 basic patterns selected from the literature, they were redesigned to have different wall thicknesses, each with a functional grading approach. These models used in the finite element program were subjected to static testing to remain in the linear region under equal boundary conditions and loading conditions. To determine the load-bearing capacity of each structure, an equal amount of displacement (0.5 mm) was applied to each structure and the displacement characteristics and stress values of the structures were examined. Static analysis outputs such as the weight of each structure and displacement, stress and reaction force are shown in Table 3.

The comparison focused specifically on the relationship between reaction force and weight. Because an equal amount of displacement was applied to each structure and similar displacement results were obtained, although there were slight differences depending on the shape and displacement characteristics of the structural elements of the structures. Since static analyzes are performed in the elastic region, stress values remain far from the yield limit.

When the results are examined in this respect, functionally graded structures give better results in terms of load-bearing capacity compared to the original structures. Even if there are losses at certain rates in terms of lightweight design or increases in stresses, the fact that there are significant increases in load-bearing capabilities shows that functionally graded designs are preferable options. For example, although the FG re-entrant structure increased by 13% in weight and had a negative feature in terms of lightness, it increased by 68% in its load carrying ability. Due to this improvement

in load carrying ability, the increase in weight remains insignificant. Likewise, although FG rcw honeycomb and FG ellipse structures experienced a 9% and 13% increase in weight, respectively, their load carrying capabilities increased by 55% and 43%, respectively.

Displacement characteristics are also one of the outputs that are considered important in auxetic structures and evaluated in the results. In this respect, when each building is evaluated on its own, the following can be said. While in the original designs, the elements in the buildings show a proportional change in shape from top to bottom, in the functionally graded structures, the upper parts with higher wall thickness (in the designs in this study, the wall thickness of the functionally graded structures increases from bottom to top) move with a rigid behavior and the deformation change starts from the lower parts. This feature is important in terms of providing a different displacement character to the structures. In this way, displacement becomes a controllable output. If the amount of displacement due to deformation change can be controlled through different studies, it will be possible to obtain steerable structures by ensuring that the structures change deformation in the desired direction.

Functionally graded materials (FGMs) have spatial variations in composition and structure, resulting in tailored mechanical properties like strength, stiffness, and weight. When applied to auxetic structures, FGMs enhance overall performance. The study shows that FG auxetic structures significantly improve load-bearing capacity, crucial for high strength-to-weight ratio applications such as aerospace and biomedical implants. Additionally, FG auxetic structures exhibit unique and controllable displacement characteristics, making them ideal for applications requiring precise movement or energy absorption, like protective gear and flexible electronics.

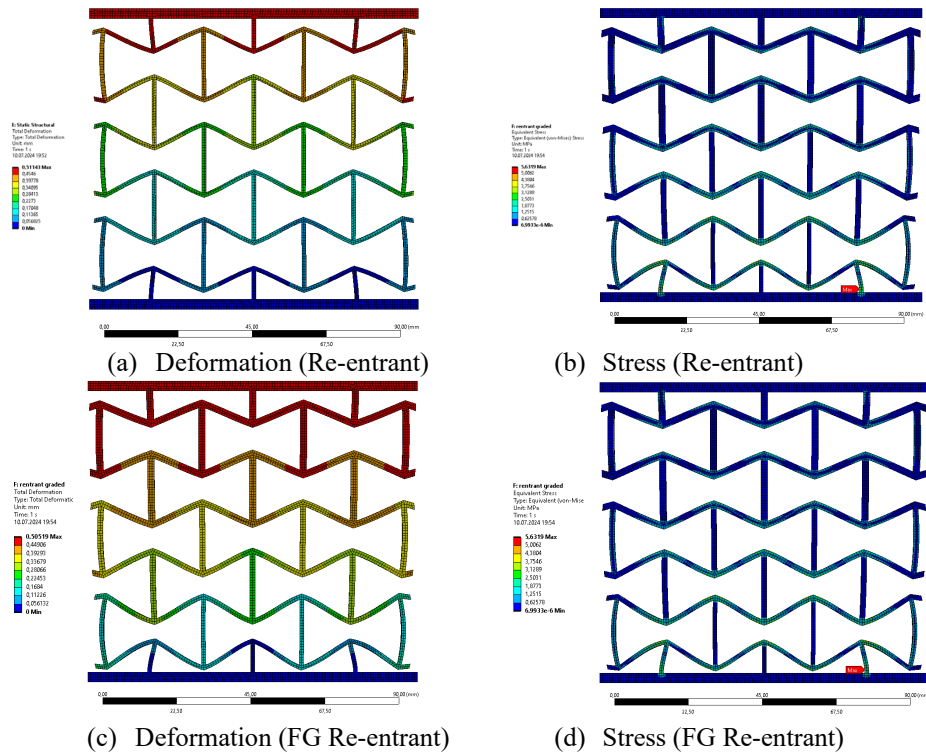


Figure 2. Deformation and stress results of re-entrant and FG re-entrant model with 0.5 mm displacement in the compression direction

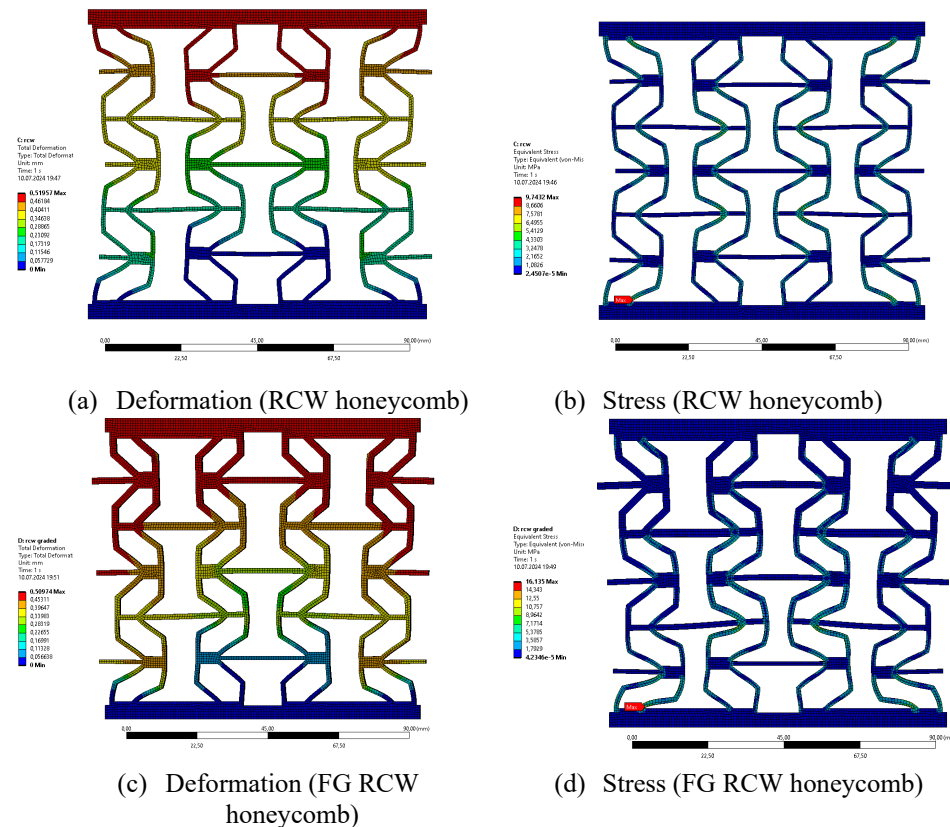


Figure 3. Deformation and stress results of RCW honeycomb and FG RCW honeycomb model with 0.5 mm displacement in the compression direction

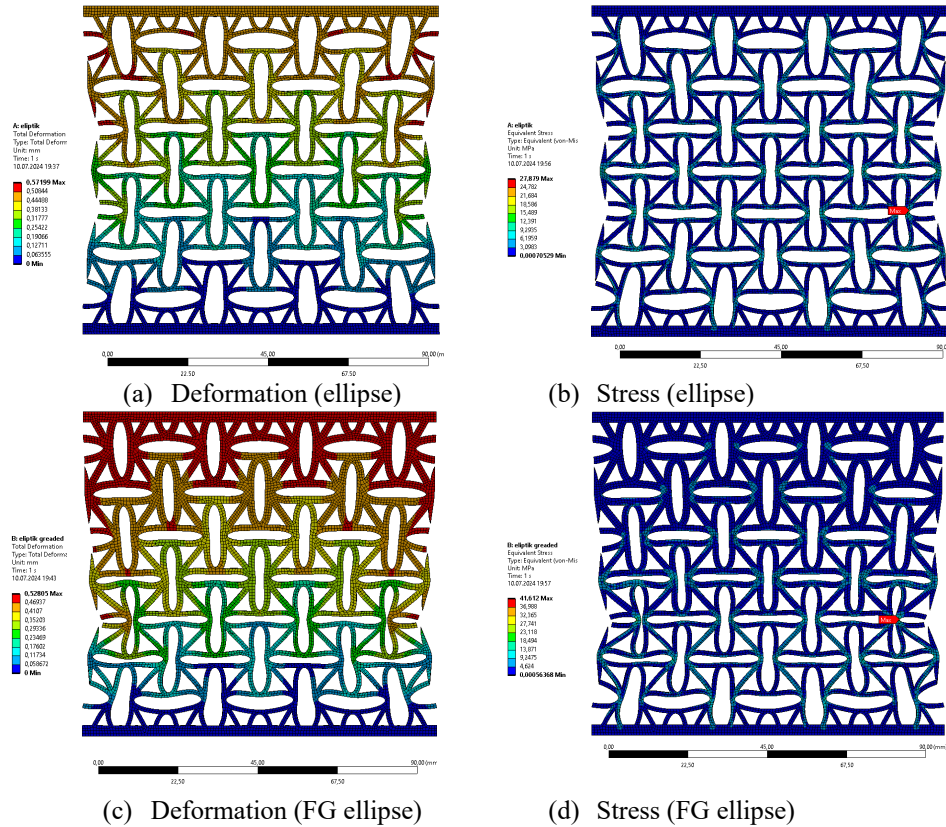


Figure 4. Deformation and stress results of ellipse and FG ellipse model with 0.5 mm displacement in the compression direction

Table 3. Analysis results of auxetic structures

| | Weight (kg) | Difference (%) | Total deformation (mm) | Equivalent stress (MPa) | Difference (%) | Force reaction (N) | Difference (%) |
|--|-------------|----------------|------------------------|-------------------------|----------------|--------------------|----------------|
| Re-Entrant Geometry | 0,120 | | 0,51143 | 4,259 | | 57,38 | |
| Functionally Graded Re-Entrant Geometry | 0,136 | %13 | 0,50719 | 6,783 | %59 | 96,37 | %68 |
| RCW Honeycomb Geometry | 0,151 | | 0,52034 | 13,827 | | 321,3 | |
| Functionally Graded RCW Honeycomb Geometry | 0,165 | %9 | 0,51068 | 22,061 | %59 | 500,2 | %55 |
| Ellipse Geometry | 0,234 | | 0,56699 | 40,08 | | 2918,8 | |
| Functionally Graded Ellipse Geometry | 0,266 | %13 | 0,57888 | 48,828 | %21 | 4189,5 | %43 |

4.CONCLUSION

In this study, the mechanical behaviors of auxetic structures were examined after they were redesigned using a functional grading approach. The results show that functionally graded auxetic structures have much better

load-bearing capacity than the original designs, even though they have a small increase in weight. This improvement is especially clear in the FG re-entrant, FG rcw honeycomb, and FG ellipse structures, which saw large increases in their ability to carry loads—68%, 55%, and

43%, respectively—while only gaining a little extra weight. These results suggest that the small weight increase is worth it because of the big improvements in performance, making functionally graded designs a good choice for situations where strength and load-bearing capacity are important.

Additionally, the study pointed out that functionally graded auxetic structures have unique displacement characteristics. The way they deform can be controlled by changing the design. This ability to control deformation creates new possibilities for custom mechanical responses in applications that need precision and flexibility, such as in aerospace, medical implants, protective equipment, and flexible electronics.

In conclusion, using functional grading in auxetic structures not only improves their mechanical properties but also allows for new and creative design options for high-performance applications. Future research could focus on optimizing these structures for specific uses, especially by controlling how they deform to get the desired results.

ACKNOWLEDGMENTS

This work has been supported by Yildiz Technical University Scientific Research Projects Coordination Unit under project number FYL-2023-5861.

This article was presented orally at the 7th International 3D Printing Technologies and Digital Industry Congress and the abstract was printed in the "Abstract Book".

ABBREVIATIONS

| | |
|---------|---------------------------------|
| ABS | Acrylonitrile Butadiene Styrene |
| CFR-PLA | Carbon Fiber Poly(lactic Acid) |
| FDM | Fused Deposition Modeling |
| FGS | Functionally Graded Structure |
| PLA | Poly(lactic Acid) |
| R&D | Research and Development |
| RCA | Re-entrant Chiral Auxetic |
| RCW | Re-entrant Combined-Wall |
| SLA | Stereolithography |

REFERENCES

1. Ken E. E., "Auxetic polymers: a new range of materials" *Endeavour*, Vol. 15, Issue 4, Pages 170–174, 1991.

2. Uzun M., "Negatif Poisson Oranına Sahip (Auxetic) Malzemeler Ve Uygulama Alanları Negative Poisson Ratio (Auxetic) Materials and Their Applications" *J Text Eng*, Vol.77, Pages 14–18, 2017.

3. Öztürk B., "3 Boyutlu Yazıcı İle Üretilen Sandviç Yapıların Statik Ve Dinamik Yük Altında Davranışlarının İncelenmesi", Yüksek Lisans Tezi Bursa Teknik Üniversitesi, 2020.

4. Özen AT., "Re-Entrant Şekilli Ökzetik Yapıların Ve Bor Nitrür Katkılı Filamentlerin Katmanlı İmalat İle Üretimi Ve Karakterizasyonu", Yüksek Lisans Tezi, Gazi Üniversitesi, 2021.

5. Ergene, B., Yalçın, B., "Eriyik yığma modelleme (EYM) ile üretilen çeşitli hücreli yapıların mekanik performanslarının incelenmesi" [Investigation On Mechanical Performances Of Various Cellular Structures Produced With Fused Deposition Modeling (FDM)] [article in Turkish], *Journal of the Faculty of Engineering and Architecture of Gazi University*, Vol. 38, Issue 1, Pages 201-218, 2023.

6. Yazdani Sarvestani H., Akbarzadeh A. H., Niknam H., Hermenean K., "3D printed architected polymeric sandwich panels: Energy absorption and structural performance." *Composite Structures*, Vol. 200, Pages 886-909, 2018.

7. Alomarah, A., Ruan, D., Masood, S., Sbarski, I., Faisal, B., "An Investigation Of In-Plane Tensile Properties Of Re-Entrant Chiral Auxetic Structure", *The International Journal of Advanced Manufacturing Technology*, Vol. 96, Pages 2013-2029, 2018.

8. Li, X., Wang, Q., Yang, Z., Lu, Z., "Novel Auxetic Structures With Enhanced Mechanical Properties. *Extrem Mech Lett*", *Extreme Mechanics Letters*, Vol. 27, Pages 59-65, 2019.

9. Li, C., Shen, H.S., Wang, H., "Nonlinear Dynamic Response Of Sandwich Plates With Functionally Graded Auxetic 3D Lattice Core", *Nonlinear Dynamics*, Vol. 100, Pages 3235-3252, 2020.

10. Alomarah, A., Masood, S.H., Sbarski, I., Faisal, B., Gao, Z., Ruan, D., "Compressive Properties Of 3D Printed Auxetic Structures: Experimental And Numerical Studies", *Virtual and Physical Prototyping*, Vol. 15, Issue 1, Pages 1-21, 2020.

11. Zhou, Y., Pan, Y., Chen, L., Gao, Q., Sun, B., "Mechanical Behaviors Of A Novel Auxetic Honeycomb Characterized By Re-Entrant Combined-Wall Hierarchical Substructures", *Materials Research Express*, Vol. 9, Issue 11, 115802, 2022.

12. Türkoğlu, İ.K., “3 Boyutlu Eklemeli Üretim Yöntemiyle Üretilmiş Termoplastik Esaslı Ökzetik Çekirdek Geometrilik Sandviç Yapıların Statik ve Dinamik Yükler Altında Davranışının İncelenmesi”, Doktora Tezi, [Investigation of Behavior of Thermoplastic Sandwich Structures With Auxetic Core Geometries Produced by 3 Dimensional Additive Manufacturing Method Under Static and Dynamic Loads] [PhD Thesis in Turkish], Bursa Uludağ University, ProQuest Dissertations Publishing, 2020.
13. Yousefi, A., Jolaiy, S., Lalegani Dezaki, M., Zolfagharian, A., Serjoui, A., Bodaghi, M., “3D-Printed Soft And Hard Meta-Structures With Supreme Energy Absorption And Dissipation Capacities In Cyclic Loading Conditions”, *Advanced Engineering Materials*, Vol. 25, Issue 4, 2201189, 2023.
14. Cheng, X., Zhang, Y., Ren, X., Han, D., Jiang, W., Zhang, X.G., et. al., “Design And Mechanical Characteristics Of Auxetic Metamaterial With Tunable Stiffness”, *International Journal of Mechanical Sciences*, Vol. 223, 107286, 2022.
15. Gülcan, O., Şimşek, U., Kavas, B., “Metal Additive Manufactured Functionally Graded Structures” , *Mühendis ve Makine*, Vol. 62, Issue 702, Pages 1-22, 2021.
16. Karaca, A.A., “Auxetic malzemelerin deneysel olarak ve sonlu elemanlar metodu ile incelenmesi”, Yüksek Lisans Tezi, Bursa Teknik Üniversitesi, Bursa, 2016.
17. Kabaoğlu, C., “Investigation Of Sandwich Composites With Auxetic Core Under Static Loading”, *El-Cezeri Journal of Science and Engineering*, Vol. 9, Issue 1, Pages 350-359, 2022.
18. Demirbaş, M.D., Demir, O., “Determination Of Static Behavior Of Sandwich Composites With Negative Poisson Ratio”, *International Journal of Engineering Research and Development*, Vol. 14, Issue 1, Pages 347-359, 2022.
19. Murat, F., Korkmaz, İ.H., Şensoy, A.T., Kaymaz, İ., “Eklemeli Üretim İle Elde Edilen Fonksiyonel Kademelendirilmiş Gözenekli İmplantlar”, *Gazi Üniversitesi Fen Bilimleri Dergisi Part C: Tasarım ve Teknoloji*, Vol. 7, Issue 3, Pages 540-553, 2019.
20. Zhu, Y., Jiang, S., Zhang, Q., Li, J., Yu, C., Zhang, C., “A Novel Monoclinic Auxetic Metamaterial With Tunable Mechanical Properties”, *International Journal of Mechanical Sciences*, Vol. 236, 107750, 2022.
21. Han, D., Ren, X., Zhang, Y., Yu Zhang, X., Gang Zhang, X., Luo, C., et. al., “Lightweight Auxetic Metamaterials: Design And Characteristic Study”, *Composite Structures*, Vol. 293, 115706, 2022.
22. Hao, J., Han, D., Zhang, X.G., Zhang, Y., Jiang, W., Teng, X.C., et. al., “Novel Dual-Platform Lightweight Metamaterials With Auxeticity”, *Engineering Structures*, Vol. 270, 114891, 2022.
23. Páscoa F.T., Machado C.M., Cardoso J.O., Borges J.P., Velhinho A., “Methodology for modelling and simulation of tailored 3D functionally graded auxetic metamaterials” *The International Journal of Advanced Manufacturing Technology* Vol. 125, Pages 4647–4661, 2023.
24. Etemadi E., Hosseinabadi M., Scarpa F., Hu H., “Design, FDM printing, FE and theoretical analysis of auxetic structures consisting of arc-shaped and Dumbbell-shaped struts under quasi-static loading” *Composite Structures* Vol. 326, 117602, 2023.
25. Ge Z., Hu H., Liu Y., “A finite element analysis of a 3D auxetic textile structure for composite reinforcement” *Smart Materials and Structures* Vol. 22, 084005, 2013.
26. Li Z.Y., Wang X.T., Ma L., Wu L.Z., Wang L., “Auxetic and failure characteristics of composite stacked origami cellular materials under compression” *Thin-Walled Structures* Vol. 184, 110453, 2023.
27. Devalk, T., Lakes, R., “Poisson’s Ratio And Modulus of Gyroid Lattices”, *Physica Status Solidi*, Vol. 258, Issue 12, 2100081, 2021.
28. Ha, C.S., Plesha, M.E., Lakes, R.S., “Chiral Three-Dimensional Isotropic Lattices With Negative Poisson’s Ratio”, *Physica Status Solidi*, Vol. 253, Issue 7, Pages 1243-1251, 2016.
29. Hassan, A., Abood, A.M., Khalaf, H.I., Khazal, H., “A review of functionally graded materials including their manufacture and applications”, *International Journal of Mechanical Engineering*, Vol. 7, Issue 1, Pages 744-755, 2022.
30. Hüner B., Kısı M., Uysal S., Uzgören İ.N., Özdoğan E., Süzen Y.O., et al. “An Overview of Various Additive Manufacturing Technologies and Materials for Electrochemical Energy Conversion Applications” *ACS Omega*, Vol. 7, Issue 45, Pages 40638–40658.

31. Shekhar N., Mondal A., “Synthesis, properties, environmental degradation, processing, and applications of Polylactic Acid (PLA): an overview” *Polymer Bulletin*, Vol. 81, Issue 13, Pages 11421-11457, 2024.

32. Farah S., Anderson D.G., Langer R.. “Physical and mechanical properties of PLA, and their functions in widespread applications —A comprehensive review” *Adv Drug Deliv Rev*, Vol. 107, Pages 367–392, 2016.



ULUSLARARASI 3B YAZICI TEKNOLOJİLERİ
VE DİJİTAL ENDÜSTRİ DERGİSİ

INTERNATIONAL JOURNAL OF 3D PRINTING
TECHNOLOGIES AND DIGITAL INDUSTRY

ISSN:2602-3350 (Online)

URL: <https://dergipark.org.tr/ij3dptdi>

AN INDUSTRIAL APPLICATION OF DIGITAL TWIN FOR A SMART FACTORY MODEL USING COPPELIASIM

Yazarlar (Authors): Cüneyt KILIÇ , Kamil ÇETİN , Mehmet Erdal ÖZBEK 

Bu makaleye şu şekilde atıfta bulunabilirsiniz (To cite to this article): Kılıç C., Çetin K., Özbek M. E., “An Industrial Application of Digital Twin for A Smart Factory Model Using Coppeliiasim” *Int. J. of 3D Printing Tech. Dig. Ind.*, 8(3): 316-325, (2024).

DOI: 10.46519/ij3dptdi.1452734

Araştırma Makale/ Research Article

Erişim Linki: (To link to this article): <https://dergipark.org.tr/en/pub/ij3dptdi/archive>

AN INDUSTRIAL APPLICATION OF DIGITAL TWIN FOR A SMART FACTORY MODEL USING COPPELIASIM

Cüneyt KILIÇ^a, Kamil ÇETİN^{a,b}, Mehmet Erdal ÖZBEK^{a,b}

^aIzmir Katip Celebi University, Faculty of Engineering and Architecture, Department of Electrical and Electronics Engineering, Izmir, TURKIYE

^bIzmir Katip Celebi University, Akıllı Fabrika Sistemleri Uygulama ve Araştırma Merkezi, Izmir, TURKIYE

*Corresponding Author: kamil.cetin@ikcu.edu.tr

(Received: 14.03.2024; Revised: 06.11.2024; Accepted: 25.11.2024)

ABSTRACT

A digital twin is quickly becoming a necessary component of manufacturing. When combined with Internet of Things (IoT) technology, it is possible to fulfil Industry 4.0's requirement for a digital transformation to create a smart factory. Many IoT devices, such as sensors, detect physical phenomena in their environments, collect data, and communicate. Digital twins that mimic the features and capabilities of real physical IoT devices can also be realized. Digitalization using digital twin requires not only IoT sensors but also software tools for virtualization. However, there are limited number of practical applications for the digitalization of large and complex systems. In this work, a smart factory model is used to develop its digital twin. Because the simulation software of industrial automation system manufacturers is licensed and different systems are incompatible with each other for digital twin, CoppeliaSim digital twin software, which is open source and can work independently of the industrial automation system model, was used in this study. The corresponding physical sensor data is transferred to CoppeliaSim in real time. Moreover, three scenarios were realized by achieving bilateral data transmission and control between the physical and digital twin models. Instant status monitoring presents the performance of digital twinning. While most of the digital twin studies in the literature are carried out either by transferring data only from the virtual system to the physical system or only from the physical system to the virtual system, in this study, simultaneous data exchange was implemented between the real and virtual systems.

Keywords: Digital Twin, Internet of Things, Smart Factory, Industry 4.0, CoppeliaSim.

1. INTRODUCTION

The quality of life and the advantages that technological developments offer to the human beings are seen through the revolutions in industry. The most recent stage of the industrial revolution, known as "Industry 4.0," is centred on deploying cutting-edge technologies to digitalise production processes [1-2]. The traditional manpower-based factories continue to be replaced by smart factories or smart working environments that are digitalized and therefore they are able to reduce the unskilled manpower. The ever-increasing production and efficiency requirements with reduced costs is a reality that every manufacturing company demands. The Internet of Things (IoT) has made it possible for Industry 4.0 to become

increasingly digital. IoT connects physical items to the Internet so that they may be managed remotely, making production processes smarter and more efficient [2-3]. IoT technology converts data taken from the physical world into a digital form with developed sensors. The transfer of those data to the virtual environment ensures the digitalization and named as "digital twinning" of the physical world [4]. Using digital twin technology, a synchronized virtual representation of a real-world object is created in a digital environment [1, 4-5]. The object transferred to the virtual environment is a real-time measured data. In this way, it is possible to easily and effectively monitor and analyze the performance of the physical object in the digital

environment [6]. The digital twin is widely applied in various industry sectors, including agriculture, electricity generation, healthcare, and smart factory environments [7]. Because it enables free design testing and early problem discovery, a digital twin is the recommended technology for enhancing production integration and quality [8].

While the digital twin embraces big industry manufacturing processes, there are also small-scale system models mentioned in the literature. For example, Park et al. [9] studied about reinforcement learning and the realization of a digital twin of the micro smart factory model. In [10], a digital twin of a real-life painting robot arm is created using the CoppeliaSim simulation software [11]. In [12], another digital twin study carried out in the Gazebo simulation software is related to the localization of the robot [13]. It was also shown that digital twin technology was used in the Gazebo simulation software of an autonomous mobile robots [14]. In the study of Al-Geddawy et al. [15], a digital twin of a low-cost system was realized in a different simulation environment called RoboDK [16]. Similarly, the UR3 robot arm is observed, whose digital twin was realized in CoppeliaSim [17].

As mentioned above, digital twin studies in the literature have increased recently and mostly simulation studies of small-scale systems such as robot arms or one-way control from the simulation to the real system have been provided. The aim of this paper is to raise awareness about the creation of a digital twin of a large-scale factory model while maintaining bidirectional control between physical and simulation systems. Thus, the remaining of this paper is organized as follows: Section 2 explains the working system of the smart factory and its creation in the simulation software. Section 3 shows the communication method between the software and the smart factory. Section 4 presents the experimental studies and results. Section 5 briefly evaluates and discusses the study with the results. Finally, the paper terminates with discussions and future works in Conclusion section.

2. PHYSICAL AND DIGITAL TWIN MODELS OF THE SMART FACTORY

Computer-aided design (CAD) and simulation programs are needed to create a smart production system and to realize a digital twin of this system based on real data. There are many designs and simulation software developed to build a digital twin of the real system in virtual environments. CAD modeling software (e.g., SolidWorks [18], AutoCAD [19], SketchUp [20]) is consulted to create an exact replica of the designs of physical objects in the real world and the designs in the virtual environment [21]. Those environments are generally CoppeliaSim, Matlab [22], Gazebo, RoboDK. In this study, SolidWorks having the most common library, is preferred as the CAD program. The distributed control architecture of the open-source CoppeliaSim robotic simulator software (formerly known as V-REP) is built on an integrated development environment. Each object/model in CoppeliaSim can be independently controlled using an API (Application Programming Interface) client, a plug-in, and an embedded script. CoppeliaSim's versatility and suitability for multi-robot applications stem from these properties. The programming languages Lua [23], Octave [24], Matlab, C/C++, Python, and Java are also supported. According to Rohmer et al. [25], CoppeliaSim is utilised as a digital twin, for fast algorithm development, factory automation simulations, and rapid prototyping and validation. Programmable Logic Controller (PLC) is used to control production lines, motors and robotic systems in smart factory environments.

2.1. Physical Twin of Smart Marble Factory

In this study, we aim to build a digital twin of a marble factory. For this purpose, we use a smart marble factory scale model shown in Figure 1 in our Smart Factory Systems Application and Research Center (AFSUAM) laboratory. In this section, a brief information is given about the working principle of our model. It consists of two production lines and three workstations. The first workstation of the smart factory model, shown in Figure 2, will be used to create its digital twin. The first workstation has conveyors, ovens, temperature sensors, distance sensors, direct current (DC) encoder motors, PLC, relays, microprocessor (MPU) and robot arms. In the first workstation, the slabs of marble are placed on the production line with

the help of a robot arm, manually filled with epoxy process to close the cracks on the front surface, mesh and epoxy processes are applied again to the back surface for durability, and drying processes are carried out to dry the applied epoxy. In the rest of the article, the first workstation of the smart factory scale model is simply called a physical twin.



Figure 1. Smart factory scale model in AFSUAM laboratory.

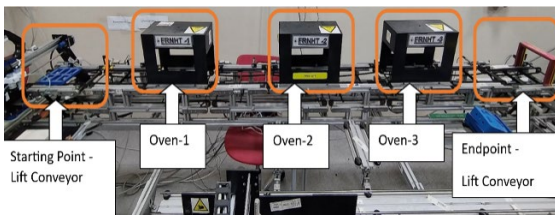


Figure 2. The first workstation of smart factory scale model: Locations of ovens and lift conveyors.

The electrical connection schematics of the motors, drives, sensors, MPUs, PLC and central data acquisition and control unit used in the physical twin of the first workstation of the smart factory model photographed in Figure 1 and Figure 2 is drawn in Figure 3. The 8 DC motors were used for the 8 conveyors. For the sensors, the 3 MAX6675 K-type thermocouples and the 11 IME12-08NPSZC0S model inductive proximity sensors were used, which are efficient and offer high performance. Arduino Uno was used as the MPU and Python was preferred for programming language. Mitsubishi FX5U PLC module with high input output speed was used for data collection and control operations. An API is required to ensure communication between the simulation program CoppeliaSim and the PLC system. For this communication, the Python programming language is used as the API between the personal computer (PC) on which CoppeliaSim

is run and the PLC where the smart factory model is controlled. Therefore, a double-sided control of the factory model is provided in the virtual environment with real-time data.

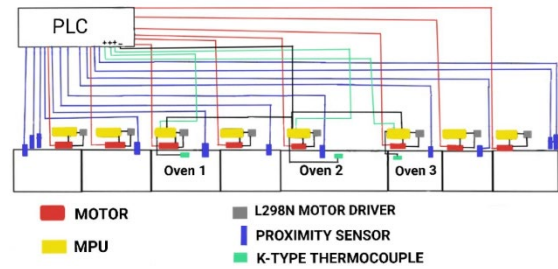


Figure 3. Electrical connection schematics of the equipment in the smart factory scale model.

As shown in Figure 4, the connections of the equipment used in the physical twin are as follows. For the 24V supply voltage of the PLC, the red (+) and blue (-) cables of the SMPS (Switch Mode Power Supply) are connected to the L (+) and N (-) pins of the PLC, respectively. The DC encoder motors used for conveyors have six cables (red, black, green, blue, yellow, white). For the motor power, red (+) and black (-) cables are connected to the out1 and out2 inputs of the motor driver, respectively. The yellow and white cables are for the encoder A and B outputs of the motor, respectively, and these outputs are connected to the digital inputs of the PLC. The blue and green cables are for the encoder supply and ground and are connected to the 5V and ground pins of the MPU, respectively. The enable, in1, and in2 pins of the motor driver are connected to the MPU pins through the brown, green, and purple cables, respectively. The MAX6675 K-type thermocouple has five wires (black, red, yellow, blue, green). The red and black cables are for the 5V supply and ground connections of the MPU, respectively. The yellow, blue, and green cables are for 'sck', 'cs' and 'so' connections of the MPU, respectively. The temperature values received from the MPU are converted to values in the range of 0-255 in the MPU code, and these values are applied as voltage to the analog input (Built-in Analog Input) of the PLC. The proximity sensor has three cables (black, blue, brown). The connections of the proximity sensor are as follows, brown (+) and blue (-) cables are connected to the (+) and (-) poles of the SMPS, respectively. The cable that transfers

proximity sensor data is the black cable, and it is connected to the digital input of the PLC.

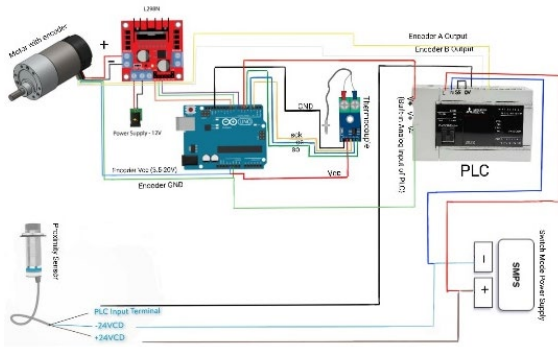


Figure 4. Physical twin connections between sensors, motors/drivers, MPU, PLC input and outputs.

The Mitsubishi FX5U PLC is used to control all subsystems in the physical twin and receive all sensor data and is programmed with the ladder method. As shown in Figure 4 and explained above, the input and outputs of PLC are connected to the sensors and motors/drivers used in the physical twin. The physical twin has a three degree-of-freedom robot arm at the starting and ending points. In addition, there are a total of twelve conveyors, six conveyors on the upward line and four conveyors on the downward line and excluding two lifting type conveyors at the starting and ending points. Lift type conveyors are conveyors that have the ability to move up and down. The operation of the conveyors is carried out by DC encoder motors integrated into the conveyor. DC encoders are electromechanical devices that, when the motor shaft they are linked to moves, generate digital electrical signals. There are three ovens placed on the conveyors in the upward line. These ovens (i.e., FRNHT-1, FRNHT-2, FRNHT-3) are placed on the third, fifth, and sixth conveyors, respectively. The temperature sensors are integrated into the three ovens. The proximity sensors used to detect the marble slabs are integrated into each conveyor.

The operation of the lift conveyors and oven lines of the physical twin is shown in the working diagram given in Figure 5. In this flow diagram, the decision-making process is carried out by checking whether the proximity sensors on the system detect the product or not.

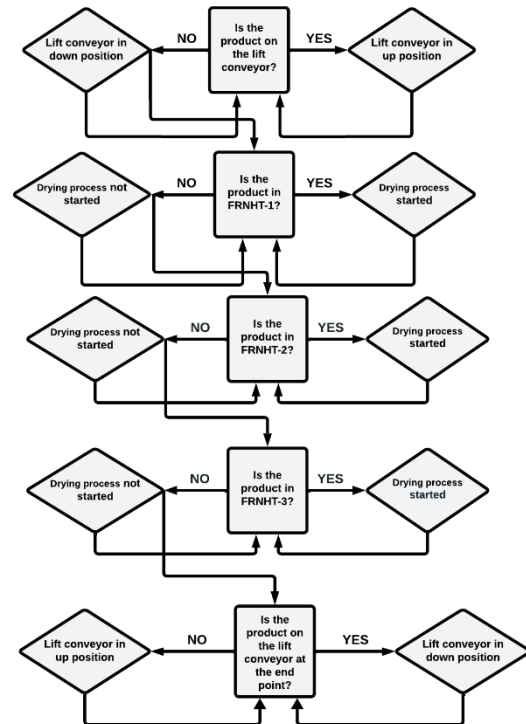


Figure 5. Flow diagram of lift conveyors and oven lines in the first workstation of the smart factory scale model.

The robot arm being at the starting point of the first workstation places the marble block on which the epoxy has been applied and which is desired to be dried, onto the transport tray on the first lift type conveyor. The lift type conveyor is in the down position before the starting moment. Proximity sensors connected to the conveyor move to the up position after detecting the marble placed on the transport tray on the conveyor. Once the proximity sensors detect the product, the motors start, and the conveyor starts moving. When the transport tray leaves the lift conveyor, it is detected by proximity sensors and the conveyor is allowed to return to its down position. When the transport tray moving on the conveyor reaches the oven areas on the third, fifth, and sixth conveyors, respectively, the drying process is started thanks to the proximity sensors. Drying processes take place within the time and temperature specified by the user. After the drying process is completed, the marble comes out as a semi-finished product. When the transport tray reaches the lift conveyor at the end point, the conveyor, which is normally in an up position, comes to a down position as a result of the proximity sensors detecting the semi-finished

product. The semi-finished product on the tray is taken with the help of a robot arm and placed on smart transport wagons. After the semi-finished product is picked by the robot arm, the transport tray returns to its starting position via the downward conveyors to place the new product on it.

2.2. Digital Twin of the Physical Twin

In this section, a digital twin of the physical factory model created in the real environment is designed in the simulation (virtual) environment for monitoring and double-sided control. The digital twin of the smart factory is realized using the CoppeliaSim simulation software. All parts of the physical twin in the real environment are drawn on Solidworks and uploaded to CoppeliaSim in Unified Robotics Description Format (URDF) and Standard Triangle Language (STL) format. After the designed drawings are loaded into the simulation environment, the dimensions of the materials used in the physical twin are applied in the simulation environment and the design of the real system is established by combining the drawings. The length of the lift conveyors is 35 cm. The five of the upward conveyors is 35 cm long, the remaining is 70 cm long. Six of the downward conveyors are 70 cm long and the remaining is 35 cm long. The width of all conveyors is 26.3 cm. The ovens are 35 cm deep, 25 cm long, and 17.8 cm wide. The established simulation environment, as shown in Figure 6, shows the locations of the equipment (conveyors and ovens) used in the system, where the physical twin is replicated on the CoppeliaSim simulation software.

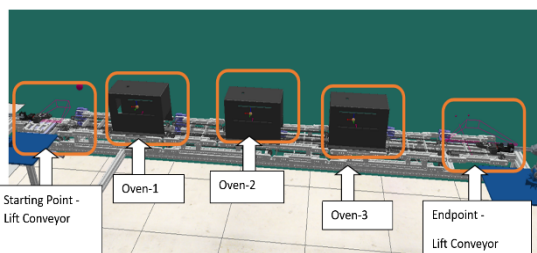


Figure 6. Simulation of the first workstation of the smart factory scale model on CoppeliaSim.

After the installation in the simulation environment, the necessary tools such as sensors and conveyor movement providers are integrated into the system with the help of simulation tools in environment. The tools are written in the Lua programming language, and

they are ensured to work according to the requirements in the physical twin.

3. COMMUNICATION BETWEEN THE PHYSICAL AND DIGITAL TWIN

After the installation of the real system in the simulation environment, bidirectional data flow and control must be ensured between the real and virtual systems in order to fully establish digitalization [26]. Firstly, in order to enable data flow between the real and virtual systems, the PC on which the CoppeliaSim simulation runs and the PLC that enables the real system to operate must communicate. An API is written using the Python language so that CoppeliaSim can communicate with the PLC used in the physical twin. Python is a useful programming language that contains the necessary libraries of PLC and CoppeliaSim simulation. As shown in Figure 7, the PLC-PC communication and PC-CoppeliaSim communication are carried out using the necessary software and hardware.

3.1. PLC-PC Communication

Mitsubishi PLC uses GX-Works3 as the program interface. In the PLC part of the communication, the SeamLess Message Protocol (SLMP) communication protocol is used on GX-Works3. In the PC part of the communication, the "HslCommunication" library of the Python language is used. The HslCommunication library is a library that supports industrial communication protocols in the Python programming language [27]. With this method, PLC and PC communication is provided on the software. In terms of hardware, the Ethernet ports are used for maintaining communication between the PLC and the PC.

3.2. PC-CoppeliaSim Communication

For the software-based communication between the PC and CoppeliaSim, the "sim" library of the Python language and the following necessary communication codes are used with `sim.simxStart(,);`

- `connectionAddress`
- `connectionPort`
- `waitUntilConnected`
- `doNotReconnectOnceDisconnected`
- `timeOutInMs`
- `commThreadCycleInMs`

In the CoppeliaSim, it is communicated with the `simRemoteApi.start(connectionPort)` code.

With this method, the PC and CoppeliaSim are communicated.

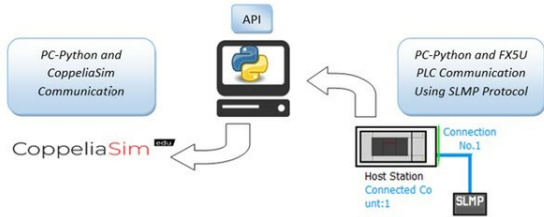


Figure 7. PLC-PC and PC-CoppeliaSim communication diagrams.

Many of the fundamental functional applications of industrial software development, including Mitsubishi PLC software, are integrated with the HslCommunication Library, an industrial IoT-based computer communication architecture implementation. An example part of the Python code for PLC-PC and PC-CoppeliaSim communication via the HslCommunication plugin can be seen in Figure 8. In this code, first, "sim" library is imported with HslCommunication plugin and Arduino MPU is connected to PC via the serial COM8 port by determining the IP address and baud rate. Then, using the "MelsecMcNet" node of the HslCommunication plugin, the motor velocity data, temperature and proximity sensor values are read from Arduino's pins to send commands to the client CoppeliaSim.

```
import sim, serial, time
from HslCommunication import MelsecMcNet, SoftBasic
arduino = serial.Serial(port='COM8', baudrate=9600, timeout=1)

if __name__ == "__main__": melsecMcNet = MelsecMcNet("192.168.1.10", 4001)
# Connect to CoppeliaSim
clientID = sim.simxStart('127.0.0.1', 19999, True, True, 500, 5)

def send_command(command): arduino.write(f"{command:0f}".encode())

while True:
    #sim.simxGetFloatSignal(clientID, "velocity_data", sim.simx_opmode_oneshot)
    send_command(a[1])
    x1 = melsecMcNet.ReadInt32("D0")
    x2 = melsecMcNet.ReadInt32("D5")
    Ps_x0=melsecMcNet.ReadBool("X0")
    Ps_x1=melsecMcNet.ReadBool("X1")
    Ps_x2=melsecMcNet.ReadBool("X2")
    Ps_x3=melsecMcNet.ReadBool("X3")
    print("Temperature 1,2,3 :")
    printReadResult(x1)
    printReadResult(x2)
    print("Proximity 0,1,2,3 :")
    printReadResult2(Ps_x0)
    printReadResult2(Ps_x1)
    printReadResult2(Ps_x2)
    printReadResult2(Ps_x3)

    if arduino.readline().decode('utf-8').strip():
        sim.simxSetStringSignal(clientID, "velocity", str(line), sim.simx_opmode_blocking)
    time.sleep(1)
```

Figure 8. A part of a long Python code with HslCommunication library for PLC-PC and PC-CoppeliaSim communication.

4. EXPERIMENTAL STUDIES AND RESULTS

After the communication infrastructure between physical and digital twin has been completed, experimental studies are carried out

for three different scenario examples to demonstrate the operability of the system. The scenarios performed are listed as follows:

- Controlling the physical twin through the digital twin
- Controlling the digital twin through the physical twin
- Providing simultaneous double-sided control between the physical and the digital twin

4.1. PLC-PC Communication

As an example for the first scenario, as seen in Figure 9, when the proximity sensors used in the digital twin detect the product placed by the robot arm on the first workstation, the DC encoder motors connected to the conveyors in the physical twin are started and then the speed values of the motor are recorded according to the voltage change. The proximity sensors in CoppeliaSim determine that the DC encoder motor in the real system moves or does not move, depending on whether it detects the product or not.

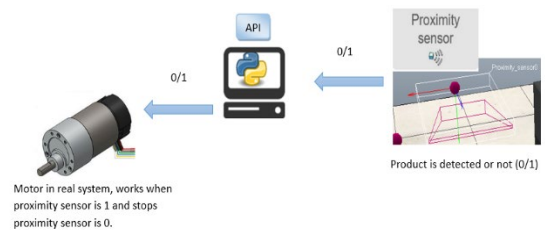


Figure 9. The relationship between the proximity sensors in the digital twin and the motors in the physical twin.

4.2. Controlling the Digital Twin Through the Physical Twin

As an example for the second scenario, as seen in Figure 10, when the proximity sensors used in the physical twin detect the product placed on the lift conveyor with the help of the robot arm, the "True" or "False" values are sent to the digital twin and then the lift conveyors in the simulation environment move or not move according to the "True" or "False" values, respectively. As shown in Figure 11 and Figure 12, the proximity sensor in the real system ensures that the lift conveyor in CoppeliaSim moves or does not move, depending on whether it detects the product or not.

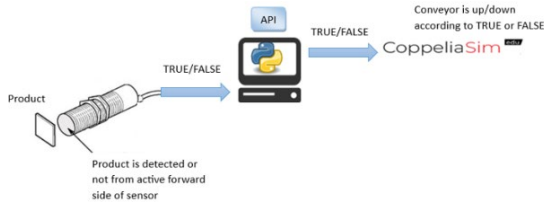


Figure 10. The relationship between the proximity sensors in the physical twin and the lift conveyors in the digital twin.

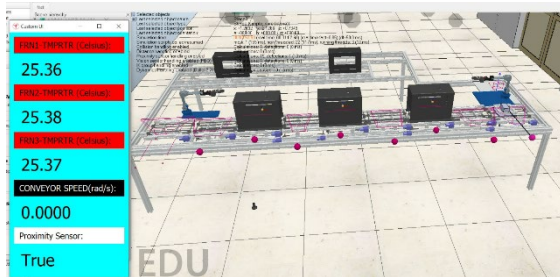


Figure 11. The lift conveyor in CoppeliaSim is controlled with the proximity sensors in the real system. In the “True” state, the lift conveyor moves to the upward position.

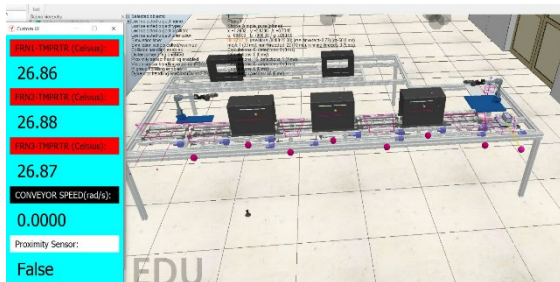


Figure 12. The lift conveyor in CoppeliaSim is controlled with the proximity sensors in the real system. In the “False” state, the lift conveyor moves to the downward position.

4.3. Double-Sided Control Between the Physical and the Digital Twin

The physical twin can be controlled via the digital twin and the digital twin can also be controlled via the physical twin, as shown in Figure 13. As an example for the third scenario, the example scenarios applied above are implemented simultaneously in a single scenario. In this scenario, the temperature data obtained from the temperature sensors in the oven lines, the speed data obtained from the DC encoder motor connected to the conveyor, and the data obtained from the proximity sensors used to detect the positions of the marble slabs received from the physical twin are transferred to the CoppeliaSim interface, and the digital twin is operated according to these real data. The interface shown in Figure 14 is created

using the "xml" language in CoppeliaSim. On the other hand, the speed values of the motors can be adjusted as desired via the digital twin, and in this way the speeds of the real motors in the physical twin can be controlled. Thus, instant status monitoring and simultaneous double-sided control of the physical and digital twin is provided.

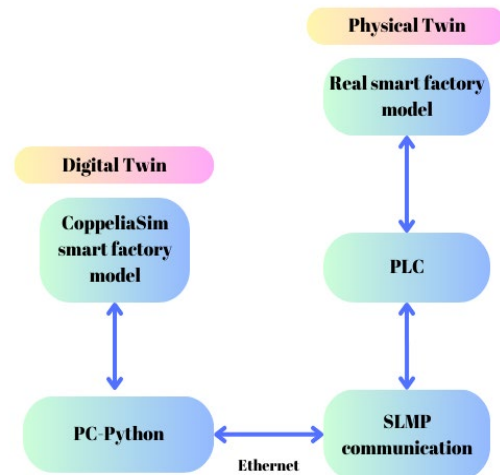


Figure 13. Double-sided control block diagram.

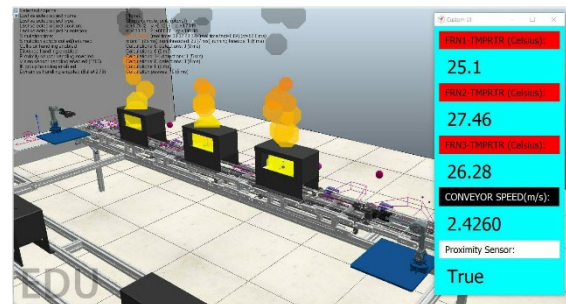


Figure 14. Implementation of the digital twin in CoppeliaSim with the real oven temperatures, motor speeds and proximity sensors’ data coming from the smart factory scale model.

4.4. DC Encoder Motor Data

Via the CoppeliaSim interface, the voltage values in the range of 0-12 Volts are applied to the DC encoder motor used in the physical twin, and the speed data of the motor in radians per second and the current data drawn by motor can be plotted as shown in Figure 15.

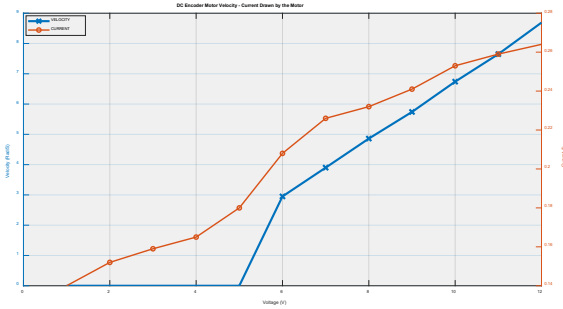


Figure 15. Speed change of the DC encoder motor in rad/s and current drawn by the motor when the voltage is applied in the range of 0-12V.

4.5. Oven Temperature Data

The real temperature values in the oven lines are sent to the digital twin via the physical twin and displayed on the CoppeliaSim interface. As shown in Figure 16, the temperature values recorded every second show the temperature values in the laboratory environment of the smart factory model.

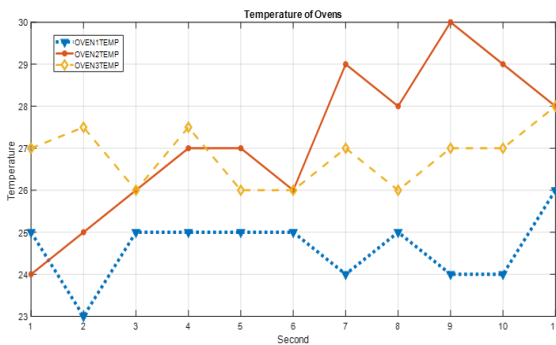


Figure 16. Recorded temperature data of three ovens transferred from the physical twin to the digital twin.

5. EVALUATION AND DISCUSSION

While most digital twin studies in the literature [1-8] are carried out either by transferring data from the virtual system to the physical system only, as we did in the first experimental scenario, or from the physical system to the virtual system only, as we did in the second experimental scenario, we can simultaneously exchange data between the real and virtual systems, as we have shown in the third experimental scenario in this study. To exemplify this, with the two studies we conducted in the third experimental scenario, we simultaneously transferred the motor velocity data from the virtual system to the real system and loaded the temperature data from the real system to the virtual system.

As seen in Figure 15, although the DC motor draws a maximum current of 0.18A until 5V voltage is applied, the rotation speed of the motor shaft is 0rad/s as seen from the encoder data. When the voltage is applied to the motor step by step from 5V to 12V, the current consumed increases gradually from 0.14A to 0.28A and the rotation of the motor shaft accelerates from 0rad/s to 9rad/s in approximately linear. According to the different voltage values sent from the CoppeliaSim interface, the movement of the real motor in the physical twin could be observed simultaneously. On the other hand, as seen in Figure 16, the values of three different temperature sensors were measured every second between 23 and 30 centigrade degrees for 11 seconds. The sensor data on the real physical twin was sent to the CoppeliaSim interface and temperature changes could be observed simultaneously. Although it is stated that double-sided data transfer between the physical and digital twins is performed simultaneously, there is a negligible time delay of around a few milliseconds due to the Ethernet communication between the PLC and the PC.

6. CONCLUSION

In this study, a synchronized digital twin of the first workstation of the scale model of the smart marble factory located in AFSUAM has been created in the CoppeliaSim simulation software. The communication of the digital twin with the PLC of the smart factory model and the PC on which the CoppeliaSim program is running has been carried out using an API. In order to test the overall system, three different scenarios have been implemented on the system. According to the results of these scenarios, the control of the real system through the simulation environment, the control of the simulation environment over the real system, and the control of both scenarios as a single scenario were achieved simultaneously between the virtual and the real system. We believe that with this digital twin model and double-sided simultaneous control method we have developed, different system designs for the smart factory model can be realized faster and easier.

The current study is restricted to a single marble factory workstation model. There are several obstacles to overcome before this digital twin can fully capture the scope of the smart factory, with its numerous interconnected workstations and intricate manufacturing procedures. More research is needed to create a digital twin model that fully captures the smart factory because of problems including growing data volumes, network congestion, and processing power demands. In-depth testing to assess the scalability and performance of the digital twin across the board in the smart marble plant can be carried out by addressing more comprehensive scalability testing. This means that further research can be done in the future that calls for the system to manage bigger data amounts, more devices, and more intricate physical interactions. In addition, in the smart factory model, it will be possible to detect and immediately intervene in production malfunctions that may occur in the future, as well as to monitor the real-time status of the real system and perform product performance analysis.

ACKNOWLEDGEMENT

This study was supported by Scientific and Technological Research Council of Turkey (TUBITAK) under the Grant Number 123E288. The authors thank to TUBITAK, İzmir Kâtip Çelebi University Smart Factory Systems Application and Research Center (AFSUAM) and Kur Mermer San. ve Tic. A.S. for their supports.

REFERENCES

1. Kumas, E., & Erol, S., "Endüstri 4.0'da Anahtar Teknoloji Olarak Dijital İkizler", *Politeknik Dergisi*, Vol. 24, Issue 2, Pages 691-701, 2021.
2. Kalsoom, T., Ahmed, S., Rafi-ul-Shan, P. M., Azmat, M., Akhtar, P., Pervez, Z., & Ur-Rehman, M., "Impact of IoT on Manufacturing Industry 4.0: A new triangular systematic review", *Sustainability*, Vol. 13, Issue 22, Pages 12506, 2021.
3. Dilibal, S., and Şahin, H., "İsbirlikçi endüstriyel robotlar ve dijital endüstri.", *International Journal of 3D Printing Technologies and Digital Industry* Vol. 2, Issue 1, 86-96, 2018.

4. Tao, F., Zhang, H., Liu, A., & Nee, A. Y., "Digital twin in industry: State-of-the-art", *IEEE Transactions on industrial informatics*, Vol. 15, Issue 4, Pages 2405-2415, 2018.
5. Tao, F., Xiao, B., Qi, Q., Cheng, J., & Ji, P., "Digital twin modeling", *Journal of Manufacturing Systems*, Vol. 64, Issue 1, Pages, 372-389, 2022.
6. Sharma, A., Kosasih, E., Zhang, J., Brintrup, A., & Calinescu, A., "Digital twins: State of the art theory and practice, challenges, and open research questions", *Journal of Industrial Information Integration*, Vol. 30, Issue -, Pages 100383, 2022.
7. Liu, M., Fang, S., Dong, H., & Xu, C., "Review of digital twin about concepts, technologies, and industrial applications", *Journal of Manufacturing Systems*, Vol. 58, Issue 1, Pages 346-361, 2021.
8. Leng, J., Wang, D., Shen, W., Li, X., Liu, Q., & Chen, X., "Digital twins-based smart manufacturing system design in Industry 4.0: A review", *Journal of manufacturing systems*, Vol. 60, Issue 1, Pages 119-137, 2021.
9. Park, K. T., Son, Y. H., Ko, S. W., & Noh, S. D., "Digital twin and reinforcement learning-based resilient production control for micro smart factory", *Applied Sciences*, Vol. 11, Issue 7, Pages 2977, 2021.
10. Chanchaen, R., Chaiprabha, K., Wuttisittikulij, L., Asdornwised, W., Saadi, M., & Phanomchoeng, G., "Digital twin for a collaborative painting robot, *Sensors*", Vol. 23, Issue. 1, Pages 17, 2022.
11. Coppelia Robotics "Robot simulator CoppeliaSim: create, compose, simulate, any ...", <https://www.coppeliarobotics.com/>, February 10, 2024.
12. Ren J., Nalpantidis, L. And Andersen N. A. & Ravn., O. "Building Digital Twin of Mobile Robotics Testbed Using Centralized Localization System," in 11th International Conference on Control, Mechatronics and Automation (ICCMA), Pages 139-145, Grimstad, 2023.
13. Open Robotics, "Gazebo", <https://gazebo.org/home>, January 20, 2024.

14. Stączek, P., Pizoń, J., Danilczuk, W., & Gola, A., A digital twin approach for the improvement of an autonomous mobile robots (AMR's) operating environment-A case study. *Sensors*, Vol. 21, Issue 23, Pages 7830, 2021.
15. Al-Geddawy, T., "A digital twin creation method for an opensource low-cost changeable learning factory," *Procedia Manufacturing*, vol. 51, no. 1, Pages 1799-1805, 2020.
16. RoboDK Inc., "RoboDK: Simulator for industrial robots and offline programming", <https://robodk.com/>, October 15, 2023.
17. Pires, F., Cachada, A., Barbosa, J., Moreira, A. P. and P. Leitão, "Digital Twin in Industry 4.0: Technologies, Applications and Challenges," in *IEEE 17th International Conference on Industrial Informatics (INDIN)*, Pages 721-726 Helsinki, Finland, 2019.
18. Dassault Systèmes, "SOLIDWORKS | 3D CAD Design Software & PDM Systems", <https://www.solidworks.com/>, February 21, 2024.
19. Autodesk, "AutoCAD", <https://www.autodesk.com/>, February 21, 2024.
20. Trimble Inc., "SketchUp: 3D Design Software | 3D Modeling on the Web", <https://www.sketchup.com/>, January 25, 2024.
21. Magrin, C. E., Del Conte, G. And Todt, E., "Creating a digital twin as an open-source learning tool for mobile robotics," in *Latin American Robotics Symposium (LARS), Brazilian Symposium on Robotics (SBR), and Workshop on Robotics in Education (WRE)*, Pages 13-18, Natal, 2021.
22. MathWorks, "Mathematical computing software for engineers and scientists", <https://www.mathworks.com/>, February 28, 2024.
23. PUC-Rio, "The Programming Language Lua", <https://www.lua.org/>, February 28, 2024.
24. Eaton, J. W. "GNU Octave ", <https://octave.org/>, February 22, 2024.
25. Rohmer, E., Singh, S. P., & Freese, M., "V-REP: A versatile and scalable robot simulation framework," in *IEEE/RSJ international conference on intelligent robots and systems*, Pages 1321-1326, Tokyo, 2013.
26. Nascimento, F. H., Cardoso, S. A., Lima, A. M. and Santos, D. F., "Synchronizing a collaborative arm's digital twin in real-time," in *Latin American Robotics Symposium (LARS), Brazilian Symposium on Robotics (SBR), and Workshop on Robotics in Education (WRE)*, Pages 230-235, Salvador, 2023.
27. Richard Hu, "HslCommunication", <https://pypi.org/project/HslCommunication/>, February 25, 2024.



ULUSLARARASI 3B YAZICI TEKNOLOJİLERİ
VE DİJİTAL ENDÜSTRİ DERGİSİ

INTERNATIONAL JOURNAL OF 3D PRINTING
TECHNOLOGIES AND DIGITAL INDUSTRY

ISSN:2602-3350 (Online)

URL: <https://dergipark.org.tr/ij3dptdi>

TENSILE BEHAVIOUR OF Ti6Al4V LATTICE STRUCTURES PRODUCED BY LASER POWDER BED FUSION AND DESIGN CRITERIA

Yazarlar (Authors): Doruk Gürkan^{ID*}, Binnur Sagbas^{ID}, Kadir Kiran^{ID}

Bu makaleye şu şekilde atıfta bulunabilirsiniz (To cite to this article): Gürkan D., Sagbas B., Kiran K., "Tensile Behaviour of Ti6Al4V Lattice Structures Produced by Laser Powder Bed Fusion and Design Criteria" *Int. J. of 3D Printing Tech. Dig. Ind.*, 8(3): 326-336, (2024).

DOI: 10.46519/ij3dptdi.1522530

Araştırma Makale/ Research Article

Erişim Linki: (To link to this article): <https://dergipark.org.tr/en/pub/ij3dptdi/archive>

TENSILE BEHAVIOUR OF Ti6Al4V LATTICE STRUCTURES PRODUCED BY LASER POWDER BED FUSION AND DESIGN CRITERIA

Doruk Gürkan^{a*}, Binnur Sagbas^b, Kadir Kiran^{c,d}

^a Istanbul Gedik University, Faculty of Engineering, Mechanical Engineering Department, TÜRKİYE

^b Yildiz Technical University, Faculty of Mechanical Engineering, Mechanical Engineering Department, TÜRKİYE

^c Suleyman Demirel University, School of Civil Aviation, Department of Aircraft Maintenance and Repair, Isparta, TÜRKİYE

^d Suleyman Demirel University, Innovative Technologies Application and Research Center, Design and Manufacturing Laboratory, Isparta, TÜRKİYE

* Corresponding Author: doruk.gurkan@gedik.edu.tr

(Received: 25.07.2024; Revised: 26.09.2024; Accepted: 22.10.2024)

ABSTRACT

Although additive manufacturing (AM) technology has many advantages in manufacturing complex geometries, it is not always possible to have desired results and performance due to its inherent limitations. This situation becomes crucial in manufacturing of lattice structures that are commonly used in aerospace, biomedical, etc. areas. The lattice structure design is easier with AM technologies, therefore process and lattice parameters must be carefully reviewed especially on biomedical properties. Titanium alloys are widely used for additive manufacturing of those implants with laser powder bed fusion (LPBF) technology. By doing so, we are able to achieve porous, lightweight and durable bone implants that aim to reflect bone properties. Due to these benefits of lattice structures and their ease of design, many studies focus on lattice structures, but their design, manufacturing and implementation features have not been completely deduced. As such, lattice topology and design may affect mechanical properties of the parts and manufacturing quality. In this aspect, three different strut-based lattice topologies (octahedron, dodecahedron and star), as potential bone implant structures were selected and tensile test specimens accommodating these topologies were manufactured with Ti6Al4V powder using laser powder bed fusion (LPBF). All the manufactured specimens were subjected to tensile tests and the results were reported.

Keywords: Additive Manufacturing, Lattice Structures, Laser Powder Bed Fusion, Ti6Al4V, Tensile Test, Orthopedic Bone Implants.

1. INTRODUCTION

Additive manufacturing (AM) is one of the continuously developing, popular and widespread production methods. Traditional manufacturing methods may be unsuitable for the production of complex lattice structures. However, AM technologies ensure to achieve this goal [1]. Laser powder bed fusion (LPBF) is one of the most commonly used AM technologies that use thermal laser energy to melt and deposit alloy powders layer by layer [2]. 3D complex geometries are freely produced as near net shape components by the CAD data of the part [3].

Lattice structures are a form of periodic porous structures which are unique three-dimensional cell structures formed by continual unit cells and can be easily manufactured with LPBF [4]. Unit cells are specified by the geometrical dimensions and bonding of their elements which are linked at specific interchange sections. These sections are related to their topological features [5]. Lattice structures can be classified as many aspects and the most common types are strut-based and triply periodic minimal surfaces (TPMS) [6]. In this

study, it was focused on the strut-based lattice structures.

Strut-based lattices can be easily optimized and their features altered due to the desired specifications with unit cell and process parameters [7]. Mechanical, acoustic, thermal, dielectric, damping, biocompatibility and many other properties are obtained in this way [8]. Especially biomedical studies can be beneficial with lattice structures and their features. Metallic orthopedic implants are desired to be close in mechanical and biocompatible properties of human bone. Reducing the stiffness through lower values and less elasticity modulus are the utmost objectives during manufacturing implants because of alloy characteristics [9]. Titanium and its alloys are widely used because of their biomedical adaptation and Ti6Al4V is one of the common alloys [10]. However, titanium has a high elasticity modulus (~90-110 GPa) and it must be reduced for biomedical applications due to the stress shielding phenomenon. Stress shielding causes an elastic modulus miss-match effect between the Ti implant and the bone tissue and bone tissue is damaged over time which causes unable to sustain its function [11-12]. The porous and lattice structures of titanium parts can reduce mechanical properties to appropriate levels and prevent stress shielding. However, since it is not clear to what extent unit lattice designs and porosity ratios will decrease the mechanical properties, the reduced properties of newly developed lattice designs should be investigated with standard mechanical tests such as tensile and compression tests [13-14].

Several different design approaches were examined in the literature to conclude tensile testing of lattice structures because the repeatability of manufacturing is challenging for AM lattice structures [15-16]. Some issues may occur such as recoater blade damages during manufacturing when the design of lattice structures is not suitable and the uniformity of parts is affected this way [17]. This situation also affects the tensile test properties due to the incompatibility of manufacturing. Researchers studied different methods to overcome these problems. Dingye et al. [18] reported that manufacturing lattice tensile test structures as different cross sections and build directions. They showed these design parameters affect

tensile properties. Also, some successful designs were manufactured without defects and introduced for tensile test implementation. Ananda et al. [19] designed lattice structures with several lattice topologies. Their design was provided with a 6 mm hole on the grip section to prevent any torsional stress on the lattice structure. Yang et al. [20] used heat treatment on their lattice structure design. However, the authors did not report the effect of these procedures and compare them with not implemented specimens.

It can be seen that the repeatability of the manufacturing of tensile test specimens and their test fulfillment were inadequate and needed further research due to design aspects. Manufacturing of lattice tensile test specimens are challenging process despite of many studies in this area. Strut-based topologies may be more challenging when they are produced as thin strut diameters. In this aspect, two different groups of tensile test specimens with different support designs were introduced in this study. Dodecahedron, star and octahedron lattice structures manufactured as tensile test specimens and their design effects were discussed both on manufacturability and mechanical test feasibility.

2. MATERIAL AND METHOD

The tensile test specimens accommodating three different lattice structures were manufactured by laser powder bed fusion (EOSINT M280-200W) using Ti6Al4V powder as octahedron, star and dodecahedron topology. The chemical composition of Ti6Al4V (EOS Ti64) powder supplied by the same company is given in Table 1. Process parameters were selected from default parameter sets (i.e., skin exposure type) included in EOS PSW software. Specifically, 170 W laser power, 1250 mm/s scan speed, 30 µm layer thickness and 100 µm hatch distance were used during the manufacturing of the test specimens. Manufacturing was carried out Z-axis for all parts and designs.

Table 1. The chemical composition of Ti6Al4V powder (%) [22]

| Ti | Al | V | Fe | O | N | C | H | Y |
|----|-----|-----|-----|-----|-----|-----|-----|-----|
| 88 | 6.7 | 4.5 | 0.2 | 0.1 | 0.1 | 0.1 | 0.1 | 0.2 |

Tensile test specimen designs were completed in accordance with ASTM-E8/E8M-16a

standard [23-25], as shown in Fig. 1. The thickness of the specimen was 2.5 mm. Three different lattice structures were chosen as dodecahedron, octahedron and star. Siemens NX version 12.0 (Siemens AG, Germany) was used for the design of strut base structures. In this study, two different design strategies were followed, as shown in Fig. 1. In the first design

strategy (i.e., Fig. 1(a), (b) and (c)), tensile test specimens have lattice structures at gauge section while in strategy two (i.e., Fig. 1(d), (e) and (f)), the entire body of specimens have been covered with lattice structures. Here note that 2 mm volume support structures were included in these designs.

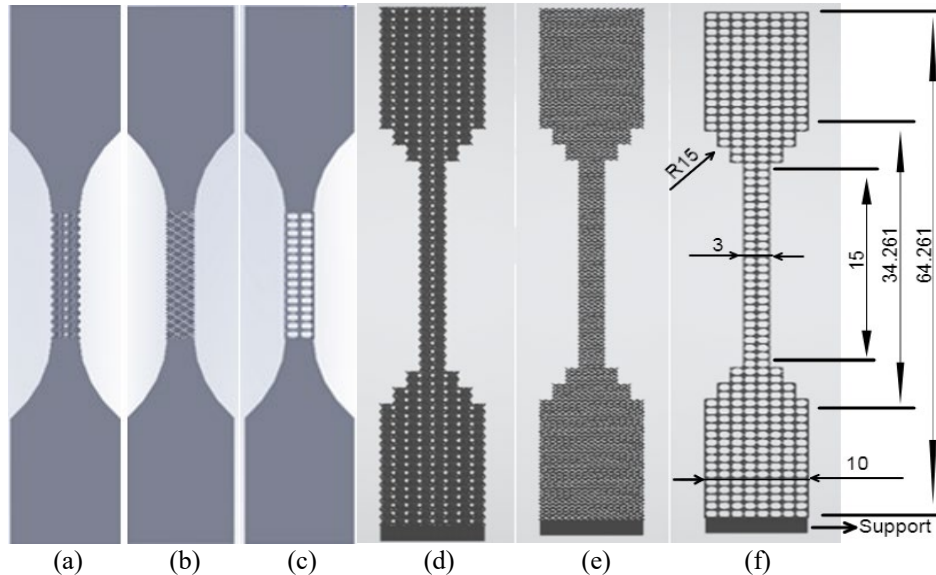


Figure 1. Schematic representation of the revised dimensions of the tensile specimens in accordance with the ASTM-E8/E8M-16a standard. All dimensions were the same for both design groups (a-star center latticed, b-dodecahedron center latticed, c- octahedron center latticed, d-star full lattice, e-dodecahedron full lattice, f-octahedron full lattice). The thickness of the specimen was 2.5 mm.

However, the samples were broken due to the recoater blade crash during manufacturing process of specimens (a), (b) and (c), thereby new support structures were designed and included in those specimens using Magics software. The details for these supports are given in the next section.

All the lattice structures were produced as thin strut build which has not been mostly studied in the literature. The strut diameter was chosen as 0.25 mm and the unit cell dimensions were chosen as 1.25 mm x 1.25 mm x 1 mm (x , y and z , respectively). In this way, the topological pore size has been increased.

On the other hand, the following corrections were made after the raw design for full lattice structures (i.e., Fig. 1(d), (e) and (f)).

Some of the open-ended profiles on the tensile specimens are secured to avoid the need for support structures [26]. It has been seen that the design of the descending form of stair steps is

important both for production and performing a suitable tensile test (Figure 2).

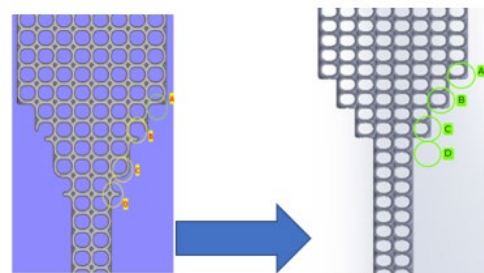


Figure 2. Constructing the openings (B, C, D) in the picture to the structure indicated by A is shown on the right (octahedron).

Likewise, there were some outward struts in star lattice specimens. Thus, a similar modification procedure was also applied to this specimen, as shown in Figure 3.

Such disturbances occur during the lattice construction of the raw design due to the topological effects of lattice structures [7].

Therefore, these types of defects did not occur in dodecahedron lattice topology (Figure 4). In order to preserve the common design method, changes were made as same as other lattice topologies.

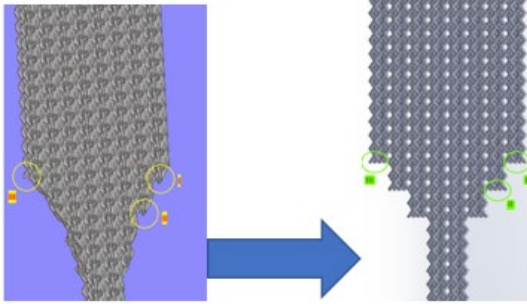


Figure 3. In star lattice structure, the parts that do not closed-contact the parts from the bottom or sides (I and II) and the parts that do not close contact from the bottom point (III).

Tensile tests were performed using a calibrated universal mechanical tester (Instron 8872, Instron, USA). All the tests were performed at a constant strain rate of 0.1 mm/min and specimens were placed centrally.

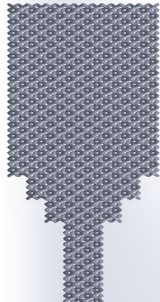


Figure 4. The final version of the dodecahedron lattice structure with stair steps.

The elastic modulus was calculated using slope of the linear elastic section in the stress-strain curve. Non-linear sections were not taken for calculation. Here note that Excel program was used for all the calculations.

On the other hand, scanning electron microscopy (SEM) investigations on the manufactured specimens were completed via Zeiss EVO LS 10 (Zeiss, UK) with a secondary electron detector.

3. EXPERIMENTAL FINDINGS

3.1. Contact Support Structure Design of Center Latticed Structure

During the manufacturing process, multiple recoater blade crashes occurred due to thin sections of the lattice structures. Consequently, due to the low stiffness of the samples, all the samples were broken and the manufacturing process was interrupted. These failed manufacturing results are given in Figure 5.

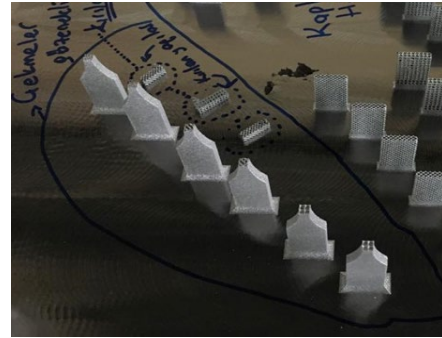


Figure 5. Failed manufacturing of tensile test specimens

To prevent this situation, first the shell support structure was designed. This support structure did not contact the tensile specimen and there is an approximately 0.15 mm gap between the support structure and the test specimen. Based on the manufacturing experience, it was thought that this support structure might not provide enough strength to the test specimen to withstand the forces coming from the recoater. To guarantee the success of the second manufacturing, two contact support structures were created in the second support design, as seen in Figure 6. These supports were placed in the direction which is perpendicular to the recoating direction, and they have contacts in the radiused portions of the specimen whereas there is no contact between the support structure and test specimens in the gauge portion. Note that approximately 0.15 mm clearance was provided in this section. As such, the manufacturing of all the specimens was completed successfully, as shown in Figure 7.

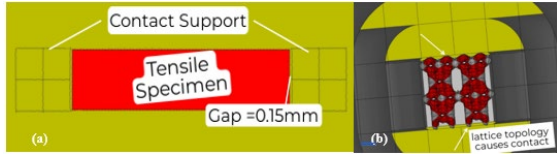


Figure 6. Contact support structures (a) and their relationships with lattice topology (b).



Figure 7. Manufactured tensile test specimens with contact support structure design.

Detailed inspection of the support structure-tensile test specimen interface was performed by the SEM. As can be seen from Figure 8, clearance between the support structures and test specimen gradually increases from the direction of the building platform to the top of the specimens due to residual stress in the support structures. This phenomenon allows us to easily remove the support structures from the specimen.

3.2. Tensile Tests

Three test specimens for each design were manufactured and tested. Stress-strain curves of tensile test specimens of center latticed structure design can be seen in Figure 9. The fractured test samples were given in Figure 10.

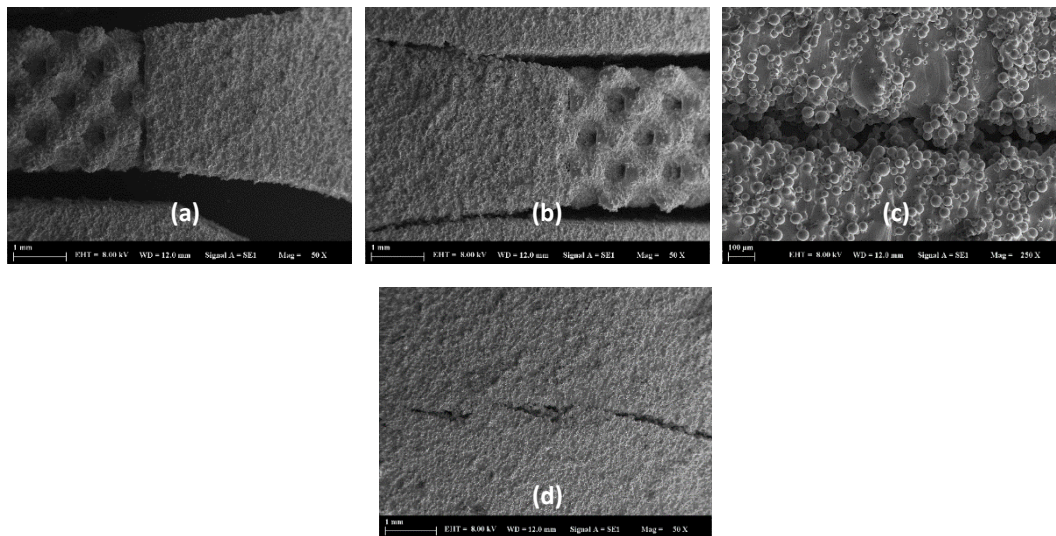


Figure 8. The support structure of center latticed sample design (Lattice-bulk structure transition (a), support structure-specimen transition (b), wide support structure separation lines (c) and tight support structure separation lines (d)).

As can be seen from the graphs, the high resonance problem experienced during the tensile tests and the resulting faulty graph curves occurred during this test phase. With all these evaluations, it was decided to not interpret the tensile test results. As can be seen in the

figure below, the samples fractured at the lattice transition zone except octahedron-2 specimen. The thin strut diameter and design aspect prevented obtaining the desired results from tensile tests.

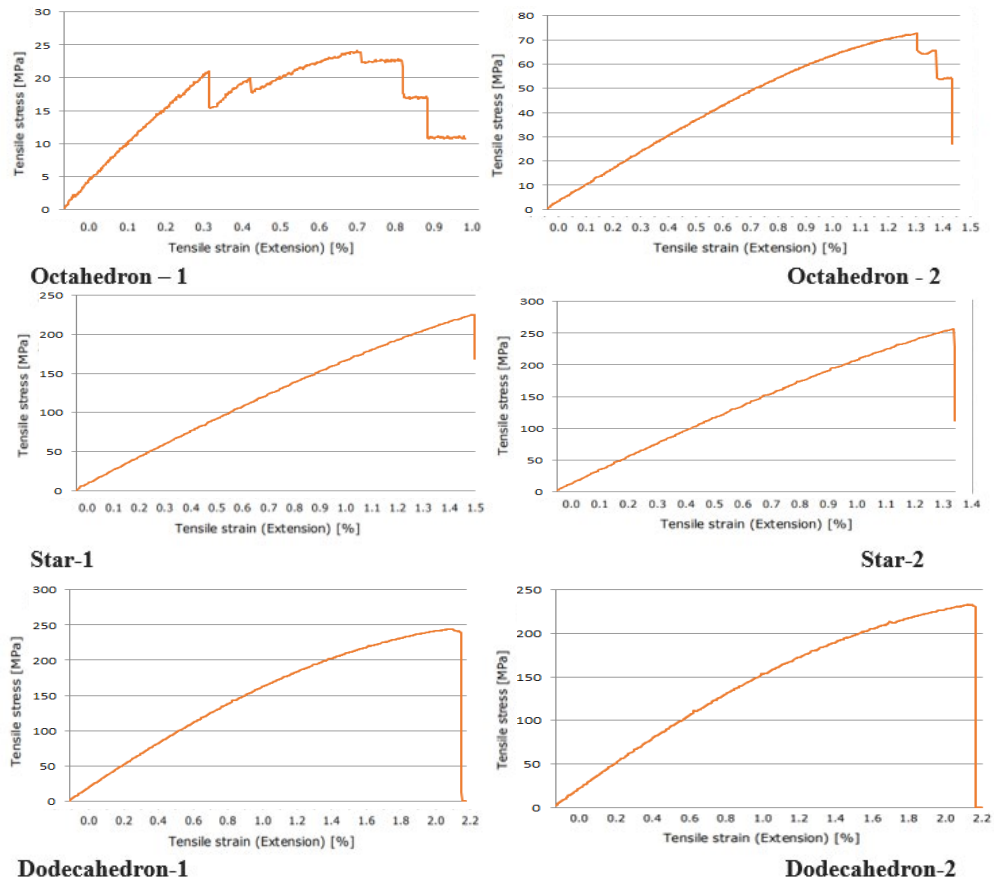


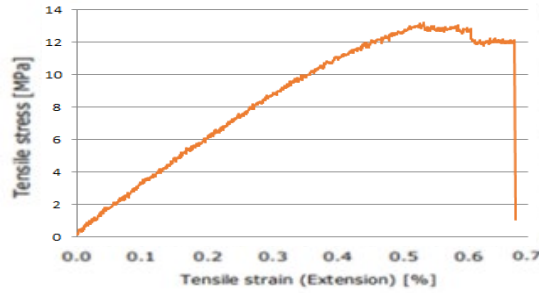
Figure 9. Stress-strain curves of tensile test specimens with center latticed structure design.

Stress-strain curves of full lattice structure designs were given in Figure 11. The fractured test samples were given in Figure 12.

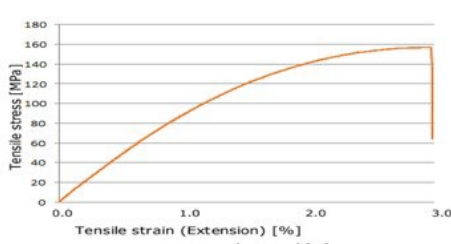
were given in Figure 11. The fractured test



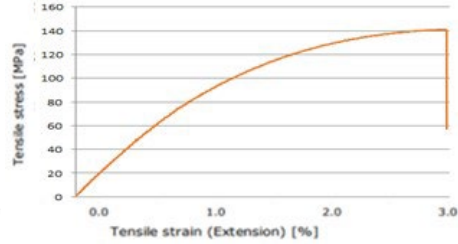
Figure 10. Fracture points of parts at the end of the tensile tests. Octahedron (a and b), star (c and d) and dodecahedron (e and f).



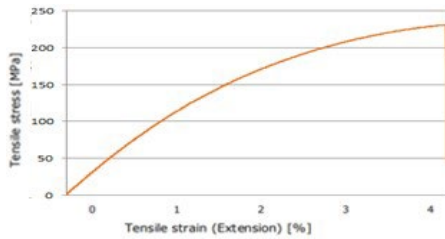
Octahedron-3



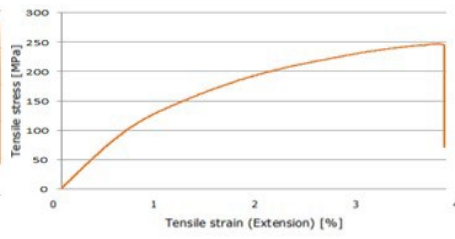
Dodecahedron-3



Dodecahedron-4



Star-3



Star-4

Figure 11. Tensile test results of full lattice structure design

Octahedron-3 specimen also showed a high resonance problem and it can be seen in center latticed design structures. These types of problems might be related to thin strut diameter and topological characteristics. The higher porosity of the lattice structure may have caused much more resonance problems for octahedron topology. Fracture of the star-4 specimen occurred near the center which means that this design eliminated the stress concentration problem [27]. This was a difficult problem to solve for thin strut diameter design specimens, but it has been successful as can be seen in this example. Test results were shared in Table 2. Fractures of other parts did not occur near the center as same as star-4 specimen, therefore similar example was found in the literature and the test results can be evaluated [20].

It was seen that similar results were obtained in the literature studies when the results were evaluated and that the appropriate elastic modulus was provided for bone implant applications [20, 28-30]. Star, dodecahedron and octahedron lattice structures showed the best results respectively when the elastic modulus was evaluated. Star lattices showed elastic modulus values between 10.8-14.8 GPa.. These results make them a good cortical bone implant material candidate. [31]. Dodecahedron lattices was between 7.7-7.8 GPa, while octahedron lattice was between 2.5 GPa. These lattices are more likely suitable for cancellous bone applications.

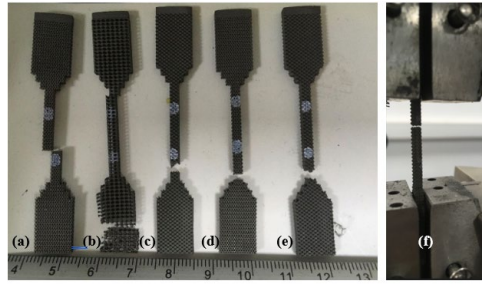


Figure 12. Star-4 (a), octahedron-3 (b), dodecahedron-4 (c), star-3 (d), dodecahedron-3 (e) and fracture example (f)

Table 2. Tensile test results of full lattice structure design

| Specimen | Maximum Tensile Stress (MPa) | Maximum Tensile Strain (mm/mm) | Maximum Load (kN) | Elastic modulus (MPa) | Fracture Elongation (%) |
|----------------|------------------------------|--------------------------------|-------------------|-----------------------|-------------------------|
| Octahedron-3 | 13.25 | 0.04 | 0.86 | 2460.8 | 0.6 |
| Star-3 | 231 | 0.03 | 1.44 | 14823.47 | 3.1 |
| Star-4 | 247.24 | 0.03 | 1.54 | 10824.84 | 3.3 |
| Dodecahedron-3 | 157.1 | 0.25 | 0.98 | 7843.24 | 2.8 |
| Dodecahedron-4 | 141.35 | 0.25 | 0.88 | 7789.96 | 2.6 |

Fracture surface images were obtained by SEM investigations (Figure 13). The presence of shallow dimples and the formation of flat planes (smooth) indicate brittle fracture for octahedron lattice and the overall fracture morphology caused this appearance [32]. Numerous dimples and high tear ridges show higher ductility for

star and dodecahedron and also show high toughness [33]. There are also cleavages in these lattice structures which provide quasi-cleavage tensile failure mechanism [34]. Star lattice has higher quasi-cleavage behavior than dodecahedron lattice.

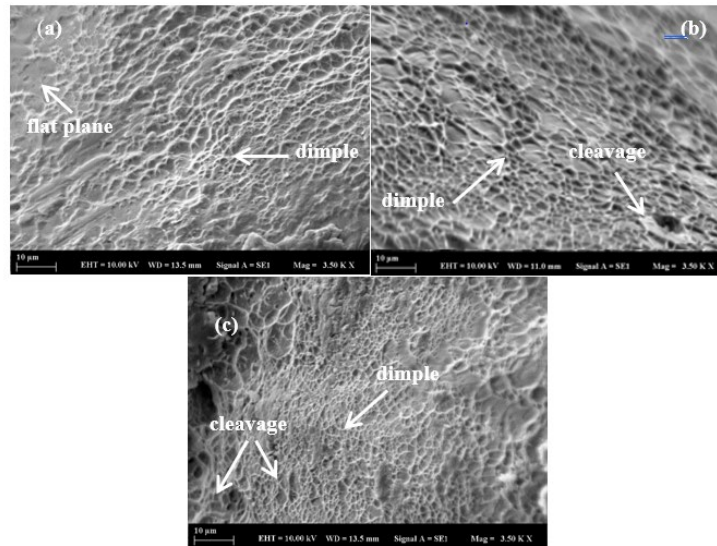


Figure 13. Fracture morphology SEM images of octahedron (a), dodecahedron (b) and star (c).

4. RESULTS

The tensile test is less preferable than the compression test because of the necessity of proper design for thin strut lattice structures. Successful manufacturing is related to proper design optimizations and secondary modifications such as post-process treatments. In this study, Ti6Al4V strut-based lattice structure designs and tensile test properties were examined for biomedical applications. Design optimization effects were shown. Dodecahedron, star and octahedron lattice topologies were used and manufactured by LPBF. The following observations were made after the study.

The proposed designs were successfully completed and their manufacturing was performed with two different support structures. Both designs were compared and their advantages and disadvantages were discussed. It was seen that full lattice structure designs were more suitable for tensile tests. Undesirable situations occurred on center latticed structure design during tensile tests and test results could not be obtained. It was seen that the star lattice topology had better mechanical performance than the other two lattice topologies after examining results from the full lattice structure design. Dodecahedron and octahedron lattice topologies followed star lattice topology respectively. It was seen that all three lattice topologies were suitable for biomedical implant applications due to their mechanical properties.

ACKNOWLEDGMENTS

This study was an extension of research conducted as part of the PhD thesis “Eklemeli İmalat ile Elde Edilen İmplant Yüzeylerinde Biyoaktif Kaplamaların Gerçekleştirilmesi” (in Turkish) and generated from it.

This work was supported by Yildiz Technical University Scientific Research Projects Coordination Unit (Project Number: FDK-2021-4135). This article was presented orally at the 7th International 3D Printing Technologies and Digital Industry Congress and the abstract was printed in the Abstract Book.

REFERENCES

1. Distefano, F., Pasta, S., Epasto, G., “Titanium Lattice Structures Produced via Additive Manufacturing for a Bone Scaffold: A Review”, *Journal of Functional Biomaterials*, Vol. 14, Issue 3, Pages 125, 2023.
2. McGaffey, M., Zur Linden, A., Bachynski, N., Oblak, M., James, F., Weese, JS., “Manual polishing of 3D printed metals produced by laser powder bed fusion reduces biofilm formation”, *PloS one*, Vol. 14, Issue 2 Pages e0212995, 2019.
3. Gao, M., He, D., Wu, X., Tan, Z., Guo, X., “Design, Preparation, and Mechanical Property Investigation of Ti-Ta 3D-Auxetic Structure by Laser Powder Bed Fusion”, *Advanced Engineering Materials*, Vol. 25, Issue 16, Pages 2300242, 2023.
4. Zhang, Y., Aiyiti, W., Du, S., Jia, R., Jiang, H., “Design and mechanical behaviours of a novel tantalum lattice structure fabricated by SLM”, *Virtual and Physical Prototyping*, Vol. 18, Issue 1, Pages e2192702, 2023.
5. Gan, M., Wu, Q., Long, L., “Prediction of Residual Deformation and Stress of Laser Powder Bed Fusion Manufactured Ti-6Al-4V Lattice Structures Based on Inherent Strain Method”, *Materials Research*, Vol. 26, Pages e20220516, 2023.
6. Pugliese, R., Graziosi, S., “Biomimetic scaffolds using triply periodic minimal surface-based porous structures for biomedical applications”, *SLAS technology*, Vol. 28, Issue 3, Pages 165-182, 2023.
7. Maconachie, T., Leary, M., Lozanovski, Z., Zhang, X., Qian, M., Faruque, O., Brandt, M., “SLM lattice structures: Properties, performance, applications and challenges”, *Materials & Design*, Vol. 183, Pages 108137., 2019.
8. Korkmaz, ME., Gupta, MK., Robak, G., Moj, K., Krolczyk, GM., Kuntoğlu, M., “Development of lattice structure with selective laser melting process: A state of the art on properties, future trends and challenges”, *Journal of Manufacturing Processes*, Vol. 81, Pages 1040-1063, 2019.
9. Zargarian, A., Esfahanian, M., Kadkhodapour, J., Ziaei-Rad, S., Zamani, D., “On the fatigue behavior of additive manufactured lattice structures”, *Theoretical and Applied Fracture Mechanics*, Vol. 100, Pages 225-232, 2019.
10. Nalli, F., Cortese, L., Concli, F., “Ductile damage assessment of Ti6Al4V, 17-4PH and AlSi10Mg for additive manufacturing”, *Engineering Fracture Mechanics*, Vol. 241, Pages 107395, 2021.

11. Manvendra, T., Kumar, P., "Fracture Performance Evaluation of Additively Manufactured Titanium Alloy", *Advanced Materials for Biomechanical Applications*, Pages 215-227, CRC Press, UK, 2022.
12. Naghavi, SA., Tamaddon, M., Garcia-Souto, P., Moazen, M., Taylor, S., Hua, J., Liu, C., "A novel hybrid design and modelling of a customised graded Ti-6Al-4V porous hip implant to reduce stress-shielding: An experimental and numerical analysis", *Frontiers in Bioengineering and Biotechnology*, Vol. 11, Pages 1092361, 2023.
13. Khorasani, A., Gibson, I., Awan, US., Ghaderi, A., "The effect of SLM process parameters on density, hardness, tensile strength and surface quality of Ti-6Al-4V", *Additive manufacturing*, Vol. 25, pages 176-186.
14. Khorasani, AM., Gibson, I., Ghaderi, A., Mohammed, MI., "Investigation on the effect of heat treatment and process parameters on the tensile behaviour of SLM Ti-6Al-4V parts", *The International Journal of Advanced Manufacturing Technology*, Vol. 101, Pages 3183-3197, 2019.
15. Liu, F., Zhou, T., Zhang, T., Xie, H., Tang, Y., Zhang, P., "Shell offset enhances mechanical and energy absorption properties of SLM-made lattices with controllable separated voids", *Materials & Design* Vol. 217, Pages 110630, 2022.
16. Fry, AT., Crocker, LE., Lodeiro, MJ., Poole, M., Woolliams, P., Koko, A., et al., "Tensile property measurement of lattice structures", *NPL Report Mat.*, Pages 119, 2023.
17. Tekerek, E., Perumal, V., Jacquemetton, L., Beckett, D., Halliday, HS., Wisner, B., Kontsos, A., "On the process of designing material qualification type specimens manufactured using laser powder bed fusion". *Materials & Design* Vol. 229, Pages 111893, 2023.
18. Dingye, Y., Weixing, Z., Yuli, M., Bo, H., "Numerical Prediction and Experimental Analysis of the Anisotropy of Laser Powder Bed Fusion Produced Ti-6Al-4V Body-Centered Cubic Lattice Structure", *Journal of Materials Engineering and Performance*, Vol. 32, Issue 7, Pages 2963-2972, 2023.
19. Ananda, V., Saravana, KG., Jayaganthan, R., Srinivasan, B., "Distortion Prediction in Inconel-718 Part Fabricated through LPBF by Using Homogenized Support Properties from Experiments and Numerical Simulation", *Materials*, Vol. 15, Issue 17, Pages 5909, 2023.
20. Yang, X., Ma, W., Gu, W., Zhang, Z., Wang, B., Wang, Y., Liu, S., "Multi-scale microstructure high-strength titanium alloy lattice structure manufactured via selective laser melting" *RSC advances* Vol. 11, Issue 37, Pages 22734-22743, 2021.
21. Asherloo, M., Wu, Z., Delpazir, MH., Ghebreiesus, E., Fryzlewicz, S., Jiang, R., et al., "Laser-beam powder bed fusion of cost-effective non-spherical hydride-dehydride Ti-6Al-4V alloy", *Additive Manufacturing*, Vol. 56, Pages 102875, 2022.
22. EOS Gmbh, EOS Titanium Ti64 data sheet. <http://www.eos.info/>. Accessed 7 August 2023.
23. Zhang, S., Chertmanova, S., Chou, K., "Surrogate Pore Generations in L-PBF Ti64 and Effects on Mechanical Behavior", *International Manufacturing Science and Engineering Conference*, Pages 84256, Cincinnati, 2020.
24. Rauniyar, SK., Chou, K., "Porosity analysis and pore tracking of metal AM tensile specimen by Micro-CT", *2019 International Solid Freeform Fabrication Symposium*, Austin, 2019.
25. Zhang, S., Rauniyar, S., Shrestha, S., Ward, A., Chou, K., "An experimental study of tensile property variability in selective laser meltin", *Journal of Manufacturing Processes*, Vol. 43, Pages 26-35, 2019.
26. Jiang, J., Xu, X., Stringer, J., "Support structures for additive manufacturing: a review", *Journal of Manufacturing and Materials Processing*, Vol. 2, Issue 4, Pages 64, 2018.
27. Wang, Z., Tang, SY., Scudino, S., Ivanov, YP., Qu, RT., Wang, D., et al., "Additive manufacturing of a martensitic Co-Cr-Mo alloy: Towards circumventing the strength-ductility trade-off", *Additive Manufacturing*, Vol. 37, Pages 101725, 2020.
28. Luo, JP., Huang, YJ., Xu, JY., Sun, JF., Dargusch, MS., Hou, CH., et al., "Additively manufactured biomedical Ti-Nb-Ta-Zr lattices with tunable Young's modulus: mechanical property, biocompatibility, and proteomics analysis", *Materials Science and Engineering: C*, Vol. 114, Pages 110903, 2020.
29. Mutlu, B., "Tensile testing of square structure built with electron beam melting", *Revista de Metalurgia*, Vol. 57, Issue 3, Pages e200, 2021.

30. Soro, N., Brodie, EG., Abdal-hay, A., Alali, AQ., Kent, D., Dargusch, MS., “Additive manufacturing of biomimetic Titanium-Tantalum lattices for biomedical implant applications”, *Materials & Design*, Vol. 218, Pages 110688, 2022.
31. Milazzo, M., Contessi Negrini, N., Scialla, S., Marelli, B., Farè, S., Danti, S., Buehler, M. J. “Additive manufacturing approaches for hydroxyapatite-reinforced composites”, *Advanced Functional Materials*, Vol. 29, Issue 35, 1903055, 2019.
32. Li, Z., Wu, H., Liu, B., Wen, H., Li, H., Shi, J., Tang, X., “Interfacial microstructure and mechanical properties of forging and SLM hybrid manufacturing Ti-6Al-4V parts”, *Materials Letters* Vol. 339, Pages 134101., 2023.
33. Xu, S., Liu, H., Zhang, J., Cai, X., Si, C., “Effect of Heat Treatment Temperature and Cooling Rate on Microstructure and Tensile Properties of Selective Laser Melted Ti-6al-4v Alloy”, Available at SSRN 4493087, 2023.
34. Ge, J., Huang, Q., Wang, Y., Zhang, C., Liu, Q., Lu, Z., Yin, S., “Microstructural optimization and mechanical enhancement of SLM Ti6Al4V TPMS scaffolds through vacuum annealing treatment”, *Journal of Alloys and Compounds*, Vol. 934, Pages 167524,2022.



ULUSLARARASI 3B YAZICI TEKNOLOJİLERİ
VE DİJİTAL ENDÜSTRİ DERGİSİ

INTERNATIONAL JOURNAL OF 3D PRINTING
TECHNOLOGIES AND DIGITAL INDUSTRY

ISSN:2602-3350 (Online)

URL: <https://dergipark.org.tr/ij3dptdi>

REDESIGN AND FABRICATION OF STENT DESIGNS PRODUCED BY COMMON METHODS BY OPTIMIZING FOR MELT ELECTRO WRITING (MEW) METHOD

Yazarlar (Authors): Fatih KÖSE^{ID}*, Alper TEZCAN^{ID}

Bu makaleye şu şekilde atıfta bulunabilirsiniz (To cite to this article): Köse F., Tezcan A., “Redesign and Fabrication of Stent Designs Produced by Common Methods by Optimizing for Melt Electro Writing (Mew) Method” *Int. J. of 3D Printing Tech. Dig. Ind.*, 8(3): 337-351, (2024).

DOI: 10.46519/ij3dptdi.1536130

Araştırma Makale/ Research Article

Erişim Linki: (To link to this article): <https://dergipark.org.tr/en/pub/ij3dptdi/archive>

REDESIGN AND FABRICATION OF STENT DESIGNS PRODUCED BY COMMON METHODS BY OPTIMIZING FOR MELT ELECTRO WRITING (MEW) METHOD

Fatih KÖSE^a , Alper TEZCAN^a 

^aIstanbul Arel University, Engineering Faculty, Mechanical Engineering Department, TURKIYE

* Corresponding Author: fatihkosemakine@gmail.com

(Received: 20.08.2024; Revised: 14.12.2024; Accepted: 16.12.2024)

ABSTRACT

The main discussion is about the differences compared to other methods. The aim is to observe the advantages and disadvantages of the stent produced using the MEW manufacturing technique and to apply the production principles. This study presents the design of a mesh-patterned stent and details the production stages using a Mew manufacturing method. Melt Electro Writing (MEW) method is a 3D writing method that is progressing and developing day by day with its use in many fields from industry to medicine. With this method, semi-flexible structures can be produced with rigid polymers. Polycaprolactone (PCL) material is preferred due to its low melting temperature and degradable structure in this production technique based on electrohydrodynamic principles to produce highly efficient, micron fibers. New methods and solutions are emerging in line with the studies carried out in this field. Stents made of nitinol are the most commonly used stents. Nitinol stents cannot be removed again as a result of placement. For this reason, various difficulties may occur in cases of recurrent blockage in the same area. It is also disadvantageous in terms of material and production costs. In the ongoing studies, it is observed that the focus is on stents that can be absorbed by the body and perform mineral supplementation. Biodegradable stents provide absorption by melting in the vessel. In this study, a stent with a grid pattern design made of Polycaprolactone (PCL) material was produced with a melt electro writing device with a rotary table. The comparison of the 316L metal stent produced by conventional production methods with the same dimensions and designs and the stent produced by MEW method from PCL material is explained by simulation and analyses, and it is shown in which cases it is more efficient and in which cases it is dysfunctional. It has been shown that stents produced with polycaprolactone (PCL) in MEW method are more efficient in terms of flexibility, biocompatibility and biodegradability than 316L metal stents produced by conventional methods. While PCL stents are suitable for short-term applications with their flexibility and biocompatibility advantages, 316L stainless steel stents can be preferred for situations requiring long-term performance and mechanical durability. The specific advantages and disadvantages of both materials are important points to be considered during stent selection. In addition to the modification and improvement of PCL materials, it has been observed that design is one of the most important factors in stent efficiency, and future studies can contribute to the development of stents that provide better performance, especially by focusing on the ability and technology of MEW devices to produce every design based on design-oriented production.

Keywords: Melt Electro Writing, Cardiovascular Stent, Cardiovascular Stent Manufacturing Techniques, Cardiovascular Stent Production with Melt Electro Writing Method.

1. INTRODUCTION

This study presents the design of a mesh-patterned stent and details the production stages using a Mew manufacturing method. The ease of production and the functionality of the material are discussed, and the advantages and disadvantages of PCL material are identified.

Comparisons are made with metal stents, which are among the traditional methods. It is concluded that PCL stents have a bright future in terms of processing parameters and biocompatibility, indicating they will have a larger market share in the industry in the future. While PCL stents are suitable for short-term

applications due to their flexibility and biocompatibility advantages, 316L stainless steel stents may be preferred for situations requiring long-term performance and mechanical durability. The unique advantages and disadvantages of both materials are important points to consider during stent selection. Future studies focusing on the modification and improvement of these materials may contribute to the development of stents with better performance.

Stents are used to restore circulation by expanding the vessel after occlusion of the vessels. It is widely used because it has advantages over other methods applied to open the veins. It is frequently used in the brain, kidney and leg vessels, as well as in the heart vessels.

One of the most commonly used stents is stents made of nitinol. It is not possible to remove nitinol stents again as a result of their placement. For this reason, various difficulties may occur in cases of recurrent occlusion in the same area. It is observed that the focus is on stents that can be absorbed by the body and supplement minerals in the ongoing studies. Biodegradable stents dissolve in the vessel and provide absorption. However, the excessive accumulation of minerals contained in the material in the body also poses different risks. The general purpose of the studies is to eliminate the risk by minimizing it.

Melt Electro Printing (MEW) technique is a frequently used and continuously developed 3D printing technique in this field. It enables the production of cardiovascular stents with rigid polymers with high resolution flexible structures. Especially in the MEW method, it is seen that stents produced with Polycaprolactone (PCL) are efficient in terms of flexibility, biocompatibility and biodegradability. 4D printing and smart materials could positively change the future of cardiovascular stent design [13-15].

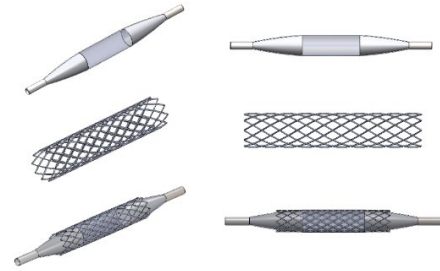


Figure 1. Stent, balloon and stent-balloon design.

Stents, which can be produced in different sizes and thicknesses according to the vascular structure in which they are used, are generally produced in 2-4 mm thickness and 10-30 mm in length. Before the procedure, there is a deflated stent balloon in the stents in the shrunken form. The balloon, which is attached to a long thin tube, is 1-2 mm wide. Stent, Balloon and Stent-Balloon Design is shown in Figure 1.



Figure 2. Stent application in the occluded vessel.

The stent, which is placed in the occluded part of the vessel, provides the crushing of the elements that cause the obstruction by inflating the balloon. The main purpose is to remove the obstruction and provide blood flow at standard values. During the procedure, the crushing or fragmentation of the elements that cause occlusion in the vessel is perceived as damage by the body and creates an intervention reflex in that area. Therefore, narrowing may occur in the same area after a short time. The placed stent prevents re-narrowing. Stent application in the occluded vessel is shown in Figure 2.

It is essential not to damage the vein during the procedure. The stent to be used should be selected according to the vascular structure. It is important that the stent is flexible and can be placed. In addition, it must have the strength to meet the pressure in the vein. It must have

biocompatibility, corrosion resistance, back collapse strength and high fatigue strength.

Cardiovascular Stents are used to restore circulation by expanding the vessel after occlusion of the vessels. It is widely used because it has advantages over other methods applied to open the veins. It is frequently used in the brain, kidney and leg vessels, as well as in the heart vessels.

With the development of materials science, treatment techniques and new manufacturing processes, a variety of stents have been developed. In this way, the development has shifted from the initial bare metal stents (BMS) to drug-eluting stents (DES) and bioabsorbable stents (BRS) made of biodegradable polymers or metals [10]. The MEW method provides a great advantage in terms of integrating biodegradable or drug-eluting properties through polymeric materials used in stent manufacturing. MEW (MEW) method in the production of stents is developing day by day with the studies carried out and its preferability is increasing. MEW method is a technique using biological tissue production. Cell-encapsulated hydrogels and (sub)micrometer fibres are used as raw materials. This method enables the production of mechanically durable structures by combining bioprinting and MEW techniques. As a result of the processing of thermoplastic biopolymer materials, especially PCL, under high voltage by reaching the required parameter values, a micron-scale, high resolution and precise product emerges. Basically, the MEW technique provides high-resolution production using melt extrusion and electrohydrodynamic fibre extraction. High yields are achieved by processing micro-nano ribbons in layers. Melt electroprinting (MEW) is a solvent-free (i.e. without volatile chemicals), high-resolution three-dimensional (3D) printing method that enables the production of semi-flexible structures with rigid polymers [3].

The material generally used in MEW production technique is polycaprolactone (PCL). PCL material is widely used especially in medical applications and tissue engineering field due to its biocompatible and biodegradable

properties. In addition, its low melting temperature and good processability make it suitable for use in MEW technique.

Looking at the studies in the literature, it is observed that one of the important factors in stent efficiency is the design structure, based on the comparison of PCL material and finite element analyses between the most commonly used grid pattern, ellipse pattern and circle pattern designs. Based on the current MEW Device technology, the grid pattern stent, which is the most optimal pattern that can be produced in these devices, will be designed and manufactured with the standard and workflow sequence shown in the study, and the finite element analyses will be compared by simulating the stents with 316L material produced by the traditional production method with the same dimensions of the grid pattern and the stents produced from PCL material.

1.1. Stent Types

Stents vary according to their application areas, according to the practitioner system, according to their structure and according to their design. According to the application areas; There are four types of stents: Carotid, Coronary, Renal and Peripheral stents. According to the implementing system; There are two types of stents: balloon and self-opening stents. According to their structure; There are three types of stents: Drug-eluting stents, Bare metal stents, and Dissolvable stents. According to their design; There are five types of stents: Grid, Circular, Spiral, Cylindrical and Special type stents. In this study, stents that can be expanded with a balloon with a grid pattern design will be produced. Stent types are shown in figure 3.

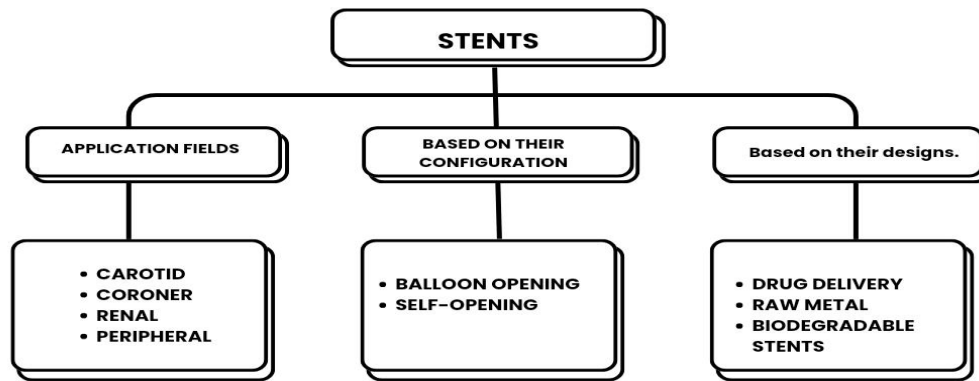


Figure 3.Types of stent

1.2.Melt Electrowriting (Mew) Production Technique

Melt electroprinting (MEW) technique is called a new manufacturing technique that is developing day by day used for 3D printing. Semi-flexible structures can be produced with rigid polymers. The most important rule in this technique can be said to be able to apply the most appropriate printing parameters. It is of great importance that it can be highly functional in the processing and production of biomaterials

such as PCL. Widely used in manufacturing, PCL is preferred in terms of thermal efficiency, mechanical suitability, design flexibility and biocompatibility. The MEW technique creates micron-scale fibers, ensuring precise production with high resolution. In summary, it can be said that it is a production technique based on electrohydrodynamic principles to produce high-efficiency, micron fibers. Melt electrowriting technique shown in figure 4.

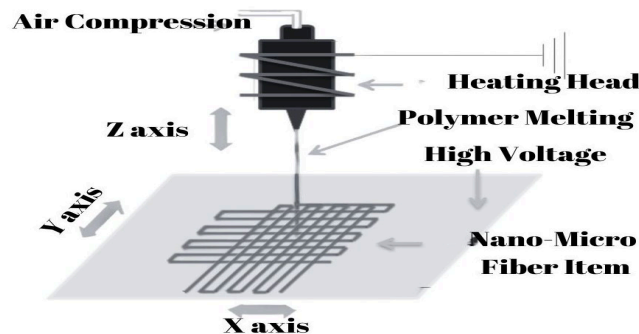


Figure 4. Melt electrowriting technique.

1.3.Traditional Bare Metal Stent Production Technique

With the spread of cardiovascular diseases, the demand for the production and use of different stents has increased. The common point of the studies is to achieve more efficient and safe results. With material science, treatment techniques and new manufacturing techniques, the transition from simple Bare Metal stents to Drug-eluting stents and Biodegradable stents has been achieved. The leading brands of commonly used stents are approved by the necessary organizations. Again, many of them are stents made of stainless steel tubes that expand with balloons. These stent designs, which are between 8-38 mm in length, can be manufactured as open or closed cell. The mechanical behavior and strength of these stents

are specified by standards. Traditional Bare Metal Stents can be manufactured with 316 L stainless steel, CoCr (Cobalt-Chromium) Alloys, Nitinol (Nickel-Titanium) or Ti (titanium) alloys. Alloys containing iron, such as 316L, degrade as a result of a decrease in corrosion resistance in long use. Due to their behavior in the body environment, the producibility of more resistant and durable stents with CoCr alloys has been specified. However, both the excellence in corrosive resistance, high strength results and material lightness reveal that stents produced with Ti and Nitinol alloys are more efficient. Although the densities and weights of 316L and CoCr alloys are higher than Nitinol and Ti Alloys, their processing costs are lower [4,5].

Table 1. Mechanical strength of materials used in the production of traditional bare metal stents.

| Material | Intensity (g/cm ³) | Elongati on at Fracture (%) | Yield Strength (MPa) | Tensile Strength (Mpa) | Young's Modulus (GPa) | Tempe rature (°C) |
|----------|-----------------------------------|--------------------------------------|----------------------------|------------------------------|-----------------------------|-------------------------|
| Nitinol | 6.45 | 50 | 690 | 895 | 83 | 1310 |
| Titanium | 4.429 | 14 | 786 | 950 | 110 | 1660 |
| CoCr | 10 | 20 | 560 | 960 | 210 | 1454 |
| 316L | 8 | 40 | 310 | 668 | 193 | 1390 |

Mechanical strength of materials used in the production of traditional bare metal stents shown in Table 1.

For example, 100 µm thick stainless steel sheet plates are laser cut using cut-out geometry. The plates are formed into cylindrical form and joined by laser spot welding. Or it can be manufactured by cutting Steel Cylinder Tubes of appropriate size and thickness using laser. Afterwards, the final product is reached by electropolishing. Traditional bare metal 316l steel stent shown in Figure 5.

**Figure 5.** Traditionally manufactured 316l steel stent.

2.MATERIALS AND METHODS

2.1.Device Selected For Production

In this study, Melt Electro Writing device was used for production. Melt electro writing (MEW) device and its technical specifications are shown in figure 6 and table 2 respectively.

**(A) Melt Electro Writing Device****(B) Rotary Table****Figure 6.** (A) Melt electro writing (MEW) Device, (B) Rotary table.

Table 2. MEW device technical specifications.

| | | |
|--|---|----------------------------|
| Melt Electrowriting Technology | : | Pneumatic Driven Extrusion |
| Melt Electrowriting High Voltage Range | : | 0kV- 15kV DC |
| Melt Electrowriting Current Range | : | 0 μ A- 150 μ A |
| Printing Pressure Resolution | : | 0.1 psi |
| Air Pressure Range | : | 0 kPA- 800 kPA |
| Z Resolution Per Microstep | : | 1 μ m |
| XY Resolution Per Microstep | : | 1 μ m |
| Printhead Temperature Range | : | Room Temperature - 265°C |
| Layer Resolution | : | <10 μ m |
| Collector Rotation Speed Range | : | 0-5000 |

2.2. Stent Design

Stent sizes vary according to the vascular structure where the stent will be placed and the needs of the patient. When the products of the manufacturers are examined, it is seen that the diameter of the stents varies between 2.0 mm and 5.0 mm, while their length varies between 8 mm and 38 mm, and the wall thickness varies between 0.1 mm and 0.3 mm. However, smaller or larger diameters and different lengths and wall thicknesses may also be available if required. The choice of diameter depends on the diameter of the intervened vessel. Which length is used depends on the length of the lesion and the anatomy of the vessel in the area where it will be placed. Thickness can affect the stent's durability and ability to maintain patency. In the ISO25539-2:2012 standard, the design, performance and size requirements of standard stents are specified. During stent placement, doctors usually use angiographic images and imaging techniques such as intravascular ultrasound (IVUS) to determine the optimal stent diameter and length. Since each patient's anatomy is different, personalized planning is important. In this study, a grid pattern stent design with a diameter of 3 mm, a length of 30 mm and a wall thickness of 0.125 mm was selected. In the selection of this pattern, the most optimal production between the functionality of the stent product and the capabilities of the device used was taken into consideration. Among the most commonly used grid pattern, ellipse pattern and circle pattern designs, based on the comparisons of PCL material and finite element analysis; It is observed that one of the important factors in

stent efficiency is the design structure [6]. In this study, it was concluded that the most suitable pattern that can be produced in various trials according to the movement and speed of the nozzle in xyz directions, the voltage of the rotary table and the rotational speed parameters in the current MEW device used for stent production may be in the form of a grid. The selected design was drawn with the help of the Solidworks program and modeled in 3D.

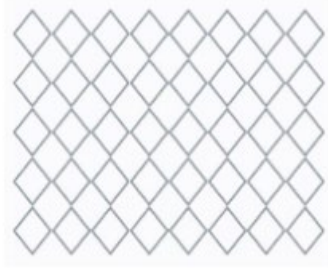
The stent design was made in the Solidworks program as defined below.

- Drawing the circle with a diameter of 3 mm, which forms the cylindrical diameter of the stent.
- In order to create the geometry of the stent design, drawing a clockwise 1-revolution arc with a diameter of 3 mm and a length of 30 mm, perpendicular to the circle wall, with an initial angle of 180 degrees.
- With the Sweep command, the drawn spring is brought to the solid cylindrical solid form with a thickness of 0.125 mm, which is the wall thickness of the design.
- In order to create the geometry of the stent design, drawing a 1-revolution, 3 mm diameter and 30 mm long arc perpendicular to the circle wall, counterclockwise with an initial angle of 180 degrees.
- With the Sweep command, the drawn spring is brought to the solid cylindrical solid form with a thickness of 0.125 mm, which is the wall thickness of the design.
- Selective reproduction of arcs in solid form

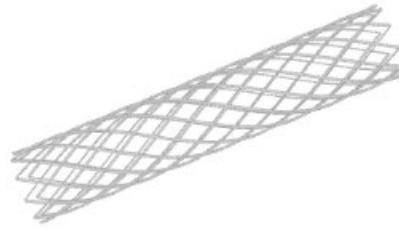
with geometry duplication at 360 degree equal intervals.

is shown in Figure 7, and the design stages listed above are shown in Figure 8.

The two-dimensional version of the stent design



(A) Open Display Of The Stent



(B) Folded Closed Form Of The Stent

Figure 7. Design of the stent with diamond pattern.

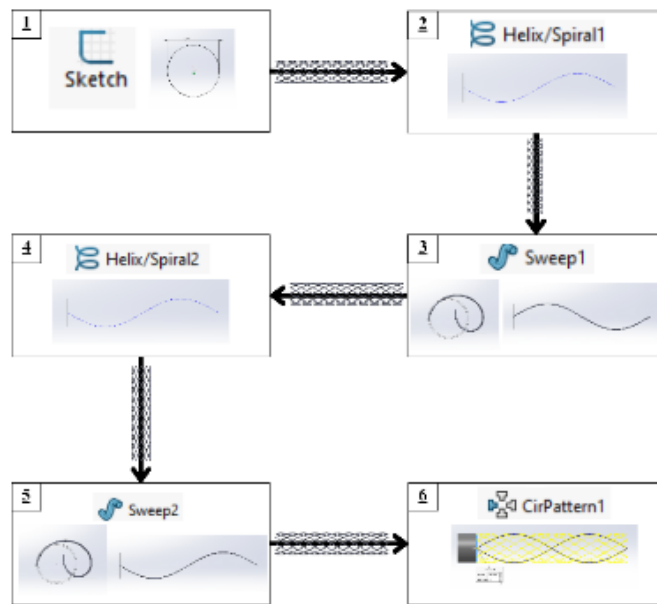


Figure 8. Stent design workflow chart.

2.3. Use Of Pcl In Melt Electrowriting Technique

Most thermoplastic materials can be used in the MEW production technique. However, due to its low melting temperature and degradable structure, Polycaprolactone (PCL) is the most commonly used material. PCL is known as a biodegradable and biocompatible polymer with high mechanical strength properties. PCL

polymer, which has advantages such as less immune reactivity after implantation and suitability for mechanically supporting bone cells, has flexibility in design and is widely used in biomedical applications [1,2,7]. The Physical Properties of PCL Material are shown below in Table 3.

Table 3. Physical properties of pcl material.

| Polymer | Solvent | Melting Temperature (°C) | Glass Transition Temperature (°C) | Elastic Modulus (GPa) |
|---------|---|--------------------------|-----------------------------------|-----------------------|
| PCL | Chloroform: Hexafluoroi, sopropanol, Dichloromethane, Toluene | 58-63 | -60 | 0.3- 0.6 |

The long-term degradation time of the PCL material, which is in the class of synthetic polymers, its ability to be produced in different pore sizes and its easy shaping behavior can also be listed among the reasons for preference. These features cause more functional results in the human body in line with the stent structure and usage purposes. Criteria such as Polymer Melting Temperature (°C), Glassy Transition Temperature (°C), Young's Modulus (GPa), Solvent Polymer Used, Unit Structure are in

accordance with the MEW production technique compared to other polymers. For these reasons, in this study, PCL material was determined as the production material.

The long-term degradation time of the Polycaprolactone (PCL) material, which is in the class of synthetic polymers, its ability to be produced in different pore sizes and its easy shaping behavior can also be listed among the reasons for preference.

2.4. Stent Production With Melt Electrowriting Technique

The diamond patterned stent commonly used in this study is made of PCL material with a width of 3 mm and a length of 30 mm by Melt Electro Writing method. The work flow chart for production is shown in figure 9.

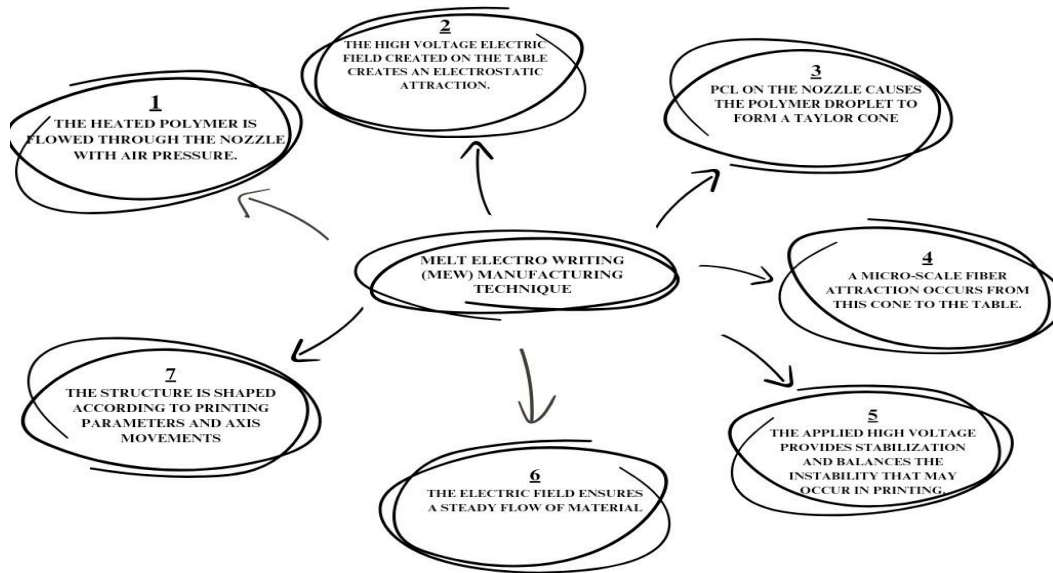


Figure 9. Work flow chart for melt electro writing technique and stent manufacturing process.

Melt Electro Writing (MEW) method can be used in stent production. As a result of the processing of thermoplastic biopolymer materials, especially PCL, under high voltage by reaching the required parameter values, a micron-scale, high-resolution and sensitive product emerges. Basically, the Melt Electro Writing (MEW) Technique provides a high-resolution production using melt extrusion and electrohydrodynamic fiber drafting. High efficiency is achieved by processing micro-nano strips in layers.

The production process is respectively; The heated polymer is flowed through the nozzle with air pressure, the high-voltage electric field created on the table creates an electrostatic attraction. The polymer on the nozzle causes the

droplet to form a Taylor cone. From this cone to the table, a micro-scale fiber attraction occurs. The applied high voltage provides stabilization and balances the instability that may occur in printing. The electric field ensures that the flow of material occurs in a constant manner. The structure is shaped according to the printing parameters and axis movements.

The most important element in the MEW Technique can be defined as the determination of the correct parameters. The melting temperature of the polymer, the applied pressure and nozzle feed speed, the speed of movement of the print head on the axes used, and the distance between the nozzle and the table directly affect the quality of production.

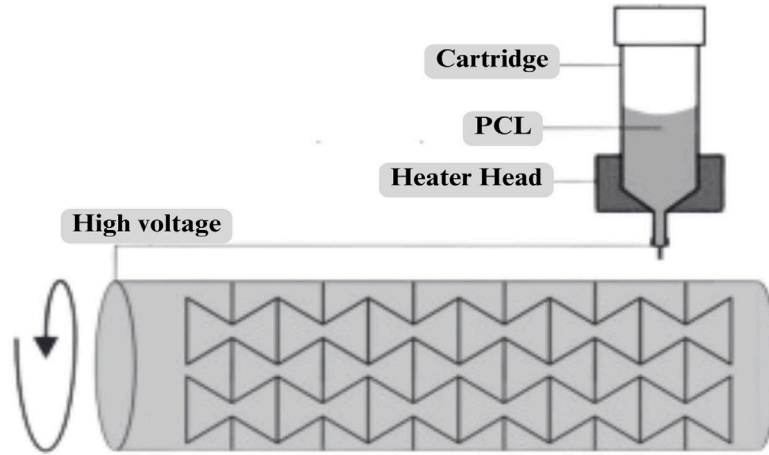


Figure 10. Melt electrowriting technique stent production principle.

Melt electrowriting technique stent production principle is shown in Figure 10. In order for the stent or any material to be produced by the MEW method, the 3D design of the relevant material must be made in a computer environment and a 3D design file must be created. After the 3D design file is created, the G-codes that determine the movements of the MEW production device, the working conditions, and the position of the part on the table are determined with another interface program and transferred to the MEW device. G-code can be defined as a programming language that guides work on all CNC machines. G-code stands for "Geometric Code". This

programming language is used to command a machine or device what to do or how to perform a process during production. The G-code tells the machine or device how much it will move on which axis, how much the movement speed will be and which path it will follow for manufacturing. In standard 3D printers or electro writing devices, additive layers are created on the table and the specified shape or product is revealed with G-code commands. For flawless manufacturing, G-codes suitable for the design and device should be written and transmitted to the device. An example of the Standard MEW Technique G-Code is shown in Figure 11.

```

1: X
2: G92 X-4 Y-4 F500
3: G1 X30 Y-4 A[R<_A>+0.1] B[R<_B>+0.39]
4: G1 X30 Y30 A[R<_A>+0.1] B[R<_B>+0.39]
5: G1 X-4 Y30 A[R<_A>+0.1] B[R<_B>+0.39]
6: G1 X-4 Y-4 A[R<_A>+0.1] B[R<_B>+0.39]
7:
8: G1 X0 Y0 A[R<_A>+0.1] B[R<_B>+0.39] F500
9: G1 X0 Y26 A[R<_A>+0.1] B[R<_B>+0.39]
10: G1 X3
11: G1 X3 Y0 A[R<_A>+0.1] B[R<_B>+0.39]
12: G1 X6
13: G1 X6 Y26 A[R<_A>+0.1] B[R<_B>+0.39]
14: G1 X9
15: G1 X9 Y0 A[R<_A>+0.1] B[R<_B>+0.39]
16: G1 X12
17: G1 X12 Y26 A[R<_A>+0.1] B[R<_B>+0.39]
18: G1 X15
19: G1 X15 Y0 A[R<_A>+0.1] B[R<_B>+0.39]
20: G1 X18
21: G1 X18 Y26 A[R<_A>+0.1] B[R<_B>+0.39]
22: G1 X21
23: G1 X21 Y0 A[R<_A>+0.1] B[R<_B>+0.39]
24: G1 X24
25: G1 X24 Y25.5 A[R<_A>+0.1] B[R<_B>+0.39]
26:
27: Z1
28:
29: G1 X0.5 Y25.5 A[R<_A>+0.1] B[R<_B>+0.39]
30: G1 Y22
31: G1 X23.5 Y22 A[R<_A>+0.1] B[R<_B>+0.39]
32: G1 Y19
33: G1 X0.5 Y19 A[R<_A>+0.1] B[R<_B>+0.39]
34: G1 Y16
35: G1 X23.5 Y16 A[R<_A>+0.1] B[R<_B>+0.39]
36: G1 Y13
37: G1 X0.5 Y13 A[R<_A>+0.1] B[R<_B>+0.39]
38: G1 Y10
39: G1 X23.5 Y10 A[R<_A>+0.1] B[R<_B>+0.39]
40: G1 Y7
41: G1 X0.5 Y7 A[R<_A>+0.1] B[R<_B>+0.39]
42: G1 Y4
43: G1 X23.5 Y4 A[R<_A>+0.1] B[R<_B>+0.39]
44: G1 Y1
45: G1 X0 Y1 A[R<_A>+0.1] B[R<_B>+0.39]
    
```

Figure 11. example of g-codes entered into the device for production by melt electro-writing technique

After entering the correct parameters, the molten polymer in the heater printhead is properly printed directly on the table. Printing is carried out via software compatible with the MEW device and a computer connection.

Designs saved in the appropriate format can be produced by transferring them from the computer to the device.

The production of cylindrical microfiber stents produced by the MEW Technique is carried out with a rotating tubular thrust bed connected to the rotary system. While the rotary table, which is placed in place of the standard table, performs a constant rotational movement in the direction of the entered speed and direction, the print head moving in the direction of the x-axis on the table performs production as in the basic principle. In this system, it is important to optimize the table rotation speed and printhead speed based on the number of layers in order to realize the production at the desired quality. After being designed in 3D in the computer

environment in accordance with the MEW device, grid pattern stents produced from PCL material with diameters of 2 mm, 3 mm and 4 mm, 30 mm length and 0.125 mm wall thickness were produced with G-codes produced by entering the parameters such as placement, nozzle temperature, rotary table rotation speed, placement of the stent on the table, feed rate of the nozzle in the x, y direction, etc., together with the shape obtained in accordance with the MEW technique. Examples of grid pattern stents of different diameters produced in the MEW device are shown in Figure 12.

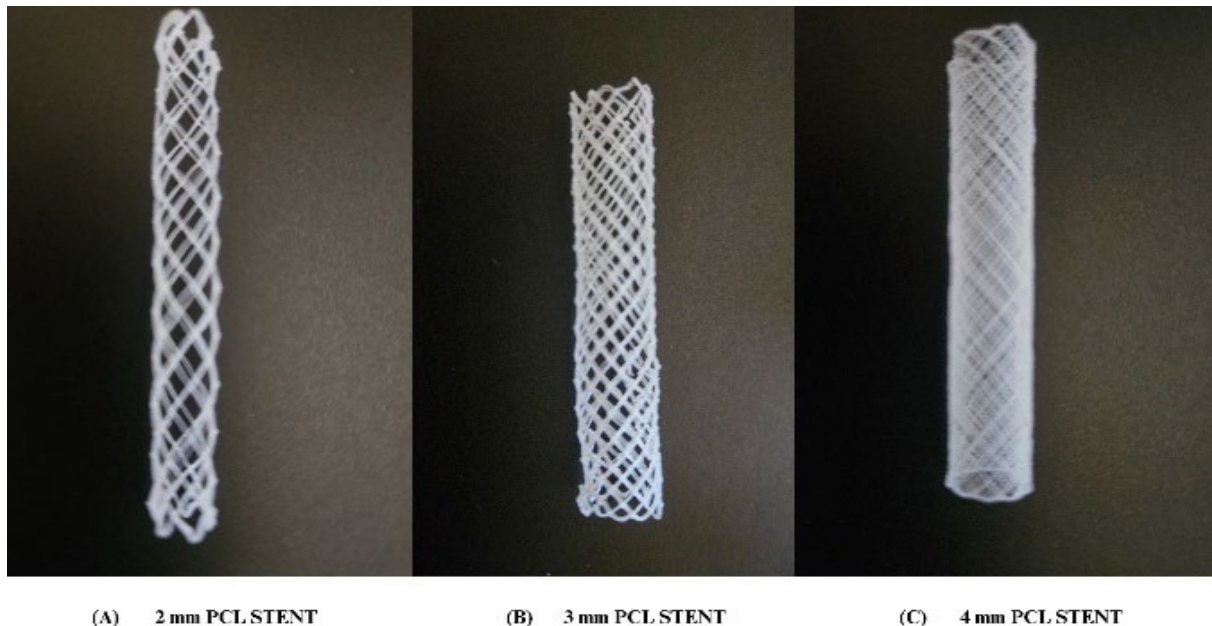


Figure 12. Stent models made of PCL material with (A) 2 mm, (B) 3 mm and (C) 4 mm diameter, 30 mm length and 0.125 mm wall thickness with a grid pattern produced in the MEW device.

2.5. Finite Element Analysis (FEA)

The high prevalence of cardiovascular diseases has increased the demand for the use of different stents. It is important to design and manufacture safer stents for coronary angioplasty to prevent stent narrowing. However, prototyping and mechanical testing of new stent designs are challenging, time-consuming and costly procedures. Therefore, parametric models and finite element simulations are used to help designers improve stent designs [12].

(FEA) to predict Equivalent Von-Mises Stress, Radial Recoil and Factor of Safety using ANSYS work bench software. Stent of different geometry are modeled using SOLIDWORKS and then structural analysis is performed on Stents of seven different materials viz. SS 316L

Stent, Cobalt Chromium L-605 Stent, Bio-Degradable Stent (PCL), Nitinol Stent (Austenite), Elgiloy Stent, Tantalum Stent, Cobalt Chromium MP35 N Stent under normal blood pressure. The 'Radial recoil', Equivalent 'Von-Mises Stress' and 'Factor of Safety' of various stent materials using same stent design and same boundary conditions are compared. The results reveal that the L-605 Cobalt Chromium has low radial recoil and 316 L Stainless Steel is having highest factor of safety among the selected stent materials[19].

The designed stent design was subjected to static simulation in Ansys programme using 316L and PCL material values. The ISO 25539 standard is a standard that specifies general

requirements and test procedures for stents. It includes different tests used to evaluate the mechanical properties of stents as well as biocompatibility, safety and efficacy. To test the durability of stents against external influences, their resistance under a certain force is evaluated. these tests are performed with loads ranging from 10 N to 100 N. Adhering to the above-mentioned standards, it was aimed to investigate the stresses at the grid intersections

on the -y and +y surfaces when pressure is applied from the inside, assuming that the balloon in the stent is inflated, assuming that there is a blockage in the upper and lower parts of the vessel. The ends of the design were considered fixed and subjected to a force of 10 N distributed along the stent from the designed outer surface points [8]. The fixed surfaces and applied forces are shown in Figure 13.

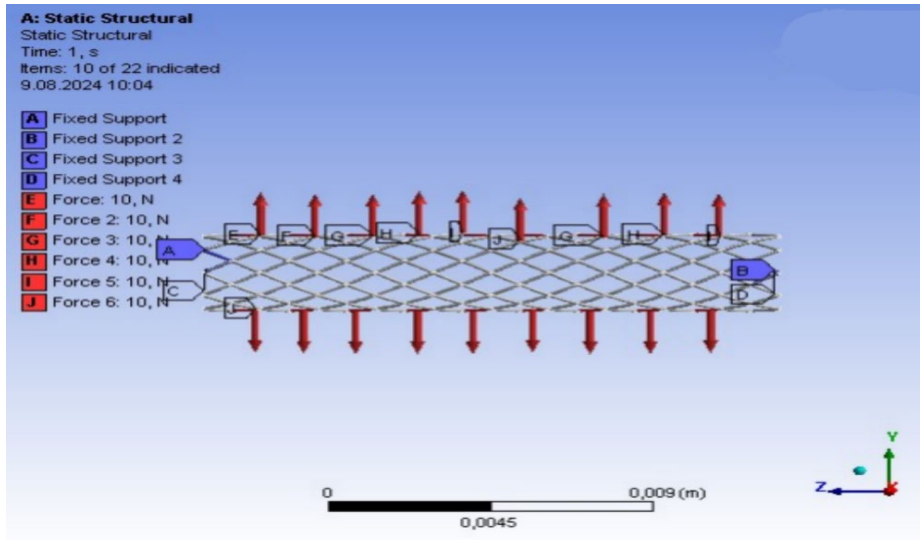


Figure 13. Fixed points and applied forces for FEA static analysis.

Equivalent Elastic Stress (Von Mises) and Displacement results of the finite element analysis performed in Ansys are shown in Figure 14.

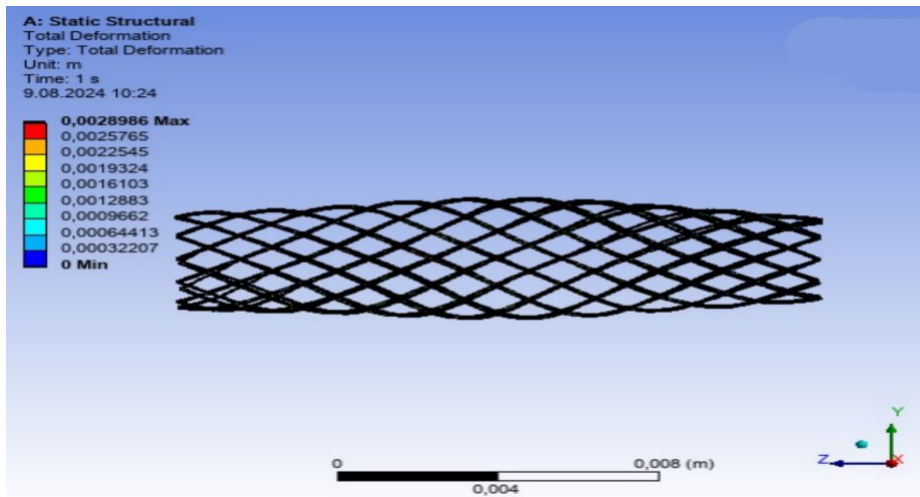


Figure 14. 316L material displacement results for FEA static analysis.

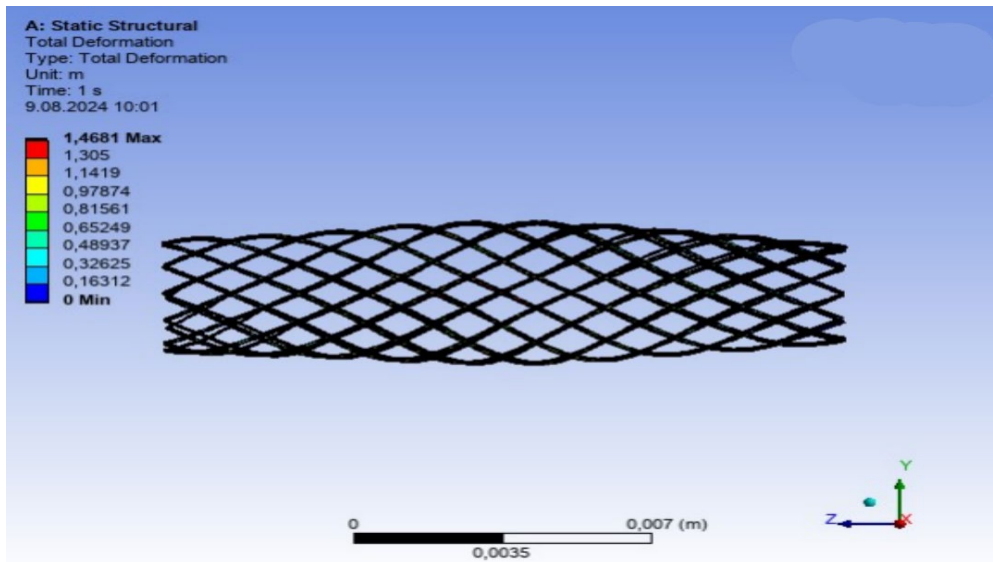


Figure 15. PCL material displacement results for FEA static analysis.

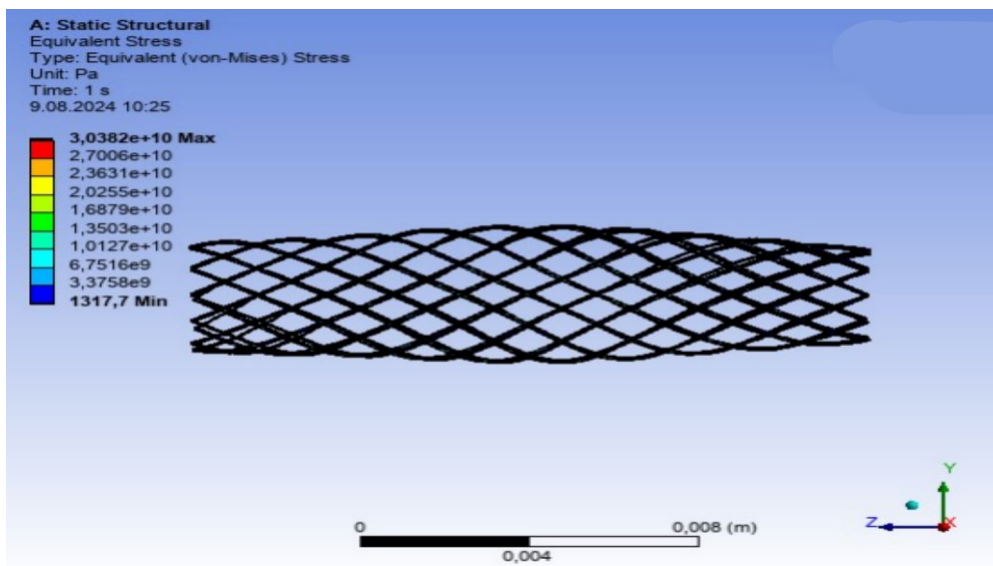


Figure 16. 316L material Von Mises results for FEA static analysis.

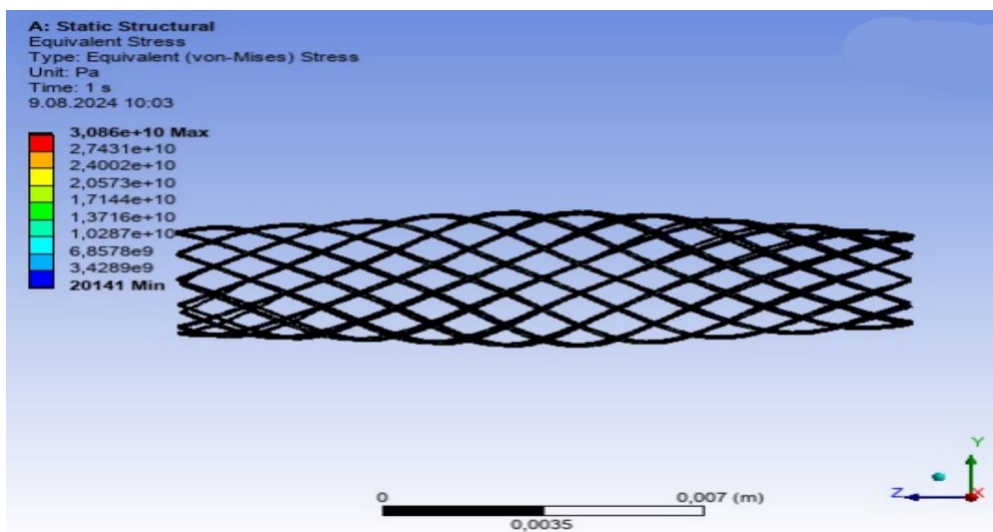


Figure 17. PCL material Von Mises results for FEA static analysis.

3. FINITE ELEMENT ANALYSIS (FEA) RESULTS

Detailed information and results of the simulation and finite element analysis of the identical design of a metal stent with a grid pattern made of 316L material, which is one of the commonly used stent types, and a stent with a grid pattern made of biodegradable PCL material with biocompatibility by MEW method are shown in Table 4. The ends of the design were considered fixed and the design the PCL stent can undergo severe plastic deformation under applied loads and potentially lose its structural integrity. The maximum displacement value of 1.4681 m is very high, which is an advantage in terms of flexibility in biomedical applications, but a major disadvantage in terms of mechanical durability. PCL Stent Advantages, Biodegradability provides an advantage for long-term implantation. It offers flexibility thanks to its low elastic modulus and has high adaptability in intravascular applications. Disadvantages, High deformation and low mechanical strength can lead to rapid deterioration of structural integrity. Due to the very low yield stress, there is a risk of structural failure when exposed to high loads. 316L Stent, Advantages: High mechanical strength and low deformation characteristics provide long-term stability. The high yield stress indicates that the stent can maintain its structural integrity even under high loads. Disadvantages, Non-biodegradability may lead to possible complications in long-term permanent implantations. It is more limited in flexibility than PCL, which may lead to adaptation difficulties in intravascular applications. Although the PCL stent offers some advantages due to its biodegradability, it

was subjected to a force of 10 N distributed along the stent from the grid intersection points on the upper and lower outer surfaces. PCL Equivalent (Von-Mises) Stress $3,086e+010$ Pa, 316L Equivalent (Von-Mises) Stress $3,0382e+010$ Pa, PCL Result Displacement Maximum 1,4681 m, 316L Result Displacement Maximum $2,8986e-003$ m results were observed. According to these results; the following conclusions were reached. The results of the finite element analysis show that has major disadvantages in terms of mechanical durability due to its low yield stress and high deformation capacity. This may cause the stent to lose its structural integrity and functionality in a short time. However, its biodegradability turns this disadvantage into an advantage.

The 316L stent, on the other hand, offers a longer-lasting and more stable option with its high mechanical strength and low deformation properties. However, its non-biodegradability may pose potential risks in long-term implantations. Therefore, additional strategies such as biocompatible coatings or surface modifications may need to be considered in the design of the 316L stent. This adds to the already high cost and manufacturing difficulty. In conclusion, both materials have advantages and disadvantages in specific applications. Depending on the field of application and duration of use, the choice of material and stent design should be optimised. In the field of biomedical engineering, supporting such designs with further analyses and experimental verifications will contribute to the development of safe and effective implants.

Table 4. Analysis Results

| | 316L STENT | PCL STENT |
|--------------------------------------|------------------------------|----------------------------|
| MASS | : 2,3783e-005 kg | 3,7196e-006 kg |
| VOLUME | : 2,9901e-009 m ³ | 2,9901e-009 m ³ |
| DENSITY | : 8.007,89 kg/m ³ | 1.021,01 kg/m ³ |
| MESH NODE COUNT | : 157209 | 157209 |
| NUMBER OF MESH ELEMENTS | : 69870 | 69870 |
| MESH PASS RATE | : 0,272 | 0,272 |
| MAXIMISED LAYERS | : 5 | 5 |
| GROWTH RATE | : 1,2 | 1,2 |
| TARGET MESH QUALITY (DEFAULT) | : 5,e-002 | 5,e-002 |
| APPLIED FORCE | : 10 N | 10 N |
| YIELD STRESS | : 200 MPa | 30 MPa |
| EQUIVALENT (VON-MISES) STRESS | : 3,0382e+010 Pa | 3,086e+010 Pa |
| RESULT DISPLACEMENT MAXIMUM | : 2,8986e-003 m | 1,4681 m |

4. CONCLUSION AND EVALUATION

In this study, the design of a stent with a grid pattern and its production with the mew production method is described together with its stages. the ease of production and the functionality of the material are explained, and a comparison with the metal stent, which is one of the leading traditional methods, is made. the reason for not going into detail in the finite element analysis is that the main purpose of the study is the production of stents from PCL material by MEW method and also to open the door to detailed scans and analyses that we will perform in future studies.

In future studies, it is aimed to produce different models and production techniques together, to produce medicated and timed stents in coordination with the medical and biomedical fields and to test them in the laboratory environment. In the future, when biodegradable medicated stents are produced for vascular damage and treatment, timely and most accurate treatment can be applied in diseases.

Based on the results of this study, it is understood that the MEW method has a bright future in terms of advantages in terms of ease of production, processing parameters and biocompatibility and will have a higher share in the sector in the future. In terms of disadvantages, it is seen that it is not possible to work in every design with the current possibilities due to deficiencies such as low mechanical strength results and the inability of the device to produce every design in production.

Since the production of the most optimal design will best serve the general purpose of the material, the method that can produce the design in the easiest and most efficient way comes to the fore. This problem will be eliminated with the development of MEW devices in the future. Maximum benefit will be achieved with devices that can produce the most ideal designs.

When we reach the point where we can produce the design we want with technological corrections such as easier movement of the print head in different axes in line with device mechanical and software developments, development of the rotating drum system and optimisation with software, it will become possible to make instant and fast productions suitable for the vessel structure, occlusion

structure or usage structure with the MEW method. The ability to produce all design models in devices will lead to the emergence of more efficient and effective designs, faster development of existing technology through trial and error, and easier fight against diseases in the field of medicine [11].

Design-oriented development of the devices used in MEW Technique will provide maximum benefit with more specific designs of this method, which already provides high efficiency.

Stainless steel is the most popular material for conventional stents and has excellent mechanical behaviour during deformation. However, stents made of stainless steel remain permanently in the body and can cause complications or lead to blockage of the vessel. To overcome these shortcomings, biodegradable stents that dissolve and disappear in the body over time should be developed [16].

In conclusion, the choice of stent should be balanced according to the specific requirements of the application. While PCL stents are suitable for short-term applications with their flexibility and biocompatibility advantages, 316L stainless steel stents may be preferred for situations requiring long-term performance and mechanical durability. The specific advantages and disadvantages of both materials are important points to be considered during stent selection. Future studies focusing on modification and improvement of these materials may contribute to the development of stents with better performance [17-18].

REFERENCES

1. Abbasi, N., "Effect of Offset/ Gradient melt electrowritten (MEW) PCL scaffolds in bone regeneration", *Advanced Materials Science Research*, Vol. 3, Issue 2, 2020.
2. Abbasi, N., Lee, R.S.B., Ivanovski, S., Love, R.M., Hamlet, S., "In vivo bone regeneration assessment of offset and gradient melt electrowritten (MEW) PCL scaffolds", *Biomater Res.*, Vol. 24, Issue 17, 2020.
3. Abdullah, A.C., Ozarslan, O., Farshi, S.S., Dabbagh, S.R., Tasoglu, S., "Aggregate", Vol. 2024, e495, 2024.

4. Bhullar, S.K., Lekesiz, H., Karaca, A.A., Cho, Y., Willerth, S.M., Jun, M.B.G., “Characterizing the Mechanical Performance of a Bare-Metal Stent with an Auxetic Cell Geometry”, *Applied Sciences*, Vol. 12, Issue 2, 910, 2022.
5. Carter, A.J., Lee, D.P., Yeung, A.C., “Metalizing with new stent designs”, *Catheter Cardiovasc Interv.*, Vol. 53, Issue 3, Pages 426-428, 2001.
6. Çıkılı, M.B., “Design Parameters for Bio-absorbable Stent Production with Additive Manufacturing”, *Proceedings of International Conference on Mechanical Engineering*, Pages 360-364, UET, Lahore, Pakistan, 2020.
7. Darroch, C., Asaro, G.A., Gréant, C., Suku, M., Pien, N., van Vlierberghe, S., Monaghan, M.G., “Melt electrowriting of a biocompatible photo-crosslinkable poly(D,L-lactic acid)/poly(ϵ -caprolactone)-based material with tunable mechanical and functionalization properties”, *Journal of Biomedical Materials Research, Part A*, Vol. 111, Issue 6, Pages 851–862, 2023.
8. Dolan, F., Lally, C., Prendergas, P.J., “Cardiovascular stent design and vessel stresses: a finite element analysis”, *Journal of Biomechanics*, Vol. 38, Pages 1574-1581, 2005.
9. Kim, D.B., Choi, H., Joo, S.M., Kim, H.K., Shin, J.H., Hwang, M.H., Choi, J., Kim, D.G., Lee, K.H., Lim, C.H., Yoo, S.K., Lee, H.M., Sun, K., “A comparative reliability and performance study of different stent designs in terms of mechanical properties: foreshortening, recoil, radial force, and flexibility”, *Artificial Organs*, Vol. 37, Issue 4, Pages 368–379, 2013.
10. Polanec, B., Kramberger, J., Glodež, S., “A review of production technologies and materials for manufacturing of cardiovascular stents”, *Advances in Production Engineering & Management*, Vol. 15, Pages 390-402, 2020.
11. Schlun, M., Martin, H., Grabow, N., Schmitz, K.P., “Design strategy for balloon-expandable stents made of biodegradable polymers using finite element analysis”, *Biomedizinische Technik, Biomedical Engineering*, Vol. 47, Issue 2, Pages 831–834, 2002.
12. Tayyebi, S., Ghasemi Gilavan, S., Mokhlesabadi, M., Barati, S., Fatourae, N., “Parametric Design and Finite Element Simulation of Coronary Stents”, 2020, Pages 271-276.
13. Thorsnes, Q., Turner, P., Ali, M., Cabral, J., “Integrating Fused Deposition Modeling and Melt Electrowriting for Engineering Branched Vasculature”, *Biomedicine*, Vol. 11, 3139, 2023.
14. Vahabli, E., Mann, J., Heidari, B.S., Lawrence-Brown, M., Norman, P., Jansen, S., De-Juan-Pardo, E., Doyle, B., “The Technological Advancement to Engineer Next-Generation Stent-Grafts: Design, Material, and Fabrication Techniques”, *Advanced Healthcare Materials*, Vol. 11, Issue 13, e2200271, 2022.
15. Wegner, F., Friedrich, T., Wattenberg, M., Ackers, J., Sieren, M.M., Kloeckner, R., Barkhausen, J., Buzug, T.M., Graeser, M., von Gladiss, A., “Bare-Metal Stent Tracking with Magnetic Particle Imaging”, *International Journal of Nanomedicine*, Vol. 19, Pages 2137–2148, 2024.
16. Xu, C., Yin, Z., Roy-Chaudhury, P., Campos, B., Hou, G., Schulz, M., “The Development of a Magnesium Biodegradable Stent: Design, Analysis, Fabrication, and In-vivo Test”, *Medical Research Archives*, Vol. 8, 2020.
17. Yageng Li, Yixuan Shi, Yuchen Lu, Xuan Li, Jie Zhou, Amir A. Zadpoor, Luning Wang, Additive manufacturing of vascular stents, *Acta Biomaterialia*, Volume 167, 2023, Pages 16-37
18. Das A, Mehrotra S, Kumar A. Advances in Fabrication Technologies for the Development of Next-Generation Cardiovascular Stents. *Journal of Functional Biomaterials*. 2023; Vol. 14, Issue 11, Pages 544.
19. Rahul Kumar Choubey, Sharad K. Pradhan, Prediction of strength and radial recoil of various stents using FE analysis, *Materials Today: Proceedings*, Volume 27, Issue 3, Pages 2254-2259 2020,



ULUSLARARASI 3B YAZICI TEKNOLOJİLERİ
VE DİJİTAL ENDÜSTRİ DERGİSİ

INTERNATIONAL JOURNAL OF 3D PRINTING
TECHNOLOGIES AND DIGITAL INDUSTRY

ISSN:2602-3350 (Online)

URL: <https://dergipark.org.tr/ij3dptdi>

EKLEMELİ İMALAT TEKNOLOJİSİYLE ÜRETİLMİŞ DÜZ VE KAVISLI KARBON FİBER TAKVİYELİ POLİMER MATRİSLİ KOMPOZİTLERİN KISA-KIRIŞ

SHORT-BEAM STRENGTH COMPARISON OF
ADDITIVELY MANUFACTURED FLAT AND CURVED
CARBON FIBER-REINFORCED POLYMER MATRIX
COMPOSITE MATERIALS

Yazarlar (Authors): Sedat Süsler 

Bu makaleye şu şekilde atıfta bulunabilirsiniz (To cite to this article): Süsler S.,
“Eklemeli İmalat Teknolojisiyle Üretilmiş Düz ve Kavisli Karbon Fiber Takviyeli Polimer
Matrisli Kompozitlerin Kısa-Kiriş Mukavemetlerinin Karşılaştırılması” *Int. J. of 3D Printing
Tech. Dig. Ind.*, 8(3): 352-360, (2024).

DOI: 10.46519/ij3dptdi.1534538

Araştırma Makale/ Research Article

Erişim Linki: (To link to this article): <https://dergipark.org.tr/en/pub/ij3dptdi/archive>

EKLEMELİ İMALAT TEKNOLOJİSİYLE ÜRETİLMİŞ DÜZ VE KAVISLİ KARBON FİBER TAKVİYELİ POLİMER MATRİSLİ KOMPOZİTLERİN KISA-KİRİŞ MUKAVEMETLERİNİN KARŞILAŞTIRILMASI

Sedat Süsler^a 

^aKocaeli Üniversitesi, Havacılık ve Uzay Bilimleri Fakültesi, Havacılık ve Uzay Mühendisliği Bölümü, TÜRKİYE

* Sorumlu Yazar: sedat.susler@kocaeli.edu.tr

(Geliş/Received: 16.08.24; Düzeltme/Revised: 26.09.24; Kabul/Accepted: 01.10.24)

ÖZ

Bu çalışmada, eklemeli imalat teknolojisi kullanılarak üretilmiş düz ve kavisli polimer matrisli kompozitlerin kısa-kiriş mukavemetleri karşılaştırmalı olarak incelenmiştir. Sürekli filaman imalatı yöntemiyle üretilen tek yönlü sürekli karbon fiber takviyeli kompozit kısa-kirişler, geometrik olarak birbirinden farklı üç numune grubu olarak sınıflandırılmış ve üretimlerinin ardından üç-nokta eğilme testine tabi tutulmuştur. Kuvvet ve deplasman verileri test sırasında elde edilip, grafiksel olarak kuvvet-deplasman ve gerilme-deplasman eğrileriyle test gidişatı gözlemlenmiştir. Özgül mukavemet kavramı da çalışmaya dahil edilerek, kısa-kiriş mukavemeti karşılaştırmasına nesnellik kazandırılmıştır. Kavisli kompozit kısa-kiriş, eşdeğer özelliklere sahip düz bir kirişe göre az bir miktar daha düşük mukavemete sahipken, enerji depolama kapasitesinde artış meydana gelmiştir. Kavisli kirişin kalınlığı %50 oranında ve içerdiği karbon fiber oranı 2 katı artırıldığındaysa, mukavemet değerini %19 arttırmış gözükse de özgül mukavemet değerinde %23 düşüş meydana getirmiştir. Çalışma, eriyik biriktirmeli modelleme temelli yeni bir teknik olan sürekli filaman imalatı teknolojisiyle üretilen kompozitlerin, henüz yeterli seviyede araştırılmamış mekanik performanslarını anlamaya yönelik katkı sunma, farkındalık yaratma ve gelecekteki mühendislik uygulamaları için yol gösterici nitelikte olma gayreti içindedir.

Anahtar Kelimeler: Eriyik Biriktirmeli Modelleme, Sürekli Filaman İmalatı, Kısa-Kiriş Mukavemeti, Katmanlar Arası Kayma Mukavemeti, Kavisli Yapılar, Sürekli Fiber Takviyeli Kompozit.

SHORT-BEAM STRENGTH COMPARISON OF ADDITIVELY MANUFACTURED FLAT AND CURVED CARBON FIBER-REINFORCED POLYMER MATRIX COMPOSITE MATERIALS

ABSTRACT

This study presents a comparative analysis of the short-beam strength of flat and curved polymer matrix composites which were manufactured by using additive manufacturing technology. Unidirectional continuous carbon fiber-reinforced composite short beams which were manufactured through the continuous filament fabrication method, had been classified into three geometrically distinct sample groups and then subjected to three-point bending tests. Force and displacement data were obtained during the test, and the test progression was observed graphically along the force-displacement and stress-displacement curves. The concept of specific strength was also included into the study to provide an objective basis for comparing short-beam strength. Although the curved composite short-beam exhibited slightly lower strength than a flat beam with equivalent properties, its energy storage capacity increased. However, when the thickness of the curved beam was increased by 50% and the carbon fiber content was doubled, its strength increased by 19%, although a 23% decrease in specific strength was observed. This study aims to contribute to the understanding of the adequately unstudied mechanical

performance of 3D-printed composites with continuous filament fabrication, which is a new technique based on fused deposition modeling, to raise awareness, and to provide guidance for future engineering applications.

Keywords: Fused Deposition Modelling, Continuous Filament Fabrication, Short-Beam Strength, Interlaminar Shear Strength, Curved Structures, Continuous Fiber Reinforced Composite.

1. GİRİŞ

Ekleme imalat (Eİ), yaygın olarak bilinen adıyla 3 boyutlu (3B) baskı, malzeme bilimi ve mühendisliği alanında devrim yaratmıştır. Yapıların katman katman imalatına dayanan bu teknik, geleneksel üretim yöntemleriyle üretimi zor veya imkânsız olan hem karmaşık ve özelleştirilmiş hem de optimize edilmiş yüksek performanslı yapıları düşük maliyetle üretmeyi mümkün kılmıştır [1]. Partikül veya kısa fiber formunda fiberlerle takviye edilmiş polimer kompozit 3B baskı filamentini geliştirme ve 3B yazıcılara entegre etme ulusal literatürde de kendine yer bulmaktadır [2]. Uzun ve sürekli fiberlerin termoplastikler içine entegrasyonu ile birlikte daha yüksek performanslı polimer kompozit parçaların üretilebilirliği için, filament malzeme geliştirme yanında 3D baskı cihazları ve tekniklerinin de geliştirilmesini gerektirir. Çeşitli Eİ teknikleri arasında daha yeni ve geliştirmeye açık bir teknoloji olan sürekli filaman imalatı (SFİ) tekniği, eriyik biriktirmeli modelleme (EBM) tekniğiyle üretilen polimer yapıların sürekli fiberlerle takviye edilerek polimer matrisli kompozit formunda basılabilmesinin önünü açan çok yönlü ve erişilebilir bir yöntem olarak öne çıkmıştır. İkili nozul içeren bir ekstrüdere sahip baskı cihazları kullanan bu teknik, tasarım esnekliğiyle birlikte malzeme verimliliği ve fiber yönelimi ile dağılımının hassas kontrolü yoluyla mekanik özellikleri özelleştirme ve iyileştirme imkânı gibi önemli avantajlar sunar. Bir nozul, eriyik termoplastik veya kısa/partikül takviyeli termoplastik malzeme birikimi için kullanılırken, diğer nozul; sürekli karbon, cam veya aramid fiber demeti içeren polimer kompozit filament tarafından beslenir [3]. Sürekli fiberlerin entegrasyonu, 3B baskı yapıların mekanik özelliklerini artırarak, üstün özgül mukavemet, sertlik ve dayanıklılık sağlar ve bu yapıları havacılık ve otomotiv endüstrisi uygulamaları için oldukça arzu edilir hale getirebilir [4].

Eİ yöntemiyle üretilmiş sürekli ve uzun fiberlerle güçlendirilmiş kompozitlerin çeşitli

yükleme koşulları altındaki mekanik performanslarının değerlendirilmesi, hem gerçek sanayi uygulamalarındaki potansiyel ve sınırlamalarını anlamak, hem de 3D baskı cihazları ve malzemelerinin güncellenmesi için kritik öneme sahiptir. Bu bağlamda; kilit bir parametre, kompozit malzemenin katmanlar arası kayma mukavemetinin (KAKM) bir ölçütü olan kısa-kiriş mukavemetidir (KKM). ASTM D2344/2344M-22 standardı [5], düz ve kavisli polimer matrisli kompozitlerin üç-nokta eğilme testi yoluyla kısa kiriş mukavemetini belirlemek için standartlaştırılmış bir yöntem sağlar. Gerçek sanayi uygulamalarında, düz veya kavisli kısa-kiriş formuna uyan yapıların tasarımı ve üretimi için dayanımı ölçülebilmek adına basitleştirilmiş bir model yaratır. Hasar moduna bağlı olarak, malzemenin kayma kuvvetlerine ve kayma kaynaklı delaminasyonlara karşı direncinin güvenilir bir ölçüsünü sunar.

Literatür incelendiğinde, ticarileşmiş durumdaki Markforged® endüstriyel ve masaüstü baskı cihazları ile SFİ metodu özelinde yoğunlaşmış bir araştırma birikimi gözükmektedir. Daha önce yayınlanan derleme makalelerde, SFİ temelli 3B baskı teknolojiyle üretilmiş sürekli fiberli kompozit malzemelerin çeşitli yüklemeler altındaki mekanik özellikleri ve etki eden baskı parametreleri üzerine yapılmış çalışmalar kapsamlı bir şekilde incelenmiş ve sınıflandırılmıştır [6-8]. SFİ yöntemiyle üretilen 3B baskılı sürekli fiber destekli kompozit malzemelerin KKM ve/veya KAKM değerlerinin analiz edildiği çalışmalar [9-13] incelendiğinde, üretilen kısa kirişlerin hem düz formda olduğu hem de düz bir numune üretiminde optimum baskı yatağı yerleşimi olan, numune yüzeyi üzerinde (flat) basıldığı belirlenmiştir. Yazarların bilgisi dahilinde, 3B yazıcıyla üretilmiş sürekli fiber destekli kavisli polimer kompozit malzemelerin KKM değerlerinin analiz edildiği ve düz form ile karşılaştırılmalı olarak sunulduğu bir çalışma literatürde mevcut değildir.

DeneySEL sonuçların karşılaştırmalı olarak sunulduğu bu çalışmada, sürekli ve tek yönlü karbon fiberlerle takviye edilerek EBM'ye dayalı SFİ tekniğiyle üretilmiş düz ve kavisli kısa-kiriş formundaki polimer kompozitlerin maksimum kuvvetleri, KKM değerleri ve hasar modları incelenmiştir. Karbon fiber demetlerini kavisli yapıdaki kirişe gömebilecek şekilde, baskı yatağında kenar üzerinde yerleşim (on-edge) yöntemi uygulanmıştır. Devamında, kavisli kısa-kiriş modelin kalınlığı ve içine gömülen sürekli karbon fiber miktarı artırılarak üçüncü bir kiriş konfigürasyonu daha karşılaştırmalı çalışmaya dahil edilerek, bu parametrelerin test çıktılarına olan etkisi gösterilmiştir. Testleri yapılan tüm kısa-kiriş numunelerinin kuvvet-deplasman ve kısa-kiriş gerilmesi-deplasman grafikleri de gösterilip yorumlanmış; devamında da maksimum kuvvet ve KKM değerleri ve bunların ortalamaları tablolarla karşılaştırılmıştır. Yapılan üç-nokta eğilme testleri sonucu meydana gelen hasarlara ait resimler de incelenmiştir.

2. MATERYAL VE METOT

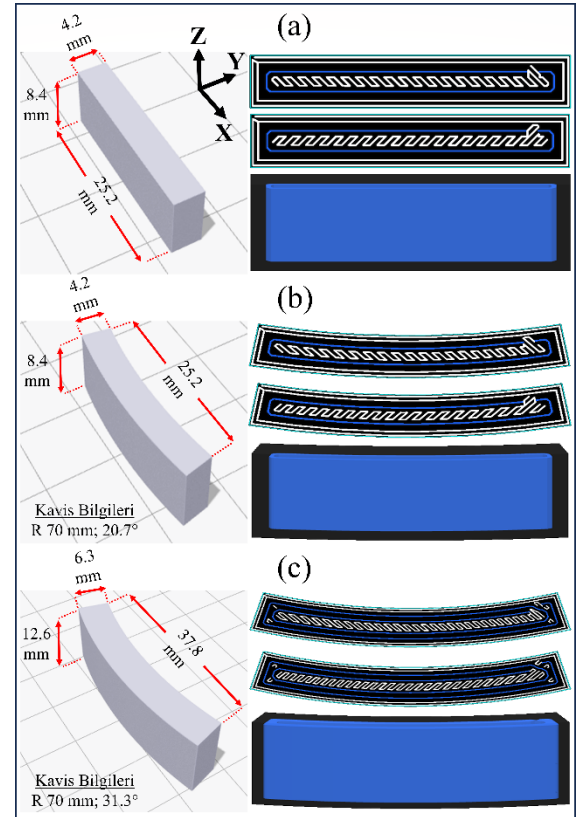
Üç-nokta eğilme testleri ve bu testlerde kullanılmış numunelerin üretimleri sırasıyla, Queen's University Belfast Makina ve Havacılık ve Uzay Mühendisliği Fakültesi'nde yer alan Malzeme Test ve Öğrenci Tasarım Laboratuvarı bünyesinde gerçekleştirildi.

Üretimler için kullanılan Markforged Mark Two masaüstü 3B yazıcı [14], termoplastik ve fiber filament makaraları tarafından ayrı ayrı beslenen iki ısıtılmış nozul kullanarak, sürekli ve uzun fiber takviyeli termoplastik üretme kabiliyetine sahiptir. Termoplastik ve SFİ fiber nozullar için çalışma sıcaklıkları sırasıyla, yaklaşık 275 °C ve 250 °C'dir. Termoplastik malzeme olarak, bir poliamid türü olan, geleneksel naylon malzemesinden daha güçlü ve sert yapıdaki Nylon White kullanılmıştır. Karbon fiber takviyesi için kullanılan 3B yazıcının diğer filamentiyse aslında bir çeşit önceden geleneksel naylon emprenye edilmiş karbon fiber demetidir ve katı halde 0.3 mm çapında filament formda bulunur. Filament bütünlüğünü oluşturan içindeki naylon, fiber nozulundan geçerken sıcaklık etkisiyle erir ve içindeki sürekli karbon fiber demeti, istenen baskı alanına dağınk bir şekilde gömülür. Karbon filament, alüminyum 6061-T6 kadar sert ve ondan daha yüksek mukavemet değerlerine ulaşabilir. 1.4 g/cm³ yoğunluğa, 60

GPa çekme elastisite modülüne ve 800 MPa çekme mukavemetine sahiptir [15].

Düz ve kavisli numunelerin boyutlandırılmasında kullanılan temel parametre numunelerin kalınlık (h) değeridir. L , numune uzunluğu ve b , numune genişliği olmak üzere, ASTM D2344/2344M-22 standardına [5] göre, $L=6.0 \times h$ ve $b=2.0 \times h$ olarak atanmıştır. Kavisli numunelerde L uzunluğu, minimum veter uzunluğu olarak tanımlanır. Kavisin eğrilik yarıçapı 70 mm olmalıdır.

'D', düz kısa-kiriş ve 'K', kavisli kısa-kiriş bir numuneyi simgeleyen harf kodlarıdır. 'T1', 4.2 mm h değerini simgelerken, 'T2' ise %50 daha kalın ve iki katı miktarda karbon fiber takviyeli bir numune yaratacak şekilde, 6.3 mm kalınlığındaki h değerine ait kodlardır. Bu tanımlamalar ışığında, 'D-T1', 'K-T1' ve 'K-T2' kod gruplarıyla simgelenmiş üç farklı numune grubu bu çalışmada üretilmiştir. Boyutlandırma bilgilerine dayanarak üç farklı numune grubuna ait boyut değerleri Şekil 1'de gösterilmiştir.



Şekil 1. Numune boyutlandırması ile üstten ve yandan numunenin iç yapısı: (a) D-T1, (b) K-T1 ve (c) K-T2.

Eiger yazılımına [16] gönderilen STL formatındaki çizimler kullanılarak, aşağıdaki Çizelge 1’de yer alan baskı girdileriyle Şekil 1’de yer alan her numune grubu için üstten ve yandan numune içi baskı oryantasyonları elde edilmiştir. STL dosyası elde edilirken, kavisli numunelerin 3D baskıyla üretiminde kritik olan açısal tolerans değeri 1° seçilerek yüksek çözünürlükte baskı tercih edildi. Baskı yatağında on-edge inşa şekli kullanılarak, kavisli numunelerin hem destek kullanımı olmadan üretilmesi hem de numuneler içinde tek yönlü sürekli karbon fiber yönelimi sağlandı. Düz numuneler, h boyunca 0.125 mm baskı katman kalınlığıyla üretime izin veren flat konumlu inşa edilmeye uygun olmakla birlikte, kavisli numunelerle sağlıklı bir karşılaştırma için on-edge olarak üretildi. Sonuç olarak, tüm numune grupları, Şekil 1’de yer alan yandan oryantasyon görüntülerinde gösterildiği gibi, b boyunca 0.125 mm baskı katman kalınlığı değeriyle üretilerek yoğun karbon fiber gömülümü b boyunca sağlandı. Bununla birlikte, Çizelge 1’de belirtilen çatı/tabana katman sayısı değeri, baskı cihazı için minimum 5 olması gerektiğinden, b boyunca numunenin üst ve alt kısmında 0.625 mm kalınlığında Nylon White malzemesinden hem iyi bir yüzey pürüzlülüğü hem de içerideki karbon/naylon katmanları için su sızdırmazlık sağlayan, bölgeler oluşturuldu. On-edge inşa metoduyla, sırasıyla ‘T1’ ve ‘T2’ h değerleri için toplamda 2 ve 4 tek yönlü karbon fiber takviyeli katman elde edilebildi. Baskı cihazına ait minimum takviye edilen genişlik kriteri, en küçük takviye edilen alan ve minimum fiber uzunluğu gibi sınırlamalar ile tek yönlü fiber oluşturma açısından önemli eş merkezli fiber seçimi bu değerlerin elde edilmesinde etkili olmuştur [17]. Numune orta kısmı ile iyi bir yüzey pürüzlülüğü ve su sızdırmazlık için önemli ve 2 olarak atanan duvar katmanları Nylon White ile %100 katı dolgu ile doldurulmuştur. Şekil 1’de yer alan bitişik iki baskı katmanına ait üst oryantasyon görüntülerinde (numune kesiti), mavi çizgiler karbon/naylon nozul bölgelerini ve beyaz çizgiler de Nylon White bölgelerini göstermektedir.

Çizelge 1. Baskı girdileri.

| Parametre | Girdi |
|--------------------------|----------------------------|
| Dolgu Tipi | Katı Dolgu |
| Dolgu Yoğunluğu | %100 |
| Duvar Katmanı Sayısı | 2 |
| Çatı/Taban Katman Sayısı | 5 |
| Fiber Örüntü Alanı | Tüm Grup |
| Fiber Dolgu Tipi | Eş Merkezli Fiber |
| Eş Merkezli Fiber Sayısı | 1 (T1 için) 2 (T2 için) |
| Destek Kullanımı | Hayır |
| Brim Kullanımı | Evet |

Eiger yazılımıyla öngörülen, Çizelge 2’de yer alan baskı çıktıları kontrol edildikten sonra, her bir numune grubu için 5 adet üretim gerçekleştirilmiştir. Çizelge 2’de, v_m her bir numune içeriğindeki Nylon White hacmini verirken, v_f karbon/naylon hacmini vermektedir. Sürekli fiber destekli bölgenin hacim oranı olarak tanımlanabilecek V_r ; v_f ’nin (v_m+v_f) ’ye oranı olarak bulunur. V_r ifadesinin, literatürde geleneksel metotlarla üretilen kompozit malzemeler için kullanılan fiber hacim oranı (V_f) ifadesiyle karıştırılmaması gerekir. Çünkü, V_r ifadesine karbon filamentinde bulunan naylon hacmi de dahil edilmektedir. Her bir numune grubunun bir numunesine ait, brim için kullanılan Nylon White miktarı hariç, kütle (m) değerleri de çizelgede ayrıca belirtilmiştir.

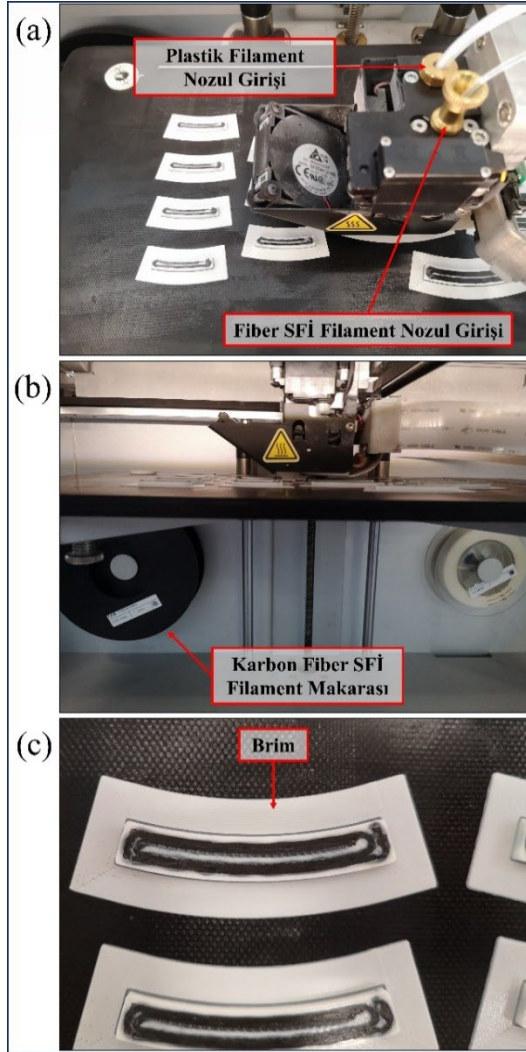
Çizelge 2. Numune gruplarına ait baskı çıktıları.

| Numune Grubu | v_m [cm ³] | v_f [cm ³] | V_r [%] | m [g] |
|--------------|--------------------------|--------------------------|-----------|---------|
| D-T1 | 1.89 | 0.32 | 14.5 | 1.07 |
| K-T1 | 1.90 | 0.33 | 14.8 | 1.10 |
| K-T2 | 3.53 | 1.59 | 31.1 | 3.89 |

‘K-T1’ numune grubu, düz numune grubuyla aynı h ve b değerlerine sahip olmakla birlikte, L değeri, kavisli numune için minimum veter uzunluğu olmasından dolayı V_r ve m değerleri az bir miktar daha büyüktür. ‘K-T2’ numune grubunun, ‘T1’ kalınlığındaki kavisli numune grubuna göre, h yanında b ve L değerleri de %50 oranında artmıştır. Bu artışlar, V_r ve m değerinde, sırasıyla 2.1 ve 3.5 kata varan belirgin artışları da beraberinde getirdi.

Şekil 2’de, yapılan 3B baskı üretimleri farklı açıdan çekilen fotoğraflarla belgelenmiştir. Şekil 2(a)’da kavisli numunelerin imalatlarına dair genel görünümle birlikte, plastik filament ve fiber SFİ filament nozul girişleri

gösterilmiştir. Şekil 2(b)'de imalat anına ait yandan görünümle birlikte, karbon fiber SFİ filament makarası görülmektedir. Şekil 2(c)'de, 'T2' h değerine sahip bir kavisli numunenin karbon fiber demetlerinin numune içine gömülümü ve yayılımı gösterilmiştir. 3B yazıcı, baskı sırasında herhangi bir baskı katmanını oluştururken her iki nozul eş zamanlı olarak çalışmaz. Öncelikle fiber SFİ filament nozulu aktive olur ve sürekli fiber takviyeli bölgeler oluşturulur. Devamında da plastik filament nozulu aktive olur ve o baskı katmanına polimer kısımları ekler ve son şeklini verir. Şekil 2(c), karbon fiberlerin yerleştirilmesinden sonrasında ve fiberler etrafına ve ortasına Nylon White eklenmesinden öncesini gösterir ki, plastik ilavesinin daha sonra eklenmesiyle, Şekil 3'te gösterildiği gibi, karbon fiber demetlerinin dağılımını daha düzgün bir forma dönüştürür.



Şekil 2. 3D baskıyla üretim anına ait (a) genel görünüm, (b) yandan görünüm ve karbon fiber SFİ filament makarası ve (c) karbon fiber demetlerinin eklenmesi ve yayılımı.



Şekil 3. T1 kalınlık değerine sahip bir numunenin karbon fiber takviyeli nylon ve Nylon White malzemelerinin nihai yerleşiminin görünümü.

On-edge imalata dayalı olarak, baskı yatağıyla geniş bir temas yüzeyi olmadığından, baskı sırasında oluşabilecek eğilme sorununu çözen bir çeşit kenarlık kullanılır. Baskı yatağındaki numunelerin tabanlarını çevreleyen brim adı verilen bu yapılar Şekil 2(a) ve Şekil 2(c)'de belirgin şekilde gözükmemektedir. İlk dört baskı katmanında numuneyle birlikte basılan brim yapılar, üretimin ardından herhangi bir alet kullanmadan el yordamıyla kolaylıkla numuneden ayrılabilir yapıdadır.

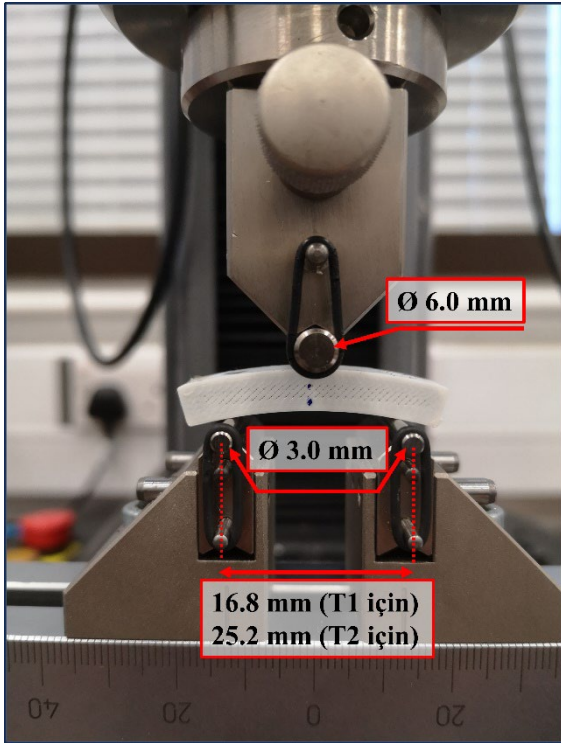
Üretimleri tamamlanan her bir numune grubuna ait kısa-kiriş numunelerinin genişlik ve kalınlık değerleri kumpas kullanılarak ölçüldü. Çizelge 3'te bu değerler listelenmiştir.

Çizelge 3. Kısa kiriş numunelerine ait ölçülen genişlik ve kalınlık değerleri.

| Numune Kodu | b [mm] | h [mm] |
|-------------|----------|----------|
| D-T1-1 | 8.35 | 4.35 |
| D-T1-2 | 8.35 | 4.26 |
| D-T1-3 | 8.35 | 4.32 |
| D-T1-4 | 8.30 | 4.32 |
| D-T1-5 | 8.34 | 4.27 |
| K-T1-1 | 8.26 | 4.31 |
| K-T1-2 | 8.26 | 4.31 |
| K-T1-3 | 8.35 | 4.31 |
| K-T1-4 | 8.29 | 4.25 |
| K-T1-5 | 8.32 | 4.31 |
| K-T2-1 | 12.54 | 6.45 |
| K-T2-2 | 12.63 | 6.42 |
| K-T2-3 | 12.50 | 6.47 |
| K-T2-4 | 12.57 | 6.40 |
| K-T2-5 | 12.62 | 6.42 |

Ölçümlerin tamamlanmasının ardından, ASTM D2344/2344M-22 standardı [5] rehberliğinde, Şekil 4'te gösterildiği gibi üç-nokta eğilme testi yapıldı. Lloyd LS5 test cihazı [18] ve alt ve üst şeklinde iki parçalı üç-nokta eğilme aparatı kullanıldı. Test için 62 HRC sertlikte çelikten imal edilen, sırasıyla 6.0 mm çapında ve 3.0 mm çapında, yükleme ve destek silindirleri kullanıldı. İki destek silindiri arasındaki açıklık değeri, numunenin kalınlığına bağlıdır ve $4.0 \times h$ değerine sahip olmalıdır. Testler, yükleme silindiri 1.0 mm/dakika hızla kirişlerin tam

ortasından basma kuvveti uygulayacak şekilde yapıldı.



Şekil 4. Test düzeneği ve kavisli bir numunenin düzenek üzerinde yerleşimi.

Her bir test boyunca 10 Hz örnekleme hızıyla kuvvet (P) ve deplasman verileri toplandı. Testin herhangi bir anındaki kısa-kiriş gerilmesi (F):

$$F = 0.75 P/bh \quad (1)$$

formülüyle elde edilir. Test sırasında, hasardan önce elde edilen maksimum kuvvet, P_m ile simgelenirse, KKM (F^{sbs}) aşağıdaki gibi hesaplanır:

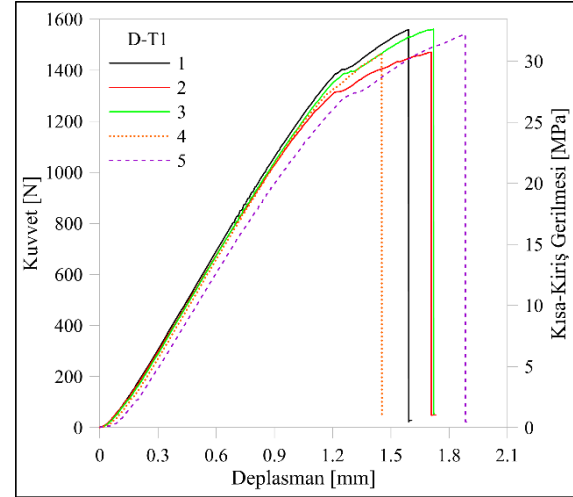
$$F^{sbs} = 0.75 P_m/bh \quad (2)$$

Test sonucunda elde edilen F^{sbs} , katmanlar arası kayma, çekme ve basma etkisinde eğilme hasarı ve elastik olmayan deformasyon hasarları için geçerlidir. Bununla birlikte, elde edilen F^{sbs} , ancak katmanlar arası bir kayma hasarı mevcutsa KAKM olarak da tanımlanır.

3. DENEYSEL BULGULAR

Kavisli kısa-kiriş performansından önce, karşılaştırma yapmak açısından düz kısa-kiriş performansını referans değer olarak elde etmek önemlidir. 'D-T1' numune grubuna ait kuvvet-deplasman ve gerilme-deplasman grafikleri

Şekil 5'te gösterilmiştir. Tüm numuneler, P_m değerlerine ulaştıktan sonra keskin bir şekilde kuvvette sıfıra doğru kayıp yaşayarak katastrofik hasara uğradı. Ortalama 1.2 mm deplasman değerine kadar lineere yakın bir yönelim izleyen eğriler, devamında hasara kadar lineer olmayan bir ilerleme gösterip hasara uğramıştır. Hasar anına kadar ulaştığı maksimum deplasman değerleri, F^{sbs} değerlerine göre daha geniş bir saçılım göstermiştir.



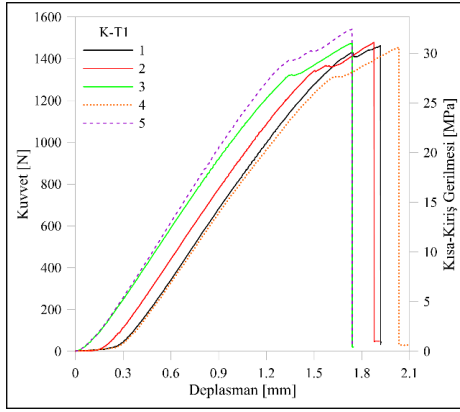
Şekil 5. Düz ve T1 kalınlığına sahip numunelerin Kuvvet-Deplasman ve Kısa-Kiriş Gerilmesi-Deplasman eğrileri.

Çizelge 4'te 'D-T1' numune grubunun her bir numunesine ait P_m ve F^{sbs} değerleri gösterilmiş ve numune grubuna ait elde edilen ortalama değerlerle standart sapmaları vurgulanmıştır. Numune grupları arasında daha efektif bir karşılaştırma için, özgül mukavemet (F^{sbs}/ρ) de her bir numune için hesaplanarak ortalama değeriyle birlikte çizelgeye dahil edilmiştir. ρ , yoğunluk değeridir ve Çizelge 2'de yer alan m ve baskı için toplam harcanan malzeme hacmi (v_m+v_f) kullanılarak hesaplanmıştır.

Çizelge 4. Düz ve T1 kalınlığına sahip numunelerin P_m , F^{sbs} ve F^{sbs}/ρ değerleriyle birlikte ortalama sonuçları ve standart sapmaları.

| Numune Kodu | P_m [N] | F^{sbs} [MPa] | F^{sbs}/ρ [kN.m/kg] |
|----------------|--------------|--------------------|-----------------------------|
| D-T1-1 | 1559 | 32.2 | 66.5 |
| D-T1-2 | 1472 | 31.0 | 64.1 |
| D-T1-3 | 1562 | 32.5 | 67.1 |
| D-T1-4 | 1463 | 30.6 | 63.2 |
| D-T1-5 | 1541 | 32.5 | 67.0 |
| Ortalama | 1519 | 31.8 | 65.6 |
| Standart Sapma | 43 | 0.8 | 1.6 |

'K-T1' numune grubuna ait kuvvet-deplasman ve gerilme-deplasman grafikleri Şekil 6'da gösterilmiştir. Genel eğilim olarak, ulaşılan F^{sbs} az bir miktar daha düşük gözükürken, aynı zamanda hasardan önceki maksimum deplasman değerleri, düz kısa-kiriş numunelerine göre belirgin şekilde daha yüksektir. Bu durum, kavisli numunelerin aynı kalınlıktaki düz numunelere göre daha fazla enerji depolayabildiğinin bir ölçütü sayılabilir. Şekil 5 ve Şekil 6'daki her numune eğrisinin altındaki alan hesaplanarak, 'D-T1' ve 'K-T1' için elde edilen enerji değerlerinin ortalamaları sırasıyla 1.47 mJ ve 1.52 mJ elde edilmiştir. Kavisli kırıta yaklaşık %3 enerji depolama artışı olmuştur. Hasardan hemen önceki bölümdeki eğrilerin eğilimi, düz numunelerle benzerlik göstermektedir.



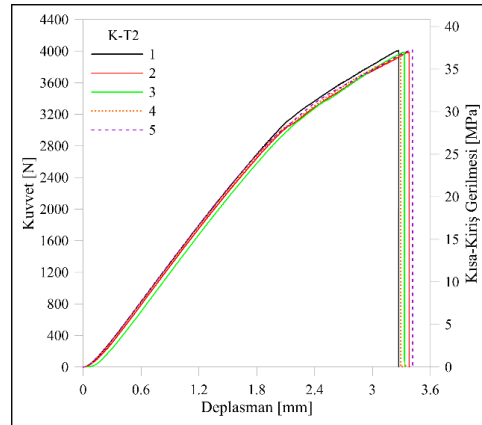
Şekil 6. Kavisli ve T1 kalınlığına sahip numunelerin Kuvvet-Deplasman ve Kısa-Kiriş Gerilmesi-Deplasman eğrileri.

Maksimum değerler ve bu değerlerin ortalamaları açısından daha belirgin karşılaştırmak yapmak için, 'K-T1' numune grubu için de Çizelge 5 hazırlanmıştır. Kavisli numunelerde, düz numunelere göre, F^{sbs} ve özgül F^{sbs} değerlerinde, sırasıyla %2 ve %4 düşüş gerçekleşmiştir. 'K-T1' grubu standart sapması, düz numunelerinkine göre daha iyi bir değerdir.

Çizelge 5. Kavisli ve T1 kalınlığına sahip numunelerin P_m , F^{sbs} ve F^{sbs}/ρ değerleriyle birlikte ortalama sonuçları ve standart sapmaları.

| Numune Kodu | P_m [N] | F^{sbs} [MPa] | F^{sbs}/ρ [kN.m/kg] |
|----------------|--------------|--------------------|-----------------------------|
| K-T1-1 | 1463 | 30.8 | 62.5 |
| K-T1-2 | 1478 | 31.1 | 63.1 |
| K-T1-3 | 1475 | 30.7 | 62.3 |
| K-T1-4 | 1456 | 31.0 | 62.8 |
| K-T1-5 | 1541 | 32.2 | 65.4 |
| Ortalama | 1483 | 31.2 | 63.2 |
| Standart Sapma | 30 | 0.5 | 1.1 |

'K-T2' numune grubuna ait kuvvet-deplasman ve kısa-kiriş gerilmesi-deplasman grafikleri Şekil 7'de gösterilmiştir. P_m , F^{sbs} ve deplasman verilerinde belirgin artış gözlemlenmiş ve malzemenin enerji depolama kapasitesi artmıştır. Hasar anına kadar ulaşılan maksimum deplasman değerleri ve F^{sbs} değerleri, diğer iki numune grubuna göre dar bir saçılım göstermiştir. Bu durum, Eİ ile üretilmiş polimer kompozit malzemeler için kalınlık ve V_r artışıyla birlikte daha tahmin edilebilir bir kısa-kiriş performansı sunmuştur. Hasardan hemen önceki bölümdeki eğrilerin eğilimi de daha düzgün ve bu performans analizini destekler durumdadır. Diğer numune gruplarında olduğu gibi, 'K-T2' için de hasarın keskin bir kuvvet düşüşüyle gerçekleştiği görülmüştür.



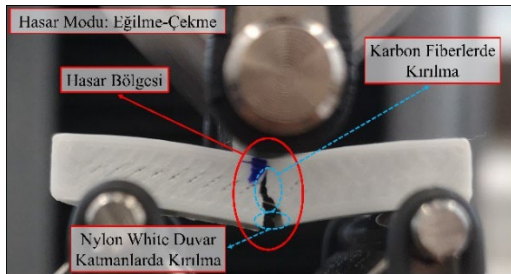
Şekil 7. Kavisli ve T2 kalınlığına sahip numunelerin Kuvvet-Deplasman ve Kısa-Kiriş Gerilmesi-Deplasman eğrileri.

Çizelge 6'da 'K-T2' numune grubuna ait limit değerler incelendiğinde, V_r miktarındaki artış, 'K-T1' numune grubuna göre mukavemet değerini %19 arttırmış gözükse de özgül mukavemet değerinde %23 düşüş meydana getirmiştir. Standart sapma değerleri de Şekil 7'deki eğrilerin eğilimini destekler şekilde, tüm gruplar içinde en düşük değerlere sahiptir.

Çizelge 6. Kavisli ve T2 kalınlığına sahip numunelerin P_m , F^{bs} ve F^{bs}/ρ değerleriyle birlikte ortalama sonuçları ve standart sapmaları.

| Numune Kodu | P_m [N] | F^{bs} [MPa] | F^{bs}/ρ [kN.m/kg] |
|----------------|--------------|-------------------|----------------------------|
| K-T2-1 | 4008 | 37.2 | 48.9 |
| K-T2-2 | 3989 | 36.9 | 48.6 |
| K-T2-3 | 3990 | 37.0 | 48.7 |
| K-T2-4 | 3931 | 36.7 | 48.2 |
| K-T2-5 | 4016 | 37.2 | 48.9 |
| Ortalama | 3987 | 37.0 | 48.7 |
| Standart Sapma | 30 | 0.2 | 0.3 |

Şekil 8’de testler sırasında karşılaşılan tek hasar modu, ‘K-T1-1’ numunesi özelinde gösterilmiştir. Düz ve ‘T2’ kalınlıklı kavisli numunelerde de şekildeki gibi çekme gerilmesinin baskın olduğu eğilme hasarı gözlemlenmiştir. Öncelikle, Nylon White duvar (h boyunca) ve çatı/tabana katmanları (b boyunca) tarafından çevrilen ve gerilmeyi domine eden numune iç kısmındaki karbon fiber demetleriyle takviyeli naylon katmanların çekme mukavemetinin aşılmasından kaynaklı fiber kırılmaları meydana gelmiştir. Bu durumun devamında, zaten gerilme yüklü durumdaki ve yeterince plastik uzama gerçekleştirilmiş esnek fakat zayıf mukavemete sahip alt Nylon White duvar ve çatı/tabana bölgelerinde de kırılmalar meydana gelerek şekildeki hasar görüntüsü oluşmuştur. Numunelerin kesmeye uygun olmayacak şekilde çok küçük olması yanında, Nylon White çatı/tabana katmanların daha kritik numune iç kesit yüzeyini örtmesi nedeniyle ileri seviye görüntüleme teknikleri kullanılarak olası bir katmanlar arası kayma delaminasyon hasarı gözlemi yapılmamıştır ve bu hasar olasılığı ihmal edilmiştir.



Şekil 8. Hasar modu.

4. SONUÇLAR

Bu çalışmada, EBM tekniğinin ileri bir süreci olarak tanımlanabilecek SFİ kullanılarak üretilen düz ve kavisli tek yönlü karbon fiber takviyeli kompozit kısa kirişlerin dayanım performansı deneysel olarak incelendi. 70 mm

eğrilik yarıçapına sahip kavisli kompozit kısa-kiriş, eşdeğer özelliklere sahip düz bir kirişe çok yakın KKM değerine ulaşabilmiştir. Az bir miktar düşüşle mukavemetini koruyarak, hasardan önce bir miktar daha fazla enerji depolayabilecek şekilde deplasmana sahip olmuştur. Kavisli numunenin kalınlığı %50 oranında ve içerdiği karbon fiber miktarı iki katına çıkarılırken eğrilik yarıçapı sabit tutulduğunda, boyutsal değerlerindeki artışa bağlı olarak mukavemet değerinde belirgin artışa ulaşılmıştır. Bununla birlikte, daha sağlıklı bir karşılaştırma amacıyla elde edilen özgül mukavemet değerleri incelendiğinde, karbon fiber oranının iki katına çıkarılması ancak ve ancak kalınlık değerinde artışla gerçekleştirilebildiği için, özgül mukavemet değerinde belirgin düşüş gözlemlenmiştir. Kavisli tek yönlü numunelerin flat olarak baskı yatağı üzerinde üretilebilme imkanı, bu ters orantılı durumu aksi yöne değiştirebilir.

Bu çalışmada, farklı numune geometrileri arasında mekanik performansın sağlam bir karşılaştırması sunulacak çeşitli mühendislik alanlarında SFİ ile üretilmiş kompozitlerin tasarımı ve uygulanması için değerli bilgiler sağlanmıştır. El yöntemiyle üretilmiş sürekli fiber takviyeli polimer matrisli kompozitler üzerine büyüyen bilgi birikimine katkıda bulunuldu. Özellikle, havacılık ve otomotiv alanındaki endüstriyel uygulamalarda karşılaşılan yapısal sınırlamalar nedeniyle, yeterince uzun olmayan kavisli kompozit kiriş yapıların eklemeli imalat yöntemiyle de üretilebilirliği ve eksik olan yönler hakkında farkındalık yaratılmıştır.

Ultrason tekniğiyle görüntüleme yönteminin, 3B baskıyla üretilmiş ve özellikle delaminasyon hasarı gözlemi için yararlı olabilecek bir teknik olduğu önerilmektedir. Gelecek çalışmalarda, kısa-kiriş performansının farklı eğrilik yarıçaplarına sahip kavisli yapılar üzerinde de incelenebileceği ve ultrason tekniğiyle hasar analizinin çalışmalara dahil edilebileceği tavsiye edilmektedir. Ayrıca, tek yönlü kavisli yapıları flat olarak baskı yatağında da üretebilecek ve farklı malzemelerle aynı takviyeye izin verebilecek şekilde hibrit kompozit yapıların çeşitli yüklemeler altında davranışlarının incelenmesini sağlayacak 3D baskı ekstrüderleri ve cihazlarının tasarımı üzerine yoğunlaşılması da tasarımcılar için önerilerdir.

TEŞEKKÜR

Bu çalışmanın gerçekleşmesi sürecindeki katkılarından ötürü Queen's University Belfast öğretim üyelerinden Doç. Dr. Zafer Kazancı'ya teşekkür ederim.

KAYNAKLAR

1. Karagöz, İ., Danış Bekdemir, A. ve Tuna, Ö., "3B yazıcı teknolojilerindeki kullanılan yöntemler ve gelişmeler üzerine bir derleme", Düzce Üniversitesi Bilim ve Teknoloji Dergisi, Cilt 9, Sayı 4, Sayfa 1186-1213, 2021.
2. Altun, S. ve Sekban, B., "3B yazıcılar için cam fiber katkılı kompozit filament üretimi ve mekanik özellikleri", Int. J. of 3D Printing Tech. Dig. Ind., Cilt 7, Sayı 1, Sayfa 64-67, 2023.
3. Süsler, S. and Kazancı, Z., "Delamination strength comparison of additively manufactured composite curved beams using continuous fibers", Polymers, Vol. 15, Issue 19, Pages 3928, 2023.
4. Brunken, B., Barocio, E., Favaloro, A. and Kunc, V., "Fused filament fabrication of fiber-reinforced polymers: A review.", Addit. Manuf., Vol. 21, Pages 1-16, 2018.
5. ASTM International, "ASTM D2344/D2344M-22 Standard Test Method for Short-Beam Strength of Polymer Matrix Composite Materials and Their Laminates", https://doi.org/10.1520/D2344_D2344M-22, April 2, 2024.
6. Fijul Kabir, S.M., Mathur, K. and Seyam, A.F.M., "A critical review on 3D printed continuous fiber-reinforced composites: History, mechanism, materials and properties", Compos. Struct., Vol. 232, Pages 111476, 2020.
7. Handwerker, M., Wellnitz, J. and Marzbani, H., "Review of mechanical properties of and optimisation methods for continuous fibre-reinforced thermoplastic parts manufactured by fused deposition modelling", Prog. Addit. Manuf., Vol. 6, Pages 663-677, 2021.
8. Jamal, M.A., Shah, O.R., Ghafour, U., Qureshi, Y. and Bhutta, M.R., "Additive manufacturing of continuous fiber-reinforced polymer composites via fused deposition modelling: A comprehensive review", Polymers, Vol. 16, Pages 1622, 2024.
9. Yang, C., Tian, X., Liu, T., Cao, Y. and Li, D., "3D printing for continuous fiber reinforced thermoplastic composites: Mechanism and performance", Rapid Prototyp. J., Vol. 23, Pages 209-215, 2017.
10. Caminero, M.A., Chacón, J.M., García-Moreno, I. and Reverte, J.M., "Interlaminar bonding performance of 3D printed continuous fibre reinforced thermoplastic composites using fused deposition modelling", Polym. Test., Vol. 68, Pages 415-423, 2018.
11. Iragi, M., Pascual-González, C., Esnaola, A., Lopes, C.S., and Aretxabaleta, L., "Ply and interlaminar behaviours of 3D printed continuous carbon fibre-reinforced thermoplastic laminates; effects of processing conditions and microstructure", Addit. Manuf., Vol. 30, Pages 100884, 2019.
12. Yavas, D., Zhang, Z., Liu, Q. and Wu, D., "Interlaminar shear behavior of continuous and short carbon fiber reinforced polymer composites fabricated by additive manufacturing", Compos. Part B Eng., Vol. 204, Pages 108460, 2021.
13. Santos, J.D., Fernández, A., Ripoll, L. and Blanco, N., "Experimental characterization and analysis of the in-plane elastic properties and interlaminar fracture toughness of a 3D-printed continuous carbon fiber-reinforced composite", Polymers, Vol. 14, Pages 506, 2022.
14. Markforged®, "Mark Two 3D Printer", <https://markforged.com/3d-printers/mark-two>, September 1, 2023.
15. Markforged®, Carbon Fiber, <https://markforged.com/materials/continuous-fibers/continuous-carbon-fiber>, September 25, 2024.
16. Markforged®, "Eiger Software", <https://www.eiger.io/>, September 1, 2023.
17. Markforged®, Design Guide for 3D Printing with Composites, <https://static.markforged.com/downloads/CompositesDesignGuide.pdf>, September 1, 2023.
18. Lloyd Instruments, Lloyd LS5 Testing Machine, <https://www.ametektest.com/products/material-testers/single-column-test-stands/l5-series>, September 15, 2023.



ULUSLARARASI 3B YAZICI TEKNOLOJİLERİ
VE DİJİTAL ENDÜSTRİ DERGİSİ

INTERNATIONAL JOURNAL OF 3D PRINTING
TECHNOLOGIES AND DIGITAL INDUSTRY

ISSN:2602-3350 (Online)

URL: <https://dergipark.org.tr/ij3dptdi>

EXAMINING THE RELATIONSHIP BETWEEN SUSTAINABLE MATERIAL AND BUILDING DESIGN IN BUILDING CONSTRUCTION WITH ADDITIVE MANUFACTURING

Yazarlar (Authors): Kübra SÜMER HAYDARASLAN 

Bu makaleye şu şekilde atıfta bulunabilirsiniz (To cite to this article): Haydaraslan K. S., “Examining the Relationship Between Sustainable Material and Building Design in Building Construction with Additive Manufacturing” *Int. J. of 3D Printing Tech. Dig. Ind.*, 8(3): 361-369, (2024).

DOI: 10.46519/ij3dptdi.1537779

Araştırma Makale/ Research Article

Erişim Linki: (To link to this article): <https://dergipark.org.tr/en/pub/ij3dptdi/archive>

EXAMINING THE RELATIONSHIP BETWEEN SUSTAINABLE MATERIAL AND BUILDING DESIGN IN BUILDING CONSTRUCTION WITH ADDITIVE MANUFACTURING

Kübra SÜMER HAYDARASLAN^a 

^aSuleyman Demirel University, Faculty of Architecture, Department of Architecture, Turkiye

* Corresponding Author: kubrahaydaraslan@sdu.edu.tr

(Received: 23.08.2024; Revised: 15.11.2024; Accepted: 12.12.2024)

ABSTRACT

Building production with additive manufacturing techniques increase. This technique accelerated building construction works. Building production with additive manufacturing techniques increase. This technique accelerated building construction works. Building construction using additive manufacturing techniques draws attention because it requires less skilled labor, can be built in a shorter time, reduces costs, and contributes to sustainability. On the other, this technique enables the on-site production of buildings and the construction of complex building designs. This study aims to investigate the effect of using sustainable materials on building energy consumption in constructing complex-designed buildings. The effect of using geopolimer, a sustainable material, on building energy performance in square and free-form buildings was investigated. Additionally, the buildings in these forms were modelled with single-layer and double-layer walls, and the impact of layers on energy consumption was examined. On the other side, the effects of building forms in different directions were also examined. In the study, the effects of different scenarios were examined using the building energy simulation program. As a result of the study, it was determined that the building form was effective in the energy consumption of the building. It was also found that in the free-form building, the exterior wall orientation affected the building energy consumption. When the exterior walls of buildings of the same form and orientation were made double-layer instead of single-layer, a 60% decrease in heating energy consumption and a 12% decrease in cooling energy consumption was observed. The study is important in terms of the relationship between free building form and energy consumption.

Keywords: Geopolymer, Additive Manufacturing, Building Energy Consumption, 3D Printed Building, Industry 4.0

1. INTRODUCTION

The world population is estimated to reach 8.5 billion in 2030 and 9.7 billion in 2050 [1]. Urbanization accelerates due to population growth. Housing demand is expected to increase by 60% with increasing urbanization. It is estimated that there will be a 75% increase in CO₂ emissions with the increase in urban areas [2]. One of the most important causes of climate change is CO₂ emissions. Reducing this emission in the construction sector is important for reducing the effects of climate change [3].

The energy consumed for heating and cooling buildings and the energy consumed in industry constitute 40% of the total energy consumed [4-5]. In addition, 65% of this energy consumed is

provided by fossil resources. In Europe, 60% of the total energy is consumed by buildings in cities [6]. In addition, in the EU directive on improving the energy performance of buildings in 2018, it was stated that 50% of the energy consumed in EU countries was spent on heating and cooling buildings [7]. In Turkey, while the final energy consumption of buildings was 19.5 MTEP in 2000, this value increased by 66% in 2015 and reached 32.4 MTEP. The share of the building sector in final energy consumption reached 32.8%, surpassing the industrial sector. Therefore, it is important to reduce the energy consumption of existing and newly constructed buildings. Additionally, it is estimated in the studies that energy consumption will increase by 50% in 2050 compared to 2018 [8]. The

construction industry is looking for solutions to reduce energy consumption [9]. This situation shows the importance of new construction technologies.

Industrial revolutions have changed the production methods of all sectors, as well as the construction industry. The first radical changes in the construction industry began with the settled life. The other radical change was the use of cement and steel. The radical change expected today is building construction with digital production techniques. The world is experiencing a big transformation with Industry 4.0. It is predicted that with the widespread use of industrial robots containing automation and artificial intelligence in construction, production speed will increase, and less energy will be used. Research shows that the construction industry has serious potential and there will be radical changes in the construction industry within ten years [10-12]. In addition, it is estimated that with the development of digital production technologies, there will be developments in building materials, components, and design freedom [13-15].

Digital production is a technique in which computer-aided design and production technologies are used together. This technique is important in the construction industry in terms of its suitability for on-site production and allowing the construction of complex designs. In some research, it is suggested the use of additive manufacturing, a digital production technique, in building construction [16-17]. 3D printing based on extrusion is one of the most widely used techniques in additive manufacturing. The materials used in structures constructed with extrusion technique are different from the materials used in traditional construction techniques. The concrete-like material to be used in the extrusion technique must have sufficient extrusion capacity [18]. Therefore, the mortar created for printing must be fluid, have sufficient setting time and mechanical strength [19]. Research conducted in recent years suggests the use of geopolymer in 3D printing [19-20].

Geopolymer materials are formed by activating aluminosilicate materials such as fly ash, ceramic waste, metakaolin, and silica fume [21-24]. Geopolymer has high application potential due to its high chemical and thermal resistance,

ability to be obtained from industrial and waste products, contribution to the economy, and prevention of environmental pollution [20]. Research shows that approximately 820 million tons of construction waste is generated in Europe every year [25-26]. The use of geopolymer, developed from waste materials as an alternative to Portland cement used in construction, stands out with its contribution to the environment [27-28] (Figure 1).

Since the 1980s, geopolymer materials have been viewed as alternatives to Portland cement because of their low CO₂ emissions and performance advantages. Researchers have suggested the use of geopolymers in structures due to their properties such as high strength, temperature resistance and durability [29-30]. Geopolymer has potential for use due to its chemical and thermal resistance, rapid mechanical strength development, and economic and environmental benefits such as being a waste product [31]. These materials are resistant to acid attack, fire and high temperatures [32-34]. Since its discovery, geopolymer materials have also attracted attention as a promising material for building restoration. It is also used for concrete repair at airports, railways and military bases in Australia [34].

There are studies in the literature examining the use of geopolymers in building production. In a study, the static strength of fly ash-based geopolymer mortar after 3D printing was investigated. At the end of the study, it was concluded that the static strength of the geopolymer mortar was high. The study also stated that it is possible to use traditional construction methods and 3D printing techniques together [35]. In another study on mortars, the technical properties and application methods of mortars produced from cement, fly ash, silica fume, blast furnace slag, fine aggregate, superplasticizer, viscosity modifier, and fiber materials used in the extrusion technique were investigated. The effects of the properties such as tensile, stress, viscosity, etc. of these mortars with different properties on 3D printing were investigated. As a result of the study, they concluded that geopolymers were promising for extrusion mortar in 3D printing from technical, environmental, and economic perspectives [36].

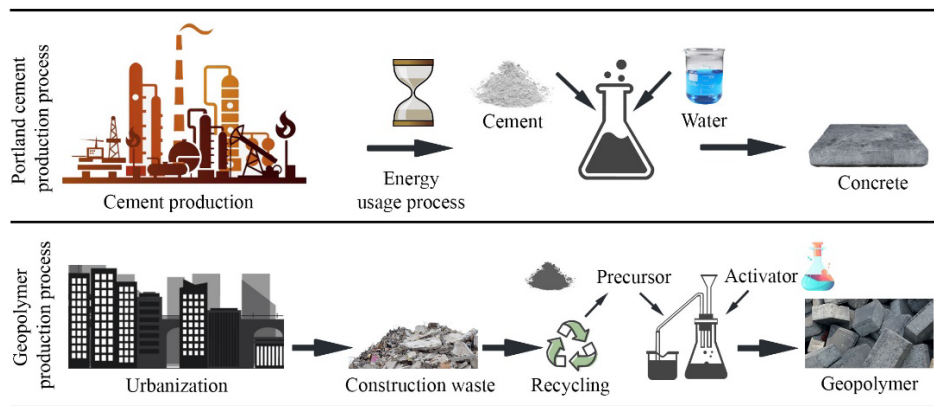


Figure 1. Portland cement and geopolymer production process

In another study, a slag-based geopolymer material was developed for use in the construction of buildings with 3D printing. The pressure strength of the geopolymer material developed in the study was increased. In the study, it was shown that the production of large structural elements was possible [37].

In 1997, the additive manufacturing technique was used for the first time in building construction [38]. Studies were conducted examining the potential use of this technique in buildings. In a study examining the contribution of the technique to environmental sustainability, it was stated that it would also contribute to the freedom of designs [11]. The additive manufacturing method allows building facades to be designed in free forms [39]. Building construction processes are long in traditional construction methods. This situation causes an increase in the need for housing. The potential of this technology, enables building production with additive manufacturing techniques, has accelerated studies on this subject. In this study, it was examined that the potential of using sustainable materials in the construction of buildings produced with additive manufacturing techniques. For the study, the square and free form building plans, thought to be printed with 3D printing, were created. The geopolymer material was used in the production of these buildings. In the study, the changes in energy consumption according to different building plans were examined.

2. MATERIAL AND METHODS

In this study, the relationship between the use of sustainable materials in building production and building design was examined. Four different scenarios were created: Two of the scenarios

were for a building have a square plan, with single and double-layer walls, and the other scenarios were for a building have a free-form plan, with single and double-layer walls. These scenarios were modelled through the building energy simulation program. Then, the effects of changes in the building surface and wall properties on the energy performance of the building were examined.

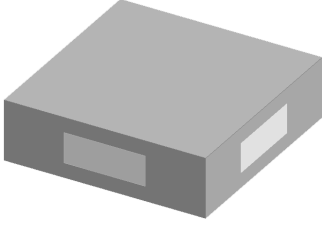
2.1. Reference Building

Two plans were created in the study to examine the relationship between the use of sustainable materials and building design. The first of these plans is square, the other is free form. The square planned building is the reference building. These buildings are open-plan, detached residences. It is assumed that the buildings were created using a 3D printer extrusion technique. Geopolymer, the most used material in 3D printing of buildings, was used in building production [27-40]. The reference building in the study is in Istanbul where is in the II. Degree day zone according to the TS 825 Standard for Thermal Insulation Rules in Buildings [41]. Building technical specifications were created by considering climatic conditions (Table 1).

2.2. Sustainable Mortar Properties Used in 3D Printing

In the study, geopolymer material was used in 3D printed buildings. Geopolymer materials are obtained by activating materials such as fly ash, ceramic waste, metakaolin, and silica fume [21-24]. A study was conducted with slag-based, fly ash-based, metakaolin-based, and lime alkali-activated slag-property geopolymer materials.

Table 1. Reference building properties

| | | | | |
|---|--------------------------------------|--|---------------------------|-------------------------|
|  | Meteorological data | Meteonorm İstanbul 2024 IPCC AR4 A1B Scenario | Occupancy | 4 persons |
| | Building Materials Properties | | Indoor temperature | 21 °C |
| | $U_{\text{external wall}}$ | 0.57 W/m ² K | U_{floor} | 0.57 W/m ² K |
| | $U_{\text{ceiling (Unused Attic)}}$ | 0.38 W/m ² K | U_{window} | 1.8 W/m ² K |
| | Infiltration | 0.8 (n/h) | | |

It was concluded that fly ash-based geopolymers are more advantageous in terms of carbon emission and cost compared to geopolymers with other properties [27-40]. Therefore, fly ash-based geopolymer was used in this study (Table 2).

Table 2. Geopolymer technical properties

| Properties | k (W/m K) | C_p (J/Kg K) | ρ (Kg/m ³) |
|----------------------|-----------|----------------|-----------------------------|
| Geopolymer (fly-ash) | 1,35 | 891 | 2199 |

2.3. Numerical Simulation

There are passive and active measures that can be taken during the building design phase to increase the energy efficiency of buildings. Passive measures aim to reduce the building's energy needs through maximum use of renewable energy sources. Active measures are related to the mechanical systems of buildings [9]. Design support systems have been developed to examine the effects of these measures on the energy efficiency of the building [42]. One of these systems is the creation of building energy simulations. Some programs have been developed to create building energy simulations. The most widely used program in recent years and the one that produces the most realistic results is the DesignBuilder building energy simulation program [43-45]. This program can analyse issues such as the building's energy efficiency, CO₂ emissions, and comfort conditions [46]. In the study, passive measures were examined using the DesignBuilder building energy simulation program. Building forms, orientations, and wall layer scenarios were created for the study. The base areas and volumes of the scenarios created in the study are the same. The scenario plans were given in Figure 2.

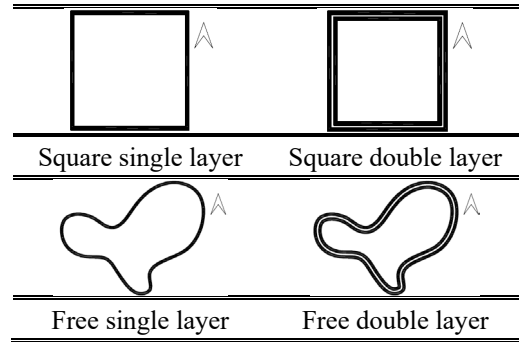


Figure 2. The scenario plans

3. RESULTS and DISCUSSION

3.1. Effect of Building Plan Design

For the study, square and free form building plans were created to examine the effect of building form on energy consumption. The effect of building form on heating and cooling energy consumption was investigated. Annual energy consumed for heating and cooling was calculated. The study also examined the relationship between form and direction. The obtained results are given in Figure 3.

In the free-form structures, wall surface areas vary depending on the direction. This situation affected the energy consumption of buildings at different rates. When the square plan building was accepted as the reference building, the energy consumed for heating purposes increased by 5.29%, 5.42%, 6.18%, 6.22%, 5.72%, 5.30%, 5.25% and 5.07% at FF 0°, FF 45°, FF 90°, FF 135°, FF 180°, FF 225°, FF 270°, FF 315° values, respectively. The square form was more compact than other forms. Therefore, the energy required to heat this form was less than other forms. When the surface area of the building in relation to the outside environment increased, the amount of energy required for heating increased. According to the different direction analysis results, the lowest heating energy consumption was in the square-shaped building, while the highest energy consumption was in FF 135°. This was related

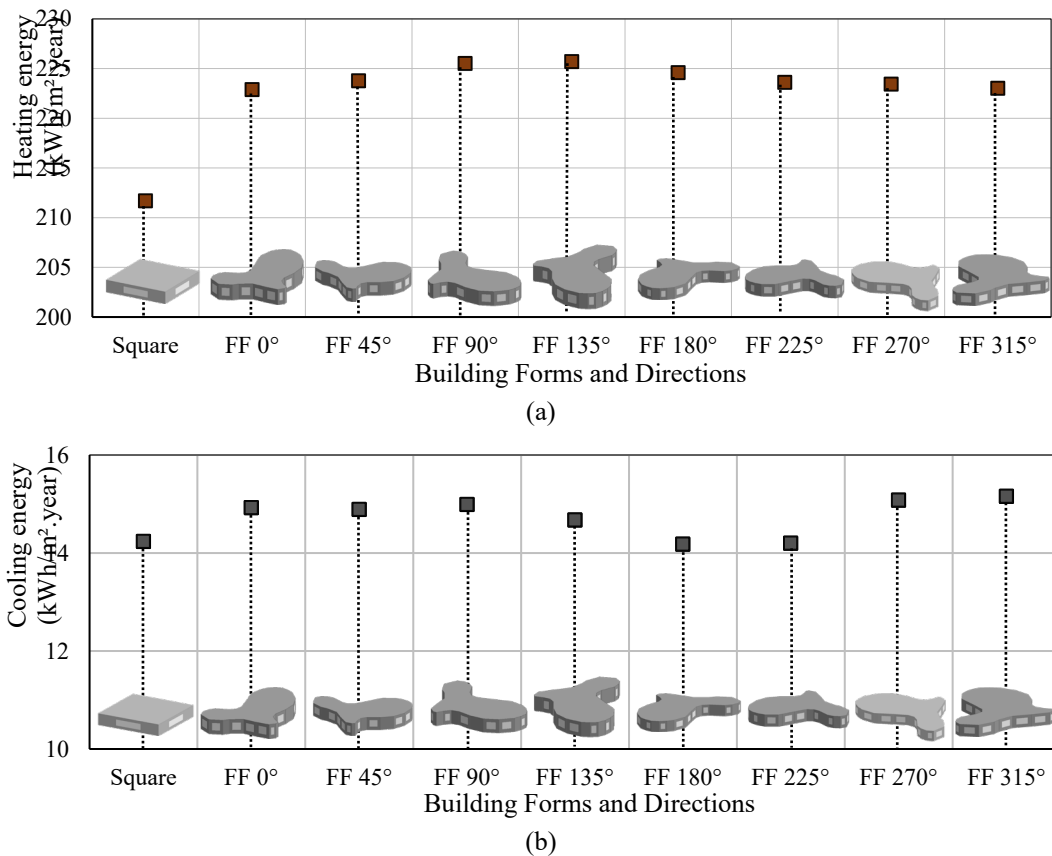


Figure 3 (a). Effect of building form on energy consumption for heating **(b).** Effect of building form on energy consumption for cooling

to the fact that the largest surface of the free form building in this direction was in the north. Increasing the surface width in the direction where the least sunlight comes increased the heating load. The results obtained showed that the heating energy requirement varied according to the building form. Studies on building form in the literature confirm this situation. Rashdi and Embi [47] studied the changes in the electrical energy required for cooling buildings in hot climates when the building form is T, L, U, I, ellipse and round. At the end of the study, it was stated that I-shaped buildings consume less energy for cooling than L-shaped buildings. They emphasized that this situation is related to the expansion of the building surface area.

When the square-formed building was accepted as the reference building in the study, the energy consumed for free-form buildings in different directions varied. When the square form was accepted as the reference, there was an increase of 4.85%, 4.38%, 5.06%, 2.92%, 5.92%, 6.11% compared to FF 0°, FF 45°, FF 90°, FF 135°, FF 270°, FF 315°, respectively. Compared to the

reference, there was a decrease of 0.39% and 0.27% at FF 180° and FF 225°. It is expected that the amount of energy required for cooling will be less in buildings with compact structures. The cooling load was calculated to be less in the FF 180° direction, where the surface area received less sunlight. This shows that increasing the surface area of the building relative to the outside environment reduces the amount of energy required for cooling. In the literature, Kocagil and Oral [48] examined the effect of building form on the heating and cooling loads of buildings in hot-dry climate regions. Six different forms and four different architectural plans were used in the study. Among the studied forms, the lowest heating and cooling load was in the inner courtyard plan and the highest was in the L-type plan. This situation is related to surface areas.

However, the variability of the glass ratios on the surfaces also affects the cooling load. Neves and Marques [49] studied the effect of changing the wall-to-glass ratio on building energy consumption in Sao Paulo, which has a hot climate. In the study, the cooling load was

reduced by 40% by changing the window/wall ratio. According to the analysis of this studies results, the lowest cooling energy consumption was in FF 180°, while the highest energy consumption was in FF 315°. The results showed that building form and orientation have an impact on the amount of energy required to cool the building.

3.2. Effect of Building Exterior Wall Layer

In the study, the effect of using single or double layers in building walls on energy consumption was investigated. Annual heating and cooling energy consumption was calculated for different forms of buildings in case of single or double-layer wall use. Additionally, the situation where the buildings were in different directions was also examined (Figure 4 (a), (b)). The study showed that the energy consumed for heating was reduced if the walls were double layered in all models. This was related to the fact that the heat transfer through the double-layered wall was less than the single-layered wall [50]. In the case of double-layer walls, heating energy consumption decreased by 3.52%, 5.49%, 8.18%, 8.88%, 7.38%, 5.19%, 3.84%, 2.96% at FF 0°, FF 45°, FF 90°, FF 135°, FF 180°, FF 225°, FF 270° and FF 315°, respectively, compared to the reference building. In a compact square-plan building spent less energy for heating. In addition, the differentiation of the building form in different directions changed the distribution of the heating load according to the directions. The study showed that cooling energy consumption was reduced when the walls were double-layered instead of single-layered in all models. In the case of double-layer walls, cooling energy increased by 9.20%, 6.44%, 4.55%, 2.24%, 2.00%, 11.21%, 11.50% at FF 0°, FF 45°, FF 90°, FF 135°, FF 225°, FF 270°, FF 315° respectively, compared to the reference building. There was a 0.12% decrease at FF 180°. When the heating and cooling loads of single-layer and double-layer walls at the same directions were compared; the double-layer wall heating loads of FF 0°, FF 45°, FF 90°, FF 135°, FF 180°, FF 225°, FF 270° and FF 315 are 65.41%, 65.99%, 65.48%, 64.87%, 64.68%, 64.99%, 65.55%, 65.97%, 66.20% less than the single-layer heating load, respectively. When the cooling load was examined, a reduction of 11.39%, 7.71%, 9.83%, 12.02%, 12.11%, 11.14%, 9.38%, 6.96%, and 7.21% was

observed in the double-skinned wall, respectively. It was observed that the amount of energy spent on heating and cooling decreases at all angles in the double-layered wall.

4. CONCLUSIONS

In the construction industry, building construction times are insufficient for shelter. The reason for this is that the construction period of the structure is long with traditional construction methods. In addition, the construction sector accounts for 40% of total energy consumed. Additive manufacturing technologies have high potential for reducing energy consumption. Developments in building production technology with additive manufacturing have accelerated the work in this field. Building production with additive manufacturing is important in terms of fast and on-site production, reduced labor force, cost reduction potential and contribution to sustainability. Additionally, this technology enables designers to implement flexible designs. Flexible designs that overcome application difficulties can both increase the comfort conditions of users and provide aesthetic solutions. In this study, the relationship between the use of sustainable materials in building production and building design was examined. The results obtained in the study are summarized below.

- The results showed that the building form is effective on the heating energy consumption of buildings.
- Compact building forms provide advantages in reducing the energy needs for heating and cooling.
- In climates where heating energy is high, large surfaces of free building forms should be oriented south, and in cold climates, north.
- Positioning large surfaces is important to reduce energy consumption in free-form structures. Whether the building walls are single-layer or two-layer affects the energy consumption of the building.
- Heat transfer is reduced in the double-layered wall, which reduces the energy consumption of the building.

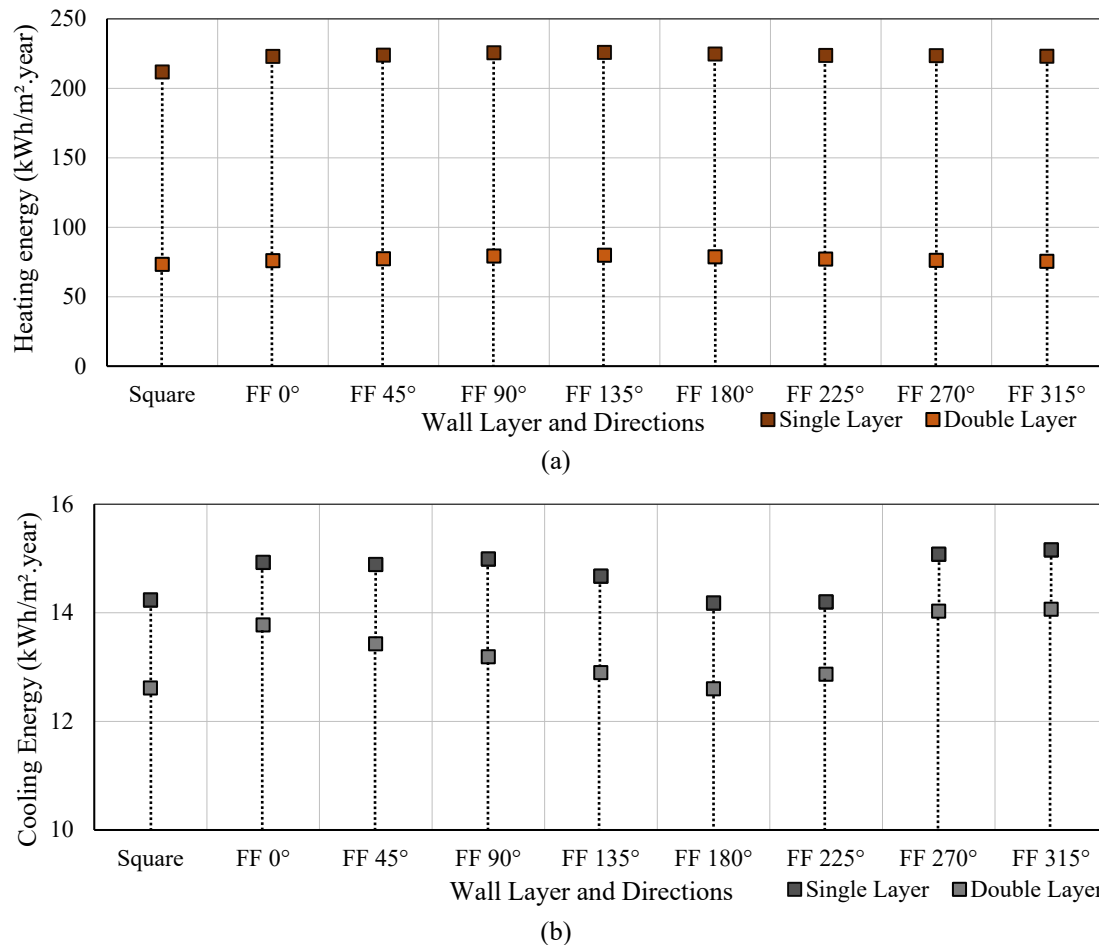


Figure 4 (a). Effect of building form and number of layers on energy consumption for heating **(b).** Effect of building form and number of layers on energy consumption for cooling

The study results are important in terms of the relationship between additive manufacturing technologies and sustainable material use. It also provides guidance on the importance of building orientation in the freeform design of buildings. However, since traditional construction methods have been used for many years, buildings can be constructed with readily available equipment and less cost. Digital fabrication techniques require high research and development. Although the application is easy in digital production, the initial investment cost is high. Therefore, there are still challenges in additive manufacturing techniques.

REFERENCES

1. United Nations Department of Economic and Social Affairs (UN DESA), "World Population Prospects 2022: Summary of Results", <https://population.un.org/wpp/Publications>, 5 May 2024.
2. Glavic, P., "Evolution and current challenges of sustainable consumption and production", *Sustainability*, Vol.13, Issue 16, Pages 9379, 2021.

3. Sümer-Haydaraslan, K., Yaşar, Y., "Evaluation of building design strategies according to the effects of climate change by simulation-based optimisation: a case study for housing in different climate regions", *International Journal of Global Warming*, Vol.30, Issue 1, Pages 33-59, 2023.

4. Zhan, J., Liu, W., Wu, F., Li, Z., Wang, C., "Life cycle energy consumption and greenhouse gas emissions of urban residential buildings in Guangzhou City", *Journal of Cleaner Production*, Vol.194, Pages 318-326, 2018.

5. International Energy Agency, "Global Energy & CO₂ Status Report", <https://www.iea.org/reports/global-energy-co2-status-report-2019>, 15 January 2024.

6. www.iea.org/ International Energy Agency, Energy Technology Perspectives. 20 Temmuz 2023.

7. EPBD 2018, Directive 2010/31/EU of the European Parliament and of Council of 30 May 2018 on the energy performance of buildings (recast), EU Commission, Official Journal of the European Union, 2018.

8. Energy Information Administration, "International Energy Outlook 2021", <https://www.eia.gov/todayinenergy/detail.php?id=49876>, 10 January 2024.
9. Sümer-Haydaraslan, K., Dikmen, N., "Investigation of the effects of curtain wall angle on energy consumption in buildings", *Journal of the Faculty of Engineering and Architecture of Gazi University*, Vol.39, Issue 1, Pages 315-326, 2024.
10. Linner, T., Pan, W., Hu, R., Zhao, C., Iturralde, K., Taghavi, M., Trummer, J., Schlandt, M., Bock, T., "A technology management system for the development of single-task construction robots", *Construction Innovation*, Vol.20, Pages 96-111, 2020.
11. Ghaffar, S.H., Corker, J., Fan, M., "Additive manufacturing technology and its implementation in construction as an eco-innovative solution", *Automation in Construction*, Vol.93, Pages 1-11, 2018.
12. Brischetto, S., Maggiore, P., Ferro, C.G., "Special Issue on Additive Manufacturing Technologies and Applications", *Technologies*, Vol.5, Issue 3, Page 58, 2017.
13. Dong S., Yu Y., "Numerical and experimental studies on capturing behaviors of the inflatable manipulator inspired by fluidic origami structures", *Engineering Structures*, Vol.245, 112840, 2021.
14. Zhu A., Pauwels P., De Vries B., "Smart component-oriented method of construction robot coordination for prefabricated housing", *Automation in Construction*, Vol.129, 103778, 2021.
15. Gebhard L., Mata-Falc'on J., Anton A., Dillenburger B., Kaufmann W., "Structural behaviour of 3D printed concrete beams with various reinforcement strategies", *Engineering Structures*, Vol.240, 112380, 2021.
16. Ma, G., Wang, L., Ju, Y., "State-of-the-art of 3D printing technology of cementitious material an emerging technique for construction", *Science China Technological Sciences*, Vol.61, Pages 475-495, 2018.
17. Weng, Y., Li, M., Ruan, S., Wong, T.N., Tan, M.J., Yeong, K.L.O., Qian, S., "Comparative economic, environmental and productivity assessment of a concrete bathroom unit fabricated through 3D printing and a precast approach", *Journal of Cleaner Production*, Vol.261, 121245, 2020.
18. Sümer-Haydaraslan K., "Examining the effect of digital manufacturing and traditional building construction techniques on the building production process", *Journal of Science and Technology*, Vol.3, Issue 3, Pages 1-13, 2024.
19. Robayo-Salazar, R., Mejía de Gutiérrez, R., Villaquirán-Caicedo, M. A., Arjona, S.D., "3D printing with cementitious materials: Challenges and opportunities for the construction sector", *Automation in Construction*, Vol.146, 104693, 2023.
20. Youssef, N., Rabenantoandro, A.Z., Lafhaj, Z., Dakhli, Z., Chehade, F.H., Ducoulombier, L., "A novel approach of geopolymer formulation based on clay for additive manufacturing", *Construction Robotics*, Vol.5, Pages 175-190, 2021.
21. Davidovits, J., "Properties of Geopolymer Cements", *International Conference on Alkaline Cements and Concretes*, Pages 120-128, Kiev, 1994.
22. Khale D., Chaudhary, R., "Mechanism of geopolymerization and factors influencing its development: a review", *Journal of Materials Science*, Vol.42, Pages 729-746, 2007.
21. Brooks, J.J., Megat Johari, M.A., Mazloom, M., "Effect of admixtures on the setting times of high-strength concrete", *Cement and Concrete Composites*, Vol.22, Issue 4, Pages 293-301, 2000.
24. Bouzoubaâ, N., Lachemi, M., "Self-compacting concrete incorporating high volumes of class F fly ash", *Cement and Concrete Research*, Vol.31, Issue 3, Pages 413-420, 2001.
25. Ciampa, D., Cioffi, R., Colangelo, F., Diomedi, M., Farina, I., Olita, S., "Use of unbound materials for sustainable road infrastructures" *Applied Sciences*, Vol.10, Issue 10, 3465, 2020.
26. Galvez-Martos, J.L., Styles, D., Schoenberger, H., Zeschmar-Lahl, B., "Construction and demolition waste best management practice in Europe", *Resources, Conservation and Recycling*, Vol. 136, Pages 166-178, 2018.
27. Poblocki, K., Pawlak, M., Drzewdzon, J., Gawdzik, B., Jacewicz, D., "Clean production of geopolymers as an opportunity for sustainable development of the construction industry", *Science of The Total Environment*, Vol.928, 172579, 2024.
28. Singh, N.B., Middendorf, B., Geopolymers as an alternative to Portland cement: an Overview, *Construction and Building Materials*, Vol.237, 117455, 2020.

29. Abdel-Ghani, N.T., Elsayed, H.A., Abdel Moied, S., Geopolymer synthesis by the alkali-activation of blastfurnace steel slag and its fire-resistance. *HBRC Journal*, Vol.14, Issue 2, Pages 159-164, 2019.
30. Lv, X., Wang, K., He, Y., Cui, X., A green drying powder inorganic coating based on geopolymer technology, *Construction and Building Materials*, Vol. 214, Pages 441-448, 2019.
31. Youssef, N., Rabenantoandro, A.Z., Lafhaj, Z., Dakhli, Z., Chehade, F. H., Ducoulombier, L., A novel approach of geopolymer formulation based on clay for additive manufacturing, *Construction Robotics*, Vol 5, Pages 175-190, 2021.
32. Pacheco-Torgal, F., Alkali-activated binders: a review. Part 2. About materials and binders manufacture. *Construction and Building Materials*, Vol. 22, Pages 1315-1322, 2008.
33. Liu, Y., Su, P., Li, M., You, Z., Zhao, M., Review on evolution and evaluation of asphalt pavement structures and materials, *Journal of Traffic and Transportation Engineering*, Vol. 7, Issue 5, Pages 573-599, 2020.
34. Shill, S.K., Al-Deen, S., Ashraf, M., Hutchison, W., Resistance of fly ash based geopolymer mortar to both chemicals and high thermal cycles simultaneously, *Construction and Building Materials*, Vol. 239, 117886, 2020.
35. Panda, B., Singh, G.B., Unluer, C., Tan, M.J., "Synthesis and characterization of onepart geopolymers for extrusion-based 3D concrete printing", *Journal of Cleaner Production*, Vol. 220, Pages 610-619, 2019.
36. Saruhan, V., Keskinates, M., Felekoğlu, B., "A comprehensive review on fresh state rheological properties of extrusion mortars designed for 3D printing applications", *Construction and Building Materials*, Vol. 337, 127629, 2022.
37. Xia, M., Sanjayan, J., "Method of formulating geopolymer for 3D printing for construction applications", *Materials & Design*, Vol. 110, Pages 382-390, 2016.
38. Pegna, J., "Exploratory investigation of solid freeform construction", *Automation in Construction*, Vol.5, Issue 5, Pages 427-437, 1997.
39. Mohsen, A., "Design to manufacture of complex building envelopes", Pages 42-100, Springer, Berlin, 2020.
40. Nguyen, L., Moseson, A.J., Farnam, Y., Spatari, S., "Effects of composition and transportation logistics on environmental, energy and cost metrics for the production of alternative cementitious binders", *Journal of Cleaner Production*, Vol.185, Pages 628-645, 2018.
41. Turkish Standardization Institute, 'TS825: thermal insulation requirements for buildings', TSE, 2018.
42. Al-Sallal, K.A., Solar access/shading and building form: Geometrical study of the traditional housing cluster in Sana'a, *Renewable Energy*, Vol.8, Issues 1-4, Pages 331-334, 1996.
43. Chan, A.L.S., "Developing future hourly weather files for studying the impact of climate change on building energy performance in Hong Kong", *Energy and Buildings*, Vol. 43, Issue 10, Pages 2860-2868, 2011.
44. Alam, M., Jamil, H., Sanjayan, J., Wilson, "Energy saving potential of phase change materials in major Australian cities", *Energy and Buildings*, Vol.78, Pages 192-201, 2014.
45. Kuznik, F., Virgone, J., "Experimental assessment of a phase change material for wall building use", *Applied Energy*, Vol.86, Issue 10, Pages 2038-2046, 2009.
46. DesignBuilder Software, "Tutorials", www.designbuilder.co.uk, June 3, 2024.
47. Rashdi, W., and Embi. M., Analysing Optimum Building Form in Relation to Lower Cooling Load, *Procedia-Social and Behavioral Sciences*, Vol.222 Pages 782-790, 2016.
48. Kocagil, I. E., and Oral, G. K., The Effect of Building Form and Settlement Texture on Energy Efficiency for Hot Dry Climate Zone in Turkey. *Energy Procedia*, Vol. 78, Issue 2315, Pages 1835-40, 2015.
49. de Oliveira Neves, L. and Marques, T. H. T., Building Envelope Energy Performance of High-rise Office buildings in Sao Paulo City, Brazil, *Procedia Environmental Sciences*, Vol. 38, Pages 821-29, 2017.
50. Haydaraslan, E., Çuhadaroğlu, B., "Analysis of the Effect of Hollow Geometry of Wall Blocks on Heat Transfer", *Düzce University Journal of Science and Technology*, Vol.10, Issue 4, Pages 2028-2038, 2022.



ULUSLARARASI 3B YAZICI TEKNOLOJİLERİ
VE DİJİTAL ENDÜSTRİ DERGİSİ

INTERNATIONAL JOURNAL OF 3D PRINTING
TECHNOLOGIES AND DIGITAL INDUSTRY

ISSN:2602-3350 (Online)

URL: <https://dergipark.org.tr/ij3dptdi>

COMPARATIVE STUDY OF MATERIAL EXTRUSION AND VAT PHOTOPOLYMERIZATION ADDITIVE MANUFACTURING TECHNIQUE USING SQUARE BASE PYRAMID AS AN ARTIFACT AND APPLICATIONS

Yazarlar (Authors): Bhanu Prakash Bisht^{ID}, Vijaykumar Toutam^{ID}, Sanjay R. Dhakate^{ID}

Bu makaleye şu şekilde atıfta bulunabilirsiniz (To cite to this article): Bisht B. P., Toutam V., Dhakate S. R., “Comparative Study of Material Extrusion and Vat Photopolymerization Additive Manufacturing Technique Using Square Base Pyramid as An Artifact and Applications” *Int. J. of 3D Printing Tech. Dig. Ind.*, 8(3): 370-386, (2024).

DOI: 10.46519/ij3dptdi.1540408

Araştırma Makale/ Research Article

Erişim Linki: (To link to this article): <https://dergipark.org.tr/en/pub/ij3dptdi/archive>

COMPARATIVE STUDY OF MATERIAL EXTRUSION AND VAT PHOTOPOLYMERIZATION ADDITIVE MANUFACTURING TECHNIQUE USING SQUARE BASE PYRAMID AS AN ARTIFACT AND APPLICATIONS

Bhanu Prakash Bisht ^{a, b} , Vijaykumar Toutam ^{a, b} , Sanjay R. Dhakate ^{a, b} 

^aAcademy of Scientific and Innovative Research (AcSIR), CSIR-National Physical Laboratory, Dr K. S. Krishnan Marg, New Delhi 110012, India.

^bAdvanced Materials and Device Metrology Division, CSIR-National Physical Laboratory, Dr. K. S. Krishnan Marg, New Delhi 110012, India.

* Corresponding Author: toutamvk@nplindia.org

(Received: 20.08.2024; Revised: 14.12.2024; Accepted: 16.12.2024)

ABSTRACT

A comparative analysis of Material Extrusion and VAT Photopolymerization 3D printing is done using various geometrical models, including square base pyramid, co-centric circular stamps, and lattice structures. The pyramid with Council of Scientific and Industrial Research (CSIR) and National Physical Laboratory (NPL) logos, texts printed by both techniques is studied for its dimensional accuracy as per the process parameters. The 3D printed specimen by Material Extrusion measured an average layer thickness of $\sim 104 \mu\text{m}$ and VAT Photopolymerization measured a layer thickness of $\sim 54 \mu\text{m}$. The calculated void volume of the printed pyramid due to the staircase effect is $\sim 2.9 \%$ for the Material Extrusion and $\sim 0.14 \%$ for the VAT Photopolymerization. Mechanical properties of ASTM D638 tensile test samples based on build orientation showed anisotropy for Material Extrusion, whereas VAT Photopolymerization printed test samples are isotropic. The degree of anisotropy (DOA) of 0.35, modulus of elasticity (MOE) of 1.7 GPa and ultimate tensile strength (UTS) of 62 MPa are measured for the Material Extrusion printed test sample. The ZXY build-oriented test sample showed the lowest values compared to all the other build orientations. Comparatively, the MOE and UTS for the VAT Photopolymerization printed samples are equal for all build orientations and are $\sim 950 \text{ MPa}$ and $\sim 39 \text{ MPa}$, respectively. The applicability of the present comparison of 3D printing techniques is demonstrated through functionality studies of printed stamps for ring electrodes and lattice structures as templates. The active area of the Fused deposition modeling (FDM) printed ring electrodes for maximum resolution is 17 times larger compared to that of Digital light processing (DLP) printed stamps. Additionally, the mean pore size for FDM-printed lattice structures was found to be $\sim 650 \mu\text{m}$, while the lattice structure printed by DLP using Polyurethan acrylate resin exhibited a pore size of $\sim 220 \mu\text{m}$. This analysis evaluates the dependence of stamp size due to print resolution specific to the technique. The importance of this research lies in addressing the growing demand for optimized 3D printing processes in manufacturing applications, such as sensors, electrodes, and structural components. By comparing dimensional accuracy, surface finish, print resolution, and mechanical properties, this study offers valuable insights into how the selection of printing techniques and process parameters can significantly influence the final product's performance.

Keywords: Additive Manufacturing, Staircase Effect, Build Orientation, Test Artifact, FDM Vs DLP, Printing Parameters, Ring Electrode.

1. INTRODUCTION

Additive Manufacturing (AM) is a freeform, direct digital, rapid, and additive fabrication of prototypes, tools, patterns, and concept parts as well as functional devices for direct application

and service as per American Society for Testing and Materials (ASTM) F42 Technical Committee [1]. As per ASTM 52900:2021, additive manufacturing is categorized into seven distinct processes; binder jetting, directed

energy deposition, material extrusion, material jetting, powder bed fusion, sheet lamination, and vat photopolymerization [2]. For the application and functionality of the printed models and for industrial production, certain criteria should be met, like surface finish, dimensional tolerance, mechanical properties, density, physical, and chemical properties [3]. Fused deposition modeling (FDM), based on material extrusion, is the most widely practiced additive manufacturing (AM) technique, involving precisely controlled layer-by-layer deposition of thermoplastic polymer through a heated nozzle. This method produces objects with a dimensional accuracy of the order ~ 100 μm by extruding molten material onto a build stage, where it solidifies and forms layers that adhere together [4].

Despite its simple process and moderate accuracy, FDM competes with alternative polymer-based AM technologies such as Powder Bed Fusion (PBF) and VAT photopolymerization (VPP). Due to its ease of deposition and accessibility, a variety of feedstock materials have been developed and are still emerging. Starting from basic thermoplastics like Polylactic acid (PLA) and Acrylonitrile butadiene styrene (ABS) and engineered plastics like Polyether ether ketone (PEEK) and Polyetherimide (PEI) to biopolymers, the library of materials is huge [5]. It caters needs of several industries like prosthetics, implants, and surgical tools in the medical industry [6], functional and carbon composites for energy storage [7], sensors [8], biopolymers for tissue engineering, and prototype designing of several components in the aeronautical and automobile industries [9].

Despite several advantages associated with the FDM technique and its application for several fields, the technique suffers from poor surface finish, weak mechanical strength of build parts, and build orientation-dependent anisotropy in physical and mechanical properties. These drawbacks are mostly related to the method of deposition [10]. The layer-by-layer deposition makes volumetric gaps on the surface and internal filling. The build orientation brings structure instability along one axis, and the viscoelastic nature of the polymer during extrusion brings interfacial bond instability based on the temperature of extrusion and speed. Also, the dimensional accuracy is

influenced by print speed, nozzle, and bed temperature [11].

VAT Photopolymerization (VPP) based AM technique creates 3D models by selectively curing a resin, layer by layer in a VAT using a light source forming complex geometries with very high resolution [12]. Digital light processing (DLP) is a preferred choice for creating 3D models with applications requiring complex geometries and intricate features with high resolution, speed, and smooth surface finish [13]. Unlike FDM, DLP prints 3D models by curing each layer through flash projection rather than mechanical movement. This effectively reduces the complexity of printing. Also, resolution of less than 50 μm can be achieved with great and intricate details [14]. The curvature effects and voids seen in FDM printing are eliminated largely by this mode of printing. Different resins starting from standard, structural to elastomeric resins are available as per application [15]. Resins being in liquid form can be easily mixed with several additives like nano-powders, carbon, and ceramic materials making composites for 3D printing [16]. Despite these advantages, resin printing is limited only to prototyping in fields like dentistry, jewelry, and medical implants and applications in antenna designing and fabrication, low to high dielectric materials for the electronic industry [17-18]. The feasibility of printing multi-materials using VAT photopolymerization has also hindered the advancement of this technique. The resin material used for printing is thermosetting which is brittle in nature and has mechanical properties not suitable for fatigue, wear, and tear [19]. It offers fewer material options than other 3D printing technologies. Post-processing requirements can be complex and time-consuming. The disposal of unused resin, and handling chemicals and photopolymer components raises environmental problems [20].

To print a quality product in terms of dimensional accuracy and mechanical stability by additive manufacturing, 3D printer, and process parameters must be optimized. For 3D printing, hardware conditions like tolerances of stepper motors, load bearing of the gears and railing, and thermal expansion of material used for building printers play major roles in the reproducibility of printed parts [21]. This is

generally optimized by the manufacturer of the machine. At the user end, process parameters play a crucial role in the dimensional tolerance and surface finish of the printed models. There are several process parameters that can be optimized when it comes to FDM like layer thickness, layer/raster width, raster angle, printing speed, nozzle and bed temperature, build orientation, infill pattern, infill percentage, and outer layers [22].

Ferretti P et al. established a relation between optimization for fabrication of lower defect-free 3D models [23]. Gao X et al. highlight the mechanical anisotropy of FDM-printed parts by changing the raster angle and build direction [22]. Bakhtiari H et al. study the influence of FDM printing parameters on the compressive properties and surface roughness of PLA specimens [24]. Bouzaglou O et al. studied the effect of material selection, printing factors such as path (layer thickness and raster angle), build (infill and building orientation), and temperature parameters (nozzle or bed temperature) on mechanical properties [25]. Many of the researchers worked on the Design of experiment (DoE) such as the Taguchi method, full factorial, and response surface methodology (RSM) for optimizing the process

parameters and minimizing the number of experiments [26].

Factors affecting DLP printing are divided into two categories: one is related to the machine, and the other is related to the photocurable resin. Machine-related parameters are layer thickness, light emitting diode power, flux uniformity, etc. Resin-related parameters are penetration depth, critical energy, viscosity, etc. Brighenti R et al. showed the printing process parameters of DLP on mechanical characteristics and concluded that the built specimen strength is dependent on the post-printing curing process [27]. Zhang Z et al. investigated the effect of printing layer thickness on model accuracy and found that decreasing the layer thickness from 0.10 mm to 0.05 mm increases the accuracy of the DLP 3D printing model [28]. Jiang T et al. studied the forming performance and characteristics and found that as the layer thickness increases from 0.02 to 0.22 mm, the dimensional accuracy first increases and then decreases for the DLP printed specimen [29]. Sector wise strength and weakness of FDM and DLP printing have been shown in Table 1.

Table 1: Sector wise strength and weakness of FDM and DLP printing.

| Sector | FDM | DLP |
|------------------------------|---|--|
| Automotive & Aerospace | Cost-effective for large prototypes and functional parts. Suitable for jigs, fixtures, and custom tools. | Limited in large-scale parts. Ideal for precision components like small gears, valves, and aesthetic parts. |
| Medical Devices | Used for creating medical models and prosthetics. | Superior for micro-scale medical devices like dental molds, surgical guides, and hearing aids. |
| Consumer Goods & Electronics | Useful for rapid prototyping of large consumer products. | Ideal for small, high-detail items like phone cases, wearables, and electronic housings. High precision enables creation of detailed product designs for miniaturized electronics. |
| Jewelry & Fashion | Limited use due to lack of fine detail. More useful for accessory molds or larger costume designs. | Preferred for small, intricate designs like rings, necklaces, and detailed accessories. |
| Architecture & Construction | Useful for printing large architectural models and prototypes. Suitable for scaled-down models of buildings and construction elements. | Best suited for fine-scale models that require accurate texture and finish (e.g., window grills, facades). |
| Education & Research | Accessible, low-cost solution for teaching, student projects, and early-stage R&D. Suitable for rapid prototyping and model validation. | Excellent for research requiring micro-precision components. Suitable for academic research focusing on photopolymers and high-detail components. |

As 3D printing is accomplished through layer-by-layer deposition and needs a file understandable by the printer, the CAD model must be tessellated. For this, the 3D model is converted to an STL file so that the printer can slice and convert it to the G-code file, the machine language that the printer can understand. Inherently the process induces several defects like chordal effect during tessellation and staircase formation for oblique and curved surfaces due to layer-by-layer deposition along with air gaps and many other voids due to raster angle and infill pattern [30]. Both the FDM and DLP techniques show the staircase effect, and it can be minimized by decreasing layer height. As the typical feature resolution of FDM is 100-150 μm and for DLP it is 50-100 μm , the staircase effect is more prominent in FDM printed models as compared to DLP printed models [31].

From molecular structures in chemistry, architectural marvels like Egyptian pyramids, and the construction of other polyhedral, square pyramids form the basic building block [32]. It is also used to represent the hierarchy in ecology [33]. When it comes to standards in physical measurements, it represents measurement traceability for an unbroken chain of

measurement for quality. The traceability pyramid creates an efficient and economical way for each lab or individual to access calibration standards.

A square pyramid has five vertices, eight edges, and five faces with four isosceles triangles making dihedral angles with the center line passing through the base [34]. These slant triangular faces are good for studying layer-by-layer deposition in terms of understanding the effect of these process parameters on surface roughness, dimensional accuracy, volumetric voids, and staircase effects. Even though there are in-depth studies and detailed reviews on FDM process parameters optimizing the dimensional accuracy and physical properties and very few studies on DLP process parameters for optimization of conditions for accurate 3D printed models. Except for the NIST test artifact which studied the dependence of process parameters for both the techniques independently, there are not many studies comparing both the techniques and the dependence on process parameters for dimensional tolerances, surface roughness, print resolution, and mechanical anisotropy of the 3D printed models (Table 2).

Table 2: The different artifacts used in literature for optimization of printing parameters.

| Tech. | Parm. | Artifact | Output | Ref |
|-------------|-------------------------------|---|---|--------------|
| FDM | Layer thickness | Pyramid, cube, and hemisphere over a platform | Surface quality, shear, and tensile strength, build time, accuracy, and precision | [35] |
| FDM | Printing speed, Layer height | ISO ASTM 52902-2021 specimen feature with coarse resolution holes | Geometrical Accuracy | [36] |
| FDM and DLP | - | NIST standard test artifact | Dimensional Uncertainty quantification | [37] |
| DLP | Exposure time | Orthogonal test samples, flowers with cylindrical small features | Resolution | [38] |
| DLP | Separation force | Cylindrical geometry, Lattice structure | Cross-section geometry and separation speed | [39] |
| FDM and DLP | - | Dental model | Trueness and precision | [40] |
| FDM and DLP | Printing speed, Exposure time | Square base pyramid artifact | Roughness, dimensional accuracy, surface finish, print resolution | In this work |

In the present study, we investigated the 3D-printed square base pyramid with Council of Scientific and Industrial Research (CSIR) and National Physical Laboratory (NPL) logos and texts on triangular facets for comparative

analysis and standardization of Material Extrusion and VAT photopolymerization AM techniques. We compared both techniques with respect to the layer thickness, edge sharpness, text resolution, and staircase effect. We also

studied interlayer bonding and mechanical strength based on build orientation through stress-strain analysis using standard tensile test samples and analyzed the uniqueness and versatility of both the techniques. To compare and study the dependence of print resolution, tolerances, and uniformity on the functionality of 3D printed models by both the techniques, two case studies, one using ring electrode stamps and the other using lattice structure have been demonstrated and analyzed.

2. MATERIAL AND METHODS

3D printing of square base pyramids with CSIR, NPL logos, and text is done by adopting FDM and DLP printing techniques. A 3D printer having a Hamera-based all-metal dual extruder is used for FDM-based printing of pyramids. The printer has a large build volume of $300 \times 300 \times 500 \text{ mm}^3$ and the capability of high-temperature extrusion up to $400 \text{ }^\circ\text{C}$. For DLP printing, an LD-002R resin printer by Creality containing a VAT of build volume of $120 \times 65 \times 165 \text{ mm}^3$ and a UV LED of 405 nm wavelength and 30 W power is used. For post-processing of printed resin models, a UW-01 washing and curing is used.

Polylactic acid (PLA) spool from Sigma-Aldrich is used for FDM printing and Polyurethane acrylate (PUAR) resin bought from Anycubic is used for DLP 3D printing. For slicing and setting process parameters during 3D printing, Simplify3D slicer software for FDM and Chitobox for the DLP technique is used.

STL files of text and logos of both CSIR and NPL and a square-base pyramid are used for 3D printing. The size of the square-based pyramid is 5 cm^3 . Arrangement and orientation of STL files of individual logos and text onto the triangular faces of the square base pyramid are done using the gizmos option available in Simplify 3D. A layer thickness of $100 \text{ }\mu\text{m}$ is chosen as it offers a balance between print quality and speed [31]. A rectilinear infill pattern with 100% density is chosen to improve the strength of printed parts. A speed of 60 mm/sec to improve the dimensional accuracy and print resolution. Extrusion multiplier is adjusted to 0.9 to avoid over deposition and match with the speed of printing [41]. As PLA is used for FDM printing, an extruder temperature of $200 \text{ }^\circ\text{C}$ and bed temperature of

$50 \text{ }^\circ\text{C}$ are used as printer parameter settings during slicing. Similarly, for DLP resin printing, the optimized process parameters are $50 \text{ }\mu\text{m}$ layer height as it is minimum lift possible with stepper angle of the stepper motor, being a flash printing technique, the infill density is 100 % by default. For proper adhesion to the build plate an initial layer exposure time of 50 sec first 8 layers followed by 6 sec for rest of the layers is chosen [42]. Table 3 below summarizes all the process parameters used for 3D printing of the CSIR-NPL pyramid and their comparison for both the FDM and DLP printing techniques.

Standard tensile test samples are fabricated by both the FDM and DLP techniques for studying mechanical properties. Tensile specimens were made in accordance with the ASTM D638 (Type IV) standard, with dimensions of length 115 mm , width 19 mm , thickness 4 mm , and waist length 32 mm . The samples were tested till failure to investigate their mechanical properties.

Concentric ring electrode stamps were modeled using Blender. Three different sizes, small (S), medium (M), and large (L) are made to ensure optimal resolution for both FDM and DLP 3D printing techniques. Lattice structure of $1 \times 1 \text{ cm}^2$ are printed by both FDM and DLP technique. Similar process parameters optimized for printing square base pyramid are used for printing ring electrode stamps and lattice structures.

Microscopic analysis of printed models is done using an MX6R optical microscope by AmScope Ltd. The layer height distribution is done using the stylus profilometer, Ambios, model XP-200 with a tip diameter of $2.5 \text{ }\mu\text{m}$ and tip force of 1.9 mN . La Jarden clay is used for taking imprints of the triangular face edges for their sharpness study. Image J software is used for the edge sharpness and layer thickness. The mechanical testing of FDM and DLP printed test samples is done using universal testing machine, Instron 5967 with a load measurement accuracy of $\pm 0.5\%$ having a capacity of 5 kN .

3. RESULT AND DISCUSSION

3.1. Slicing and Process Parameters

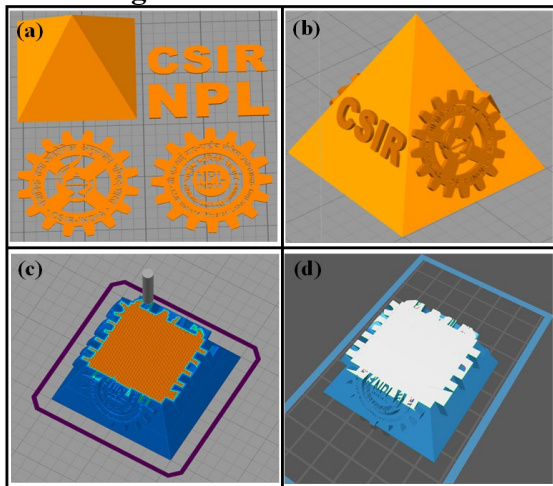


Figure 1: STL files of CSIR, NPL logos, text, and the CSIR-NPL pyramid, and the sliced images of the pyramids for FDM and DLP printing. (a) STL files of the square base pyramid and individual STL files of logos and text files, (b) STL file of merged CSIR-NPL pyramid. Image of pyramid sliced in slicer software (c) Simplify 3D (d) Chitubox.

Figure 1 shows the STL files of the CSIR-NPL pyramid with individual files consisting of CSIR, NPL logos, their text files, and the square pyramid along with the slicing of the combined STL files required for both the FDM and DLP techniques.

Figure 1a shows the individual STL files of the CSIR-NPL pyramid. Logos required for the creation of the STL file are taken from the following web links [43-44]. These image files are saved as JPG files and are converted to scalar vector graphic (SVG) files using the image online converter. The text files are created using PowerPoint and are converted to JPG and further into SVG files [45]. The square pyramid used for this study is taken from Thingiverse [46]. All these SVG files are converted into STL files using the svg2stl converter [47].

Figure 1b shows the unified STL file of the CSIR-NPL pyramid with logos and text files aligned onto the triangular faces of the square pyramid. These individual files are partially embedded into the square pyramid to avoid the separation of these from the pyramid during slicing, and to optimize the printing parameters. The 3D printed pyramid used for the current study is of dimensions with a square base of 5 cm and a vertical height of 5 cm.

The orientation of all logos and text files with the face of the pyramid is done in the slicer software. In the present case, all the logos and text STL files are aligned onto the faces of the pyramid and are exported into a single STL file, ready for slicing. ‘Allow single extrusion’ of the thin wall behavior option available in slicer software is used such that the gap in the narrow regions is filled with a single extrusion layer rather than raster infill where regular infill is not possible. This allows improvement in the resolution of printing, and smoothness. The small text found in logos can also be printed using this option.

Figures 1c and 1d show the slicing of the CSIR-NPL pyramid STL file generating G code files required for both the FDM and DLP printing. Table 3 summarizes all the process parameters used for 3D printing of the CSIR-NPL pyramid and their comparison for both the FDM and DLP printing techniques.

Table 3: Comparison of printing parameters of FDM and DLP printed 3D pyramid.

| Parameters | FDM | DLP |
|----------------------------|-----------------------------------|------------------|
| Machine | Hamera all metal extruder printer | Creality LD-002R |
| Material | PLA | PUAR Resin |
| Slicer | Simplify 3D | Chitubox |
| Layer height | 100 μm | 50 μm |
| Infill pattern | Rectilinear | Complete fill |
| Infill percentage | 100 % | 100 % |
| Speed | 60 mm/s | 6 sec/layer |
| Time | 6 h 50 min | 3 h 30 min |
| No. of outer walls | 3 | - |
| Top/bottom layer | 5 | - |
| Extrusion multiplier | 0.90 | - |
| Nozzle travel speed (XY) | 120 mm/s | |
| Bottom layer count | - | 10 |
| Bottom layer exposure time | - | 60 s |
| Other layer exposure time | - | 6 s |
| Lift up speed | - | 65 mm/min |
| Lift up distance | - | 5 mm |

3.2. Layer Thickness

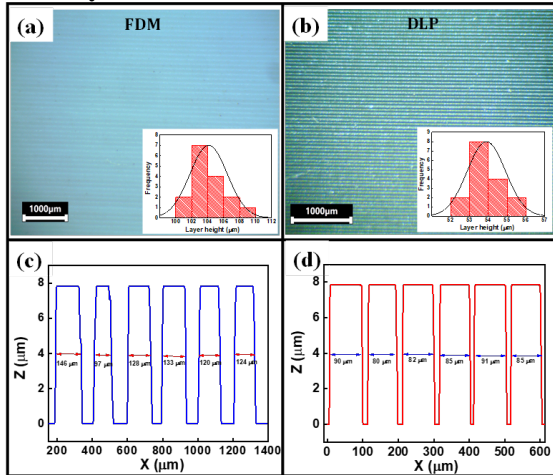


Figure 2: Optical image and statistical distribution of layer height, stylus profilometry measurement of FDM and DLP printed pyramid. Optical image of layer profile of (a) FDM, (b) DLP printed samples, and inset showing their thickness distribution respectively; Stylus profilometry analysis of (c) FDM and (d) DLP printed samples.

For a detailed analysis of the layer thickness of the FDM and DLP printed models, the surface of the 3D-printed pyramid is analyzed for their layer width and uniformity. Figure 2 shows the optical images of the face of the pyramid showing layers, along with profile analysis. Figure 2a shows the optical image of the printed layers by FDM along with the distribution analysis as shown by the histogram in the inset. From the histogram analysis, the layer width is estimated to be $\sim 104 \mu\text{m}$ with a standard deviation of 5 %. Similarly, Figure 2b shows the optical image of the printed layers on the face of the pyramid printed by the DLP technique and the histogram analysis. From the above analysis, the layer width is found to be $\sim 54 \mu\text{m}$ with a standard deviation of 4 %.

Figure 2c and 2d shows the stylus profiling of the surface shown in Figures 2a and 2b. The average width of the layers of the FDM printed pyramid measured is $\sim 130 \mu\text{m}$ and that of the resin printed pyramid is $\sim 85 \mu\text{m}$. From the above profiles, the layer width and distribution are more compared to that of optical image and histogram analysis. This increase in width is attributed to the tip convolution effect of the stylus profiler. Also, the layer height from the stylus profiler, which corresponds to roughness is the same for both the FDM and DLP printed models. Even though the DLP printed models have lower layer thickness and less distribution,

due to the tip with a large area of cross-section, the tip convolution during stylus profilometry won't be able to resolve the roughness variations. Also, it can be observed that the layer width is uniform, and the resolution is better for DLP printing by 50%. This establishes the superiority of the DLP technique over the FDM technique for smoothness, resolution, and surface finish [48]. The finer layer width and high resolution achieved with DLP printing make it ideal for industries requiring detailed and precise surface finishes, such as medical devices, and jewelry where intricate and uniform designs are essential. In contrast, FDM technique, despite its larger layer width, makes it suitable for applications in architecture, construction, automotive, and aerospace sectors [7-9].

3.3. Edge Sharpness And Print Resolution

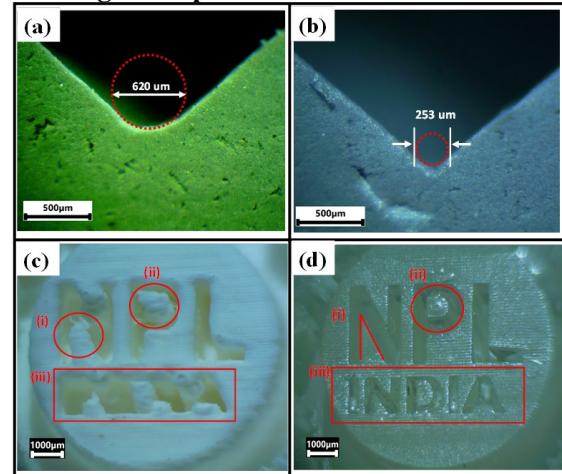


Figure 3: Edge sharpness measurement and print resolution of FDM and DLP printed pyramids: Optical image of imprint of the edges of the pyramid taken using molding clay (a) for FDM printing, (b) for DLP printing. Text resolution of the NPL logo (c) by FDM, and (d) by DLP.

Figures 3a and 3b show the sharpness of the edges of the pyramid. As FDM is a mechanical movement-based extrusion printing, during slicing, the tessellation is done such that there is a coordination between extrusion speed and the movement of the nozzle. This coordination makes the tip move slowly at the edges and the contours have a more circular finish/edges [11]. Figure 3a shows the optical image of the edge imprint taken using the clay molding technique. From the optical image, the convergence of two faces has a wide rounding with a diameter of $620 \mu\text{m}$.

Figure 3b shows the optical image of the face edge imprint taken for the DLP-printed pyramid. In comparison to edge sharpness for FDM, the convergence of two faces of the DLP printed pyramid has a sharp edge with a sharpness cross-section of $253\ \mu\text{m}$ as shown in Figure 3b. As DLP printing is a flash printing technique where the whole layer of the model is printed in a flash by curing the resin using UV light, the edges are defined thoroughly, and the resolution and the sharpness of the edges are high. From the above comparison, it is observed that the FDM-printed pyramid is more rounded at the edges of the faces compared to the DLP-printed pyramid and is 150% more rounded at the edges.

Figures 3c and 3d show the resolution of the small text achieved under FDM and DLP printing. In similar lines about the behavior of

the nozzle movement compared to flash printing of the DLP technique, the text is well defined in DLP printing compared to FDM printing [49], [50]. Allow single wall extrusion to a certain extent improves the resolution of the text printed by FDM. Also, the resolution in LCD-based DLP printing, decided by the pixel density, is proven to be better compared to the extrusion-based FDM printing. From Figure 3d (iii) compared to 3c (iii), the text with a smaller font 'INDIA' is better resolved in the DLP model. Also, the edge sharpness of the letter 'N' can also be distinguished clearly in DLP printing compared to FDM as observed in Figure 3c (i) and 3d (i). The superior sharpness possible with DLP finds applications in designing fine features in biomedical fields like microfluidic channels, and artificial organs. Whereas FDM is useful for rapid prototyping of large consumer products [6, 49, 51].

3.4. Build Orientation and Its Effect On Mechanical Properties

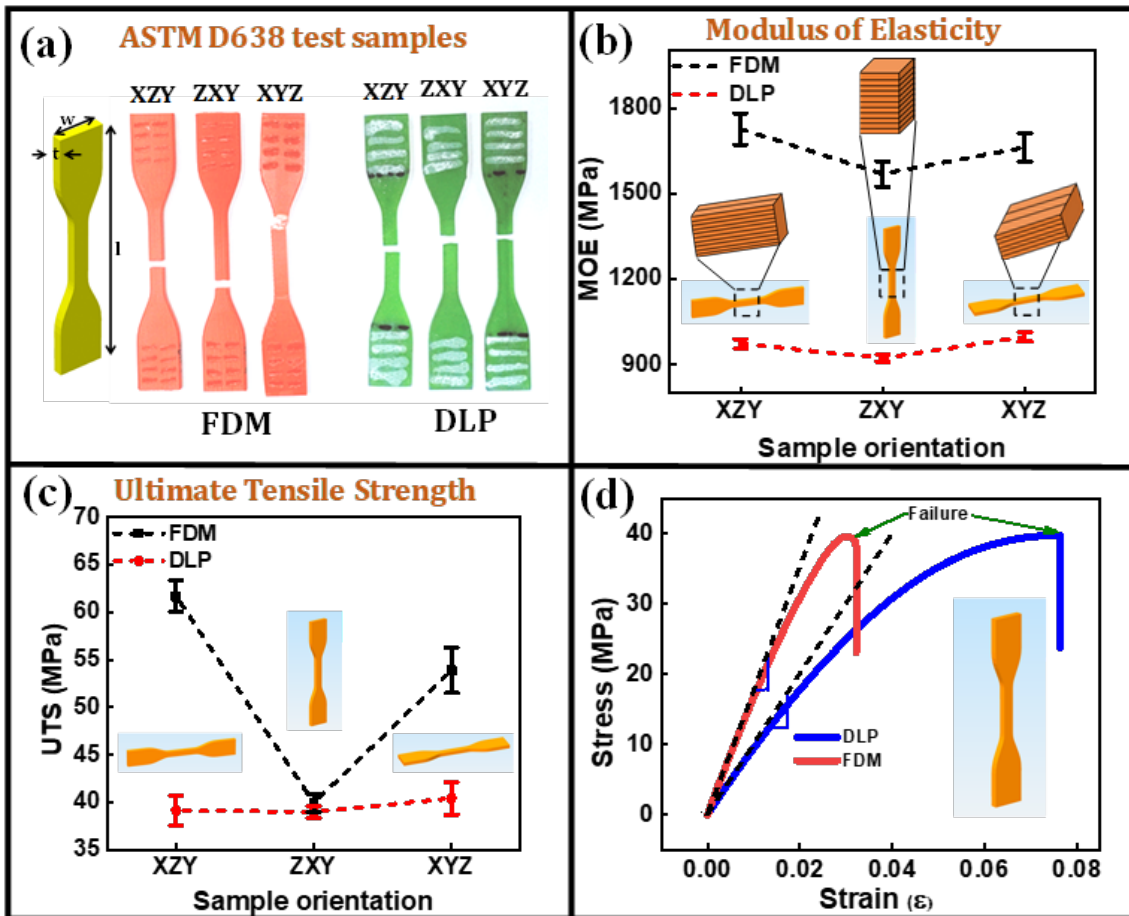


Figure 4: The image of ASTM D638 tensile test samples, Modulus of elasticity (MOE), Ultimate tensile strength (UTS), and stress-strain analysis of the FDM and DLP printed specimens. (a) Image of ASTM D638 sample after testing, (b) MOE, (c) UTS of samples printed in different orientations on the build plate, and (d) The stress vs strain analysis of vertically printed FDM and DLP test sample.

Figure 4 shows the comparison of the mechanical properties of both the FDM and DLP printed tensile test samples and the effect of build orientation on these properties. Figure 4a shows the optical image of tensile test samples printed by both the FDM and DLP techniques with three axes of build orientation namely XZY, ZXY, and XYZ respectively where the long axis is represented by the first letter of the notation followed by preceding long axes as per the nomenclature followed by ASTM 52921:2021 standard [52]. From the image, it can be observed that all the samples are tested for their tensile strength and are subjected to breaking and the breaking of all the samples has happened across the waist. Figures 4b and 4c show the modulus of elasticity (MOE) and ultimate tensile strength (UTS) of FDM and DLP printed test samples. Figure 4b shows the plot of MOE with respect to build orientation for both FDM and DLP test samples. The schematic of the test samples represents their build orientation during printing. The zoomed inset from the waist of the schematic depicts the orientation of printed layers with respect to the build platform. From the inset, it can be observed that for FDM, the XZY sample has layer-by-layer deposition in the ZY plane along the width (w) with the infill along the length. For the XYZ test sample, the layer-by-layer deposition is along the thickness (t) of the sample with infill along the length. Equivalently, the XZY sample has more filaments stranded and aligned along the length compared to that of XYZ. This makes the test sample with XZY orientation having MOE and UTS large compared to the XYZ FDM test sample. Whereas the ZXY test sample of FDM has low MOE and UTS compared to the other two orientations due to layer-by-layer deposition along the length in the z-direction having low interlayer bond strength compared to XZY and XYZ-oriented test samples. For DLP printed test samples, the MOE is low compared to FDM test samples and is equal for all build orientations. Figure 4c shows the UTS plot with respect to the build orientation for both FDM and DLP test samples. In summary, it can be observed that MOE and UTS for the FDM test samples are maximum for XZY orientation, followed by XYZ orientation, and least for ZXY orientation [53]. Whereas the MOE and UTS for the DLP printed samples are almost equal for all build orientations [54]. The MOE and UTS of XZY and XYZ FDM test samples are ~ 1.7 GPa,

62 MPa respectively, whereas the ZXY test sample has MOE and UTS ~ 1.5 GPa, 40 MPa respectively [55]. The UTS of the ZXY FDM test sample is similar compared to that of the UTS of DLP test samples ~ 40 MPa. Also, the MOE and UTS of DLP test samples are similar irrespective of build orientation, hence the tensile properties are isotropic for DLP test samples. The anisotropy in tensile properties for FDM printing is attributed to the dependence on build orientation and can be measured quantitatively by the degree of anisotropy (DOA) represented by D_a . DOA is given by the percentage of the difference between the maximum and minimum UTS and, is calculated following the equation: $D_a = [(UTS_{XZY} - UTS_{ZXY}) / UTS_{XZY}] \times 100\%$ [22]. The DOA for the FDM printed model is calculated to be 0.35 and for the DLP printed model is 0.0035. The near-zero value for DOA of DLP test samples establishes that DLP-printed 3D models have low MOE and UTS with isotropic behavior irrespective of build orientation as compared to FDM-printed models. As layer-by-layer deposition is normal to the print direction for ZXY samples of both the FDM and DLP test samples, this build orientation is suitable for comparison of interlayer bonding by both techniques. Figure 4d shows the stress-strain curves of tensile test samples printed with ZXY orientation. From Figure 4d, both the samples show equal tensile strength at the maximum load which suggests that the interlayer bonding is equal for both the FDM and DLP printed test samples. It can also be observed from the stress-strain curves that DLP printed test samples have a breaking point without any yield whereas FDM printed test samples undergo yielding beyond the strain of 0.02 and have yield over an elongation of 4 % before breaking. In the case of the FDM printed sample, for the layer-by-layer deposition of fused thermoplastic, the interface between the layers is decided by both the layer thickness and raster width. Whereas for DLP printing, the curing of photopolymer takes place both in-plane and along normal. As the polymer entanglement is more in the DLP sample and isotropic [56], [57], it shows plastic behavior from the beginning with more strain and undergoes failure abruptly at maximum tensile stress. Hence the DLP printed test sample is more brittle than the FDM sample. The ultimate tensile strength calculated from the stress-strain curves for both the FDM and DLP test samples is ~ 40 MPa. The high anisotropy of FDM-

printed parts, along with a higher modulus of elasticity, makes FDM suitable for applications that require strength along specific orientations, such as load-bearing parts, test jig in automobile, and aerospace industry. Whereas DLP-printed parts, being isotropic, offer uniform mechanical properties in all directions,

making them ideal for applications requiring consistent strength and flexibility across different orientations, such as spare parts for automobile industry, and consumer electronics [8, 58-59].

3.5. Staircase Effect and Surface Finish

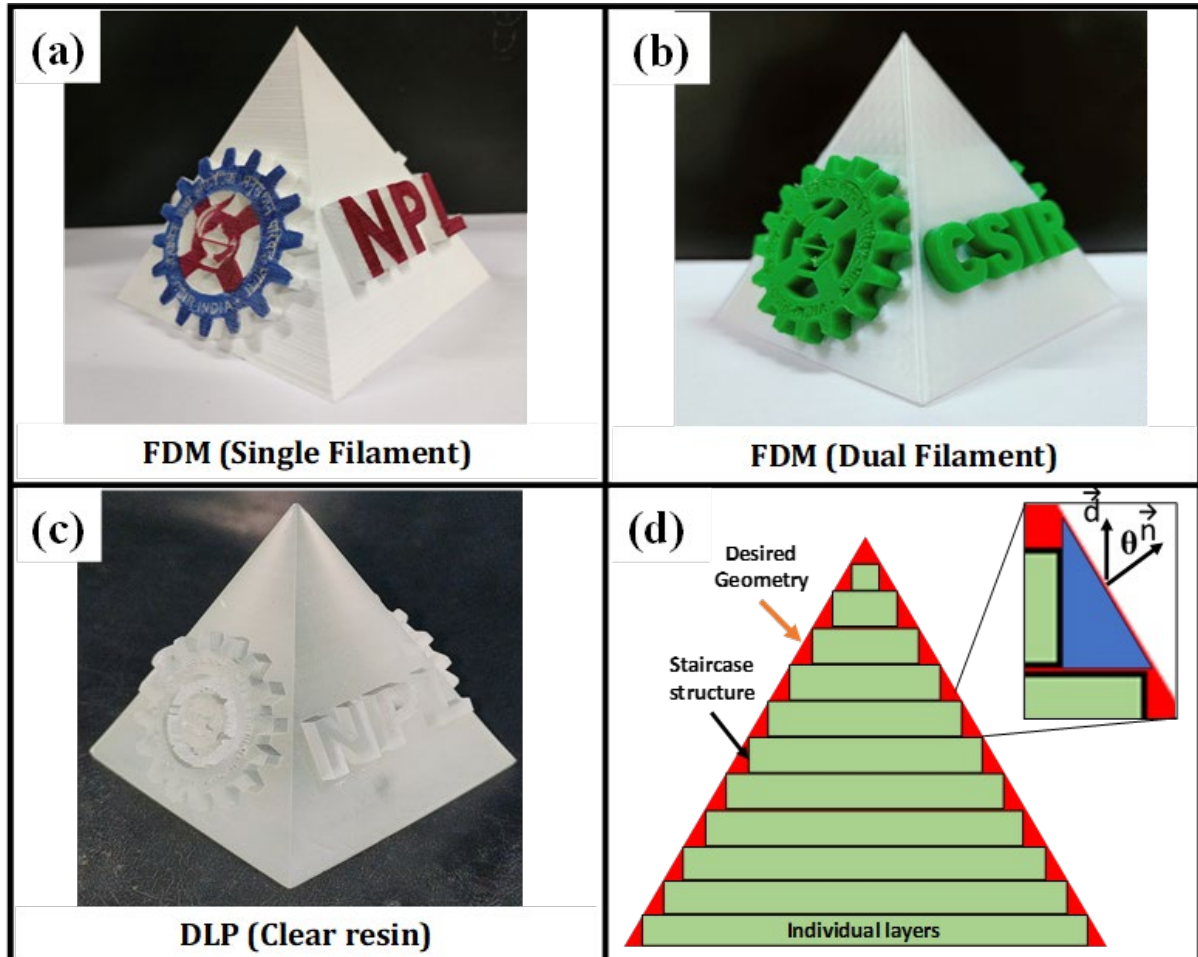


Figure 5: Image of 3D printed CSIR-NPL Pyramid printed using single filament, dual filament FDM, and DLP 3D printer and the staircase effect analysis. Pyramid printed via (a) single filament FDM, (b) dual filament FDM printing, (c) DLP printing technique, and (d) schematic of staircase effect present in 3D printed models with inset showing one such staircase.

Figure 5 shows the image of 3D-printed pyramids with FDM and DLP techniques and the staircase effect. Figures 5a and 5b show the 3D printed pyramid by single filament and dual filament extrusion FDM respectively. Figure 5a shows the pyramid printed with PLA filament (white) and the logos colored with different colors. In single filament printing the printing process is simplified with a single STL file and the distinction between individual STL files will not be there. Figure 5b shows the pyramid printed with dual filaments of PLA (white and

green). It shows the capability of multi-material printing with FDM, which is not possible with DLP resin printing. Also, the complexity of process parameters during slicing increases as the G-code is modified to control the movement of the dual head during printing. Figure 5c shows the pyramid printed by the DLP 3D printing technique using PUAR clear resin. Figure 5d shows the schematic of the staircase effect present in a 3D-printed pyramid along with the inset showing one such staircase. The actual pyramid from the STL file to be printed

is shown in the background with red color and the stacked layered pyramid shows the achievable model by 3D printing technique. The staircase effect comes into account when the surface of the build model is either oblique or circular with an angle, $0 < \theta < 90$ where θ is the angle between \vec{n} and \vec{d} . \vec{n} is normal to oblique/curved surface and \vec{d} is the vector normal to the build plate.

Based on layer thickness and tessellation density, the volume error can be calculated. For the present 3D pyramid, the triangular surface has no curvature, and the tessellation is done such that the volume error is simply dependent on layer thickness. From the dimensions of the pyramid and layer thickness used for both FDM and DLP techniques, the offset of the layer for each step resulting in the staircase effect is

calculated to be 50 μm and 25 μm respectively. Based on this, the volume error between two layers is calculated. The estimated volume error following the process parameters for both FDM and DLP printed pyramids are 2.9 and 0.14 % respectively. Comparatively, the volume error for the DLP printed pyramid is low by 40 % of that of the FDM printed pyramid. This shows the higher surface finish and better print quality of the DLP-printed pyramid. DLP's low void volume and superior surface finish make it particularly suitable for applications in dental models, intricate jewelry, and biomedical application. Whereas, FDM having a higher void volume and visible staircase effect, is more appropriate for applications in architectural models, and industrial tools where the focus is on functionality and strength over aesthetic precision [54, 60].

3.6. Functionality Of Models Printed by FDM And DLP Technique

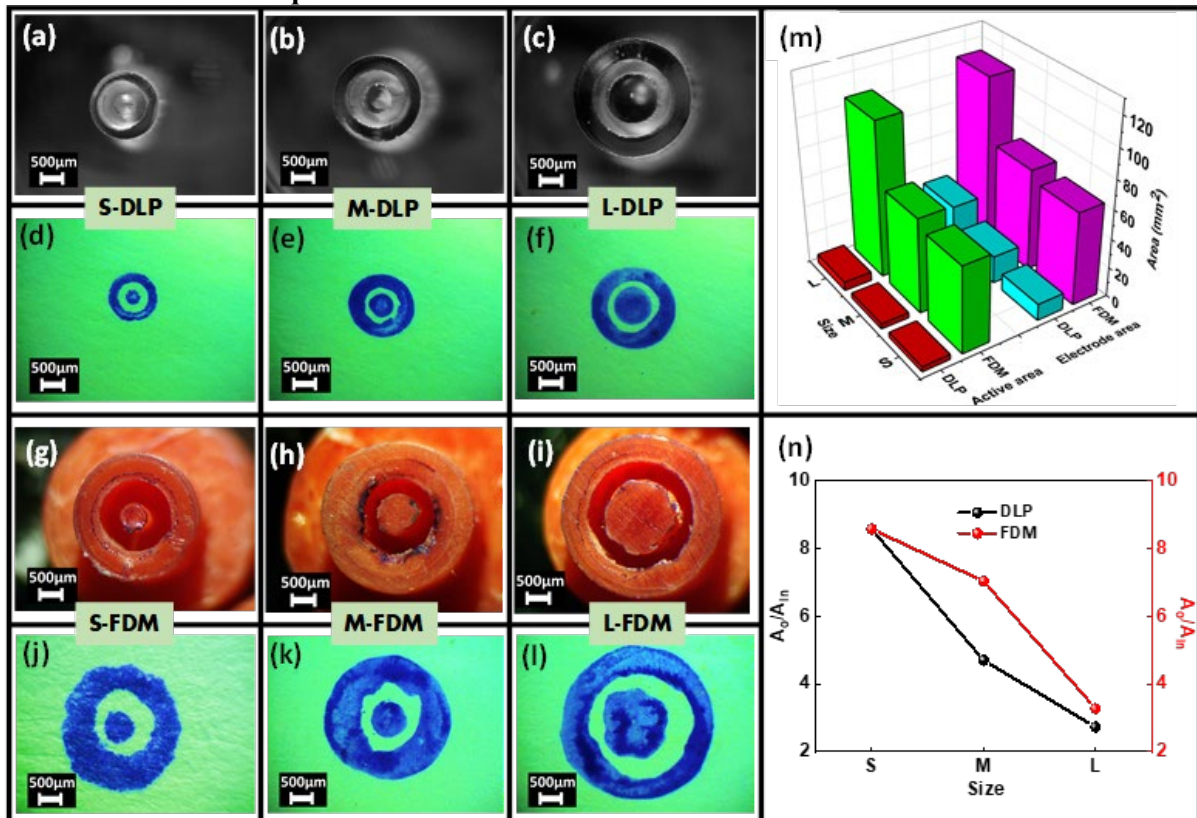


Figure 6: Stamps printed by DLP and FDM techniques along with co-axial ring electrode and their analysis. Stamps of different sizes (S, M, L) printed by DLP, Figures 6(a) – 6(c) and Figures 6(g) – 6(i) by FDM technique. Ring electrode imprints of DLP stamps, Figure 6(d) - 6(f) and FDM stamps, Figures 6(j) – 6(l). Figures 6(m), and 6(n) show the comparison of the active area, electrode area, and outer-to-inner electrode ratio of FDM and DLP printed stamps.

To understand the effectiveness of the present study, co-centric circular stamps of different sizes are printed using both techniques for the

deposition of ring electrodes [61-62]. These ring electrodes find applications in sensors, LEDs, and memory devices [63-64]. Such co-

centric circular patterns can also be used in printing Fresnel lenses for optical devices and metamaterial applications [65]. Particularly for optical sensors, the behavior of the device is determined by the active area available for exposure to the incident light. The active area for ring electrodes is defined as the area available between two co-centric electrodes for external stimulation. Minimum, the active area, lesser the noise, higher the charge collection efficiency, and greater the responsivity. The size of the ring electrode decides the compactness and device density.

Figure 6 shows the co-centric circular stamp models printed using both FDM and DLP techniques and their imprint for ring electrodes. Figures 6a to 6c show stamps with three different sizes printed using the DLP technique denoted by S-DLP, M-DLP, and L-DLP, respectively. Similarly, Figures 6g to 6i show different-sized stamps denoted by S-FDM, M-FDM, and L-FDM, respectively, printed using the FDM technique. Both the S-DLP and S-FDM stamps are printed such that the printing conditions are optimized for the highest resolution possible with these printers. For DLP printed stamp, the highest resolution is achieved by optimizing the diameter of the inner circle through exposure time and lateral width determined by no: of excited pixels. Similarly, for FDM the highest resolution for the inner electrode is achieved by optimizing the minimum no: of strands required for printing. In the case of S-DLP and S-FDM, the optimized diameters achieved are 0.3 and 0.8 mm respectively. For determining the electrode size, the outer electrode diameter is considered, and the diameter of 1 and 3 mm is observed for S-DLP and S-FDM stamps respectively.

Figures 6d to 6f represent the ring electrode imprints produced by stamping all three DLP printed models from small to large, respectively using a blue dye. Similarly, figures 6j to 6l represent the ring electrode imprints produced by stamping FDM printed models. Active area, the size of the electrodes, and the ratio of the outer to inner electrode area are compared for both techniques to understand the functionality of the printed electrodes in terms of print resolution, uniformity, and roundness.

Figure 6m, shows the bar diagram analysis of both the active area and the outer electrode area

of the imprints produced by stamps using both techniques. In the bar diagram, the grouping of both FDM and DLP for the active area and electrode size is shown along the x-axis. The y-axis represents three different-sized stamps for imprints and the z-axis represents the values of these parameters. From the analysis, it is found that the active area of the FDM imprints is 17 times larger compared to DLP-printed electrodes for all stamp sizes. Similarly, the size of the FDM-printed ring electrode is ~ 6 times that of the small stamp and 3.5 times that of the medium and large stamps printed by the DLP technique. Hence the device density of the DLP-printed ring electrodes can be 3 to 6 times larger compared to FDM-printed ring electrodes. This study emphasizes the importance of comparing both techniques to understand the functionality of printed models. Figure 6n compares the ratio of outer to inner electrodes of different stamps for both DLP and FDM techniques. From the analysis, it can be observed that the ratio for all the stamps for both techniques is the same, except for M-DLP and M-FDM where M-FDM is greater by 1.5 times. As the active area is proportional to stamp size, suggests that the outer electrode area is larger compared to other stamps.

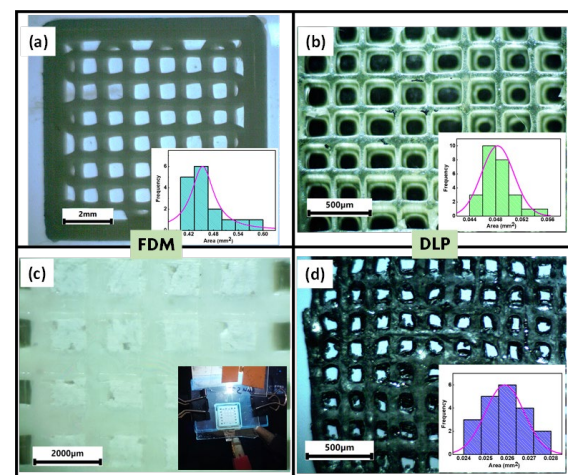


Figure 7: Functionality study of Lattice structure printed by FDM and DLP techniques. Lattice structure printed by (a) FDM and (b) DLP technique with inset showing the pore size distribution, (c) ZnO filled FDM lattice template with inset showing the photodetector fabricated using FDM lattice template, and (d) Carbonized DLP printed lattice structure with inset showing the distribution of pore size.

Another functionality of the present study can be found in designing lattice structures which can find applications as templates hosting

nanomaterials, fillers for realizing sensors, resonators, and filters [8, 66-67]. Also, chemical and thermal modification of such lattice structures can be used for applications as electrodes for batteries, fuel cells, and catalytic converters [68].

Figure 7 shows the lattice structures printed by both FDM and DLP 3D printing techniques with optimized pore size for high resolution along with their functionality. Figure 7a shows the lattice structure printed by FDM using PLA thermoplastic with an inset showing a histogram analysis of pore distribution. The mean pore size calculated from the analysis is ~ 650 μm. Similarly, the lattice structure printed by DLP using PUAR resin with histogram analysis of the pore distribution is shown in Figure 7b, and from the analysis the pore size is ~ 220 μm. Dimension and layer number of different sizes of ring electrode and lattice structure for both the techniques are given in the Table 4.

Table 4: Details of stamps and lattice structure printed by DLP and FDM techniques.

| Ring Electrode | | | | | | |
|------------------------|--------|------|------|--------|------|------|
| Parameters | FDM | | | DLP | | |
| Configuration | S | M | L | S | M | L |
| Inner ring radius (μm) | 1580 | 1630 | 3792 | 738 | 891 | 1270 |
| Outer ring radius (μm) | 2850 | 2985 | 2575 | 1204 | 1550 | 1985 |
| Total number of layer | 10 | 12 | 14 | 20 | 24 | 28 |
| Layer height (μm) | 100 | | | 50 | | |
| Lattice structure | | | | | | |
| Pore Size | 650 μm | | | 220 μm | | |
| Number of layer | 20 | | | 40 | | |

Figure 7c shows the lattice structure used as a template hosting ZnO nanoparticles. Such templates filled with nanomaterials have potential applications for fabricating out-of-plane optical sensors, strain sensors, and triboelectric generators. The inset shows the

device configuration of the out-of-plane photodetector. Figure 7d shows the carbonization of the lattice structure as shown in Figure 7b. Being a thermosetting polymer, the carbonization at 1200 °C results in a conductive lattice structure having potential application as an electrode for batteries and fuel cells. The inset of Figure 7d shows the histogram analysis of the pore size after carbonization, indicating the pore size is ~ 160 μm and a shrinkage in lattice size by ~ 27 %. The distinguishing aspects of the comparative study are the quantification of void volume due to the staircase effect and comparing both techniques for specific applications like stamps for electrode printing. Also, the edge sharpness is another distinct aspect that plays a major role in designing mechanical parts for tool matching and compatibility with the hosting system. Further the comparative study can be optimized for selective adoption of the technique and models for specific application which pertains to minimizing staircase effect, optimizing tessellation, better slicing and also instrument parameters like LED affluence, pixel density and material properties like minimizing warping and photoinitiator for high resolution.

4. CONCLUSION

A simple artifact based on a pyramid is used for comparative analysis of FDM and DLP printing techniques. The dependence on process parameters during slicing is studied for surface finish and print resolution.

- **Dimensional Accuracy:** The FDM-printed pyramid exhibited an average layer thickness of ~104 μm, whereas the DLP-printed pyramid had a much finer layer thickness of ~54 μm.
- **Staircase Effect:** The void volume due to the staircase effect was calculated to be ~2.9% for FDM and only ~0.14% for DLP, indicating better surface finish and dimensional accuracy in DLP-printed samples.
- **Edge Sharpness and Print Resolution:** DLP-printed samples exhibited superior edge sharpness and print resolution compared to their FDM counterparts. This resulted in more precise and cleaner geometries, particularly noticeable in fine-feature details.
- **Mechanical Properties:** Mechanical testing showed that the MOE for FDM-printed samples was 1.7 GPa, with UTS of 62 MPa, exhibiting anisotropic behavior. In contrast, DLP-printed

samples demonstrated isotropic properties with an MOE of ~950 MPa and UTS of ~39 MPa.

- **Degree of Anisotropy (DOA):** The FDM-printed samples showed a DOA of 0.35, indicating significant orientation-dependent mechanical properties. DLP samples, however, exhibited more consistent isotropic behavior across the structure.

- **Electrode Dimensions:** Systematic analysis of co-centric ring electrodes printed using FDM and DLP revealed that the active area of FDM imprints was 17 times larger compared to DLP-printed electrodes, indicating substantial differences in resolution and feature size across all stamp sizes.

- **Lattice Structure Analysis:** FDM-printed lattice structures showed a mean pore size of ~650 μm , while the DLP-printed lattice structures using PUAR resin had a significantly smaller pore size of ~220 μm . This highlights the variability in structural characteristics and print quality depending on the chosen printing technique.

ACKNOWLEDGES

Mr. Bhanu Prakash Bisht acknowledges Council of Scientific and Industrial Research (CSIR) & Academy of Scientific and Innovative Research (AcSIR) for fellowship and academic support. Dr. Vijaykumar Toutam acknowledges CSIR for financial support under Lab Project and in house R & D support.

REFERENCES

1. D. Godec et al., "Introduction to Additive Manufacturing," Pages 1–44, 2022.
2. "ISO/ASTM 52900:2021(en), Additive manufacturing — General principles — Fundamentals and vocabulary." Accessed: Nov. 27, 2023. [Online]. Available: <https://www.iso.org/obp/ui/#iso:std:iso-astm:52900:ed-2:v1:en>
3. Citarella R., Giannella V., "Additive Manufacturing in Industry," Applied Sciences, Vol. 11, Issue 2, Pages 840, 2021.
4. Dhinakaran V., Kumar K. P. M., Ram P. M. B., Ravichandran M., Vinayagamoorthy M., "A review on recent advancements in fused deposition modeling," Mater Today Proc, Vol. 27, Pages 752–756, 2020.
5. Kristiawan R. B., Imaduddin F., Ariawan D., Ubaidillah, Arifin Z., "A review on the fused deposition modeling (FDM) 3D printing: Filament

processing, materials, and printing parameters," Open Engineering, Vol. 11, Issue 1, Pages 639–649, 2021.

6. Patel A., Taufik M., "A study on design and development of prosthetics by fused deposition modelling," The Fourth Scientific Conference for Electrical Engineering Techniques Research (EETR2022), Vol. 2804, Issue 1, Pages 020144, 2023.

7. Foster C. W., et al., "3D Printed Graphene Based Energy Storage Devices," Scientific Reports, Vol. 7, Issue 1, Pages 1–11, 2017.

8. Bisht B. P., Toutam V., Dhakate S. R., "3D Printed Lattice Template by Material Extrusion Technique for Fabrication of Pixelated Photodetector," 3D Printing and Additive Manufacturing, Vol. 10, Issue 6, Pages 74–83, 2023.

9. Mallikarjuna B., Bhargav P., Hiremath S., Jayachristiyan K. G., Jayanth N., "A review on the melt extrusion-based fused deposition modeling (FDM): background, materials, process parameters and military applications," International Journal on Interactive Design and Manufacturing (IJIDeM) 2023, Pages 1–15, 2023.

10. Parulski C., Jennotte O., Lechanteur A., Evrard B., "Challenges of fused deposition modeling 3D printing in pharmaceutical applications: Where are we now?," Adv Drug Deliv Rev, Vol. 175, Pages 113810, 2021.

11. Baechle-Clayton M., Loos E., Taheri M., Taheri H., "Failures and Flaws in Fused Deposition Modeling (FDM) Additively Manufactured Polymers and Composites," Journal of Composites Science, Vol. 6, Issue 7, Page 202, 2022.

12. Pagac M., et al., "A Review of Vat Photopolymerization Technology: Materials, Applications, Challenges, and Future Trends of 3D Printing," Polymers, Vol. 13, Issue 4, Page 598, 2021.

13. Mu Q., et al., "Digital light processing 3D printing of conductive complex structures," Addit Manuf, Vol. 18, Pages 74–83, 2017.

14. Chaudhary R., Fabbri P., Leoni E., Mazzanti F., Akbari R., Antonini C., "Additive manufacturing by digital light processing: a review," Progress in Additive Manufacturing, Vol. 8, Issue 2, Pages 331–351, 2022.

15. Bagheri A., Jin J., "Photopolymerization in 3D Printing," ACS Appl Polym Mater, Vol. 1, Issue 4, Pages 593–611, 2019.

16. Shah M., et al., "Vat photopolymerization-based 3D printing of polymer nanocomposites: current trends and applications," *RSC Adv*, Vol. 13, Issue 2, Pages 1456–1496, 2023.
17. Colella R., Chietera F. P., Catarinucci L., "Analysis of FDM and DLP 3D-Printing Technologies to Prototype Electromagnetic Devices for RFID Applications," *Sensors*, Vol. 21, Issue 3, Page 897, 2021.
18. Bisht B. P., et al., "3D printed ZnO-Polyurethane acrylate resin composite for wide spectral photo response optical detectors," *Sens Actuators A Phys*, Vol. 351, Page 114165, 2023.
19. Quan H., Zhang T., Xu H., Luo S., Nie J., Zhu X., "Photo-curing 3D printing technique and its challenges," *Bioact Mater*, Vol. 5, Issue 1, Pages 110–115, 2020.
20. Stefaniak A. B., et al., "Particle and vapor emissions from vat polymerization desktop-scale 3-dimensional printers," *J Occup Environ Hyg*, Vol. 16, Issue 8, Page 519, 2019.
21. Kuznetsov V. E., Tavitov A. G., Urzhumtsev O. D., Mikhalin M. V., Moiseev A. I., "Hardware Factors Influencing Strength of Parts Obtained by Fused Filament Fabrication," *Polymers*, Vol. 11, Issue 11, Page 1870, 2019.
22. Gao X., Qi S., Kuang X., Su Y., Li J., Wang D., "Fused filament fabrication of polymer materials: A review of interlayer bond," *Addit Manuf*, Vol. 37, Page 101658, 2021.
23. Ferretti P., et al., "Relationship between FDM 3D Printing Parameters Study: Parameter Optimization for Lower Defects," *Polymers*, Vol. 13, Issue 13, Page 2190, 2021.
24. Bakhtiari H., Nikzad M., Tolouei-Rad M., "Influence of Three-Dimensional Printing Parameters on Compressive Properties and Surface Smoothness of Polylactic Acid Specimens," *Polymers*, Vol. 15, Issue 18, Page 3827, 2023.
25. Bouzaglou O., Golan O., Lachman N., "Process Design and Parameters Interaction in Material Extrusion 3D Printing: A Review," *Polymers (Basel)*, Vol. 15, Issue 10, 2023.
26. Harun N. H., Kasim M. S., Abidin M. Z. Z., Izamshah R., Attan H., Ganesan H. N., "A Study on Surface Roughness During Fused Deposition Modelling: A Review," *Journal of Advanced Manufacturing Technology (JAMT)*, Vol. 12, Issue 1, Pages 25–36, 2018.
27. Brighenti R., Marsavina L., Marghitas M. P., Montanari M., Spagnoli A., Tatar F., "The effect of process parameters on mechanical characteristics of specimens obtained via DLP additive manufacturing technology," *Mater Today Proc*, Vol. 78, Pages 331–336, 2023.
28. Zhang Z., Li P. L., Chu F. T., Shen G., "Influence of the three-dimensional printing technique and printing layer thickness on model accuracy," *Journal of Orofacial Orthopedics*, Vol. 80, Issue 4, Pages 194–204, 2019.
29. Jiang T., et al., "Study of Forming Performance and Characterization of DLP 3D Printed Parts," *Materials*, Vol. 16, Issue 10, Page 3847, 2023.
30. Mohamed O. A., Masood S. H., Bhowmik J. L., Blaj M., Oancea G., "Fused deposition modelling process: a literature review," *IOP Conf Ser Mater Sci Eng*, Vol. 1009, Issue 1, Page 012006, 2021.
31. Ligon S. C., Liska R., Stampfl J., Gurr M., Mülhaupt R., "Polymers for 3D Printing and Customized Additive Manufacturing," *Chem Rev*, Vol. 117, Issue 15, Pages 10212–10290, 2017.
32. C. Kittel and P. McEuen, "Introduction to solid state physics", Pages 692.
33. "Ecological pyramid - Wikiwand." Accessed: Nov. 28, 2023. [Online]. Available: https://www.wikiwand.com/en/Ecological_pyramid
34. Wikiwand, "Square pyramid," [Online]. Available: https://www.wikiwand.com/en/Square_pyramid, November 28, 2023.
35. Bochmann L., Bayley C., Helu M., Transchel R., Wegener K., Dornfeld D., "Understanding error generation in fused deposition modeling," *Surf Topogr*, Vol. 3, Issue 1, Page 014002, 2015.
36. Alexopoulou V. E., Christodoulou I. T., Markopoulos A. P., "Effect of Printing Speed and Layer Height on Geometrical Accuracy of FDM-Printed Resolution Holes of PETG Artifacts," *Engineering Proceedings*, Vol. 24, Issue 1, Page 11, 2022.
37. Mac G., Pearce H., Karri R., Gupta N., "Uncertainty quantification in dimensions dataset of additive manufactured NIST standard test artifact," *Data Brief*, Vol. 38, Page 107286, 2021.
38. Huang J., Zhang B., Xiao J., Zhang Q., "An Approach to Improve the Resolution of DLP 3D Printing by Parallel Mechanism," *Applied Sciences*, Vol. 12, Issue 24, Page 12905, 2022.

39. Manizani S. M., Zamani J., Salehi M., Shayesteh M. T., "Investigating the Effect of Separation Speed and Image Cross-Section Geometry on The Separation Force in DLP Method using FEP and PP Polymer Membranes," *International Journal of Advanced Design and Manufacturing Technology*, Vol. 64, Issue 3, Page 9, 2023.
40. Grzebieluch W., Grajzer M., Mikulewicz M., "Comparative Analysis of Fused Deposition Modeling and Digital Light Processing Techniques for Dimensional Accuracy in Clear Aligner Manufacturing," *Med Sci Monit*, Vol. 29, Page e940922, 2023.
41. Lendvai L., Fekete I., Rigotti D., Pegoretti A., "Experimental study on the effect of filament-extrusion rate on the structural, mechanical and thermal properties of material extrusion 3D-printed polylactic acid (PLA) products," *Progress in Additive Manufacturing*, Pages 1–11, 2024.
42. Yang Y., Zhou Y., Lin X., Yang Q., Yang G., "Printability of External and Internal Structures Based on Digital Light Processing 3D Printing Technique," *Pharmaceutics*, Vol. 12, Issue 3, Pages 207, 2020.
43. Council of Scientific & Industrial Research, "CSIR Logo | Council of Scientific & Industrial Research," <https://www.csir.res.in/csir-logo>, November 28, 2023.
44. "National Physical Laboratory of India - Wikiwand," https://www.wikiwand.com/en/National_Physical_Laboratory_of_India, November 28, 2023.
45. "Online SVG image converter," <https://image.online-convert.com/convert-to-svg>, November 28, 2023.
46. "Thingiverse - Digital Designs for Physical Objects," <https://www.thingiverse.com/>, November 28, 2023.
47. "SVG 2 STL," <https://svg2stl.com/>, November 28, 2023.
48. Alsoufi M. S., Elsayed A. E., "How Surface Roughness Performance of Printed Parts Manufactured by Desktop FDM 3D Printer with PLA+ is Influenced by Measuring Direction," Vol. 5, Issue 5, 2017.
49. Duan K., et al., "Monolithically 3D-Printed Microfluidics with Embedded μ Tesla Pump," *Micromachines (Basel)*, Vol. 14, Issue 2, Page 237, 2023.
50. Luo Z., et al., "Digital light processing 3D printing for microfluidic chips with enhanced resolution via dosing- and zoning-controlled vat photopolymerization," *Microsystems & Nanoengineering*, Vol. 9, Issue 1, Pages 1–13, 2023.
51. Wu Y., Su H., Li M., Xing H., "Digital light processing-based multi-material bioprinting: Processes, applications, and perspectives," *J Biomed Mater Res A*, Vol. 111, Issue 4, Pages 527–542, 2023.
52. International Organization for Standardization, "ISO/ASTM 52921:2013 - Standard terminology for additive manufacturing — Coordinate systems and test methodologies," <https://www.iso.org/standard/62794.html>, November 28, 2023.
53. Corapi D., Morettini G., Pascoletti G., Zitelli C., "Characterization of a Polylactic acid (PLA) produced by Fused Deposition Modeling (FDM) technology," *Procedia Structural Integrity*, Vol. 24, Pages 289–295, 2019.
54. Farkas A. Z., Galatanu S. V., Nagib R., "The Influence of Printing Layer Thickness and Orientation on the Mechanical Properties of DLP 3D-Printed Dental Resin," *Polymers* 2023, Vol. 15, Issue 5, Page 1113, 2023.
55. Cojocaru V., Frunzaverde D., Miclosina C. O., Marginean G., "The Influence of the Process Parameters on the Mechanical Properties of PLA Specimens Produced by Fused Filament Fabrication—A Review," *Polymers*, Vol. 14, Issue 5, Page 886, 2022.
56. Susanto B., et al., "Investigating Microstructural and Mechanical Behavior of DLP-Printed Nickel Microparticle Composites," *Journal of Composites Science*, Vol. 8, Issue 7, Page 247, 2024.
57. Dhand A. P., Davidson M. D., Zlotnick H. M., Kolibaba T. J., Killgore J. P., Burdick J. A., "Additive manufacturing of highly entangled polymer networks," *Science*, Vol. 385, Issue 6708, Pages 566–572, 2024.
58. Bisht B. P., et al., "3D printed ZnO-Polyurethane acrylate resin composite for wide spectral photo response optical detectors," *Sens Actuators A Phys*, Vol. 351, Page 114165, 2023.
59. Khosravani M. R., Soltani P., Reinicke T., "Effects of steps on the load bearing capacity of 3D-printed single lap joints," *Journal of Materials*

Research and Technology, Vol. 23, Pages 1834–1847, 2023.

60. Zhang J., Hu Q., Wang S., Tao J., Gou M., “Digital Light Processing Based Three-dimensional Printing for Medical Applications,” *Int J Bioprint*, Vol. 6, Issue 1, Pages 12–27, 2020.

61. Gonzalez-Fernandez T., Tenorio A. J., Leach J. Kent, “Three-Dimensional Printed Stamps for the Fabrication of Patterned Microwells and High-Throughput Production of Homogeneous Cell Spheroids,” *3D Print Addit Manuf*, Vol. 7, Issue 3, Pages 139–147, 2020.

62. Pinheiro A. C. Nava, Ferreira V. Souza, Lucca B. Gabriel, “Stamping method based on 3D printing and disposable napkin: Cheap production of paper analytical devices for alcohol determination in beverages aiming forensics and food control,” *Microchemical Journal*, Vol. 180, Page 107604, 2022.

63. Stromberg L. R., et al., “Stamped multilayer graphene laminates for disposable in-field electrodes: application to electrochemical sensing of hydrogen peroxide and glucose,” *Microchimica Acta*, Vol. 186, Issue 8, Pages 1–13, 2019.

64. Araujo T. A. de, Moraes N. C. de, Petroni J. M., Ferreira V. S., Lucca B. G., “Simple, fast, and instrumentless fabrication of paper analytical devices by novel contact stamping method based on acrylic varnish and 3D printing,” *Microchimica Acta*, Vol. 188, Issue 12, Pages 1–11, 2021.

65. Ali M., Alam F., Ahmed I., AlQattan B., Yetisen A. K., Butt H., “3D printing of Fresnel lenses with wavelength selective tinted materials,” *Addit Manuf*, Vol. 47, Page 102281, 2021.

66. Chen H., Guo L., Zhu W., Li C., “Recent Advances in Multi-Material 3D Printing of Functional Ceramic Devices,” *Polymers*, Vol. 14, Issue 21, Page 4635, 2022.

67. Yan L., Zhu K., Zhang Y., Zhang C., Zheng X., “Effect of Absorbent Foam Filling on Mechanical Behaviors of 3D-Printed Honeycombs,” *Polymers*, Vol. 12, Issue 9, Page 2059, 2020.

68. Khan S. A., Rahman M. A., Khraisheh M., Hassan I. G., “Advances in 3D printed periodic lattice structures for energy research: Energy storage, transport and conversion applications,” *Mater Des*, Vol. 239, Page 112773, 2024.



ULUSLARARASI 3B YAZICI TEKNOLOJİLERİ
VE DİJİTAL ENDÜSTRİ DERGİSİ

INTERNATIONAL JOURNAL OF 3D PRINTING
TECHNOLOGIES AND DIGITAL INDUSTRY

ISSN:2602-3350 (Online)

URL: <https://dergipark.org.tr/ij3dptdi>

KOMPOZİT CYSZ KAPLAMANIN DEĞİŞEN YÜKLER ALTINDA AŞINMA DAVRANIŞININ İNCELENMESİ

INVESTIGATION OF WEAR BEHAVIOR OF
COMPOSITE CYSZ COATING UNDER DIFFERENT
LOADS

Yazarlar (Authors): Ali AVCI^{id}, Muhammet KARABAŞ^{id}

Bu makaleye şu şekilde atıfta bulunabilirsiniz (To cite to this article): Avcı A., Karabaş M., "Kompozit CYSZ Kaplamanın Değişen Yükler Altında Aşınma Davranışının İncelenmesi" *Int. J. of 3D Printing Tech. Dig. Ind.*, 8(3): 387-398, (2024).

DOI: 10.46519/ij3dptdi.1546843

Araştırma Makale/ Research Article

Erişim Linki: (To link to this article): <https://dergipark.org.tr/en/pub/ij3dptdi/archive>

KOMPOZİT CYSZ KAPLAMANIN DEĞİŞEN YÜKLER ALTINDA AŞINMA DAVRANIŞININ İNCELENMESİ

Ali AVCI^{a,*} , Muhammet KARABAŞ^b 

^aHakkari Üniversitesi, Mühendislik Fakültesi, Türkiye

^bKırklareli Üniversitesi, Havacılık ve Uzay Fakültesi, Türkiye

* Sorumlu Yazar: aliavci@hakkari.edu.tr

(Geliş/Received: 16.08.24; Düzeltme/Revised: 26.09.24; Kabul/Accepted: 01.10.24)

ÖZ

Bu çalışmada, CeO₂-Y₂O₃ stabilize ZrO₂ (CYSZ) seramik kaplamalar, Al₂O₃ ve TiO₂ eklenmiş olarak, plazma püskürtme yöntemi ile bağ katmanlı AISI304 paslanmak çelik altlıklar üzerine biriktirilmiştir. Al₂O₃ ve TiO₂ ilavesinin CYSZ kaplamanın aşınma davranışına etkisi araştırılmıştır. Aşınma testi öncesinde kaplamaların ortalama yüzey pürüzlülüğünün 0.2 µm'den az olmasını sağlamak amacıyla zımparalama ve parlatma işlemleri yapılmıştır. ASTM G99-04'e göre aşınma testi, pin-on-disk cihazında 30 mm s⁻¹ hızında gerçekleştirilmiştir. Test, minimum 8000 döngü ile kuru bir durumda yapılmıştır. Aşınma testinde 4N ve 8N değişken yükler ve 6 mm çaplı Al₂O₃ bilyalar kullanılmıştır. Kaplamaların yüzey özellikleri ve aşınma özellikleri, kaplama ve aşınma testleri yapıldıktan sonra taramalı elektron mikroskobu (SEM) ve enerji dağılımlı X-ışını spektroskopisi (EDS) kullanılarak analiz edilmiştir. Numunelerin aşınma oranı mekanik profilometri kullanılarak değerlendirildi. Malzemelerin mikro sertliğini değerlendirmek için mikro Vickers test ekipmanı kullanılmıştır. CYSZ içerisine ilave edilen bileşikler sertlik değerinin artmasına neden olmuştur. Al₂O₃ 'ün seryum-itriya stabilize zirkonyaya (CYSZ) dahil edilmesinin aşınma direncinde bir artışa yol açtığını, ancak TiO₂'nin dahil edilmesinin aşınma direncinde dikkate değer değişime neden olmadığı bulunmuştur.

Anahtar Kelimeler: CYSZ, Kompozit Kaplama, Aşınma, Yükün Etkisi.

INVESTIGATION OF WEAR BEHAVIOR OF COMPOSITE CYSZ COATING UNDER DIFFERENT LOADS

ABSTRACT

In this study, CeO₂-Y₂O₃ stabilized ZrO₂ (CYSZ) ceramic coatings, with Al₂O₃ and TiO₂ added, were deposited on bond layer coated AISI304 stainless steel substrates by plasma spraying method. The effect of Al₂O₃ and TiO₂ additions on the wear behavior of CYSZ coating was investigated. An investigation was conducted to examine the impact of incorporating aluminum oxides (Al₂O₃) and titanium dioxide into YSZ coating on its wear characteristics. Prior to conducting the wear test, the coatings underwent sanding and polishing procedures to verify that the average surface roughness was below 0.2 µm. A pin-on-disk device was subjected to wear testing in accordance with ASTM G99-04, with a rotational speed of 30 mms⁻¹. The testing was conducted under dry conditions, with a minimum of 8000 cycles. The wear test utilised varied loads of 4N and 8N, with 6 mm diameter Al₂O₃ balls. After conducting the coating and wear tests, the surface properties and wear characteristics of the coatings were examined using scanning electron microscopy and energy-dispersive X-ray spectroscopy. The wear rate of the samples was assessed using mechanical profilometry. The microhardness of the materials was assessed using Micro Vickers testing equipment. The compounds added into CYSZ caused an increase in the hardness value. The results demonstrated that the addition of Al₂O₃ to cerium-yttria stabilized zirconia (CYSZ) resulted in enhanced wear resistance, while the addition of TiO₂ significantly reduced wear resistance.

Keywords: CYSZ, Composite Coating, Wear, Applying Load.

1. GİRİŞ

Aşınma makine parçalarının kullanım ömürlerini kısıtlayan en önemli hasar mekanizmalarından birisidir. Aşınma hasarları yüzey mühendisliği teknolojileri kullanılarak azaltılabilir. Bu teknolojilerden en öne çıkan ise parçaları aşınmaya dayanıklı malzemeler ile kaplamaktır. Fiziksel ve kimyasal buhar biriktirme, lazer kaplama [1-2], ısı püskürtme [3] ve elektrokimyasal kaplama [4] işlemleri ile aşınmaya dayanıklı kaplamalar üretilebilir. WC-Co, Al₂O₃ gibi aşınmaya, korozyona dayanıklı metal-seramik kaplamalar termal püskürtme teknolojileri ile başarılı şekilde üretilmektedir[5], [6]. Bu kaplamalar endüstride yaygın olarak kullanılmaktadır. Termal püskürtme ile üretilen kaplamalar sıklıkla gaz türbin motorlarına uygulanır [7], [8]. Gaz türbin motorları hava [9] ve deniz [10], [11] taşıtlarında, enerji santrallerinde [12], yaygın olarak kullanılmaktadır. Atmosferden emilen hava yanma odasında yakıt ile karışır. Motordaki panellere bağlı olan shaft yüksek hızlarda döndürülerek aracın hareketi için gerekli olan itki kuvveti elde edilir. Yanma odasında sıcaklık 1200 °C'lere kadar yükselir[13]. Motorun bu bölümündeki parçalar genelde Ni esaslı süper alaşımlardan üretilir. Fakat Ni esaslı süper alaşımlar tek başına kullanılmaz. Ni esaslı süper alaşımlardan üretilmiş parçaların sürünme dayanımını arttırmak ve korozyondan korumak için termal bariyer kaplama (TBK) adı verilen seramikler ile kaplanır. TBK sistemi bağ katman, seramik üst katman ve termal olarak büyüyen oksit tabakası (TGO) olmak üzere üç farklı katmandan oluşur. TGO bağ katman ile seramik üst katman arasında servis şartlarında oluşan bir tabakadır. Bağ katmanda alüminyumun oksijen ile reaksiyonu sonucu oluşur. Kritik kalınlığa kadar (<10µm)[14] oksijen bariyeri görevi görür. Fakat kritik kalınlığı geçtikten sonra bağ katman-seramik üst katman arasında termal genleşme uyumsuzluğu nedeniyle gerilmeler meydana gelir [15]. Böylece seramik üst katman bağ katmandan ayrılır. Bağ katman genellikle Ni veya Co esaslı metalik malzemelerden üretilir. Temel görevi altlığı oksidasyondan korumak, termal genleşme uyumsuzluklarını tolere etmektir. Seramik üst katman ise yüksek sıcaklık faz kararlılığı, yüksek sinterlenme direnci, düşük termal iletkenlik, iyi kırılma tokluğu gibi özellikler gösteren seramiklerden üretilir. En yaygın termal bariyer kaplama malzemesi itriya ile

stabilize edilmiş zirkonyadır (YSZ)[16]. YSZ Ni esaslı süper alaşımlar ile uyumlu termal genleşme katsayısı, düşük termal iletkenlik gibi termo-fiziksel özellikleri ile en uygun malzeme olarak değerlendirilebilir [17]. Fakat 1200 °C ve üzeri sıcaklıklarda YSZ de tetragonal-monoklinik faz dönüşümleri olur [18]. Bu faz dönüşümleri sonucu bir hacim genleşmesi meydana gelir. Kaplamalar erken hasara uğrar. YSZ' ye CeO₂ eklentisi bazı termo fiziksel özellikleri geliştirerek yüksek sıcaklık altında tetragonal-monoklinik faz dönüşümlerini durdurur [19-20]. İlavesen, YSZ' nin termal genleşme katsayısını metalik altlık malzeme ile daha uyumlu hale getirir. Böylece TBK'ların servis ömrü arttırılır[21]. Ayrıca CeO₂ yağlayıcı özelliğe de sahiptir. YSZ ye CeO₂ katkısı TBK'ların aşınma davranışına da olumlu etki edebilir [22].

TBK'ların tek hasar mekanizması faz dönüşümleri değildir. Servis şartlarında erozyon, aşınma, sürtünme kaynaklı mekanik hasarlar da alabilir [23]. Atmosferden motor içerisine emilen hava ile birlikte uçan partiküllerde emilir. Bu partiküllerden bazıları yanma odasındaki TBK'lar üzerinde camsı eriyik olarak birikir. Korozyona sebep olur. Bazı partiküller ise TBK'lara yapışmaz. Kaplamaya çarparak kumlama etkisi gösterir. Bu yabancı partiküller zamanla kaplamayı aşındırır. Bu nedenle TBK'ların aşınma dirençlerinin geliştirilmesi önemlidir. YSZ'ye Al₂O₃, TiO₂ gibi katkıların eklenmesi sinterlenme direnci, yüksek sıcaklık faz kararlılığı, camsı eriyik ve sıcak korozyon dayanımını geliştirir. Plazma püskürtmeli YSZ ağırlıkça (ağ.) %10-20 [24] oranında porozite içerir. Poroziteler erozyon aşınma için olduğu gibi camsı eriyik ve sıcak korozyon dayanımı için dezavantajdır. Al₂O₃, TiO₂ gibi katkılar YSZ'nin porozite yüzdesini düşürür. Camsı eriyik ve sıcak korozyon tuzlarının kaplama içlerine doğru geçmesini engeller. Böylece plazma püskürtmeli YSZ'nin korozyon direnci geliştirilmiş olur. Benzer iyileştirme etkisi plazma püskürtmeli CYSZ için de gözlemlenmiştir [25].

Shin at al. [26] plazma püskürtme ile üretilmiş YSZ kaplamanın porozite miktarının artması ile erozyon davranışının zayıfladığını rapor etmiştir. Chen at al. [27] ise YSZ+Al₂O₃-40TiO₂ ve YSZ+ ağ. %92 Al₂O₃ -ağ. 40% TiO₂ kompozit kaplamaları plazma püskürtme ile

üretmiş ve aşınma testleri sonucunda kompozit kaplamaların aşınma dayanımlarının daha iyi olduğunu bildirmişlerdir. Bu gelişmeyi ise porozite oranının düşmesi ve YSZ ile Al_2O_3 - 40% TiO_2 reaksiyonu sonucu oluşan ara fazlara bağlamışlardır. Fakat YSZ'ye bu kadar yüksek oranlarda yapılan katkılar termal iletkenliği artırır ve termal şok-çevrim ömrünü azaltır. Bu nedenle bu katkıların oranı sınırlı olmalıdır [28]. Srikanth ve Bolleddu [29] grafen oksit ilaveli alümina-titanyum oksit kompozit kaplamaların mikro yapı ve aşınma dayanımı özelliklerini incelemişlerdir. Kompozit kaplama içerisindeki grafen oksit ilavesi arttıkça daha düşük sürtünme katsayısı ve aşınma dayanımının arttığını bildirmişlerdir. Mehar ve Sapate[30] Al_2O_3 -3 TiO_2 kompozit kaplamanın içerisine ağırlık %10, %20 ve %30 olmak üzere 3 farklı oranda YSZ ilave edilip aşınma dayanımı üzerine etkilerini incelemişlerdir. Yapılan çalışmada, YSZ oranı arttıkça sürtünme katsayısı düşmüştür. Tüm çalışma koşullarında Al_2O_3 -3 TiO_2 kaplamaya nazaran ağırlık %30 YSZ içeren kaplamada aşındırıcı aşınma oranında yaklaşık iki kat azalma olduğu bulunmuştur. Franco ve arkadaşları [31] YSZ termal bariyer kaplamanın aşınma dayanımını oda sıcaklığı, 500 °C ve 750 °C gibi değişen sıcaklıklarda test etmişlerdir. Yapılan çalışmada, aşınma mekanizması olarak 25 °C'de sünek deformasyon, 500 ve 750 °C'de kırılma deformasyonu ve 1000 °C'de yine sünek deformasyon oluştuğunu bulmuşlardır. Değerlendirilen tüm numunelerdeki bu davranış, termal gerilimlerle ve kristalografik fazları nedeniyle mekanik özelliklerindeki değişikliklerle doğrudan bağlantılı olduğu tespit edilmiştir. ZrO_2 - Y_2O_3 kaplamalarda 750 °C'ye kadar aşınma testlerinden önce ve sonra sertliklerinde önemli bir farklılık göstermemiştir. Ancak, 1000 °C'de yapılan testler sırasında tetragonal- ZrO_2 fazının amorf faz pahasına artması, kaplamaların sertliğinin ve dolayısıyla aşınma performanslarının artması teşvik edilmiştir. Bai ve arkadaşları [32] YSZ kaplamanın Si_3N_4 ve Al_2O_3 aşındırıcıya karşı 25 ile 800°C arasında değişen sıcaklıklardaki aşınma davranışını incelemişlerdir. Test sıcaklığı arttıkça aşınmış yüzeydeki monoklinik- ZrO_2 'nin tane boyutu ve molar fraksiyonu tüm durumlarda azaldığı görülmüştür. Ana aşınma özellikleri, tüm sürtünmeli kayma testleri için yüzeye yakın kırılma ve parçalanmayı içeriyordu. İki tip tribo çifti arasındaki aşınma mekanizmalarındaki

fark, tribo kaynaklı etkileşimlerden kaynaklandığı bulunmuştur. Al_2O_3 aşındırıcı kayma ile karşılaştırıldığında, mekanik olarak karıştırılmış katman içerisinde amorf bir yapının önemli ölçüde oluşmasına neden olmuştur. YSZ kaplamanın Si_3N_4 aşındırıcı karşısında daha iyi bir aşınma direnci sergilediği gözlemlenmiştir.

Bu çalışmada alternatif bir seramik kaplama malzemesi olan serya-itriya ile stabilize edilmiş zirkonya kaplamalar Al_2O_3 - TiO_2 gibi ilave edilen kompozit karışımlar plazma püskürtme ile üretilmiştir. Üretilen kaplamaların farklı yükler altında aşınma davranışları araştırılmıştır.

2. MALZEME VE YÖNTEM

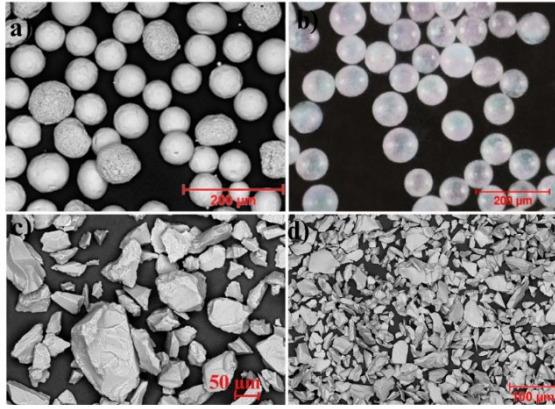
2.1. Malzemeler

Çalışmada, altlık olarak lazer kesim yöntemi ile 25.4 mm çapında kesilen AISI 304 östenitik paslanmaz çelikler kullanılmıştır. Bağlama katmanının mekanik yapışmasını geliştirmek için altlık kuponlarının yüzeyleri 200 grit alümina adı verilen ince bir aşındırıcı malzeme ile kumlanmıştır. Kumlama işlemi 30 cm mesafeden, 1 dk boyunca numunelerin tek yüzeyine uygulanmıştır. Zımparalama işleminden sonra paslanmaz çeliğin yüzey pürüzlülüğü Veeco WYKO NT1100 mekanik profilometre kullanılarak ölçülmüş olup, kumlama işleminin ardından pürüzsüzlükte dikkate değer bir artış sağlanmıştır. Altlık malzemesi, yüzey pürüzlülüğü açısından 358.68 nm'lik bir Ra değeri sergilerken, kum püskürtme sonrasında altlık malzemesinin ortalama yüzey pürüzlülüğü 2.7 µm civarında ölçülmüştür. Bağ tabakanın üretiminde Sulzer Metco AMDRY 997 (Ni 23Co 20Cr 8.5Al 4Ta 0.6Y) ticari tozu, seramik üst katmanda ise Sulzer Metco'nun ticari olarak sunduğu CYSZ ($205 NS, ZrO_2 24CeO_2 2.5Y_2O_3$), yine Sulzer Metco firmasından 105 NS ticari Al_2O_3 (2 ağırlık.% SiO_2 -98 ağırlık.% Al_2O_3) ve TiO_2 tozları kullanılmıştır. Şekil 1 tozların SEM görüntülerini gösterilmiştir. Üretilen kompozit kaplamaların karışım oranları Çizelge 1'de verilmiştir. Bağ katman üretimi yüksek hızlı oksijen-yakıt (HVOF) yöntemi ile kaplama işleminde Metco'nun DJ-2600 tabancası kullanılarak, Çizelge 2'de belirtilen parametreler göz önünde tutularak yapılmıştır. Kaplama işleminde kullanılan tabanca, 3 eksenli CNC makinesinin merkezi eksenini boyunca konumlandırılmıştır. Altlık malzemeler

ise 16 adet numune tutucuya sahip bir döner tablaya bağlanmıştır. Böylece tabancanın hareketi ve numunelerin hızının hassas kontrolü, gerekli kalınlıklarda kaplamaların elde edilmesine olanak sağlamaktadır.

Çizelge 1. Kompozit kaplamalarda kullanılan tozların ağırlıkça karışım miktarları

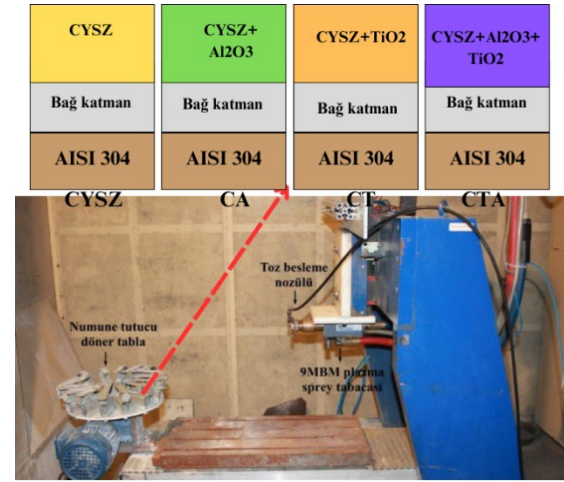
| Numune Adı | Hammadde tozları | | |
|------------|------------------|--------------------------------|------------------|
| | CYSZ | Al ₂ O ₃ | TiO ₂ |
| CYSZ | 100 | - | - |
| CA | 83 | 17 | |
| CT | 97 | | 3 |
| CTA | 80 | 17 | 3 |



Şekil 1. Biriktirilen tozların mikro yapısı a) Bağ katman, b) YSZ, c) YYSZ, d) Al₂O₃ tozu

Yüksek hızlı alev jeti hava-propan gazı karışımının oksijenle yanmasından elde edildi. HVOF yöntemi ile 85 ± 15 µm'lik gerekli bağ tabakası kalınlığını elde etmek için metal

yüzeyde 12 pasoda biriktirilmiştir. Seramik üst katmanın kaplanmasında kullanılan birincil ve ikincil gazlar ve üretim parametreleri Çizelge 3'te verilmektedir. Kaplama öncesinde YSZ, alümina ve titanyum dioksit kompozit tozları bir karıştırıcıda (turbula) alkol içerisinde 4 saat karıştırıldı. Sonrasında etüvde kurutulan tozlar, Sulzer Metco 9 MB plazma tabancası kullanılarak bir plazma sprej katmanı üzerinde başarılı bir şekilde kaplanmıştır. Kaplama işleminde kullanılan tabanca, 3 eksenli CNC makinesinin merkezi eksenli boyunca konumlandırılmış olup, hareketli tabanca, numunelerin döner tabla üzerine eşit şekilde kaplanmasını kolaylaştırmıştır. Şekil 2'te kaplamaların üretimini gösteren resim verilmektedir.



Şekil 2. Kaplamaların üretim adımları

Çizelge 2. HVOF işlem parametreleri

| Malzemeler | Basınç (Bar) | | | Akış oranı (SCFH) | | | İşlem parametreleri | | |
|------------|--------------|--------|------|-------------------|--------|------|---------------------|-------------------|-----------------|
| | Oksijen | Propan | Hava | Oksijen | Propan | Hava | Sprej mesafesi (mm) | Toz besleme (g/s) | Sprej açısı (°) |
| Amdry 997 | 10.3 | 6.2 | 7.2 | 24 | 40 | 50 | 250 | 50 | 90 |

Çizelge 3. APS kaplama parametreleri

| Parametreler | | | | | | | |
|--------------|------------------------|------------------------------------|------------------------|---------------------|---------------------|--------------------|------------|
| Akım (A) | Birincil Gaz, Ar(scfh) | İkincil Gaz, H ₂ (scfh) | Taşıyıcı Gaz, Ar(scfh) | Sprej Mesafesi (mm) | Tabanca Hızı (mm/s) | Dönme Hızı(Hz) rpm | Voltaj (V) |
| 500 | 90 | 15 | 13.5 | 75 | 200 | 40 | 60 |

Mikro yapısal İncelemeler

Üretilen kaplamaların yüzeyi ve kesitleri elektron mikroskobu ile incelenmiştir. Bu amaçla kaplamalara öncelikle metalografik taşlama ve parlatma işlemleri uygulanmıştır. Kesitlerin incelenmesi için kaplamalar elmas kesici ile kesilip sonra parlatma işlemi uygulandı. Numunelerin mikro yapı testleri farklı boyutlarda opsiyonel EDS Phenom XL SEM cihazı ile gerçekleştirilmiştir. Aşınmış parçalar SEM ile de incelenmiştir. SEM çalışmalarında aşınma tipinin özelliklerini anlamak için farklı dedektörler kullanılmıştır. EDS analizleri aşınma izleri için haritalama yöntemi kullanılarak gerçekleştirilmiştir.

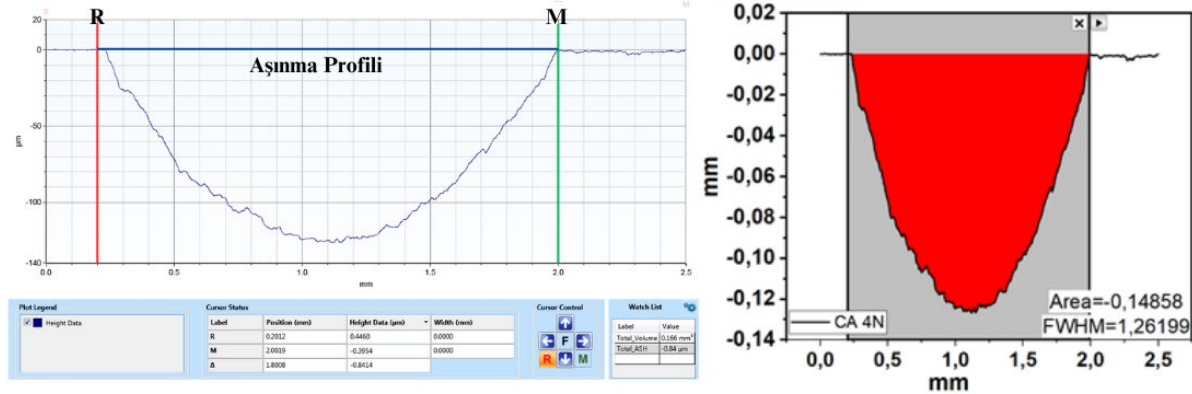
2.2. Aşınma ve Sertlik

Yüzeyin durumu, kaplamaların tribolojik özelliklerine etki eden başlıca faktördür. Numunelerin kaplama sonrası yüzey pürüzlülüğü değerleri 1.5 ila 2.4 µm arasında değiştiği ölçülmüştür. Aşınma testi öncesi kaplamaların ortalama yüzey pürüzlülük değerleri Ra 0.2'den küçük eşit olması için zımparalama ve parlatma işlemleri uygulandı. Yüzey pürüzlülüğü, 5 µm yarıçap kullanılarak yüzey üzerinde en az beş farklı yerden ölçümler alınarak hesaplanmıştır. Daha sonra numune yüzeyleri, yağların veya istenmeyen kalıntıların giderilmesi için aseton kullanılarak iyice temizlenip kurutulmuştur. Aşınma testi kaplamalara, ASTM 99-04'e göre 6000 mm alümina aşındırıcı bilya ile 8000 çevrim uygulanmıştır. Aşınma testi kuru bir ortamda 30 mm s⁻¹ hızında çalışan bir pin-on-disk cihazı (Tribo Tester, Fransa) kullanılarak gerçekleştirilmiştir. Şekil 3, mekanik profilometreden alınan aşınma izinin 2 boyutlu profilini göstermektedir. Aşınan hacmin

bulunabilmesi için ilk olarak profilometreden elde edilen aşınma grafiği OriginLab Pro yazılımı yardımıyla tekrardan çizilerek eğrinin altında kalan alan hesaplanmıştır. Sonrasında elde edilen alan aşınan çevre ile çarpılarak hacim değerine ulaşılmıştır. Aşağıdaki Denklem (1) yardımıyla aşınma miktarı bulunmuştur.

$$\text{Hacimsel aşınma miktarı} = \frac{\text{Hacim (mm}^3\text{)}}{\text{Aşınan yol (m) x uygulanan yük (N)}} = \quad (1)$$

APS teknolojisinde üretilen kaplamalar, püskürtme hızı arttıkça giderek daha sert hale gelmektedir. Kaplamadaki oksitlerin varlığı çoğu zaman sertliğini artırırken yapışma mukavemetini azaltmaktadır. Kaplama katmanlarının sertliği gözeneklilik, katmanın heterojen yapısı, uygulanan gerilim değerleri gibi faktörlere bağlı olarak dalgalanmaktadır. Sertlik ölçümleri, Bulut Makina'nın Türkiye'de ürettiği HVS1000 mikro Vickers cihazı kullanılarak kaplamaların yüzeyinden elde edilmiştir. 300 gramlık bir kütle için yükleme süresi 15 saniye olarak belirlenmiştir. Sonuç, numunenin yüzeyinde 12 farklı noktada rastgele test edilen 10 sertlik değerinin aritmetik ortalamasının hesaplanmasıyla elde edilmiştir. Bu hesaplamada en yüksek ve en küçük ölçüm değerleri dikkate alınmamıştır. Ölçüm, kenarlarda gerilim oluşmasına ve kayan uç numuneye temas ettiğinde uygulanan yükün eşit olmayan bir şekilde dağılmasına yol açabilecek hataları önlemek için kenarlardan asgari 3 mm uzak bir mesafede gerçekleştirilmiştir.

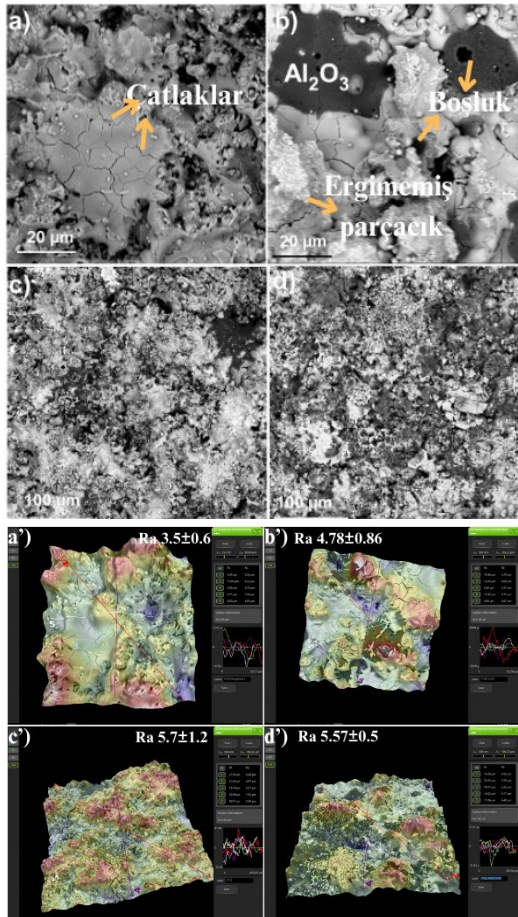


Şekil 3. Profilometre grafikleri

3. DENEYSSEL BULGULAR

3.1. Mikro yapı İncelemeleri

Şekil 4'de kaplama sonrasında çekilen SEM mikro yapı resimleri gösterilmektedir. Resimler incelendiğinde APS yönteminin karakteristik özellikleri olan yarı ergimiş veya ergimemiş parçacıklar, boşluklar ve çatlaklar görülmektedir. Şekil 4a'da özellikle çamur çatlakları çok fazla olduğu görülmektedir. Alümina ilave edilen şekil 4b numunesinde siyah bölge sert ve yoğun olan Al_2O_3 'tür. Şekil 4c ağ. %3 TiO_2 ilave edilmiş CYSZ'nin yüzey resmine ait olup boşluklu bir mikro yapı görülmektedir. Şekil 4 d'de tüm tozların karışımı olan CTA kompozit numunesinin yüzey SEM resmi verilmiştir.



Şekil. 4 Yüzey elektron mikroskobu görüntüleri; a)CYSZ, b) CA, c)CT, d)CTA, a')CYSZ yüzey pürüzlülük mikro resmi, b')CA yüzey pürüzlülük mikro resmi, c')CT yüzey pürüzlülük mikro resmi, d') CTA yüzey pürüzlülük mikro resmi

Genel olarak kaplamaların yüzey SEM resimler benzerlik göstermektedir. Şekil 4a'-d' ise aynı kaplamaların ortalama yüzey pürüzlülüğü değerleri ve yüzey pürüzlülüğü resimleri verilmektedir. CYSZ'nin yüzey pürüzlülüğü

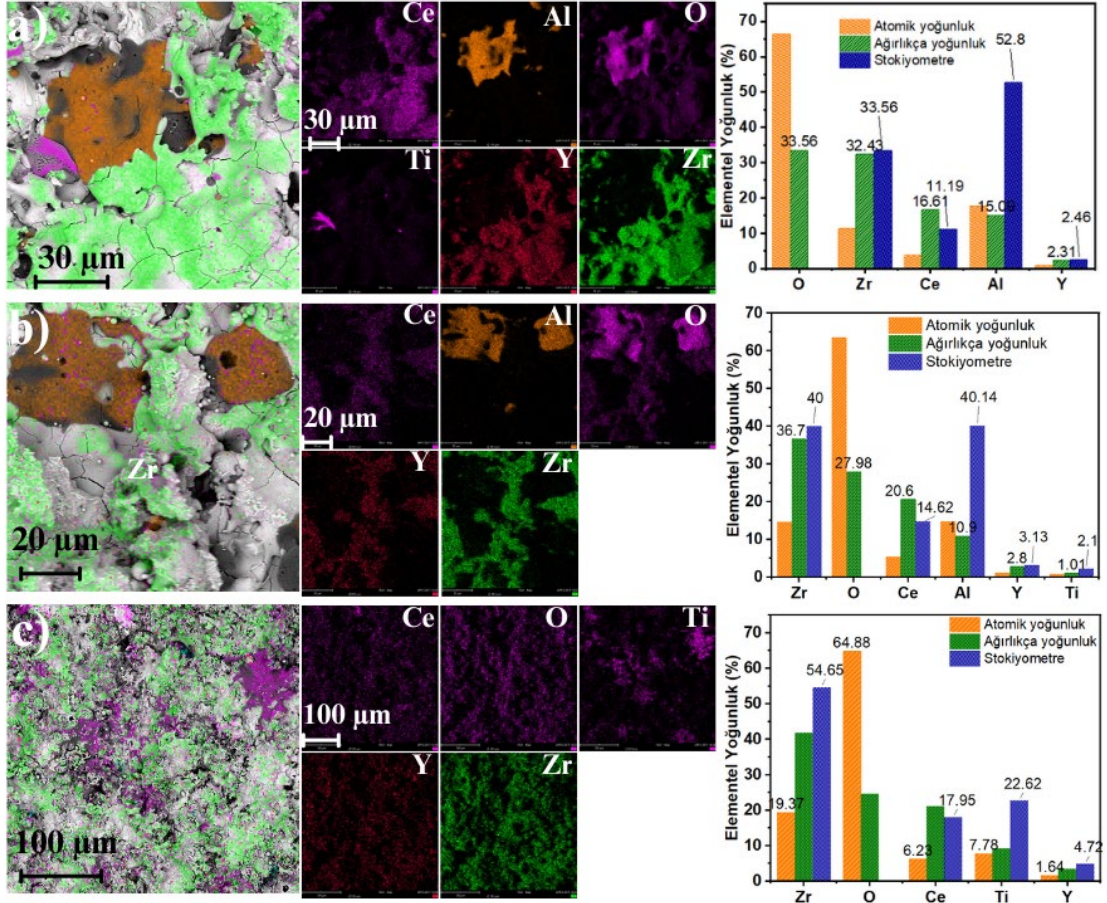
değeri $3.5 \mu m$ iken kompozit kaplamaların yüzey pürüzlülükleri artmıştır. Al_2O_3 ilavesi ile CYSZ'nin yüzey pürüzlülüğü %35 artarken TiO_2 ve $Al_2O_3 - TiO_2$ ilavesi ise yaklaşık %60 oranında artışa neden olmuştur.

Şekil 5'de APS yöntemi ile üretilen kaplamaların yüzeylerinden alınan EDS haritalama sonuçları verilmiştir. EDS haritalama sonuçlarında CYSZ içerisine ilave edilen tozların dağılımları ve varlıkları kontrol edildi. Şekil 5a'da CTA kompozit numunesine ait resimler yakından incelendiğinde; turuncu ile gösterilen bölgelerin alümina, mor bölgenin ise TiO_2 olduğu anlaşılmaktadır. Şekilde Alümina tozunun yaklaşık $30 \mu m$ genişliğinde olduğu görülmektedir. Kaplamayı oluşturan diğer elementlerin yapıdaki ağırlıkça yüzde yoğunlukları; oksijen 33.56, zirkonyum 32.4, seryum 16.6, alüminyum 15.09 ve itriyum 2.31 civarında olduğu bulunmuştur. İncelenen bölgede oksijen ile en fazla bağ yapan elementin %52.8 oranla alüminyum olduğu anlaşılmaktadır. Şekil 5b'de CYSZ içerisine %17 oranında alümina ilave edilen kompozit kaplamaların yüzey EDS sonuçları görülmektedir. Benzer şekilde oksijen ile en yüksek oranda bağ yapan elementin alüminyum (%40.4) olduğu anlaşılmaktadır. Şekil 5c'de CYSZ içerisine ağ. %3 TiO_2 ilave edilmiş kompozit kaplamaların EDS haritalama sonuçları incelendiğinde; TiO_2 'nin dağılımı daha net ortaya çıkmaktadır. Genel olarak kompozit kaplamalarda tüm elementlerin varlıkları ispatlanmış olup dağılımlarının homojen olduğu bulunmuştur.

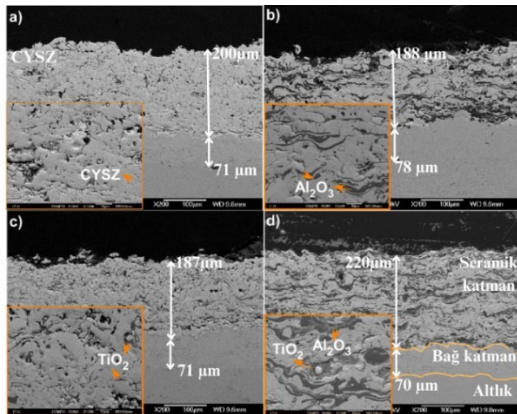
Şekil 6'te üretilen kaplamaların kesit SEM resimleri verilmiştir. Şekil 6a'da CYSZ kaplamasının kesit resminde seramik üst katmanın yaklaşık $200 \mu m$ bağ katmanının ise $70 \mu m$ civarında olduğu görülmektedir. Ayrıca CYSZ kaplamasının detay resminde yatay ve dikey çatlaklar ve boşluklar görülmektedir. Şekil 6b'de alümina ilave edilmiş kaplamasının kesit SEM resminde siyah bölgeler alümina olduğu anlaşılmaktadır. Alüminanın CYSZ ile homojen şekilde dağılım gösterdiği söylenebilir. Detay SEM resminde kaplamaların yatay şekilde uzandığı görülmektedir. Şekilden kompozit kaplamaların kalınlığının yaklaşık $188 \mu m$ bağ katmanının kalınlığının ise $78 \mu m$ olduğu ölçülmüştür. Şekil 6c'de az miktarda (ağ. %3) CYSZ içerisine ilave edilen TiO_2 'nin küçük gri bölgeler oluşturduğu ve

topaklanmadan dağılım gösterdiği görülmektedir. Seramik üst kaplamanın tabaka kalınlığı 187 μm iken bağ katmanın kalınlığı yaklaşık 70 μm olarak ölçülmüştür. Şekil 6d’de kaplamayı oluşturan tabakalar detaylı şekilde verilmiştir. Şekilde bağ katman kalınlığı 70 μm , kompozit seramik katman kalınlığı ise 220 μm olarak bulunmuştur. Şekil 6d incelendiğinde Al_2O_3 ve TiO_2 ’nin CYSZ içerisinde dağılarak

başarılı bir şekilde biriktiği söylenebilir. Tüm kesit SEM resimlerinde bağ katman üzerinde termal olarak büyüyen herhangi bir oksit tabakası görülmemiştir. Önceki çalışmamızda [33] elde ettiğimiz APS kaplamaların SEM resimlerine benzer şekilde, bu çalışmamızda da lamelar mikro yapı ve poroziteler içeren, yarı ergimiş yapılar elde edilmiştir.

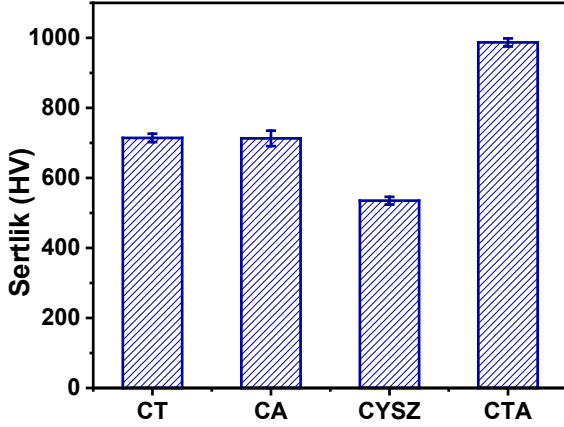


Şekil 5. EDS haritalama sonuçları; a)CTA kaplama b) CA kaplama, c) CT kaplama



Şekil 6. Kesit SEM resimleri; a) CYSZ kaplama, b)CA kaplama, c) CT kaplama, d)CTA kaplama

Şekil 7’de kaplamaların sertlik değerleri verilmektedir. CYSZ kaplamanın sertlik değeri 535 ± 11 HV iken alümina ve TiO_2 ilavesi sertlik değerinde yaklaşık %33’lük bir artışa neden olmuştur. Yapılan çalışmada [34], APS ile kaplanan alüminanın tek başına sertlik değeri 1491 HV bulunmuştur. Alüminanın sert ve yoğun yapısından dolayı CYSZ içerisine ilavesi sertlik değerini artırması beklenen bir durumdur. CTA numunesinin sertlik değeri ise 987 ± 11.5 HV olarak ölçülmüştür.

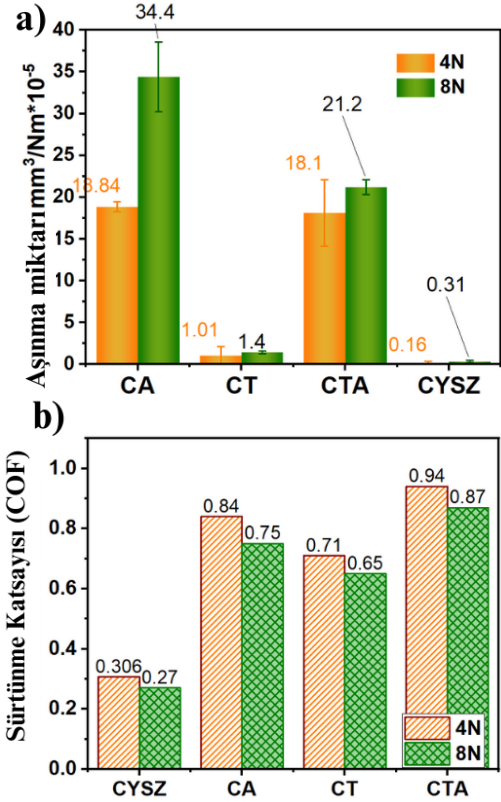


Şekil 7. Kaplamaların Vickers sertlik sonuçları

Şekil 8 a'da 4 N ve 8N yük uygulanan numunelerin profilometreden alınan aşınma oranları sonuçları verilmektedir. Her iki yük içinde en az aşınan numune CYSZ olmuştur. CYSZ 4 N yük altında yaklaşık $0.16 \text{ mm}^3 \text{ Nm}10^{-5}$ aşınırken yük 8N olduğunda $0.31 \text{ mm}^3 \text{ Nm}10^{-5}$ 'lik bir aşınma sonucu vermiştir. CYSZ'nin sertlik değerinin düşük olmasına rağmen aşınma miktarının da düşük olması CeO_2 yağlayıcı etkisi ile açıklanabilir. CeO_2 yapısı gereği yağlayıcı etkiye sahip olması aşınma sırasında yüzeyin kaygan davranmasına neden olmuştur. Nitekim, Şekil 8b'deki sürtünme katsayısı sonuçları bu durumu desteklemektedir. Tüm numuneler için aynı yük altında sürtünme katsayısı ile aşınma katsayısı arasında ters bir ilişki bulunmaktadır. Aynı numune için 4N yük altında sürtünme katsayısı yüksek 8N altındaki numunelerin sürtünme katsayısına kıyasla daha yüksek olduğu bulunmuştur. Sürtünme katsayısından alınan sonuçların aksine, 4N yük altındaki numunelerin aşınma miktarı 8N yük altındaki numunelere kıyasla daha az aşındığı hesaplanmıştır.

CYSZ numunede uygulanan yük arttığında sürtünme katsayısının düşmesi de yağlanmış bir ortam oluştuğunu desteklemektedir. CYSZ içerisine ağırlık %3 TiO_2 ilave edildiğinde aşınma miktarının 4N yük altında $1.01 \text{ mm}^3 \text{ Nm}10^{-5}$ olduğu, yük arttığında aşınma miktarının artarak $1.4 \text{ mm}^3 \text{ Nm}10^{-5}$ hesaplandığı görülmektedir. Alümina ilavesi sonrasında elde edilen CA ve CTA kaplamalarının aşınma miktarlarında önemli bir artış gözlemlenmiştir. CA kaplamasının aşınma miktarı 4N yük altında $18.8 \text{ mm}^3 \text{ Nm}10^{-5}$ iken yük 8N arttığında yaklaşık %90 oranında artarak $34.4 \text{ mm}^3 \text{ Nm}10^{-5}$ olarak hesaplanmıştır. Sert alümina ilavesinin hem aşınma miktarını hem de sürtünme katsayısını artırması CYSZ'ye göre aşınma mekanizmasının değiştiğini

göstermektedir. 4N yük altında CA numunesinin sürtünme katsayısı 0.84 iken yük arttığında 0.75 olarak bulunmuştur. CA içerisine ağırlık %3 TiO_2 ilave edilmiş numunede ise aşınma miktarı 4 N yük altında $18.1 \text{ mm}^3 \text{ Nm}10^{-5}$ iken 8N yük altında bu değer $21.2 \text{ mm}^3 \text{ Nm}10^{-5}$ olarak bulunmuştur. CA ve CTA numunelerinde 4N yük altında aşınma miktarları birbirine çok yakın çıkmışken 8N yük altında TiO_2 ilaveli numunenin aşınma miktarı daha düşük çıkmıştır. Tek başına CYSZ içerisine TiO_2 ilavesi aşınma miktarını düşürmezken alümina ile birlikte kaplandığında 8N yük altında aşınma miktarını yaklaşık %40 iyileştirdiği söylenebilir. Her ne kadar CYSZ'nin aşınma miktarı düşük olsa da Al_2O_3 ve TiO_2 ilavesi sertlik değerini önemli oranda artırmıştır.

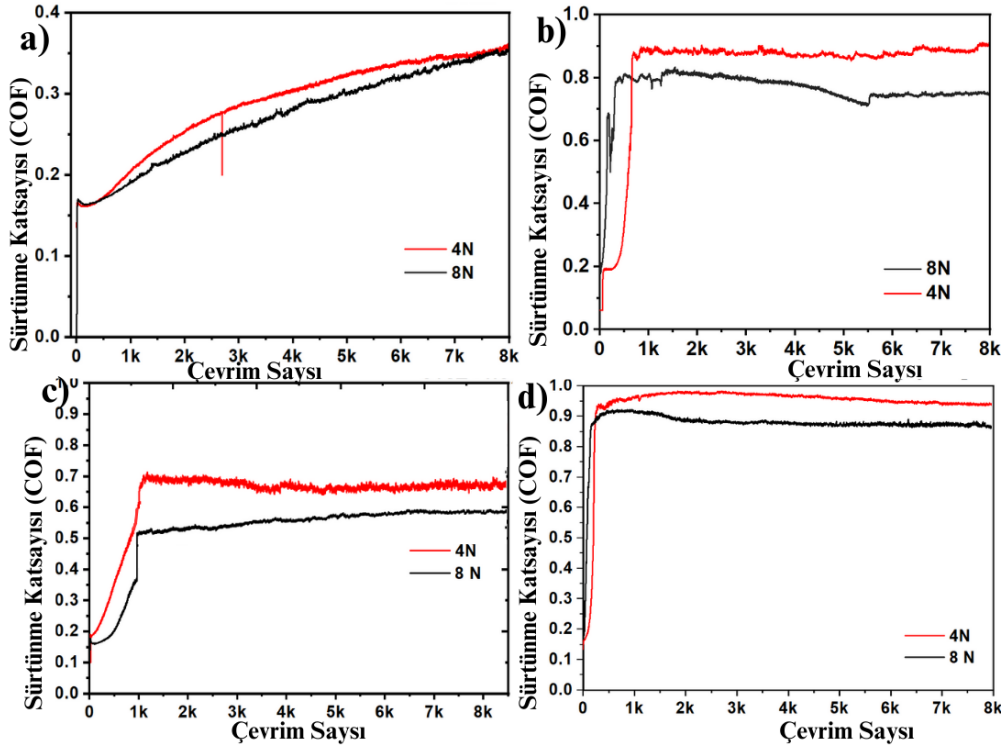


Şekil 8 Kaplamaların farklı yükler altındaki; a) Aşınma miktarı, b) Sürtünme katsayısı

Şekil 9'da kaplamaların farklı yükler altında 8000 çevrim sonrasında elde edilen sürtünme katsayısı grafikleri görülmektedir. CYSZ'nin sürtünme katsayısı her iki yük içinde yaklaşık 200 çevrimden sonra bir azalma gösterip sonrasında tekrar artmaya devam etmiştir (Şekil 9a). Sürtünme katsayısı yaklaşık 1000 çevrimden sonra yavaş yavaş kararlı hale geldi ve önemli bir değişim gözlemlenmedi (Şekil 9

b-c). Bu kararlı aşınma aşaması olarak da bilinen ikinci sürtünme ve aşınma aşaması olarak bilinmektedir [35]. Yaklaşık 500-800 çevrim arasında 4 N yük uygulanan numune ile 8 N yük uygulanan numunenin grafikleri arasındaki mesafe açılmıştır. Her iki yük için CYSZ'nin sürtünme katsayısı grafiği 8000 çevrimde üst üste gelmiştir. Al_2O_3 ilave edilmiş CYSZ numunenin sürtünme katsayısı grafiklerine bakıldığında (Şekil 9b), 4N yük altında yaklaşık 1000 çevrimden sonra kararlı hale gelmiştir. 8N yük altındaki numunede 5520. çevrim de belirgin bir iniş ve ani bir çıkış görülmektedir. Bunun muhtemel nedeni kopan bir parçacığın hareketinden olabilir. CT numunesi her iki farklı yük için 1000 çevrim sonrası kararlı hale gelmiştir. CTA numunesi de yaklaşık 500 çevrim sonrasında uygulanan her

iki yük için kararlı hale gelmiştir. Uygulanan yükün artmasıyla yüksek temas basıncı ve sürtünme ısıyla tribo-oksit oluşumu gözlenir ve bu durum sürtünme katsayısının azalmasına ve aşınma kaybının artmasına neden olmuştur [36]. Artan yük ile birlikte yüzeyde oluşan tribo-oksit tabakası deforme olursa kompozit kaplamanın yük taşıma oranı düşerek abrasif aşınmaya bağlı yüzey hasarları meydana gelmiştir. Hem ilave edilen sert TiO_2 , Al_2O_3 partikülleri, hem de aşınarak kopan partiküller aşınma oranının ve sürtünme katsayısının değişmesine neden olmuştur. Diğer bir ifadeyle sert kalıntılar aşındırıcı parçacıklar gibi davranarak sürtünme katsayısının artmasına neden olmuştur [37].



Şekil 9. 4N ve 8N yük altında oluşan sürtünme katsayısı grafikleri a) CYSZ kaplama, b) CA kaplama, c) CT kaplama, d) CTA kaplama

Benzer bir çalışmada Ji ve arkadaşları [38] aşınan parçacıklarının tekrardan sıvanarak sürtünme katsayısını artırdığını bildirmişlerdir. Şekil 10'da aşınma sonrası 4N ve 8N yük altında oluşan aşınma izleri ve izlerin EDS sonuçları görülmektedir. Şekil 10 a-d) 4N yük altında CYSZ, CA ve CT, CTA numunelerine ait aşınma SEM resimleri ve hemen üstünde EDS sonuçları detay resmi olarak verilmiştir. Her bir SEM resimlerinde plastik deformasyon ve yorulma çatlakları belirgin bir şekilde

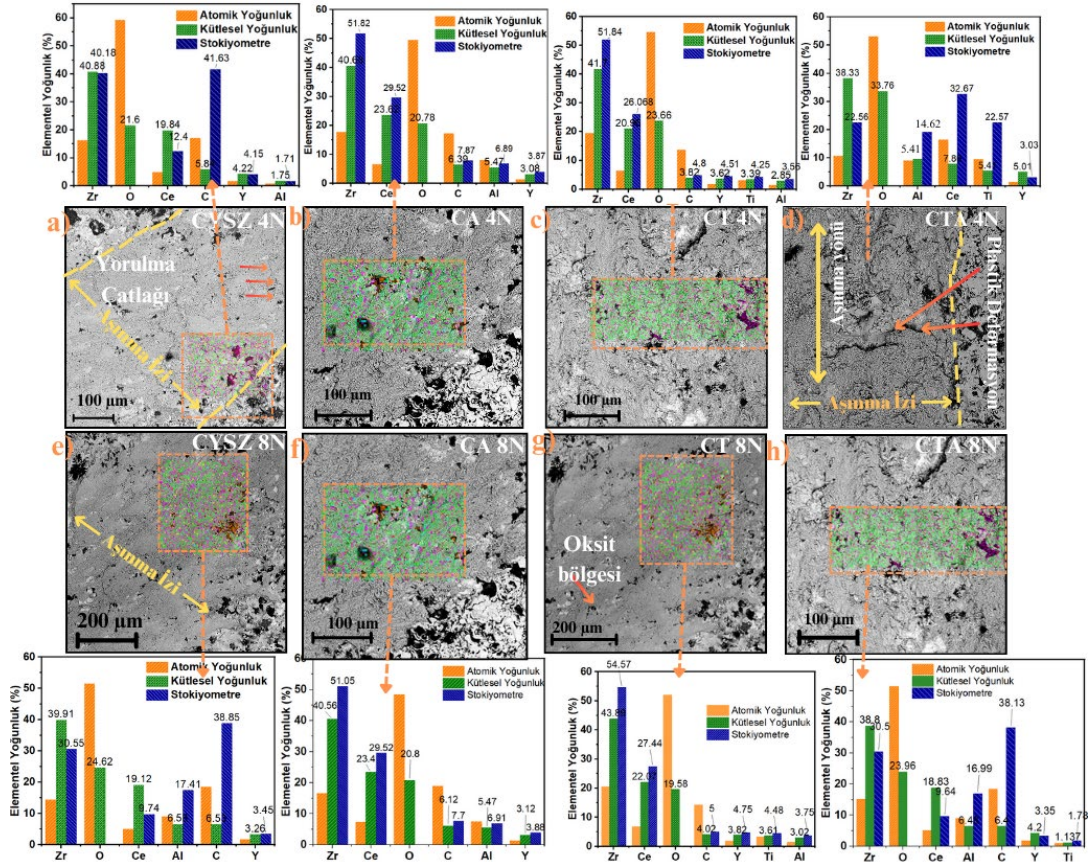
görülmüştür. Ayrıca, 4N yük altındaki her bir kaplamanın EDS sonuçlarında Al elementine rastlanmıştır. Şekil 11 d-h) 8N yük altında CYSZ, CA, CT ve CTA kaplamalarına ait aşınma SEM resimleri ve hemen altında EDS sonuçları verilmiştir. Uygulanan yük 4N'dan 8N'a çıkarıldığında alümina oranının arttığı tespit edilmiştir. Bu durum aşındırıcıdan kaplama yüzeyine alümina geçişi olduğunu göstermektedir. Çünkü adeziv aşınma, malzemelerin birbirine temas ettiği ve

birbirleriyle sürtündükleri durumlarda ortaya çıkan bir aşınma şeklidir. Bu sürtünme sonucunda, malzemelerin yüzeylerindeki atomlar arasında çeşitli etkileşimler meydana gelir ve malzemelerin yüzeylerinde hasarlar oluşabilir. Özellikle 4N yük altında adezif aşınmadan söz etmek daha doğru olacaktır. İki malzeme arasındaki yapışma ve sürtünme kuvvetleri ne kadar yüksekse, aşınma da o kadar belirgin olmuştur. Yük 8N'a artırıldığında adezif aşınmanın yanı sıra abrezif aşınma da meydana gelmiştir. Zira SEM resimlerinde bazı kopan parçacıkların varlığından söz etmek mümkündür.

4. SONUÇ

CYSZ, CYSZ/ Al₂O₃, CYSZ/ TiO₂ ve CYSZ/Al₂O₃/TiO₂ kaplamalar paslanmaz çelik üzerine atmosferik plazma spreyleme yöntemi ile başarıyla kaplanmıştır. Kaplamanın mikro yapısal ve mekanik özellikleri incelenmiştir. Yapılan EDS analizlerinde kaplamaları oluşturan tozların başarılı bir şekilde dağılım gösterdiğini ispatlamıştır. Yüzey ve kesit SEM

resimleri de kaplamanın bağ katman ile tutunmasının sıkı olduğunu herhangi bir oksitlenme olmadığını göstermiştir. Üretilen 4 farklı kompozit kaplamanın sertlik değerlerini CYSZ içeresine ilave edilen TiO₂ ve Al₂O₃ sert parçacıkların artırdığı gözlemlenmiştir. En yüksek sertlik değeri CTA adlı numune de elde edilmiştir. Kompozit kaplamalar iki farklı yük altında kuru aşınma deneyine tabii tutulmuştur. 4N yük altında sürtünme katsayısı tüm numuneler için yüksek çıkarken yük 8N' artırıldığında sürtünme katsayısı düşmüştür. 4N ve 8N yük için aşınma kaybı incelendiğinde, Al₂O₃ ihtiva eden numunelerin daha fazla aşındığı görülmüştür. Ayrıca, yük arttığında aşınma miktarının arttığı bulunmuştur. Yükün 8N'a çıkarılmasıyla tribo-oksitlerin parçalanarak ara yüzeye aktarılması adezif aşınmanın yanı sıra abrazif aşınmaya sebep olmuş ve kaplamanın aşınma miktarı artarken, sürtünme katsayısının azaldığı tespit edilmiştir.



Şekil 10. Aşınma izleri ve EDS sonuçları; a) CYSZ 4N yük altında aşınma izi ve EDS sonuçları, b) CA 4N yük altında aşınma izi ve EDS sonuçları, c) CT 4N yük altında aşınma izi ve EDS sonuçları, d) CTA 4N yük altında aşınma izi ve EDS sonuçları, e) CYSZ 8N yük altında aşınma izi ve EDS sonuçları, f) CA 8N yük altında aşınma izi ve EDS sonuçları, g) CT 8N yük altında aşınma izi ve EDS sonuçları, h) CTA 8N yük altında aşınma izi ve EDS sonuçları

KAYNAKLAR

1. Zhicheng, L., Jiangzheng, S., Chuang, H., Fan, W., Dejun, K., “Effect of laser power on microstructure and tribological performance of WC–10Co4Cr coating”, *International Journal Applied Ceramic Technology*, Vol. 20, Issue 5, Pages 2847–2859, 2023.
2. Zhu, L., Pengsheng X., Qing, L., Guiru, M., Yuan, R., Zhichao, Y., Peihua, X., Zhe, L., “Recent research and development status of laser cladding: A review” *Optics & Laser Technology*, Vol. 138, Pages 106915, 2021.
3. Yuan, J., Zhan, Q., Huang, J., Ding, S., Li, H., “Decarburization mechanisms of WC-Co during thermal spraying: Insights from controlled carbon loss and microstructure characterization”, *Materials Chemical Physis*, Vol. 142, Issue 1, Pages 165–171, 2013.
4. Qi, W., Ding, D., Luo, W., Jin, W., Kou, Q., Ge, C., Xiao, S., “Production of al–mn/wc composite coatings with electrodeposition in AlCl₃–NaCl–KCl–MnCl₂ molten salts”, *Coatings*, Vol. 13, Issue 7, Pages 1246, 2023.
5. Pulsford, J., Venturi, F., Kamnis, S., and Hussain, T., “Sliding wear behaviour of WC-Co reinforced NiCrFeSiB HVOAF thermal spray coatings against WC-Co and Al₂O₃ counterbodies”, *Surfaces and Coatings Technology*, Vol. 386, Pages 125468, 2020.
6. Bang, J., Lee, E., “Enhancing wear resistance of A390 aluminum alloy: A comprehensive evaluation of thermal sprayed WC, CrC, and Al₂O₃ coatings”, *Coatings*, Vol. 14, Issue 7, Pages 853, 2024.
7. Gaur, U.P., Kamari, E., “Applications of thermal spray coatings: A review”, *Journal of Thermal Spray and Engineering*, Vol. 4, Pages 106–114, 2024.
8. Hardwicke, C. U., Lau, Y. C., “Advances in thermal spray coatings for gas turbines and energy generation: A review” *Journal of Thermal Spray Technology*, Vol. 22, Pages 564-576, 2013.
9. Guo, L., H., Wenting, C., Wenbo, Zhaolu, Jian, X., Yiqian, H., Yang Wu, G., Lihua, G., Dongqing, L., Zhao, Z., Liangliang, W., Yuyi, G., Tiehao, Z. Qianhui, Q., Hongbo G., “Progress on high-temperature protective coatings for aero-engines”, *Surface Science and Technology*, Vol. 1, Issue 1, 2023.
10. Guo, L., Zhang, X., Liu, M., Yang, S., Dai, J. W., “CMAS + sea salt corrosion to thermal barrier coatings”, *Corrosion Science*, Vol. 218, Pages 111172, 2023.
11. Bogdan, M., Peter, I., “A comprehensive understanding of thermal barrier coatings (TBCs): applications, materials, coating design and failure mechanisms”, *Metals*, Vol. 28, Pages 101728, 2024.
12. Konter, M., Bossmann, H. P., “Materials and coatings developments for gas turbine systems and components”, *Modern Gas Turbine Systems: High Efficiency, Low Emission, Fuel Flexible Power Generation*, Peter Jansohn editor, High Efficiency, Low Emission, Fuel Flexible Power Generation, Pages 327–380, Woodhead Publishing Series in Energy, 2013.
13. Roche, J., Alvarado-Orozco, J.M., Gómez, P.A., Cano, I. G., Dosta, S., Toro, A., “Hot corrosion behavior of dense CYSZ/YSZ bilayer coatings deposited by atmospheric plasma spray in Na₂SO₄ + V₂O₅ molten salts”, *Surfaces and Coating Technology*, Vol. 432, Pages 128066, 2022.
14. Avcı, A., Eker, A.A, Eker, B., “Microstructure and oxidation behavior of atmospheric plasma-sprayed thermal barrier coatings”, In *xergetic, Energetic and Environmental Dimensions*, Ibrahim Dincer, C. Ozgur Colpan, Onder Kizilkan editors, Pages 793-814, Elsevier, 2018.
15. Wei, Z. Y., Cai, H. N., Meng, G. H., Tahir, A., Zhang, W., “An innovative model coupling TGO growth and crack propagation for the failure assessment of lamellar structured thermal barrier coatings”, *Ceramic International*, Vol. 46, Issue 2, Pages 1532–1544, 2020.
16. Jun, B., Jonsson, N., Jordan, E. H., Cooper, R. C., “CMAS deposition rate and sequence effects on cyclic life in gradient testing”, *SN Applied Science*, Vol. 5, Issue 5, Pages 138, 2023.
17. Özçelik, A., Akdoğan Eker, A., Karabaş, M., Avcı, A., Küçükyıldırım, B. O. “Enhanced CMAS and hot corrosion degradation of YSZ thermal barrier coating with nano powders”, *Surfaces and Coatings Technology*, Vol. 481, Pages 130624, 2024.
18. Li, B., Wu, J., He, X., Wang, B., Guo, L., “Sc-doped Gd₂Zr₂O₇ coating on YSZ thermal barrier coatings to resist CMAS + molten salt attack”, *Ceramic International*, Vol. 48, Issue 8, Pages 11662–11671, 2022.
19. Akin, I., Yilmaz, E., Sahin, F., Yucel, O., Goller, G., “Effect of CeO₂ addition on densification and microstructure of Al₂O₃-YSZ composites”, *Ceram International*, Vol. 37, Issue 8, Pages 3273–3280, 2011.

20. Rejab, N. A., Azhar, A. Z. A., Ratnam, M. M., Ahmad, Z. A., “The effects of CeO₂ addition on the physical, microstructural and mechanical properties of yttria stabilized zirconia toughened alumina (ZTA)”, *International Journal Refractors Metals Hard Materials*, Vol. 36, Pages 162–166, 2013.
21. Roche, J., Gómez, P. A., Alvarado-Orozco, J. M., Toro, A., “Hot corrosion and thermal shock resistance of Dense-CYSZ/YSZ bilayer thermal barrier coatings systems applied onto Ni-base superalloy”, *Journal European Ceramic Society*, Vol. 40, Issue 15, Pages 5692–5703, 2020.
22. Ali, M. K. A., Xianjun, H., “Exploring the lubrication mechanism of CeO₂ nanoparticles dispersed in engine oil by bis(2-ethylhexyl) phosphate as a novel antiwear additive”, *Tribology International*, Vol. 165, Pages 107321, 2022.
23. Pimenov, D. Y., Silva, L. R. R. Ercetin, A., Mikolajczyk, O.T., Giasin, K., “State-of-the-art review of applications of image processing techniques for tool condition monitoring on conventional machining processes”, *The International Journal of Advanced Manufacturing Technology*, Vol.130, Pages 57-85, 2024.
24. Li, B., “Study on Porosity of thermal-sprayed commercially pure aluminum coating”, *Materials*, Vol. 16, Issue, 2023.
25. Bal, E., Karabaş, M., “Effect of molten glass on degradation of stabilized zirconia thermal barrier coatings”, *Journal of the Korean Ceramic Society*, Vol. 60, Issue 2, Pages 331–343, 2023.
26. Shin, D., and Hamed, A., “Influence of micro-structure on erosion resistance of plasma sprayed 7YSZ thermal barrier coating under gas turbine operating conditions”, *Wear*, Vol. 396–397, Pages 34–47, 2018.
27. Chen, K., Song, P., Hua, C., Z., Ying, Huang T., Li, C., Lu, J., “Effect of YSZ-dopant on microstructure and hardness property of the Al₂O₃–40%TiO₂ plasma sprayed coating”, *Material Research Express*, Vol. 5, Issue 8, Pages 086504, 2018.
28. Saral, U., Toplan, N., “Thermal cycle properties of plasma sprayed YSZ/Al₂O₃ thermal barrier coatings”, *Surface Engineering*, Vol. 25, Issue 7, Pages 541–547, 2009.
29. Srikanth, A., Bolleddu, V., “Microstructural, mechanical and tribological characteristics of reduced graphene oxide (rGO) reinforced nanostructured Al₂O₃-13wt. %TiO₂ coatings”, *Journal of the Australian Ceramic Society*, 2024.
30. Mehar, S., Sapate, S.G., “Contact severity maps for plasma sprayed YSZ modified Al₂O₃-3% TiO₂ coatings”, *Ceramic International*, Vol. 50, Issue 8, Pages 13003–13013, 2024.
31. Franco, D., Vargas, F., López, E., and Ageorges, H., “Wear behavior at high temperature of ZrO₂–Y₂O₃ (YSZ) plasma-sprayed coatings”, *Journal of Material Science*, Vol. 59, Issue 1, Pages 20–37, 2024.
32. Bai, L., Zhang, H., Wan, S., Yi, G., Sun, H., “Tailoring wear and tribo-induced interaction of YSZ coating sliding against Si₃N₄ and Al₂O₃ counterparts”, *Wear*, Vol. 518–519, Pages 204628, 2023.
33. Avcı, A., Karabaş, M., Akdoğan Eker, A., Akman, E., Aslan, C., “Hot corrosion and CMAS degradation of laser-glazed YSZ coating with optimum parameter”, *Proceedings of the Institution of Mechanical Engineers, Part L: Journal of Materials: Design and Applications*, Vol. 237, Issue 11, Pages 2722-2734, 2023.
34. Avcı, A., “Termal bariyer kaplamaların oksidasyon ve sıcaklık korozyonu davranışlarının incelenmesi”, *Yüksek Lisans Tezi, Yıldız Teknik Üniversitesi İstanbul*, 2015.
35. Zhang J., “Effect of WC-12Co content on wear and electrochemical corrosion properties of Ni-Cu/WC-12Co composite coatings deposited by laser cladding”, *Surfaces and Coatings Technology*, Vol. 393, Pages 125807, 2020.
36. Gültekin, D., Duru, E., Akbulut, H., “Effect of heat treatment and applied load on mechanical and tribological properties of Ni-B-CeO₂ composite electroless coating”, *European Journal of Science and Technology*, Issue 34, Pages 573-578, 2022.
37. Zhao, Y., Wang, H., Zhang, L., Xiaofeng L., Guo, Z., Zhang, J., Yi, D., Liu, B., Bai, P., “Study on the microstructure and properties of WC-12Co cemented carbide fabricated by selective laser melting”, *Journal of Materials Research and Technology*, Vol. 20, Pages 3512–3521, 2022.
38. Ji, W., Yuan, Y., Zou, B., Dai, S., and Zhang, H. “Friction and wear behaviour of cemented carbide tool materials sliding against Al₂O₃ and Si₃N₄ ceramics under dry condition”, *Ceramic International*, Vol. 44, Issue 14, Pages 17486–17491, 2018.



ULUSLARARASI 3B YAZICI TEKNOLOJİLERİ
VE DİJİTAL ENDÜSTRİ DERGİSİ

INTERNATIONAL JOURNAL OF 3D PRINTING
TECHNOLOGIES AND DIGITAL INDUSTRY

ISSN:2602-3350 (Online)

URL: <https://dergipark.org.tr/ij3dptdi>

ERGİYİK BİRİKTİRME YÖNTEMİYLE ÜRETİLEN PVA NUMUNELERİN BASMA DAYANIMININ BULANIK MANTIKLA TAHMİNİ

PREDICTION OF COMPRESSIVE STRENGTH OF PVA
SAMPLES PRODUCED BY FUSED DEPOSITION
MODELING USING FUZZY LOGIC

Yazarlar (Authors): Ebru Kuruođlan , Osman Saltık , Koray Özsoy 

Bu makaleye řu řekilde atıfta bulunabilirsiniz (To cite to this article): Kuruođlan E., Saltık O., Özsoy K., "Ergiyik Biriktirme Yöntemiyle Üretilen PVA Numunelerin Basma Dayanımının Bulanık Mantıkla Tahmini" *Int. J. of 3D Printing Tech. Dig. Ind.*, 8(3): 399-406, (2024).

DOI: 10.46519/ij3dptdi.1548680

Arařtırma Makale/ Research Article

Eriřim Linki: (To link to this article): <https://dergipark.org.tr/en/pub/ij3dptdi/archive>

ERGİYİK BİRİKTİRME YÖNTEMİYLE ÜRETİLEN PVA NUMUNELERİN BASMA DAYANIMININ BULANIK MANTIKLA TAHMİNİ

Ebru Kuruođlan^a, Osman Saltık^b*, Koray Özsoy^b

^a Isparta Uygulamalı Bilimler Üniversitesi, Teknoloji Fakültesi, Mekatronik Mühendisliği Bölümü, TÜRKİYE
^b Isparta Uygulamalı Bilimler Üniversitesi, Isparta OSB MYO, Makine ve Metal Teknolojileri Bölümü, TÜRKİYE

* Sorumlu Yazar: osmansaltik@isparta.edu.tr

(Geliş/Received: 11.09.24; Düzeltme/Revised: 09.11.24; Kabul/Accepted: 09.12.24)

ÖZ

Bu çalışmada, Polivinil Alkol (PVA) malzemesi kullanılarak farklı işleme parametrelerine sahip numuneler üretilmiş ve basma dayanımları incelenmiştir. Bu çalışmanın amacı, PVA malzemesi kullanılarak üretilen numunelerin basma dayanımının, nozul sıcaklığı, baskı hızı ve doluluk oranı gibi işleme parametrelerine bağlı olarak bulanık mantık modelleme yöntemiyle tahmin edilmesidir. Sonuçlara göre, basma dayanımı büyük ölçüde doluluk oranına bağlıdır; doluluk oranı arttıkça basma dayanımı artmıştır. Ancak baskı hızının artışı basma dayanımını azaltmıştır. Nozul sıcaklığı ise basma dayanımını kısmen azaltmıştır. Çalışmanın en önemli katkılarından biri, bulanık mantık modelleme yöntemi kullanılarak deneysel verilerin tahmin edilmesidir. Çalışmada geliştirilen bulanık mantık modeli, nozul sıcaklığı, baskı hızı ve doluluk oranı gibi parametreler ile basma dayanımı arasındaki ilişkiyi başarılı bir şekilde modellemiş ve gerçek deneysel verilere yakın tahmin etmiştir. Bu modelin, geleneksel tahmin yöntemlerine kıyasla daha yüksek doğruluk ve tutarlılık sağladığı ortaya konmuştur. Özellikle, PVA malzemeli numunelerin farklı işleme parametreleri altında gösterdiği basma dayanımını başarılı bir şekilde tahmin edilmesinde etkili bir yöntem olduğunu göstermiştir. Sonuç olarak, çalışmada bulanık mantık modellerinin, deneysel verilerin tahmin edilmesinde etkili ve güvenilir bir yöntem olarak kullanılabileceği ortaya konmuştur. Elde edilen bulgular, PVA malzemeli numunelerin farklı işleme parametrelerine bağlı olarak basma dayanımının tahminlenmesine yönelik önemli bilgiler sunmaktadır.

Anahtar Kelimeler: Polivinil Alkol (PVA), Ergiyik Biriktirme Modelleme (EBM), Basma Dayanımı, Bulanık Mantık, Tahminleme.

PREDICTION OF COMPRESSIVE STRENGTH OF PVA SAMPLES PRODUCED BY FUSED DEPOSITION MODELING USING FUZZY LOGIC

ABSTRACT

In this study, samples with varying processing parameters were produced using Polyvinyl Alcohol (PVA) material, and their compressive strengths were investigated. The aim of this study is to estimate the compressive strength of samples produced with PVA material using a fuzzy logic modeling method, depending on processing parameters such as nozzle temperature, printing speed, and filling ratio. According to the results, the compressive strength is highly dependent on the filling rate; as the filling rate increases, the compressive strength also increases. However, the compressive strength decreases with an increase in printing speed. The nozzle temperature partially decreased the compressive strength. One of the most important contributions of this study is the prediction of experimental data using the fuzzy logic modeling method. The fuzzy logic model developed in this study successfully modeled the relationship between parameters such as nozzle temperature, printing speed, and filling ratio with compressive strength, predicting values close to the real experimental data. This model was shown to provide higher accuracy and consistency compared to traditional prediction methods. It was

demonstrated to be an effective approach for successfully predicting the compressive strength of PVA specimens under different processing parameters. The study shows that fuzzy logic models can be used as an effective and reliable method for predicting experimental data. The findings provide important information for predicting the compressive strength of PVA specimens under various processing parameters.

Keywords: Polivinil Alkol (PVA), Fused Deposition Modelling (FDM), Compressive strength, Fuzzy Logic, Prediction.

1. GİRİŞ

EBM teknolojisinde kullanılan malzemeler, geleneksel imalat süreçlerinde test edilmiş termoplastiklerdir. Temel EBM termoplastik malzemeler arasında Akrilonitril Bütadien Stiren (ABS), Polilaktik Asit (PLA), Polikarbonat (PC), PC/ABS karışımı, epoksi, epoksi reçineler, poliamid (nylon), Polivinil Alkol (PVA), termoset ve termoplastik poliüretan yer almaktadır [1]. Literatürde, özellikle PLA ve ABS gibi termoplastik malzemelerin mekanik özelliklerinin kapsamlı bir şekilde incelendiđi çok sayıda çalışma bulunmaktadır. [2-4]. PVA; genellikle PLA ve ABS filamentlerle birlikte destek yapıların üretiminde ve destek yapıların parçalardan uzaklaştırma işlemlerinde kullanılır. Endüstriyel olarak üretilen suda çözünebilen bir polimerdir [5]. Son yıllarda, PVA çođunlukla dişçilik, ilaç taşıyıcı, kontak lensler ve yapay organlar olmak üzere biyo-yazıcı gibi medikal alanındaki uygulamalarda kendine yer edinmiştir [6-7].

Bulanık mantık kavramını ilk olarak 1965 yılında Zadeh ortaya atmıştır. Zadeh'in 'bulanık küme' kavramı, klasik sistem kuramının matematiksel yöntemlerinin karmaşık ve insan faktörünü içeren sistemlerde yetersiz kalması sonucunda geliştirilmiştir [8].

Bulanık mantık, standart sayısal sistemlerde kullanılan sıfır ve bir seviyeleri yerine üyelik fonksiyonlarını kullanarak daha hassas sonuçlar üretebilir. [9] Mamo vd., çalışmasında, EBM yöntemiyle dört süreç deđişkeni belirleyerek ABS malzeme kullanarak, numuneler üzerinde deneysel çalışmalar gerçekleştirmişlerdir. Ardından, giriş ve çıkış parametrelerine dayalı bulanık mantık tabanlı bir tahmin modeli geliştirilmiştir. Sonuçlar, önerilen modelin deneysel verilerle iyi bir uyum gösterdiğini ortaya koymuştur [10]. Peng vd., çalışmalarında katman kalınlığı, dolum hızı, ekstrüzyon hızı ve hat genişliğinin imalat süresi ve boyutlar

üzerindeki etkilerini hem deneysel hem de bulanık mantık ile incelemiştir. Sonuçlar, bu yaklaşımın FDM sürecinin doğruluđunu ve verimliliđini artırabileceđini göstermiştir [11].

Ng vd., çalışmalarında, EBM 3D baskı tekniđi kullanarak içi boş PLA numuneleri için optimum PVA destek parametre ayarlarını belirlemeyi amaçlamışlardır. Deneyler sonucunda, en iyi PVA destek ayarlarının destek malzemesi kullanımı, baskı süresi ve maliyeti azalttığı gözlemlenmiştir [12]. Moradi vd., çalışmalarında, EBM yöntemiyle PVA malzemeli 3D baskı yöntemini araştırmışlar ve girdi parametreleri olarak dolgu oranı (%10-50) ile tarama deseni parametrelerini seçmişlerdir. Çalışmada çıktı olarak modül, kopma uzaması ve ağırlık ölçülmüştür. Sonuçlar, optimum numuneler için öngörülen ve gerçek yanıtların %15'in altında bir tutarsızlığa sahip olduğunu ve bunun deneyler için kabul edilebilir olduğunu göstermiştir [13].

Bu çalışmada, nozul sıcaklığı, baskı hızı ve doluluk oranı gibi önemli imalat parametreleri girdi olarak alınarak ve PVA filament malzemesi kullanılarak EBM yöntemiyle basma numuneleri imal edilmiştir. Deney tasarımı (DOE) için Taguchi yöntemi kullanılmıştır ve bu deneyde çıktı olarak modül ile basma dayanımı ölçülmüştür. Bulanık mantık, her bir yanıt için gerekli olan hedeflere ulaşmak amacıyla üç girdi parametresini optimize edecek şekilde düzenlenmiştir. PVA numuneleri için basma dayanımının bulanık mantıkla tahmini, bu çalışmada ilk kez ele alınmıştır. Çalışmanın amacı, bu girdi parametrelerinin üretilen numunelerin basma dayanımı üzerindeki etkisini deđerlendirmektir.

2. MATERYAL VE METOT

2.1. Materyal

Çalışmada, açık kaynak kodlu ve 400x300x350 mm imalat hacme sahip ZAXE Z3 marka/model EBM tipi yazıcı kullanılarak PVA malzeme ile,

basma numuneleri üretilmiştir. Çizelge 1'de PVA filamentin teknik özellikleri verilmiştir.

Çizelge 1. PVA filamentin teknik özellikleri [14]

| | |
|-------------------------------|---------|
| Filament Adı | PVA |
| Baskı Sıcaklığı (°C) | 180-230 |
| Yoğunluk (g/cm ³) | 1,25 |
| Çekme Dayanımı (MPa) | 22 |
| Kopma uzaması (%) | 360 |

Bulanık mantığın temelini, üyelik fonksiyonlarıyla belirlenen bulanık küme kavramı oluşturmaktadır. Bulanık küme içindeki her bir öğeye, 0 ile 1 arasında değişen ve üyelik fonksiyonu tarafından belirlenen bir üyelik değeri atanır. Çalışmada, genelleştirilmiş gbell üyelik fonksiyonunun a, b ve c parametrelerinin yer aldığı Denklem (1) kullanılarak bulanık mantık işlemleri gerçekleştirilmiştir [15]. Burada x: giriş değeri veya bağımsız değişken, a: fonksiyonun genişliğini kontrol eden parametre, b: fonksiyonun eğimini veya şeklini kontrol eden parametre, c: fonksiyonun merkezini veya zirvesini belirleyen parametrelerdir.

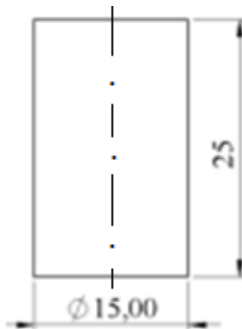
$$G_{bell}(x, a, b, c) = \frac{1}{1 + \left| \frac{x-c}{a} \right|^{2b}} \quad (1)$$

2.2. Yöntem

Çalışma yöntem bölümü basma numunelerin standart tasarımı ve EBM cihazı ile imalatı, basma deneyi, bulanık mantık modelleme kısımlarını kapsar.

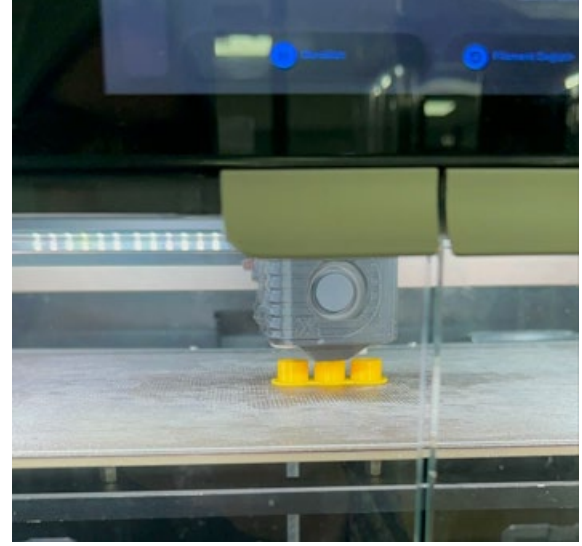
2.2.1. Basma Numunesi Tasarımı ve İmalatı

Şekil 1, EBM ile üretilen parçaların ISO 604:2002 standardına göre basma testi için test numunelerinin şekil ve boyutları verilmiştir [16].



Şekil 1. Basma numunesi (mm)

Şekil 2'de gösterildiği gibi EBM ile nozul sıcaklığı (200, 220° C), baskı hızı (30-60-80-100 mm/sn), doluluk oranı (%30-50-70-100) ile 16 farklı parametre ile basma numuneleri (Şekil 3) imal edilmiştir.



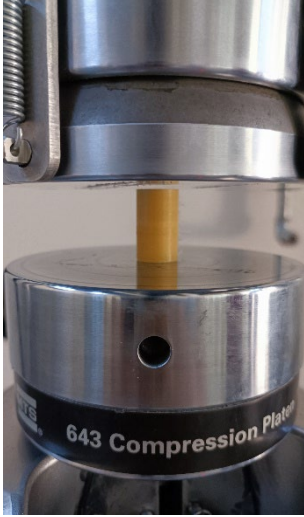
Şekil 2. EBM basma numunesi imalatı



Şekil 3. EBM basma numuneleri

2.2.2. Basma Deneyi

Basma testi, 10 kN kuvvet sensör kapasitesine sahip bir test makinesinde (AGS-X, Shimadzu Co., Kyoto, Japonya) Şekil 4'te gösterildiği gibi gerçekleştirilmiştir. Test sırasında numuneler, biri sabit diğeri hareketli olmak üzere iki aparat arasında sıkıştırmak suretiyle basma dayanımları MPa cinsinden ölçülmüştür. Test hızı ASTM D695 standardı referans alınarak 1,3 mm/s olarak uygulanmıştır. Deneysel hataları en aza indirmek amacıyla her koşul için üç numune test edilmiş ve elde edilen basma dayanımı değerlerinin ortalaması alınarak sonuçlar değerlendirilmiştir.

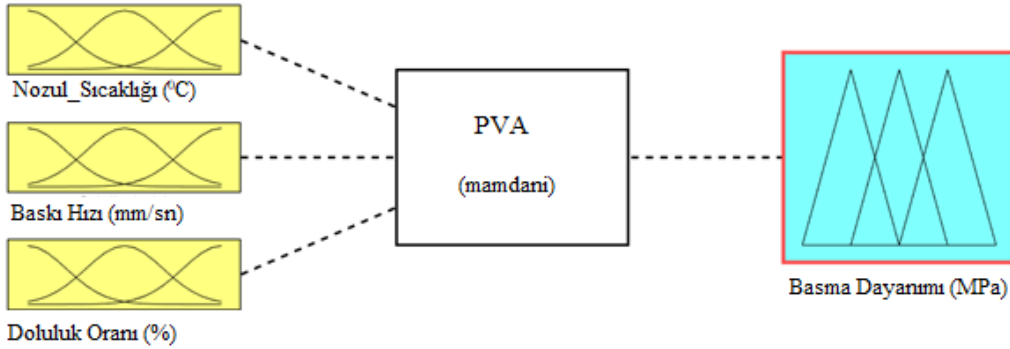


Şekil 4. Basma deneyi

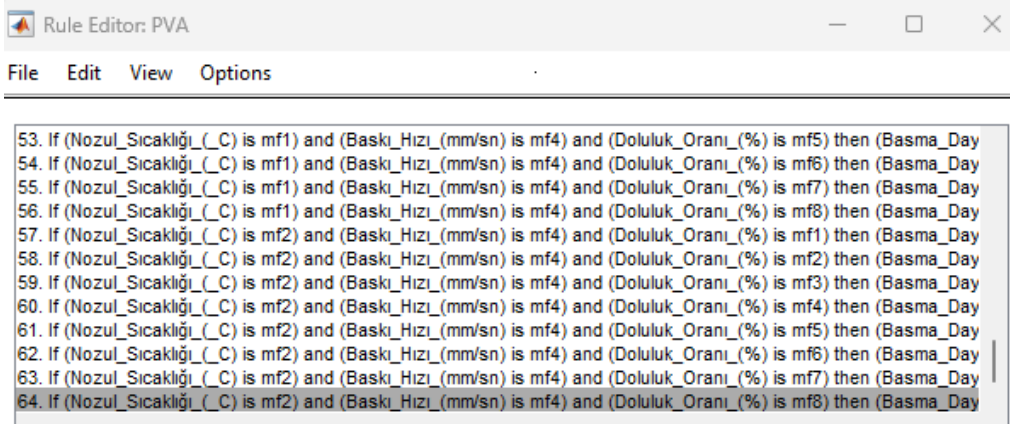
2.2.3. Bulanık Mantık Modelleme

Şekil 5'te gösterildiđi üzere, PVA malzemesi ile gerçekleştirilen basma deneyi sonuçlarına

dayanarak yapılan analizlerde, nozul sıcaklıđı, baskı hızı ve doluluk oranı gibi parametrelerin, yani giriş deđişkenlerinin basma dayanımı üzerindeki etkileri incelenmiştir. Bu bağlamda, giriş deđişkenleri olan nozul sıcaklıđı, baskı hızı ve doluluk oranı ile çıkış deđişkeni olarak basma dayanımı arasında bir ilişki kurulmuş ve bu ilişkiyi modellemek amacıyla bulanık mantık kullanılmıştır. Bu modelleme sürecinde gbell üyelik fonksiyonları tercih edilmiş ve sistemin davranışını tanımlamak için bir dizi kural tabanı oluşturulmuştur. Özellikle, PVA malzemesinin kullanıldıđı deneylerden elde edilen verilere dayalı olarak, söz konusu sistemin farklı koşullarda nasıl çalışacağını simüle etmek için nozul sıcaklıđı, baskı hızı ve doluluk oranı parametrelerine bađlı olarak geliştirilen modelde toplamda 64 farklı kuralın uygulandıđı bir bulanık mantık kural tabanı oluşturulmuştur.



(a)



(b)

Şekil 5. Bulanık mantık model a) Üyelik fonksiyonu, b) Kural tabanı

3. ARAŞTIRMA BULGULARI

3.1. PVA Numuneleri Basma Deney Sonuçları

EBM yöntemiyle imal edilen basma numunelerine uygulanan basma testi sonuçları analiz edilmiştir. Bu analizlerde, her bir deney koşulu için nozul sıcaklıđı, baskı hızı ve doluluk

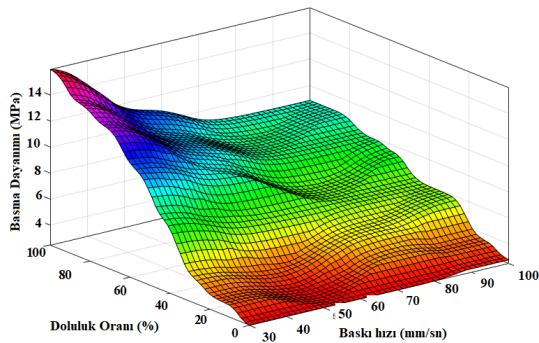
oranı parametreleri ile, üç adet numune üzerinde ayrı ayrı testler gerçekleştirilmiştir. Her bir parametre kombinasyonu için elde edilen basma dayanımı sonuçları, bu üç numune üzerinden yapılan ölçümlerin ortalaması alınarak hesaplanmıştır. Deney sonuçları detaylı bir şekilde Çizelge 2'de sunulmuştur.

Çizelge 2. Basma deneyi sonuçları

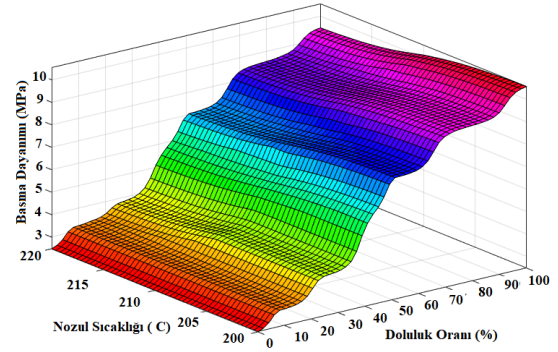
| No | Baskı Hızı (mm/sn) | Doluluk Oranı (%) | Nozul Sıcaklığı (°C) | Ortalama Basma Dayanımı (MPa) |
|----|--------------------|-------------------|----------------------|-------------------------------|
| 1 | 30 | 30 | 200 | 2,39 |
| 2 | 30 | 50 | 200 | 5,33 |
| 3 | 30 | 70 | 220 | 11,77 |
| 4 | 30 | 100 | 220 | 17,23 |
| 5 | 60 | 30 | 200 | 1,82 |
| 6 | 60 | 50 | 200 | 3,55 |
| 7 | 60 | 70 | 220 | 10,07 |
| 8 | 60 | 100 | 220 | 12,14 |
| 9 | 80 | 30 | 220 | 2,17 |
| 10 | 80 | 50 | 220 | 5,90 |
| 11 | 80 | 70 | 200 | 7,60 |
| 12 | 80 | 100 | 200 | 10,34 |
| 13 | 100 | 30 | 220 | 2,63 |
| 14 | 100 | 50 | 220 | 5,10 |
| 15 | 100 | 70 | 200 | 8,40 |
| 16 | 100 | 100 | 200 | 10,28 |

3.2. PVA Numuneleri Bulanık Mantık Sonuçları

PVA malzemeli numunelerin basma deneylerin sonuçlarına dayalı olarak oluşturulan bulanık mantık modelin çıktıları detaylı bir şekilde sunulmuştur. Nozul sıcaklığı, baskı hızı ve doluluk oranı gibi önemli parametrelerin basma dayanımı üzerindeki etkileri analiz edilerek, bulanık mantık tabanlı bir yaklaşımla elde edilen sonuçlar irdelenmiştir. Baskı hızı, nozul sıcaklığı ve doluluk oranı ile basma dayanımı ilişki 3B yüzey grafikleri Şekil 6 ve Şekil 7'de verilmiştir.

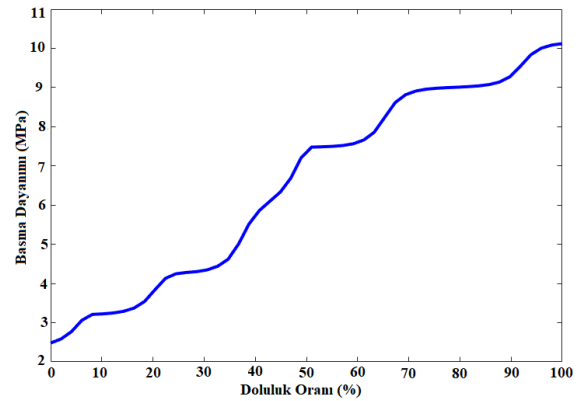


Şekil 6. Baskı hızı, doluluk oranı ile basma dayanımı ilişkisi



Şekil 7. Nozul sıcaklığı, doluluk oranı ile basma dayanımı ilişkisi

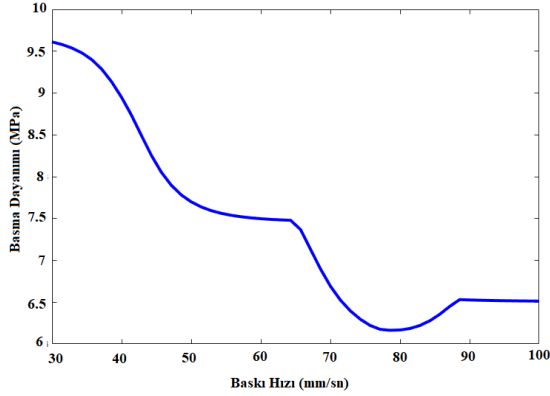
PVA malzemeli numunelerin doluluk oranı ve basma dayanımı arasındaki değişim Şekil 8'de sunulmuştur. PVA malzemeli numunelerin basma dayanımı değerlerini doluluk oranı arttıkça arttığını gözlemleyebiliriz. Bunun sebebi; doluluk oranı arttıkça, parça içindeki boşluklar azalır ve daha fazla malzeme kullanılır. Ayrıca daha yüksek doluluk oranı ile baskı sırasında katmanlar arasındaki bağlanma iyileşir ve parça içindeki yük dağılımı homojen hale gelmektedir. Doluluk oranı arttıkça parça içindeki destek yapısı da güçlenir. Sonuç olarak PVA malzemeli numunelerde basma dayanımının doluluk oranına ciddi olarak bağlı olduğu anlamına gelmektedir.



Şekil 8. Doluluk oranı basma dayanımı ilişkisi

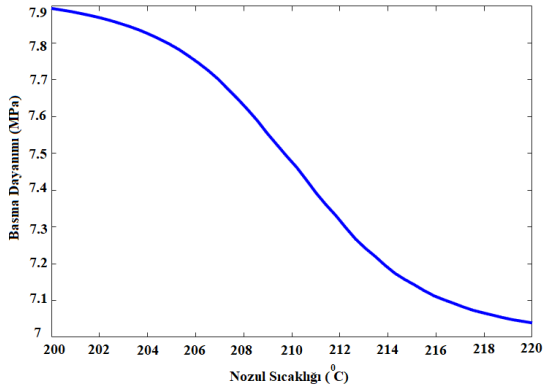
Baskı hızı ve basma dayanımı arasındaki değişim Şekil 9'da sunulmuştur. PVA malzemeli numunelerin basma dayanımı değerlerini baskı hızı arttıkça azaldığını gözlemleyebiliriz. Baskı hızı arttığında, filament malzeme daha hızlı şekilde katmanlar üzerine bırakılır ve bu durumda katmanlar arasında yeterli sıcaklıkta ve sürede bağlanma gerçekleşmez. Böylece katmanlar arası bağ zayıf olur. Ayrıca yetersiz soğuma süresi, yüzey kalitesindeki bozulmalar ve malzeme çekmesi gibi faktörler, EBM ile üretilen PVA malzemeli

parçaların basma dayanımının düşmesine neden olmuştur.



Şekil 9. Baskı hızı basma dayanımı ilişkisi

PVA malzemeli numunelerin nozul sıcaklığı ile basma dayanımı arasındaki değişim Şekil 10'da gösterilmiştir. Basma dayanımı değerlerini nozul sıcaklığı ile kısmen azaldığımızı gözlemleyebiliriz. EBM'de nozul sıcaklığı arttığında, malzemenin akışkanlığı, katmanlar arası yapışma, termal bozulma ve iç gerilimler gibi faktörler nedeniyle basma dayanımı düşer.



Şekil 10. Nozul sıcaklığı ile basma dayanımı ilişkisi

Şekil 11'de PVA malzemeden yapılan basma numunelerin basma dayanımı, farklı işleme parametrelerinin etkisi altında tahmin edilmiştir. Bu parametreler arasında nozul sıcaklığı, baskı hızı ve doluluk oranları yer almaktadır. Her bir parametre, belirli veri giriş değerlerine göre farklı kombinasyonlar halinde kullanılmış ve numunelerin basma dayanımı performansı üzerinde nasıl bir etki oluşturduğu incelenmiştir. Sonuç olarak, çalışmada bulanık mantık modelleme ile farklı giriş parametre kombinasyonlarının, basma dayanımını tahmin etmede önemli bir rol oynadığı gösterilmiştir.



Şekil 11. Bulanık mantık modelleme tahmini

PVA malzemeli EBM yöntemiyle elde edilen 3B baskı parçaların literatür çalışmaları incelendiğinde, Ilieva et al., [17] çalışmasında, kısmen hidrolize edilmiş, sorbitol ile plastikleştirilmiş polivinil alkol (PVA) filamentler, özellikle parasetamol gibi model ilaçlar için uygun bulunmuş ve karakterizasyon analizleriyle salım profilleri değerlendirilmiştir. Angjellari vd., [18] çalışmalarında elmas nanogranülleri dolgu maddesi olarak kullanılan PVA bazlı nanokompozitlerin 3B baskıda kullanımını araştırarak yenilikçi PVA-DND mürekkepler geliştirdiler. Çalışma, bu nanokompozitlerin başarılı bir şekilde basılabilir olduğunu ve farklı alanlarda geniş uygulama potansiyeline sahip olduğunu ortaya koymuştur. PVA'dan yapılan 3 boyutlu yazdırılmış numunelerin mekanik özelliklerini araştırmak ve yazıcı parametreleri ile mekanik özellikler arasında bir korelasyon kurmak için çeşitli çalışmalar yürütülmüştür [19–21].

4. SONUÇLAR

Bu çalışmada, PVA filament malzemesi kullanılarak farklı işleme parametreleriyle imal edilen basma numuneleri üzerinde kapsamlı bir basma deneyi gerçekleştirilmiştir. Deney sonucunda elde edilen veriler, numunelerin mekanik özelliklerini anlamak ve bu özellikleri tahmin edebilecek modeller geliştirmek amacıyla analiz edilmiştir. Bu bağlamda, deneysel sonuçların değerlendirilmesinde bulanık mantık modelleme yöntemi kullanılmış ve elde edilen verilerin doğruluğu ile tutarlılığı üzerine odaklanılmıştır.

Elde edilen basma deneyi sonuçlarına göre, PVA malzemesiyle üretilen numunelerin basma dayanımının büyük ölçüde doluluk oranına bağlı olduğu bulunmuştur. Doluluk oranı arttıkça numunelerin basma dayanımının belirgin bir şekilde iyileştiği gözlemlenmiştir.

Bununla birlikte, baskı hızının artmasıyla birlikte numunelerin basma dayanımının azaldığı tespit edilmiştir, bu da daha hızlı baskı süreçlerinin numunenin yapısal dayanıklılığı üzerinde olumsuz bir etki yaratabileceğini göstermektedir. Ayrıca, nozul sıcaklığının artışıyla numunelerin basma dayanımında kısmi bir azalma gözlemlenmiştir, ancak bu etki doluluk oranı ve baskı hızındaki değişiklikler kadar belirgin olmamıştır.

Çalışmanın genel amacı, deneysel verilerin yüksek doğruluk ve tutarlılıkla tahmin edilebilmesini sağlayacak alternatif modelleme yaklaşımlarını incelemek olmuştur. Bu çerçevede, bulanık mantık tabanlı modelleme yöntemlerinin, deneysel verilerin tahmin edilmesinde etkili ve güvenilir bir yöntem olarak kullanılabilirliği sonucuna ulaşılmıştır. Yapılan analizler, bulanık mantık modellerinin, özellikle değişken parametrelerin etkisi altında bulunan malzeme özelliklerinin tahmin edilmesinde önemli bir rol oynadığını ortaya koymuş ve bu modellerin, geleneksel tahmin yöntemlerine kıyasla üstün performans sergileyebileceğini göstermiştir.

ÇIKAR ÇATIŞMASI BEYANI

Yazarlar arasında çıkar çatışması bulunmamaktadır.

TEŞEKKÜR

Çalışmaya katkı sağlayan YETEM test ve analiz merkezine teşekkür ediyoruz.

KAYNAKLAR

- Duman B., Özsoy K. “Üç Boyutlu (3B) Baskı Teknolojileri”, Sayfa 222, Gece Kitapevi, Ankara, 2018.
- Özsoy, K., Erçetin, A., Çevik, Z. A. “Comparison of mechanical properties of PLA and ABS based structures produced by fused deposition modelling additive manufacturing”, *Avrupa Bilim ve Teknoloji Dergisi*, Vol. 27, Pages 802-809, 2021.
- Rodríguez-Panes, A., Claver, J., & Camacho, A. M. “The influence of manufacturing parameters on the mechanical behaviour of PLA and ABS pieces manufactured by FDM: A comparative analysis”, *Materials*, Vol. 11, Issue 8, Pages 1333, 2018.
- Algarni, M., & Ghazali, S. “Comparative study of the sensitivity of PLA, ABS, PEEK, and PETG’s mechanical properties to FDM printing process parameters. *Crystals*, Vol. 11, Issue 8, Pages 995, 2021.

5. Kebeci, S., Öztürk, F. H., Temiz, A. “PVA Destek Malzemeli Çift Kafa 3 Boyutlu Yazıcı Tasarımı Ve Prototipi”, 4 th International Congress On 3d Printing (Additive Manufacturing) Technologies And Digital Industry, Sayfa 654-657, 2019.

6. Zhang, C., Yuan, X., Wiu.L., Han, Y., Sheng, J. “Study on Morphology of Electrospun Poly (Vinyl Alcohol) Mats”, *European Polymer Journal*, Vol. 41 Pages 423- 432, 2005.

7. Angjellari M., Tamburri E., Montaina L., Natali M., Passeri D., Rossi M., Terranova M.L., Beyond the concepts of nanocomposite and 3D printing: PVA and nanodiamonds for layer-by-layer additive manufacturing. *Materials & Design*, Vol. 119, Pages 12-21, 2017.

8. Kıyak, E., Kahveciođlu, A. Bulanık Mantık ve Uçuş Kontrol Problemine Uygulanması. *Havacılık ve Uzay Teknolojileri Dergisi*, Cilt 1, Sayı 2, Sayfa 63-72, 2003.

9. Işık, Y., Kehya, M., Kayabaşı, A. Araç Sınıflandırılmalı Trafik Hız Sınırı Ceza Sisteminin Bulanık Mantık Temelli Tasarımı ve Gerçekleştirilmesi. *Mühendislik Bilimleri ve Araştırmaları Dergisi*, Cilt 5, Sayı 1, Sayfa 115-126, 2023.

10. H.B. Mamo, A.D. Tura, A. Johnson Santhosh, N. Ashok, and D. Kamalakara Rao, Modeling and Analysis of Flexural Strength with Fuzzy Logic Technique for a Fused Deposition Modeling ABS Components, *Mater. Today Proc.*, Vol. 57, Pages 768–774, 2022.

11. Peng, A. Xiao, X. Yue, R. Process parameter optimization for fused deposition modeling using response surface methodology combined with fuzzy inference system. *Int. J. Adv. Manuf. Technol.*, Vol. 73, Pages 87–100, 2014.

12. Ng, N. Y. Z., Haq, R. A., Marwah, O. M. F., Ho, F. H., & Adzila, S. Optimization of polyvinyl alcohol (PVA) support parameters for fused deposition modelling (FDM) by using design of experiments (DOE). *Materials Today: Proceedings*, Vol. 57, Pages 1226-1234, 2022.

13. Moradi, M., Karamimoghadam, M., Meiabadi, S., Casalino, G., Ghaleeh, M., Baby, B., ... & Khodadad, D. Mathematical modelling of fused deposition modeling (FDM) 3D printing of poly vinyl alcohol parts through statistical design of experiments approach. *Mathematics*, Vol. 11, Issue 13, Pages 3022, 2023.

14. Esun, 2024, https://www.esun3d.com/pva-product/?gad_source=1&gclid=Cj0KCQjw_sq2BhCUARIsAIVqmQuY2OAI6kHPSVVz9dBp94SXHSTjM6accvRZMV64rupJq7tSB39J6D8aAh1aEALw_wcB, August 31, 2024.
15. Sadollah, A. Which Membership Function is Appropriate in Fuzzy System?. Open Access Peer Reviewed.,Pages 2-6, 2018.
16. Basma Testi, ISO 604:2002: Plastics – Determination of Compressive Properties, 2002.
17. Ilieva, S., Georgieva, D., Petkova, V., & Dimitrov, M., “Study and Characterization of Polyvinyl Alcohol-Based Formulations for 3D Printlets Obtained via Fused Deposition Modeling.”, *Pharmaceutics*, Vol. 15, Issue 7, Pages 1867, 2023.
18. Angjellari, M., Tamburri, E., Montaina, L., Natali, M., Passeri, D., Rossi, M., Terranova, M.L. “Beyond the concepts of nanocomposite and 3D printing: PVA and nanodiamonds for layer-by-layer additive manufacturing.” *Mater. Des.* Vol. 119, Pages 12–21, 2017.
19. Stammen, J.A.; Williams, S.; Ku, D.N.; Guldborg, R.E. “Mechanical properties of a novel PVA hydrogel in shear and unconfined compression.”, *Biomaterials*, Vol. 22, Pages 799–806, 2001.
20. Hema, M., Selvasckerapandian, S., Hirankumar, G., Sakunthala, A., Arunkumar, D., Nithya, H. “Structural and thermal studies of PVA: NH4I.”, *Journal Phys. Chem. Solids*, Vol. 70, Pages 1098–1103, 2009.
21. Noushini, A., Samali, B., Vessalas, K. “Effect of polyvinyl alcohol (PVA) fibre on dynamic and material properties of fibre reinforced concrete.”, *Constr. Build. Mater.*, Vol. 49, Pages 374–383, 2013.



ULUSLARARASI 3B YAZICI TEKNOLOJİLERİ
VE DİJİTAL ENDÜSTRİ DERGİSİ

INTERNATIONAL JOURNAL OF 3D PRINTING
TECHNOLOGIES AND DIGITAL INDUSTRY

ISSN:2602-3350 (Online)

URL: <https://dergipark.org.tr/ij3dptdi>

EXAMINATION OF MECHANICAL PROPERTIES OF FASTENERS PRODUCED WITH PET AND PLA MATERIALS IN EXTRUSION-BASED ADDITIVE MANUFACTURING METHOD

Yazarlar (Authors): Alperen DOĞRU^{ID}*, Muazzez KAÇAK^{ID}, M.Özgür SEYDİBEYOĞLU^{ID}

Bu makaleye şu şekilde atıfta bulunabilirsiniz (To cite to this article): Doğru A., Kaçak M., Seydibeyoğlu M. Ö., “Examination of Mechanical Properties of Fasteners Produced with PET and PLA Materials in Extrusion-Based Additive Manufacturing Method” *Int. J. of 3D Printing Tech. Dig. Ind.*, 8(3): 407-415, (2024).

DOI: 10.46519/ij3dptdi.1549143

Araştırma Makale/ Research Article

Erişim Linki: (To link to this article): <https://dergipark.org.tr/en/pub/ij3dptdi/archive>

EXAMINATION OF MECHANICAL PROPERTIES OF FASTENERS PRODUCED WITH PET AND PLA MATERIALS IN EXTRUSION-BASED ADDITIVE MANUFACTURING METHOD

Alperen DOĞRU^a , Muazzez KAÇAK^b , M.Özgür SEYDİBEYOĞLU^b 

^a Ege University, Aviation HVS, Aircraft Technology, TURKIYE

^b İzmir Katip Çelebi University, Metallurgical and Materials Engineering, TURKIYE

* Corresponding Author: alperen.dogru@ege.edu.tr

(Received: 16.09.2024; Revised: 31.10.2024; Accepted: 08.11.2024)

ABSTRACT

Additive manufacturing methods, with their potential to revolutionize many areas, especially spare parts production, enable the optimization of the supply chain in production processes with an on-site production approach. The increased number of users of additive manufacturing methods and easy access to material extrusion-based methods can potentially transform the manufacturing industry. In this study, to investigate the production performance of fasteners, which are indispensable components of the manufacturing industry, with additive manufacturing. This study focuses on the torque strengths, hardness, and microscope images of bolts and nuts produced by material extrusion-based additive manufacturing (MEX) using PLA (Polylactic Acid) and PET (Polyethylene Terephthalate) polymers with different production parameters. Unlike conventional manufacturing methods, M8x50 DIN (German institute for standardization) 933 bolts and M8 DIN 934 nuts were produced. The bolts produced were positioned on the MEX device in two different positions. The torque forces applied to the bolts were measured in mechanical tests. Hardness was measured, and bolt thread surfaces were examined using a stereo microscope. Data on the usage limits of polymeric bolts were determined with the data obtained.

Keywords: PLA, PET, Additive Manufacturing, Material Extrusion, Fastener

1. INTRODUCTION

Most fasteners are made of low and medium-carbon steels[1,2]. Parts exposed to repetitive vibrations may be damaged after specific periods of time. Due to this fatigue, problems may occur in the use of steel materials [3-4]. For these reasons, in the fasteners used today; polymer materials are becoming widespread for the raw material diversity of bolts and nuts, and new production methods have started to be tried [5]. Among these new production methods, additive manufacturing methods have become popular in recent years with technical advantages such as design flexibility, weight reduction with optimized structures and materials, and shorter production time for fewer production runs [6–8]. In addition, nearshoring is changing the understanding of the supply chain, and factors such as reduced storage costs can create a faster and more flexible production process. Additive manufacturing processes

stand out with their potential to revolutionize the traditional supply chain and have great potential in many industries with their decentralized production and supply structure [9].

Polymeric materials constitute the most widely used material variety in additive manufacturing methods, offering important opportunities for spare parts production. The method in which polymeric materials are most preferred is the material extrusion-based additive manufacturing method (MEX), which has the most users [10].

Polymers are increasingly used in various industrial applications, especially in producing fasteners, due to their advantages over metal alloys, such as lightweight, corrosion resistance, flexibility, and ease of processing [5]. Polymer bolts are becoming increasingly

popular, especially in marine, chemical, and outdoor applications where corrosion and metal fatigue are significant problems. Lighter than metal bolts, they are energy efficient and require less maintenance, reducing long-term costs [11-12].

Much research on metal fasteners has been carried out in literature [13–15]. However, there are only a limited number of studies on fasteners produced by the MEX method. Considering the advantages of using polymeric materials in fastener production with the MEX method, it is critical to know the materials' performances in this sense.

Harshitha et al. designed and analyzed bolts and nuts produced using the MEX method (International Standard Organization (ISO) standard) using PLA (polylactic acid) and ABS (acrylonitrile butadiene styrene) materials. In the analyses performed, it was determined that ABS is equivalent, and its shear stress is lower than PLA material and the results were confirmed in the tests performed on M12 bolts produced by the MEX method [16]. Labesh et al. similarly investigated the shear strength of M12 bolts produced by the MEX method using PLA and ABS materials. The analysis and test results showed that the safety factor of the bolts produced by the MEX method using PLA material is stronger than those made of ABS material [17]. These studies have shown that PLA material performs well in bolt production regarding shear load.

Eraliev et al. investigated the performance of bolts produced by the MEX method using three different materials under cyclic temperature changes. Although ABS bolts were weaker than PLA bolts at maximum preload, it was found that ABS bolts loosened 2.5 times less than PLA bolts at low-temperature cycling [18]. Alkhalaf et al. investigated the elastic modulus and dimensional stability of bolts produced by the MEX method using PLA material. They compared the mechanical properties of bolts produced with different infill density [19].

Zhang et al. investigated the wear properties of gears manufactured using nylon material using the MEX method. They concluded that under low to medium torque, the nylon gears produced by MEX outperformed the injection molded gears in terms of wear properties [20]. Chand et

al. investigated the dimensional and mechanical properties of nuts and bolts produced using a multi-jet 3D printer. It was determined that the dimensional deviations of the manufactured products were within tolerance levels [13].

The studies generally focused on the shear strength, wear and environmental conditions of the fasteners produced with AM. PLA and ABS materials have been intensively discussed. These polymer-based materials are the most widely used material types in the MEX method. Another polymer that has become increasingly popular in recent years is PETG (Polyethylene Terephthalate Glycol-modified) and (Polyethylene Terephthalate (PET))[21]. These materials strike a balance between the easy processability of PLA and the mechanical strength of ABS [22-23]. Furthermore, PETG's properties, such as low shrinkage rate, high impact resistance, and chemical resistance, make it an ideal choice for a variety of industrial and personal applications[24]. Nazım et al. investigated the performance of fasteners produced with MEX using PLA, PETG, and carbon fiber-reinforced nylon materials in joining aluminum sheets. The samples produced as rivets were used to join aluminum sheets by thermo-mechanical deformation. They found that the strength values of vertically produced rivets were higher than PLA and carbon fiber reinforced nylon. PETG has a higher glass transition temperature (T_g) than PLA. This has led to better performance in fasteners due to better adhesion properties [25].

As a result of the existing studies, this study was carried out to obtain literature information on the performance of fasteners produced with PLA and PET. The use of additive manufacturing methods in producing final industrial products, using polymers instead of metals to provide advantages in terms of lightweight, corrosion resistance, etc., and sustainability, is coming to the fore day by day. Fasteners, which are indispensable components of the manufacturing sector, are also affected by this change. For this reason, using PLA and PET materials in fastener production with the MEX method will contribute to the material diversity in this field.

Determination of the performance of fasteners produced by the MEX method will guide the usage areas. In this context, in our study,

M8x1,25x50 bolts in DIN (German Institute for Standardization) 933 standard and nuts in DIN 934 standard were produced by the MEX method using PLA and PET (Polyethylene Terephthalate) materials, and the hardness properties of the samples were tested, and torque tests examined performance. Additive manufacturing produces anisotropic materials and the properties change depending on the direction[26]. For this reason, the effect of infill pattern angle on torque properties was investigated in this study. All production parameters except the infill pattern angle were kept constant for each material group in the productions made with MEX. After the test, the damaged surfaces were visualized with an optical microscope.

2. MATERIALS AND METHODS

2.1. Materials

BASF's Ultrafuse PET and Ultrafuse PLA materials were used to produce bolts and nuts with the MEX. Filaments with a diameter of 2.85 mm were preferred in accordance with the MEX device used. All filaments are natural and do not contain any coloring agent.

The density values of the samples produced in the MEX method with Ultrafuse PET material are 1.329 gr/cm³, Tg value 71°C, and melt volume rate 16.3 cm³/10 min. The mechanical properties of the samples produced with this filament are tensile strength 33.4 MPa and impact strength 18.4 kJ/m² (unnotched charpy).

The density values of the samples produced with Ultrafuse PLA material in the MEX method are 1.248 gr/cm³, Tg value 61°C, and melt volume rate 21.2 cm³/10 min. The mechanical properties of the samples produced with this filament are tensile strength 34.7 MPa and impact strength 13.2 kJ/m² (unnotched charpy).

2.2. Design and Production

The drawings of the bolts with the dimensions specified in Figure 1 (a) in accordance with the M8x1,25x50 DIN 933 standard and the nuts with the dimensions specified in Figure 1 (b) in accordance with the M8x1,25 DIN 934 standard were carried out with AutoCAD Fusion 360 Computer Aided Design (CAD) program.

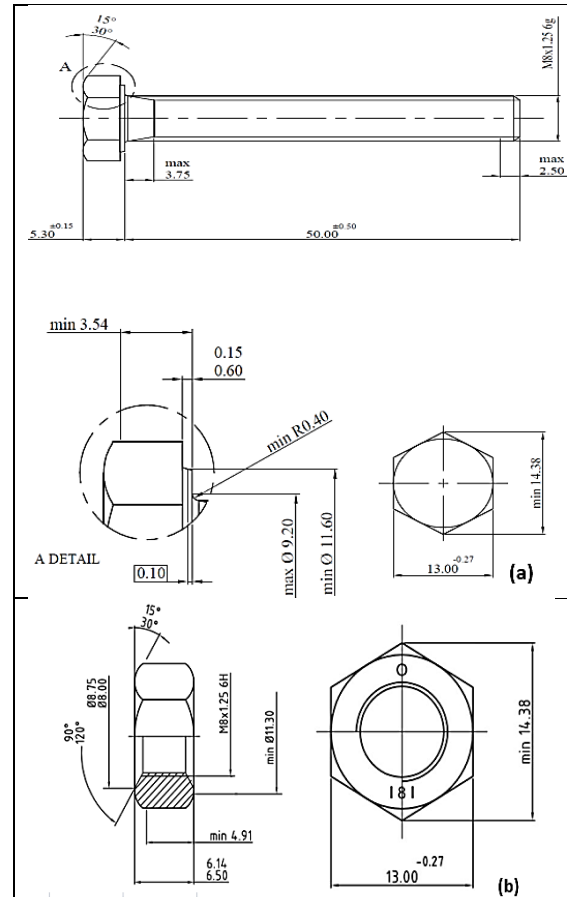


Figure 1. (a)Bolts Dimensions (b)Nuts Dimensions
The bolts and nuts whose solid models were drawn were produced by the MEX method with Ultimaker brand model 3 devices [27]. All bolts were produced with two different infill pattern angles, [0/90°] as shown in Figure 2 (a), [±45°] as shown in Figure 2 (b) and positioned on the table as shown in Figure 2 (c).

Each material group produced five pieces, each with two different infill pattern angles ([-/±45] and [0,90]). In the samples with [-/±45] infill pattern angles, the nozzle head performed extrusion at -45° and +45° angles, respectively. Similarly, those with [0/90] infill pattern angles were extruded at 0° and 90° angles, respectively. Nuts were produced in a horizontal position and with a circular pattern. In the test phase, each material was tested with a nut of its material. Polyvinyl alcohol (PVA) support material was used to facilitate the bolts' adhesion to the table and ensure their shape stability.

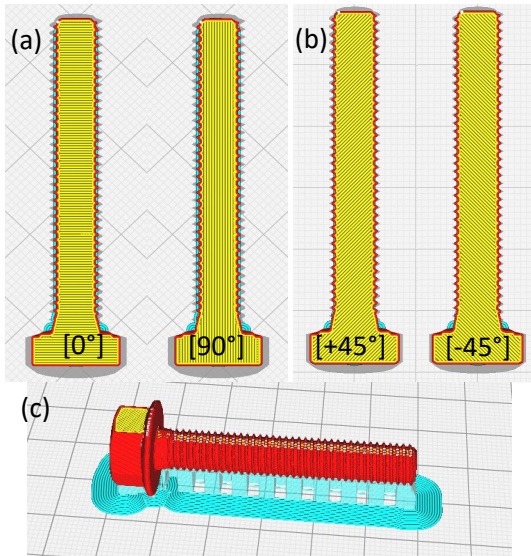


Figure 2. (a) Infill Patterns Angles [0/90] (b) Infill Pattern Angles [+45/-45] (c) Bed Table Position

The filament manufacturer's recommended values were used for all printing parameters. The fixed production parameters determined to produce bolts and nuts are specified in Table 1.

Table 1. Fixed parameters for production

| Parameter | Value |
|----------------------|-------|
| Layer Height (mm) | 0.2 |
| Infill Density (%) | 100 |
| Bed Material | Glass |
| Support Material | PVA |
| Build Plate Adhesion | Brim |

For PET material, the nozzle temperature was 230°C, the bed temperature was 85°C, and the print speed was 55 mm/s. For PLA material, the nozzle temperature was set to 210°C, the bed temperature was set to 60°C, and the print speed was 70 mm/s.

The produced bolts and results are shown in Figure 3 and Figure 4.



Figure 3. PET Bolts and Nuts Samples



Figure 4. PLA Bolts and Nuts Samples

2.3. Post-Processing

After producing M8x1,25x50 DIN 933 bolts and M8x1,25 DIN 934 standard nuts made of different materials, the final surface treatment was applied using the round die apparatus, as shown in Figure 5. The purpose of the application is to ensure that the fasteners are connected by removing the burrs on the threads.



Figure 5. Round Dies Application

To check that the bolts produced after the final surface treatment are easily connected with nuts, controls were made with the gauge shown in Figure 6.

These quality control procedures were performed to check the correctness of the thread pitch, thread angle, minor diameter (root), pitch diameter, and major diameter (crest).



Figure 6. Quality Check with Gage

2.4. Hardness Measurement

Hardness measurements were carried out with a Frank brand Shore D hardness tester, shown in Figure 7. The measured according to the ASTM D2240 Standard Test Method for Rubber Property-Durometer Hardness standard [28]. All measurements were made from bolt heads with plate surfaces.



Figure 7. Hardness Measurement

2.5. Torque Test

Torque tests of the produced bolts were applied until the bolts were damaged. The tests were carried out to see the strength of the bolts and nuts under safe load. During the test, bolts and nuts were fixed on a fixed plate and tightened with a torque meter. Torque measurements were carried out with the Yamer brand digital torque meter shown in Figure 8.



Figure 8. Torque Tests

2.6. Stereo Microscope

After the torque test, the damage to the threads of the bolts and nuts was examined with a stereo microscope. Imaging was performed with Elite brand SX45 stereo microscope.

3. RESULTS AND DISCUSSIONS

The hardness of the bolts produced by the MEX method using PLA and PET materials was measured according to the shore D scale. Figure 9 shows the results of all measurements performed. The highest shore D value was measured in bolts produced using PLA material. The hardness values of the bolts produced with PET material were measured lower regardless of the production direction. According to the Shore D test, a scale value of 100 corresponds to a spring load of 44.45 N [28]. The highest hardness value was measured as 71.64 on average in PLA bolts produced with 0/90 orientation and this value corresponds to a load of approximately 31.84 N according to the standard. The lowest shore D hardness value was measured as 60.08 on average in PET bolts produced with -/+45 orientation, and this value corresponds to a load of approximately 26.7 N according to the standard.

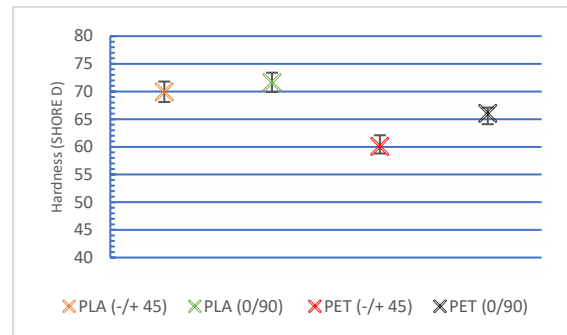


Figure 9. Shore D Hardness Results

When the results are analyzed independently of the material type, it is seen that the bolts produced in the 0/90 orientation have higher shore D hardness values than the bolts produced in the -/+45 orientation. In the deaths made from 5 points, approximately close values were measured between those with -/+45 orientation and those with 0/90 orientation in PLA bolts. This showed that hardness values were not affected by orientation in PLA bolts. In PET bolts, a slight difference was observed in hardness values depending on orientation. This is thought to be related to the cooling of the extruded polymer caused by the nozzle head's path during the PET material's orientation

changes. The pattern observed at 0/90 orientation includes a shorter time for the next layer. This may have favorably affected the interaction during the joining of the layers. The production time for a single PLA bolt was 26 minutes for 0/90 and 28 minutes for the bolt with ± 45 orientation. Similarly, the production time for PET bolts is slightly lower for 0/90 orientation.

The hardness of the bolts produced with PLA was measured to be higher than those produced with PET, regardless of the production orientation. The low Tg value of PLA compared to PET material may cause it to be harder at low temperatures [29]. In addition, PET material can be more flexible when it is amorphous, and PLA has a semi-crystalline structure due to the bonds it has, which makes PLA more rigid at room temperature [30]. PLA has a higher crystallinity than PET, increasing the material's stiffness. When PET remains in the amorphous phase, it is more flexible and has a higher impact resistance, while PLA exhibits a more rigid structure [31]. All these properties caused PLA bolts to show higher hardness properties than PET bolts. Considering the results obtained, the difference in polymer material affected the hardness value more than the production orientation.

In the torque test, the bolts were tested using nuts made of the same materials. The bolts fixed to the plates were tested with a torque meter. The applied force was measured and recorded with a digital display. Five specimens from each test group were tested, and the results are shown in Figure 10.

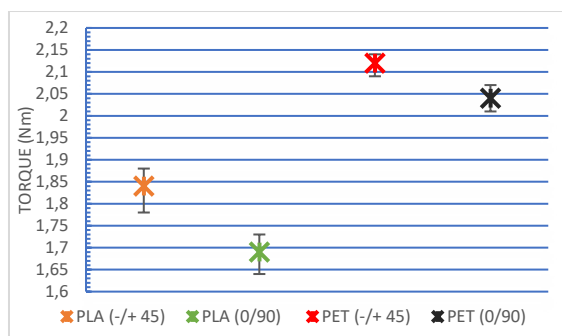


Figure 10. Torque Test Results

Higher torque values were measured for bolts with ± 45 orientation compared to bolts with 0/90 orientation. Regardless of the orientation, higher torque values were measured in bolts

produced with PET material. PLA shows higher stiffness due to its rigid structure, but it has a brittle structure and is more likely to break when excessive torque is applied [32]. Moreover, it was observed that the torque value was low in PLA samples with high hardness values. In this case, it can be interpreted that the increase in hardness gives a brittle structure feature. For this reason, lower torque values were measured for PLA bolts compared to PET bolts. PET material also has higher impact strength than PLA [23]. This may have enabled PET bolts to withstand higher torques. The tough structure of PET material allows it to perform more deformations without breaking [33]. This may be why PET bolts exhibit higher torque values than PLA bolts. In addition, the technical data sheet values of the PET and PLA materials used also confirm this situation. The impact strength of the ultrafuse PET samples was 18.4 kJ/m^2 [34] while it was 13.2 kJ/m^2 for PLA samples [35]. These test results show the foreseeable force and safety load for the forces applied to PLA and PET bolts.

After the torque test, the bolt threads were visualized with a stereo microscope. The images of PET bolts are shown in Figure 11.

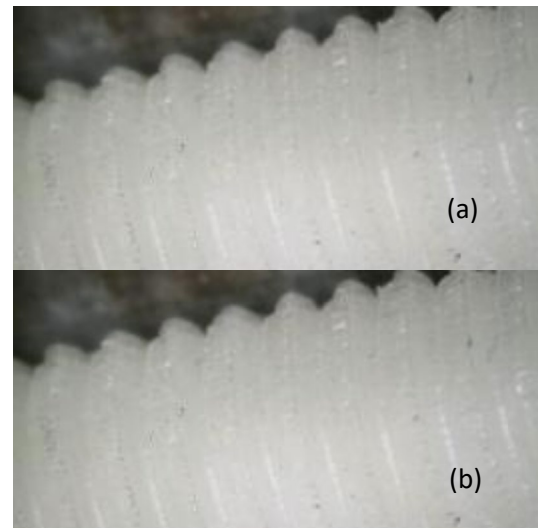


Figure 11. (a) 0/90 PET Bolt (b) ± 45 PET Bolt

It was observed that the thread depths of the bolts with a 0/90 orientation were less than those of the bolts with a ± 45 orientation. This may be the reason for the low torque values in bolts with a 0/90 orientation, as it reduces the adhesion in bolted connections.

Figure 12 shows images of PLA bolts. Similarly, less thread depth is observed in PLA bolts with a 0/90 orientation. This situation depends on the movement pattern of the nozzle during production and the positioning of the bolt to be produced.

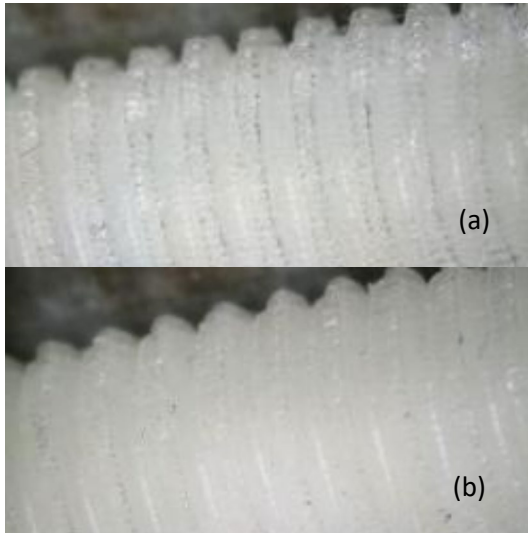


Figure 12. (a) 0/90 PLA Bolt (b) +/-45 PLA Bolt

In the movement system of the nozzle, the Ultimaker brand model 3 device used in production is moved in the Cartesian system with straight rods supported from the end. This situation is known to limit the mobility. In the newly developed CoreXY systems, corrections have been made in this regard by using fully supported linear rails [36,37].

4. CONCLUSIONS

Fasteners produced by additive manufacturing methods appear to be particularly advantageous in non-standard applications. This is especially true when large or unusually shaped fasteners are necessary to withstand low or medium loads. In this respect, the MEX process offers significant opportunities with its wide range of materials.

Hardness values were measured as 69.96 with +/-45 infill pattern angle and 71.64 with 0/90 infill pattern angle for PLA bolts. PET bolts were measured as 60.08 with +/-45 infill pattern angle and 66.04 with 0/90 infill pattern angle. Hardness increases the material's resistance to external influences and makes it more resistant to problems such as wear and deformation. For this reason, PLA bolts with high hardness values may be more advantageous for these applications.

The study measured the torque value for PLA bolts as 1.84 Nm with +/-45 infill pattern angle and 1.69 Nm with 0/90 infill pattern angle. PET bolts were measured as 2.12 Nm with +/-45 infill pattern angle and 2.07 Nm with 0/90 infill pattern angle. Considering their properties, polymeric bolts can withstand low and medium loads in areas requiring corrosion resistance. Cover assembly areas of water pumps, decoration panel cover assemblies in the white goods industry, and fasteners used in the toy industry may offer opportunities for this method.

Although polymer bolts offer many advantages, challenges such as deformation, low thermal conductivity, and fatigue over time can arise, especially in high-temperature applications. Therefore, further research and development work is needed to make polymer bolts long-lasting and reliable. In the future, with the development of new-generation polymer composites and the improvement of manufacturing techniques, polymer bolts will likely become more common and reliable.

REFERENCES

1. O'Brien, J.M.; Hosford, W.F. "Spheroidization Cycles for Medium Carbon Steels." *Metallurgical and Materials Transactions A*, Vol.33, Pages 1255–1261, 2002
2. Seo, S.W.; Jung, G.S.; Lee, J.S.; Bae, C.M.; Bhadeshia, H.K.D.H.; Suh, D.W. "Ausforming of Medium Carbon Steel." *Materials Science and Technology*, Vol. 31, Pages 436–442, 2015
3. Chen, M.; Zhai, W.; Zhu, S.; Xu, L.; Sun, Y. "Vibration-Based Damage Detection of Rail Fastener Using Fully Convolutional Networks." *Vehicle System Dynamics*, Vol.60, Pages 2191–2210, 2022
4. Shan, M.; Zhao, L.; Liu, F.; Qi, D.; Zhang, J. "Revealing the Competitive Fatigue Failure Behaviour of CFRP-Aluminum Two-Bolt, Double-Lap Joints." *Composite Structure*, Vol. 244, Pages 112-166, 2022
5. Ranjan, N. "Dimensional and Roughness Analysis of ABS Polymer-Based 3D Printed Nuts and Bolts." *Materials Today Proceedings*, Vol.48, Pages 1604–1608, 2022
6. Patpatiya, P.; Shastri, A. "Additive Manufacturing of Thermoplastic M8 Fasteners Using Photopolymer

- Jetting Technology for Low-Strength Fastening Applications”. Researchsquare, 2021
7. Parmaksız, F.; Anaç, N.; Koçar, O.; Erdogan, B. “Investigation of Mechanical Properties and Thermal Conductivity Coefficients of 3D Printer Materials.” *International Advanced Researches and Engineering Journal*, Vol. 7, Pages 146–156, 2023
8. Anaç, N.; Koçar, O.; Altuok, C., “Investigation of The Weldability of PLA Plus Sheets with Different Infill Ratios by Friction Stir Welding”, *Gazi Üniversitesi Dergisi Part C*, Vol. 12, Issue 1, Pages 282 – 296, 2024
9. Kunovjanek, M.; Knofius, N.; Reiner, G. “Additive Manufacturing and Supply Chains – a Systematic Review.” *Production Planning & Control*, Vol.33, Pages 1231–1251, 2022
10. Altıparmak, S.C.; Yardley, V.A.; Shi, Z.; Lin, J. “Extrusion-Based Additive Manufacturing Technologies: State of the Art and Future Perspectives.” *Journal of Manufacturing Processes*, Vol.83, Pages 607–636, 2022
11. Yang, K.; Bai, Y.; Ding, C. “Off-Torque and Long-Term Performance of Bolted Joints for Structural Disassembly and Reusability.” *Journal of Constructional Steel Research*, Vol.221, Pages 108-204, 2024
12. Galińska, A. “Mechanical Joining of Fibre Reinforced Polymer Composites to Metals—A Review. Part I: Bolted Joining.” *Polymers*, Vol. 12, Page 2252-2020, 2020
13. Chand, R.; Sharma, V.S.; Trehan, R.; Gupta, M.K. “A Physical Investigation of Dimensional and Mechanical Characteristics of 3D Printed Nut and Bolt for Industrial Applications.” *Rapid Prototype*, Vol.28, Pages 953–966, 2022
14. Beutler, P.; Ferchow, J.; Schlüssel, M.; Meboldt, M. “Semi-Automated Design Workflow for Bolt Clamping Interfaces to Post-Process Additive Manufactured Parts.” *Procedia CIRP*, Vol.119, Pages 596–601, 2023
15. Ferchow, J.; Kälin, D.; Englberger, G.; Schlüssel, M.; Klahn, C.; Meboldt, M. “Design and Validation of Integrated Clamping Interfaces for Post-Processing and Robotic Handling in Additive Manufacturing.” *International Journal of Advanced Manufacturing Technology*, Vol.118, Pages 3761–3787, 2022
16. Harshitha, V.; Rao, S.S. “Design and Analysis of ISO Standard Bolt and Nut in FDM 3D Printer Using PLA and ABS Materials.” *Materials Today Proceeding*, Vol.19, Pages 583–588, 2019
17. Labesh Kumar, C.; Prasad, V.; Vanaja, T. “Experimental Validation of 3-D Printed Bolts.” *International Journal of Modern Engineering Research*, Vol.3, Pages 1-12, 2017
18. Eraliev, O.; Lee, K.H.; Lee, C.H. “Self-Loosening of a 3D-Printed Bolt by Using Three Different Materials under Cyclical Temperature Changes.” *Applied Sciences*, Vol.12, Page 2001-2022, 2022
19. Alkhalaf, F.; Almughier, R.; Alolaiwy, A.; Albadrani, M. “Investigation of Elasticity in the Mechanical Properties of 3D Printed PLA Bolt Sample.” *Advances in Materials and Processing Technologies*, Vol.10, 2024
20. Zhang, Y.; Purssell, C.; Mao, K.; Leigh, S. “A Physical Investigation of Wear and Thermal Characteristics of 3D Printed Nylon Spur Gears.” *Tribology International*, Vol.141, Pages 105- 115, 2020
21. Doğru, A.; Sözen, A.; Neşer, G.; Seydibeyoğlu, M.Ö. “Numerical and Experimental Investigation of The Effect of Delamination Defect at Materials of Polyethylene Terephthalate (PET)Produced by Additive Manufacturing on Flexural Resistance.” *International Journal of 3D Printing Technologies and Digital Industry*, Vol.6, Pages 382–391, 2022
22. Kowalska, N.; Szczygieł, P.; Skrzyniarz, M.; Błasiak, S. “Influence of Machining on Selected Tensile Properties of MEX-Produced PETG Materials.” *From Smart City to Smart Factory for Sustainable Future: Conceptual Framework, Scenarios, and Multidiscipline Perspectives*, Pages 97–105, 2024
23. Popa, C.F.; Marghitas, M.P.; Galatanu, S.V.; Marsavina, L. “Influence of Thickness on the IZOD Impact Strength of FDM Printed Specimens from PLA and PETG.” *Procedia Structural Integrity*, Vol.41, Pages 557–563, 2022
24. García, E.; Núñez, P.J.; Caminero, M.A.; Chacón, J.M.; Kamarthi, S. “Effects of Carbon Fibre Reinforcement on the Geometric Properties of PETG-Based Filament Using FFF Additive Manufacturing.” *Composites Part B: Engineering*, Vol.235, Pages 109-126, 2022
25. Nazim, M.; Khan, H.A.; Khan, S.A.; Liaqat, H.; Rehman, K. “Design, Development, and Performance Evaluation of FDM-Based Fastening Techniques for Single-Lap Joints.” *The Journal of The Minerals*, Vol.76, Pages 930–940, 2024

26. Somireddy, M.; Czekanski, A. “Anisotropic Material Behavior of 3D Printed Composite Structures – Material Extrusion Additive Manufacturing.” *Material Design*, Vol. 195, Pages 108953, 2020
27. Hardware Designs for the Ultimaker 3 and Ultimaker 3 Extended Released - UltiMaker Available online: <https://ultimaker.com/learn/hardware-designs-for-the-ultimaker-3-and-ultimaker-3-extended-released/> (accessed on 21 October 2024).
28. D2240 Standard Test Method for Rubber Property—Durometer Hardness Available online: <https://www.astm.org/d2240-15r21.html> (accessed on 9 September 2024).
29. Farah, S.; Anderson, D.G.; Langer, R. “Physical and Mechanical Properties of PLA, and Their Functions in Widespread Applications — A Comprehensive Review.” *Advanced Drug Delivery Reviews*, Vol.107, Pages 367–392, 2016
30. Nguyen, T.L.; Bédoui, F.; Mazeran, P.E.; Guigon, M. “Mechanical Investigation of Confined Amorphous Phase in Semicrystalline Polymers: Case of PET and PLA.” *Polymer Engineering and Science*, Vol.55, Pages 397–405, 2015
31. Chen, H.; Pyda, M.; Cebe, P. “Non-Isothermal Crystallization of PET/PLA Blends.” *Thermochimica Acta*, Vol.492, Pages 61–66, 2009
32. Erdaş, M.U.; Yıldız, B.S.; Yıldız, A.R. “Experimental Analysis of the Effects of Different Production Directions on the Mechanical Characteristics of ABS, PLA, and PETG Materials Produced by FDM.” *Materials Testing*, Vol.66, Pages 198–206, 2024
33. Zitzenbacher, G.; Burgstaller, C.; Bembenek, M.; Kowalski, Ł.; Kosó N-Schab, A. “Research on the Influence of Processing Parameters on the Specific Tensile Strength of FDM Additive Manufactured PET-G and PLA Materials.” *Polymers*, Vol.14, Page 2446-2460, 2022
34. BASF 3D Printing Solutions PET Datasheet Available online: www.basf-3dps.com (accessed on 21 October 2024)
35. BASF 3D Printing Solutions PLA Datasheet Available online: www.basf-3dps.com (accessed on 21 October 2024)
36. Awalia, A.; Amri, N.; Sumbodo, W. “Perancangan 3D Printer Tipe Core XY Berbasis Fused Deposition Modeling Menggunakan Software Autodesk Inventor.” *Jurnal Dinamika Vokasional Teknik Mesin*, Vol.3, Pages 110–115, 2018
37. Mulyanto, F.D.; Setyoadi, Y.; Hermana, R. “The Performance Analysis of The 3D Printer Corexy FDM Type With Area X=200 Y=200 Z=200 mm.” *Jurnal Teknik Mesin Mechanical Xplore*, Vol.3, Pages 26–33, 2022



ULUSLARARASI 3B YAZICI TEKNOLOJİLERİ
VE DİJİTAL ENDÜSTRİ DERGİSİ

INTERNATIONAL JOURNAL OF 3D PRINTING
TECHNOLOGIES AND DIGITAL INDUSTRY

ISSN:2602-3350 (Online)

URL: <https://dergipark.org.tr/ij3dptdi>

THE ADVANTAGES AND IMPLEMENTATION CHALLENGES WITHIN THE SCOPE OF THE BASIC PRINCIPLES OF TRANSITION TO ZERO TRUST ARCHITECTURE

Yazarlar (Authors): Ahmet Ali SÜZEN , Osman CEYLAN 

Bu makaleye şu şekilde atıfta bulunabilirsiniz (To cite to this article): Süzen A. A., Ceylan O., “The Advantages and Implementation Challenges Within The Scope of The Basic Principles of Transition to Zero Trust Architecture” *Int. J. of 3D Printing Tech. Dig. Ind.*, 8(3): 416-427, (2024).

DOI: 10.46519/ij3dptdi.1556319

Araştırma Makale/ Research Article

Erişim Linki: (To link to this article): <https://dergipark.org.tr/en/pub/ij3dptdi/archive>

THE ADVANTAGES AND IMPLEMENTATION CHALLENGES WITHIN THE SCOPE OF THE BASIC PRINCIPLES OF TRANSITION TO ZERO TRUST ARCHITECTURE

Ahmet Ali SÜZEN^a, Osman CEYLAN^b

^a Isparta University of Applied Sciences, Faculty of Technology, Computer Engineering Department, TÜRKİYE

^b Isparta University of Applied Sciences, Uluborlu Vocational School, Department of Computer Technologies, TÜRKİYE

* Corresponding Author: ahmetsuzen@isparta.edu.tr

(Received: 26.09.2024; Revised: 29.10.2024; Accepted: 10.11.2024)

ABSTRACT

As the number of people working remotely increases, it is insufficient for organizations to protect the boundaries of their digital networks. To protect these boundaries, organizations need adaptive solutions that perform full authentication, authenticate every access request, and quickly detect and respond to both on- and off-network threats. Within this motivation, zero trust is a next generation security strategy based on the principle of “never trust, always verify”. In this study, the basic principles applied from the transition processes to zero trust architecture are evaluated and the advantages of this architecture to the security scope are examined. At the same time, the challenges that organizations that want to implement zero trust architecture will face in this transition are evaluated. The transition to zero trust architecture requires cumulative serious changes in the IT infrastructure of organizations. Zero trust architecture aims to build a system in which all information assets, users and data flow are constantly labeled as untrustworthy and therefore need to be constantly verified. The successful implementation of the zero-trust approach in organizational structures provides advantages such as dynamic authentication, increased endpoint security and strict control over data flows. However, it is also seen that challenges such as network identity management and data monitoring arise during the transition and implementation of zero trust architecture.

Keywords: Authentication, Cyber Security, Industry 5.0, Network Architecture, Zero Trust.

1. INTRODUCTION

Today, cybersecurity threats are becoming increasingly complex and traditional approaches are not sufficient to ensure the security of organizations' information systems [1]. In the wake of digitalization, threats targeting corporate network systems are increasing in both scope and complexity [2]. Given the rapid developments in the field of information technologies, particularly the proliferation of business models such as cloud computing, the use of mobile devices and remote working, traditional “perimeter-based security” models are inadequate. These models draw strict boundaries between organizations' internal and external networks, ensuring that all

elements within the internal network are secure. However, this traditional approach is not effective enough in today's distributed and dynamic corporate structures and leads to security gaps [3]. The remote working model, which has been widely used especially during and after the pandemic period, has led to the spread of the working model by establishing secure connections to corporate networks from different locations.

Zero Trust Architecture was introduced as a new generation security paradigm. Unlike traditional network security approaches, the Zero Trust model does not assume that any layer of the network is secure and provides

verification by independently evaluating each access request sent to the network [4]. The basic principle of this architecture is “never trust, always verify”. The Zero Trust principle views every entity as a potential threat, even within secure boundaries, and is based on the fact that all entities must undergo continuous authentication and authorization processes [5]. The main reason for the emergence of the Zero Trust principle is to minimize security vulnerabilities in companies and thus also to take precautions against internal threats. Especially in today's world, the widespread use of remote companies, the increasing access to services offered by cloud technology and the constant connection of users to corporate networks with various devices mean that the network's cyber attack surfaces are expanding and the number of attacks is increasing. In contrast to traditional security approaches in such architectures, the Zero Trust model aims to implement the principles of least privileged access by continuously checking communications and data traffic between systems.

Zero Trust has a security strategy that offers protection against both insider threats and external threats [4]. This architecture not only authenticates users and systems, but also implements a continuous security monitoring process by evaluating various criteria such as device health, user behavior and environmental factors. In this way, an entity accessing the system can access the system even if it is an authorized user by performing separate authentication for each resource it accesses [6].

Zero Trust Architecture has been introduced as a new generation security paradigm and makes significant contributions to meet the security requirements of Industry 5.0 based on human-machine collaboration [7]. Industry 5.0 aims for humans to play a more active role in a digitalized environment with human-machine interaction. In this case, the impact of Zero Trust Architecture on Industry 5.0 is especially important in terms of human-machine interaction and ensuring data security. Ensuring data security is a very important element in the digitalized structure of institutions. As the

digital infrastructure of Industry 5.0 continues to develop, it becomes more vulnerable to cyber threats and becomes the target of attackers [8]. Since Zero Trust Architecture adopts the approach of verifying access every time a user or system requests access, the system's resistance against these threats is increased. This provides a solution to the security needs of Industry 5.0 by ensuring the operational continuity and security of human-machine interaction in terms of data security.

The aim of this study is to assess the requirements and implementation challenges of the transition from traditional approaches to a zero-trust architecture and the impact of this process on organizational structures. In the literature, studies in this area often focus on the conceptual framework of zero trust. However, it appears that the basic principles, advantages and disadvantages, challenges and risk management involved in implementing this architecture are not sufficiently addressed. In this study, the applicability of the basic principles of the Zero Trust architecture, the challenges in the transition process and the benefits of this architecture are explained in detail. The technical and operational challenges faced by organizations currently implementing or planning to implement the Zero Trust Architecture are assessed and recommendations for organizations to successfully manage this process are presented.

2. ZERO TRUST ARCHITECTURE

Traditional network security is usually based on a perimeter-based approach. In the perimeter-based security model, the external and internal boundaries of corporate networks are defined and elements in the internal network are considered secure. This approach is usually supported by tools such as firewalls and gateways [9]. However, the weak point of this model is that attackers can move freely once they infiltrate the internal network. Considering internal computing assets as secure leads to ignoring insider threats in particular. With the proliferation of remote working, cloud-based applications and mobile devices, the expansion of network surfaces makes this traditional model even more vulnerable.

Unlike traditional network security models, Zero Trust Architecture is a security paradigm based on the principle that no entity is considered secure by default and every access request must be authenticated [5-6]. This approach is a comprehensive security strategy that enables organizations to combat insider threats as well as external threats. Zero Trust adopts an approach that can be summarized with the motto “never trust, always verify” and requires continuous monitoring and auditing to minimize security breaches.

It is known as the zero trust model for each user or system to undergo security verification. When a user or system component requests

access to a resource, it is evaluated and classified according to access policies. If the request is accepted because of this classification process, the user is classified as “Trusted” and secure access is provided. There are many logical components in the classification process and these logical components constitute the basic components of Zero Trust Architecture. The logical components used to explain the basic components of Zero Trust Architecture and the process of providing secure access in this architecture are given in Figure 1. The components shown in the figure illustrate a security model in which each access request is continuously verified through authentication and security policies [10].

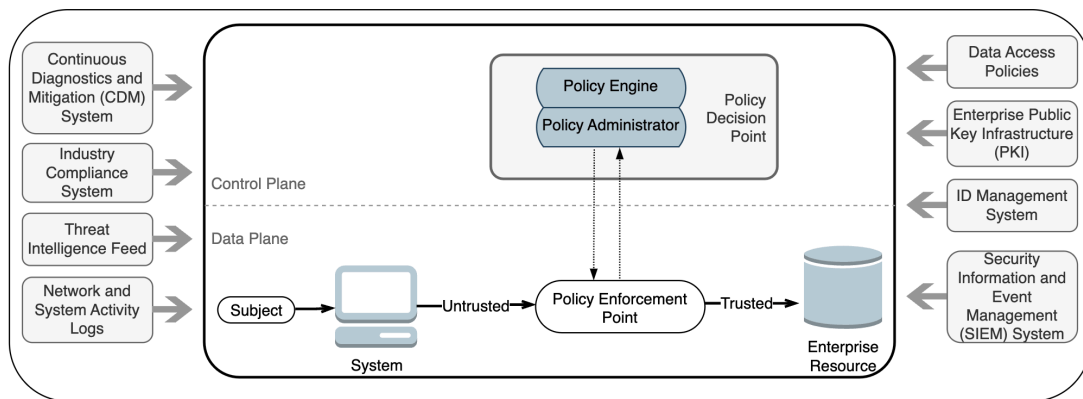


Figure 1. Core Zero Trust Logical Components [10].

2.1. Basic Principles of Zero Trust Architecture

The basic principles of zero trust architecture are based on providing a comprehensive defense against insider threats, not limiting security to threats from outside the network. This approach is based on the idea that security must be continuously verified at every point and at every level. The basic principles of Zero Trust are summarized as follows [8-9].

- **Never Trust, Always Verify:** The basic principle of Zero Trust is that every access request must be verified. This verification is not limited to user identity, but also takes into account factors such as device state, network segment, and even time and place.
- **Least Privileged Access:** Users and applications should only be authorized as

much access as they need to perform their tasks. This approach minimizes the potential attack surface and includes strict access policies to limit the impact of breaches.

- **Segmentation and Microsegmentation:** Zero Trust aims to prevent the spread of a potential attack by dividing networks into small segments. Each segment is independently protected and isolated from each other. This method provides an effective defense, especially against insider threats.
- **Continuous Monitoring and Auditing:** Zero trust requires continuous monitoring of every asset on the network and regular auditing of security controls. This process ensures that user behavior is analyzed and anomalous activity is quickly detected.

2.2. NIST SP 800-207 Framework

NIST SP 800-207 is a guide that conceptually defines the Zero Trust Architecture and describes how to implement it. This documentation emphasizes that Zero trust architecture should be considered not only as a technology solution but also as a security strategy. According to NIST SP 800-207, some key components and principles need to be considered for the successful implementation of a Zero trust architecture. These components are integrated into organizational structures to ensure that each access request is evaluated against security risk [10].

These components defined by NIST include;

- Policy Engine (PE),
- Policy Administrator (PA),
- Policy Enforcement Point (PEP)
- Data Feeds (DF) are included.

Before integrating zero trust architecture into an organization, the organization's assets, data and workflows should be determined. This provides information about the current state of an organization's data and network security before the transition to ZTA. The process of transitioning to ZTA is like other security improvements. Implementing the Risk Management Framework (RMF) steps will help an organization reduce security risk and adopt ZTA. The RMF steps involved in implementing ZTA in an organization are shown in Figure 2, including the creation of an initial inventory followed by a regular maintenance and update process. This framework, which includes steps such as the creation of an asset inventory, monitoring, evaluation and feedback, can help continuous improvement to ensure security.

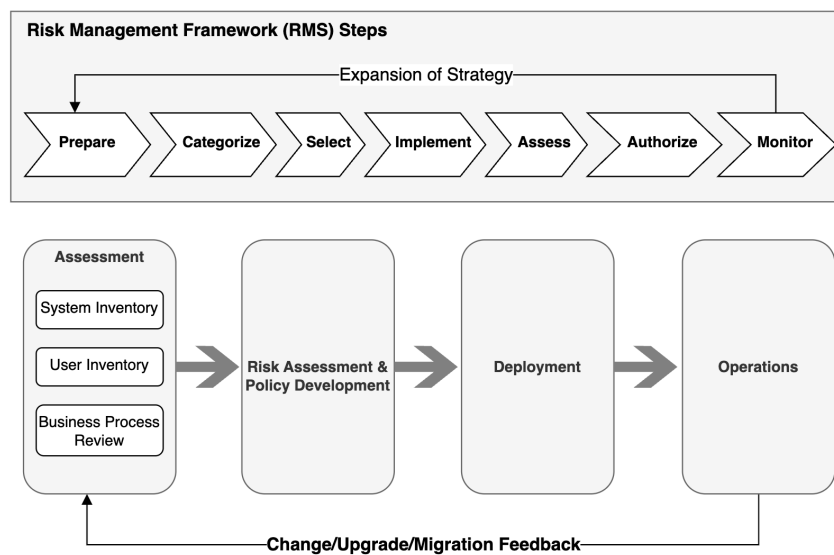


Figure 2. Zero Trust Architecture Deployment Cycle [10].

3. INTEGRATING ZERO TRUST ARCHITECTURE INTO ORGANIZATIONAL STRUCTURES

Applying the Zero Trust architecture to organizational structures is a complex process that requires reassessing and transforming the existing information technology infrastructure. This architecture requires not only technology solutions but also a restructuring of processes, policies and organizational structure. Successful integration of Zero Trust

Architecture into enterprise structures makes security a central element, taking into account the dynamic nature of systems and the ever-changing threat landscape [12].

Transitioning to a zero trust architecture in an enterprise is not only possible by upgrading the existing security infrastructure in specific areas, but by a fundamental shift in security strategy. Unlike traditional security approaches, zero trust architecture is based on the principle of not

accepting all types of network traffic as secure. Therefore, all assets of the enterprise IT infrastructure (users, devices, networks and applications) should be verified and audited at every point where they interact with each other [13].

The implementation of zero trust architecture in corporate structures requires reviewing the existing security policies of organizations and reorganizing them to comply with this architecture. This process involves not only technical elements, but also human factors and operational business processes. Implementing a zero-trust architecture will require the restructuring of a number of processes such as identity management, access control, endpoint security, data flows and continuous monitoring [13-14].

The transition to a zero trust architecture in the enterprise should be gradual and step-by-step. This transition process usually starts with the implementation of a five-step assessment scope [15].

1. **Assessment of Existing Infrastructure:** Existing systems, network structures and security policies should be comprehensively analyzed and evaluated for compatibility with zero trust architecture.
2. **Identity and Access Management:** Zero trust architecture is based on a security strategy where identity management and access control are at the center. For this reason, it is necessary to optimize the authentication processes of users and devices and to reorganize access authorizations to be least privileged.
3. **Application and Data Security:** While securing data and applications, every data flow and application traffic must be continuously monitored and verified. Micro segmentation and encryption play a key role in this process.
4. **Continuous Monitoring and Threat Detection:** Continuous monitoring and analysis, which is one of the basic principles of Zero Trust Architecture, is a

critical element to ensure the security of the corporate structure. All access requests, network traffic and user behavior should be continuously monitored, and abnormal activities should be detected.

5. **Human and Process Factor:** In addition to technological transformation, business processes and the human factor in corporate structures must also be reshaped in accordance with Zero Trust principles. Users must adapt to new access policies and authentication procedures.

The process of integrating zero trust architecture into organizational structures requires not only the purchase of new technologies, but also a change in mindset throughout the organization. A shift from a structure where security is the sole responsibility of IT teams to one where the entire organization actively contributes [16].

For this process to be successful, the following key elements should be considered [17].

- **Gradual Transition:** The transition to Zero Trust Architecture should be implemented gradually, not abruptly. A gradual integration process should be followed before the existing infrastructure and systems are completely replaced.
- **Compatibility with Legacy Systems:** It may not be possible to completely eliminate legacy systems in organizational structures. Therefore, it is important to integrate the Zero Trust Architecture with existing systems in a compatible manner.
- **Risk Management and Challenges:** Risks and challenges that may be encountered in the implementation of Zero Trust Architecture should be carefully evaluated. Organizations should pay attention to ensure business continuity during the transition process and ensure that users experience minimal disruption.

Zero Trust Architecture requires a fundamental change in the security strategies of organizations when implementing it into corporate structures. This process should be treated as a comprehensive transformation process that affects not only technological infrastructure, but also business processes and user habits. The transition to Zero Trust Architecture aims to go beyond traditional security approaches and provide a proactive security model to combat the growing threats in the modern business world [15].

3.1. Process

The implementation of a zero trust architecture in organizational structures requires a well-defined and systematic process. This process

Table 1. Process steps and breakdowns offered by RMF in the transition to Zero Trust architecture

| Process | Sub Processes |
|--|---|
| Organizational and System Preparation (PREPARE Step) | Identifying Resources and Roles Defining Security and Privacy Objectives Engagement of Key Stakeholders |
| System Categorization (CATEGORIZE Step) | Categorization of Systems Determination of Data Sensitivity |
| Control Selection (SELECT Step) | Selecting Safety Controls Extra Safety Precautions |
| Control Implementation (IMPLEMENT Step) | Implementation of Selected Controls Structuring Access Policies |
| Control Assessment (ASSESS Step) | Security Testing and Evaluation Continuous Monitoring and Threat Detection |
| System Authorization (AUTHORIZE Step) | Authorization Decision Risk Management Decisions |
| Control Monitoring (MONITOR Step) | Continuous Monitoring and Threat Detection Security Updates |

3.2. Prepare

The preparation phase is critical for the successful implementation of the Zero Trust Architecture in organizational structures. This phase includes a comprehensive assessment and planning process at both the organizational and system level. The purpose of the preparation phase is to align existing systems and processes with zero trust principles and to create the

consists of a series of steps aimed at continuously assessing and improving the security level of information systems. The Risk Management Framework (RMF) described in NIST SP 800-37 Revision 2 provides the basic methodology for this process. The RMF provides a system lifecycle approach to managing security and privacy risks and is executed through a seven-step process as shown in Table 1 [10]. This methodology ensures that systems are planned, implemented, monitored and updated in a secure manner. Following the RMF steps given in Table 1 in the transition to Zero Trust Architecture is critical to minimize security risks.

necessary infrastructure for the transition [18]. In this phase, the overall security situation of the organization is analyzed as shown in Table 2. In addition, risks are identified and necessary steps are taken to implement the zero trust architecture. Assessment of business processes and systems, at both strategic and operational levels, is essential for the successful integration of zero trust architecture.

Table 2. Process steps and breakdowns of the prepare phase in the transition to zero trust architecture

| Process | Sub Processes |
|--|--|
| Organization and Mission/Business Process Levels | Defining Mission and Security Objectives Review of Business Processes |
| System Level | Evaluation of System Architecture Review of Existing Security Controls |
| Risk Analysis | Identifying Threats and Vulnerabilities Prioritization of Risks |
| Organization and Mission/Business Process Level | Mission Driven Security ZTA Applications Suitable for Business Processes |
| System Level | Identification of Resources and System Components Selecting Appropriate Safety Measures |
| Source Categories | Workflow Specific Resources General Infrastructure Resources |
| Authorization Limit | System Components Connection Security |

3.3. Categorize

A critical step in the zero trust architecture planning process is to categorize corporate resources and workflows according to their security requirements. In this process, basic security principles such as confidentiality, integrity and availability are taken into consideration and each resource and workflow is categorized according to certain security levels as given in Table 3. The categorization of resources and workflows is the basis for the effective implementation of a zero trust architecture and helps to determine the security controls to be applied to resources [19].

In this step, resources are categorized into Low, Medium or High levels. These categories

indicate what kind of measures should be taken according to the security risk of each resource and determine which level of security will be applied in business processes. This categorization is done to ensure the security of resources and optimize the level of protection against potential threats.

Table 3. Process steps and breakdowns of the categorization phase of the Zero Trust architecture

| Process | Sub Processes |
|--|---|
| Resource Owners and Workflows | Inputs of Resource Owners Analysis of Workflows |
| System Administrators | Technical Specifications of Sources Evaluation of Existing Security Measures |
| Categorization of Resources according to Security Levels | Low Moderate High |
| FIPS 199 and FIPS 200 Standards | Confidentiality Integrity Availability |

3.4. Select

Within the Zero Trust Architecture, the select step involves identifying and implementing appropriate security controls to secure systems. This step ensures that the most appropriate security measures are defined for the systems according to the risk levels. Security controls should be tailored to the current threat environment and adapted to the requirements of business processes. In this phase, controls are selected in line with the basic principles of zero trust architecture as shown in Table 4 and the technologies required to enhance the security of business processes are identified. The selection process should be meticulously planned so that the security architecture adapts to the functional requirements and existing infrastructure of the organization [20].

Table 4. Process steps and breakdowns of the select phase in the transition to Zero Trust architecture

| Process | Sub Processes |
|------------------------------------|--|
| Control Adaptation | Basic Safety Checks Additional Safety Precautions |
| Control Overlays | Use of coatings Adaptation of coatings |
| Inputs and Planning | Inputs of Resource Owners Analysis of Business Processes |
| Continuous Monitoring and Updating | System Monitoring Updates and Security Patches |
| Additional Resources | Federal CIO Handbook and TIC 3.0 NIST SP 800-53 and 800-53B |
| Tasks and Inputs | Input from System Administrators NIST SP 800-37 Revision 2 |

3.5. Apply

Implementing security controls is a critical step for the successful integration of Zero Trust Architecture into organizational structures. The Implement phase involves integrating the security controls and policies identified in the Select step into physical and digital systems. This process provides the technical, organizational and operational steps necessary for the practical deployment of the zero trust architecture (Table 5) [17]. The infrastructure and tools required to manage and monitor systems, users and applications according to zero trust architecture principles come into play at this stage. In the implementation process, security controls are effectively implemented, making a significant contribution to minimizing risks in corporate structures.

Table 5. Process steps and breakdowns of the implement phase in the transition to Zero Trust architecture

| Process | Sub Processes |
|-----------------------------------|--|
| General Approach | Implementation of Selected Controls Least Privileged Access |
| Future Monitoring and Maintenance | Continuous Monitoring and Updating Monitoring Solutions |
| Automation and Manual Operations | Automation Manual Operations |
| Duties and Responsibilities | Managers and Operators Delegation of Tasks |

3.6. Evaluate

Once the Zero Trust Architecture has been implemented, it needs to be evaluated regularly to verify that the architecture is continuously improving and achieving its security objectives. The Assess step involves the process of measuring the effectiveness of security controls and collecting the necessary data for improvement [18]. This step tests whether the systems and security policies are suitable for a dynamic zero-trust architecture and ensures that they remain up-to-date and effective in an ever-changing threat environment (Table 6). The Assess process analyzes not only the accuracy and effectiveness of the security controls implemented, but also the impact of these controls on system performance. This step addresses issues such as how to respond to cyber security incidents and how to detect vulnerabilities in systems.

Table 6. Process steps and breakdowns of the Assess phase in the transition to Zero Trust architecture

| Process | Sub Processes |
|-------------------------------|---|
| Continuous Evaluation | Dynamic Threat Environment Evaluation on System Performance |
| Two Main Evaluation Processes | Continuous Evaluation of the System Evaluation of the Management Process |
| Automatic and Manual Controls | Automatic Scanning and Monitoring Manual Evaluation |
| Active Processes and Tests | Red Team Testing Penetration Tests |

3.7. Authorize

Authorization plays a critical role in the final phase of zero trust architecture implementations. This step refers to the formal assessment and authorization of whether a system or application meets security requirements. The authorization process ensures that a system has appropriate security controls in place before moving to the operational phase [19]. In addition, considering the dynamic nature of the zero-trust architecture, security approvals are also required during changes and updates to the systems. This step is a process that maintains the compliance of systems with security objectives through continuous evaluation and the ability to respond to dynamic changes, as shown in Table 7.

Table 7. Process steps and breakdowns of the authorize phase in the transition to Zero Trust architecture

| Process | Sub Processes |
|---------------------|--|
| Dynamic Approach | Evaluation of systems and processes The dynamic nature of zero trust architecture |
| Changes and Updates | System changes Process updates |
| Official Approval | Safety assessment Continuous monitoring and improvement |

3.8. Monitor

Monitoring is a critical component of a zero trust architecture. It involves continuous monitoring of resources, data flows and systems. Since the zero trust architecture assumes that networks and systems are not always trustworthy, it is necessary to ensure that security controls are active at all times, not just at specific times [20]. As given in Table 8, this step ensures continuous monitoring of the systems to detect new threats and react quickly to potential security breaches. The monitoring process allows early detection of security breaches and creates a rapid defense mechanism against threats. In addition, monitoring data will contribute to the development of future security policies.

Table 8. Process steps and breakdowns of the monitoring phase in the transition to Zero Trust architecture

| Process | Sub Processes |
|------------------------------------|---|
| Continuous Monitoring of Resources | Continuous monitoring of network traffic Continuous monitoring of endpoint devices |
| Technology Solutions | Available technology Data analysis and automation |
| Action Triggering | Reaction to security incidents System improvements |
| Policy Development | Observations and policy Proactive policy development |

4. TRANSITION CHALLENGES AND RISK ASSESSMENTS

While the transition to a zero-trust architecture offers significant advantages for many organizations, it also poses a variety of technical, operational and managerial challenges and risks. The core philosophy of zero trust architecture - “never trust, always verify” - represents a radical departure from traditional security approaches. In this transition, critical areas such as authentication and authorization, endpoint security, protection of data flows, and monitoring of enterprise systems stand out [21]. These challenges require organizations to restructure their workflows and IT infrastructure, update existing security policies, and adopt a new cybersecurity culture. In the following sections, the main challenges and risks in this transition process are discussed and evaluated.

4.1. Principles for Network Identity Management

A zero trust architecture requires all resources, users and devices to go through a dynamic authentication and authorization process before interacting with other entities on the network. In traditional security models, security is typically built at the perimeter of the network, and entities inside the network undergo less stringent controls. However, a zero-trust architecture requires security policies to be applied independently for each entity. In this context, network identity governance is a critical component at the core of a zero trust architecture [22].

- **Dynamic authentication and authorization:** Under a zero trust architecture, each access request must be independently authenticated. This dynamic approach ensures that users, devices and services are continuously authenticated and authorized. In traditional network models, entities are considered trusted once authenticated, whereas in zero trust architecture, each access request is subjected to a separate authentication process. In this way, every access request, even on the internal network, is treated as a threat.
- **Multi-factor authentication (MFA):** Advocates that the authentication process of a zero-trust architecture should not be limited to passwords. In particular, additional security measures such as MFA should be implemented before critical data and systems are accessed. This is an important mechanism that strengthens the security layers of the zero trust architecture and makes the authentication process more secure.
- **Identity management:** Organizations should effectively manage not only user identities but also the identities of all assets (devices, applications, services) on the network. Each asset must be continuously monitored and go through authorization processes. Identity management is a critical element, especially for large organizations that use multiple identity systems within the organization. Integrating authentication and authorization processes into a centralized structure supports the successful implementation of a zero trust architecture.
- **All data sources and computing services are considered as resources:** In a zero trust architecture, every device, every data source and every service is considered potentially untrustworthy. All resources, including endpoint devices, should be subject to the system's security policies. This approach requires continuous verification and authorization of endpoints. Organizations should keep these resources under strict security controls and monitor the movement of each resource through the system.
- **Integrity and security status of resources:** The security of endpoints also depends on keeping these devices protected with up-to-date security patches. Organizations should monitor and assess the security status of all resources they own and use. Each endpoint's configuration status, software version, security updates, etc. should be continuously checked, and security vulnerabilities should be responded to quickly when detected. This process ensures system-wide security of endpoints and increases their resilience against potential threats.

4.4. Principles Applied to Data Flows

An important component of zero trust architecture is to secure data flows. Every data flow that takes place on the network is considered a potential threat under a zero trust architecture. Therefore, data must be secured throughout the transmission process and unauthorized access must be prevented. Zero trust architecture mandates that data should only pass through securely encrypted channels and data integrity should be maintained [15].

- **All communication is secure regardless of network location:** Zero trust architecture considers all data flows as untrustworthy, regardless of whether they are internal or external. Therefore, all communications in the network must be encrypted and carried out over a secure channel. Cryptographic security measures should be used to ensure data integrity and unauthorized access should be blocked immediately.

4.3. Principles on Endpoints

The security of endpoints is of utmost importance for the successful implementation of zero trust architecture. Endpoints are among the areas where security vulnerabilities are most common. Endpoints such as mobile devices, IoT devices, virtual machines and sensors are considered the weak link of the system. Since these devices are part of the network, it is not possible to provide a holistic security without securing each of them [23].

- **Access to individual corporate resources is granted on a session-by-session basis:** In a zero-trust architecture, each access request is authenticated and authorized on a session-by-session basis. This means that every data transfer and transaction process is evaluated against security policies. Session-based control prevents unauthorized transactions and unauthorized data access.
- **Access to resources is determined by dynamic policies:** A zero-trust architecture does not limit access authorizations to resources to authentication alone. Instead, it determines access authorizations using dynamic policies such as customer identity, application state, service requirements and environmental factors. This dynamic nature allows enterprise security policies to be more fine-tuned and flexible.
- **Data collection and analysis:** A zero trust architecture requires organizations to collect as much information as possible about all entities on the network. The current state of the network, data flows and changes in system components are constantly monitored and analyzed. The collected data is used to improve the security posture of the system and detect potential threats. This process ensures a proactive security approach and increases the effectiveness of the zero trust architecture.

5. CONCLUSION

The transition to a Zero Trust architecture requires a fundamental change in the organizational security structure. However, it offers a more dynamic and comprehensive security strategy compared to traditional security models. The Zero Trust architecture is based on a system where the source, device and user are constantly authenticated and authorized and all data flows inside and outside the network are considered untrusted. The benefits of zero trust architecture include active authentication, increased endpoint security and secure monitoring of data transmissions. In particular, this approach, where potential threats within the system are not even considered trustworthy, allows organizations to develop a

proactive defense mechanism against internal and external threats. However, the challenges of implementing a zero trust architecture, such as managing network identity, endpoint security and monitoring data flow, require careful planning and technological investment.

During the transition to a zero trust architecture, organizations should conduct a comprehensive risk assessment, review their existing infrastructure and adapt their security strategies to this structure. A gradual transition and employee training are critical to the efficiency of the transition. In addition, investing in strong technological infrastructures and dynamic security systems will increase the effectiveness of zero trust architecture. As a result, zero-trust architecture allows organizations to build a more flexible and robust security structure against modern cyber threats. If the benefits and challenges that this architecture brings are handled with the right management, it will create a more secure enterprise environment and enable long-term cybersecurity success.

REFERENCES

1. Karabacak, B., "Kritik altyapılara yönelik siber tehditler ve Türkiye için siber güvenlik önerileri," Siber Güvenlik Çalıştayı, Bilgi Güvenliği Derneği, Ankara, Vol. 29, Pages 1-11, 2011.
2. Topcu, N., "Siber güvenlik: tehditler ve çözüm yolları," Cyberpolitik Journal, Vol. 6, Issue 12, Pages 155-181, 2021.
3. Thakur, K., Qiu, M., Gai, K., & Ali, M. L., "An investigation on cyber security threats and security models," IEEE 2nd International Conference on Cyber Security and Cloud Computing, Pages 307-311, November 2015.
4. He, Y., Huang, D., Chen, L., Ni, Y., & Ma, X., "A survey on zero trust architecture: Challenges and future trends," Wireless Communications and Mobile Computing, Vol. 2022, Issue 1, Article 6476274, 2022.
5. Bertino, E., "Zero trust architecture: does it help?" IEEE Security & Privacy, Vol. 19, Issue 5, Pages 95-96, 2021.
6. Syed, N. F., Shah, S. W., Shaghghi, A., Anwar, A., Baig, Z., & Doss, R., "Zero trust architecture (ZTA): A comprehensive survey," IEEE Access, Vol. 10, Pages 57143-57179, 2022.

7. Czczot, G., Rojek, I., Mikołajewski, D., & Sangho, B. (2023). AI in IIoT management of cybersecurity for industry 4.0 and industry 5.0 purposes. *Electronics*, Vol. 12, Issue 18, Pages 3800.
8. Trivedi, C., Bhattacharya, P., Prasad, V. K., Patel, V., Singh, A., Tanwar, S., ... & Sharma, G. (2024). Explainable AI for Industry 5.0: Vision, Architecture, and Potential Directions. *IEEE Open Journal of Industry Applications*.
9. D'Silva, D., & Ambawade, D. D., "Building a zero trust architecture using kubernetes," 2021 6th International Conference for Convergence in Technology (I2CT), Pages 1-8, April 2021.
10. Stafford, V., "Zero trust architecture," NIST Special Publication, Vol. 800, Issue 207, 2020.
11. Greenwood, D., "Applying the principles of zero-trust architecture to protect sensitive and critical data," *Network Security*, Vol. 2021, Issue 6, Pages 7-9, 2021.
12. Fernandez, E. B., & Brazhuk, A., "A critical analysis of Zero Trust Architecture (ZTA)," *Computer Standards & Interfaces*, Vol. 89, Article 103832, 2024.
13. Edo, O. C., Tenebe, T., Etu, E. E., Ayuwu, A., Emakhu, J., & Adebisi, S., "Zero Trust Architecture: Trend and Impact on Information Security," *International Journal of Emerging Technology and Advanced Engineering*, Vol. 12, Issue 7, Page 140, 2022.
14. Seaman, J., "Zero trust security strategies and guidelines," in *Digital Transformation in Policing: The Promise, Perils and Solutions*, Cham: Springer International Publishing, Pages 149-168, 2023.
15. Greenwood, D., "Applying the principles of zero-trust architecture to protect sensitive and critical data," *Network Security*, Vol. 2021, Issue 6, Pages 7-9, 2021.
16. Edo, O. C., Tenebe, T., Etu, E. E., Ayuwu, A., Emakhu, J., & Adebisi, S., "Zero Trust Architecture: Trend and Impact on Information Security," *International Journal of Emerging Technology and Advanced Engineering*, Vol. 12, Issue 7, Page 140, 2022.
17. He, Y., Huang, D., Chen, L., Ni, Y., & Ma, X., "A survey on zero trust architecture: Challenges and future trends," *Wireless Communications and Mobile Computing*, Vol. 2022, Issue 1, Article 6476274, 2022.
18. Ahmadi, S., "Zero trust architecture in cloud networks: Application, challenges and future opportunities," *Journal of Engineering Research and Reports*, Vol. 26, Issue 2, Pages 215-228, 2024.
19. Qazi, F. A., "Study of zero trust architecture for applications and network security," 2022 IEEE 19th International Conference on Smart Communities: Improving Quality of Life Using ICT, IoT and AI (HONET), Pages 111-116, December 2022.
20. Damaraju, A., "Implementing Zero Trust Architecture in Modern Cyber Defense Strategies," *Unique Endeavor in Business & Social Sciences*, Vol. 3, Issue 1, Pages 173-188, 2024.
21. Alevizos, L., Ta, V. T., & Hashem Eiza, M., "Augmenting zero trust architecture to endpoints using blockchain: A state-of-the-art review," *Security and Privacy*, Vol. 5, Issue 1, Article e191, 2022.
22. Gupta, A., Gupta, P., Pandey, U. P., Kushwaha, P., Lohani, B. P., & Bhati, K., "ZTSA: Zero Trust Security Architecture a Comprehensive Survey," 2024 International Conference on Communication, Computer Sciences and Engineering (IC3SE), Pages 378-383, May 2024.
23. Liu, H., Ai, M., Huang, R., Qiu, R., & Li, Y., "Identity authentication for edge devices based on zero-trust architecture," *Concurrency and Computation: Practice and Experience*, Vol. 34, Issue 23, Article e7198, 2022.



ULUSLARARASI 3B YAZICI TEKNOLOJİLERİ
VE DİJİTAL ENDÜSTRİ DERGİSİ

INTERNATIONAL JOURNAL OF 3D PRINTING
TECHNOLOGIES AND DIGITAL INDUSTRY

ISSN:2602-3350 (Online)

URL: <https://dergipark.org.tr/ij3dptdi>

A NEW SPECIFIC CARBON FOOTPRINT (SCF) THEORY OF FLOW RATE AND ENERGY CONSUMPTION VARIATIONS OF AN INDUSTRIAL INTERNAL GEAR PUMP

Yazarlar (Authors): Osman ÖZDAMAR^{ID*}, Burak ÖZTÜRK^{ID}

Bu makaleye şu şekilde atıfta bulunabilirsiniz (To cite to this article): Özdamar O., Öztürk B., “A New Specific Carbon Footprint (SCF) Theory of Flow Rate and Energy Consumption Variations of an Industrial Internal Gear Pump” *Int. J. of 3D Printing Tech. Dig. Ind.*, 8(3): 428-436, (2024).

DOI: 10.46519/ij3dptdi.1563398

Araştırma Makale/ Research Article

Erişim Linki: (To link to this article): <https://dergipark.org.tr/en/pub/ij3dptdi/archive>

A NEW SPECIFIC CARBON FOOTPRINT (SCF) THEORY OF FLOW RATE AND ENERGY CONSUMPTION VARIATIONS OF AN INDUSTRIAL INTERNAL GEAR PUMP

Osman ÖZDAMAR^a , Burak ÖZTÜRK^b 

^aBilecik Şeyh Edebali University, Osmaneli Vocational School of Higher Education, TURKEY

^bBilecik Şeyh Edebali University, Metallurgical and Materials Engineering, TUREY

* Corresponding Author: osman.ozdamar@bilecik.edu.tr

(Received: 08.10.2024; Revised: 25.11.2024; Accepted: 04.12.2024)

ABSTRACT

Pumps in fuel oil systems are mechanical equipment used for the transfer of liquid fluid from one place to another. In particular, pumps are required to transfer the maximum flow rate in the transfer units in minimum time. They consume a very high amount of energy for this transfer. In this research, research studies were carried out to ensure the transfer of the highest possible amount of fuel oil by consuming energy at optimal rates. In this experimental study, the energy consumption and flow rate were measured across a range of engine speeds (100-700 RPM) and varying gear lengths (90-100 mm). According to the findings, energy consumption reached ideal levels at 600 RPM engine speed. In addition, it was determined that the lowest CO₂ emission was obtained in the range of 600-700 RPM and by using long gear length. In addition, it is observed that the effect of gear length on energy efficiency is significant and energy consumption decreases as the gear length gets shorter. The results show that minimum energy consumption can be obtained with maximum flow rate at 609 RPM engine speed and 100 mm gear length. The ANOVA analysis used in the study reveals that the flow rate changes are 98% related to the engine speed, while the gear length is 78% effective in CO₂ emission reduction. This research provides an important contribution to energy efficiency and carbon emission reduction in industrial applications. This study provides an innovative method that can be used to achieve energy saving and environmental sustainability goals and makes valuable contributions to the literature on optimizing internal gear pump designs.

Keywords: Carbon Footprint, Energy Efficiency, Energy Consumption, Internal Gear Pump.

1. INTRODUCTION

Pumps are machines that can use electrical energy for fluid transfer through a mechanical transfer system. It is a part of a transfer system used to transport all kinds of fluids from one place to a desired different place and to control the amount of flow (flow rate) [1]. The rapid filling or emptying of tanks is one of the most important factors directly affecting the performance of these systems. However, it is not enough to perform this process quickly. It is also very important to work with minimum energy consumption during this transfer process. In other words, the system must both work fast and provide energy efficiency. Thus, performance can be kept at the highest level while reducing costs [2-3].

Technically, "energy efficiency" means using fewer energy inputs while maintaining the same level of economic activity or service, whereas "energy conservation" is a broader concept that includes reducing consumption through behavioral change or reduced economic activity. In practice, it is difficult to distinguish between these two concepts and the terms are often used interchangeably [4]. Energy efficiency means producing the same amount of goods and services using less energy or producing more goods and services with the same amount of energy. When this is achieved, businesses can gain competitive advantage both locally and internationally [5].

Among the machines that consume electricity, pumps are one of the highest energy consumers with a share of 20%. Therefore, the appropriate use of pump systems and energy efficiency has become an important issue. Although improvements in pump efficiency are limited, it has been determined that up to 30% energy savings can be achieved with proper design and optimization of pump systems [6]. Design parameters in pumps have a direct impact on efficiency and energy consumption; these parameters affect pump performance and energy consumption [7]. At the same time, the use of highly efficient pumps alone is not sufficient for a pumping system to operate at maximum efficiency. Efficient operation of pumping systems depends not only on the design of the pump, but also on the correct design of the entire system and favorable operating conditions. In an incorrectly designed or incorrectly installed system, even the most efficient pump cannot perform as expected and can become inefficient [8]. Therefore, it should not be forgotten that system design and installation play an important role in energy efficiency as well as design parameters.

Pumps are inefficient systems that cause the loss of approximately 40% of energy inputs. Optimization of these systems can be achieved through strategies such as correction of misconfigured pump systems, replacement of old and high maintenance cost systems and detection of damaged pumps. Such improvements can lead to significant energy savings in motorized pump systems, which account for approximately 25% of energy consumption in the manufacturing sector [9].

In the study conducted by Bae et al., the rotor profile was optimized using automatic design methods and multiple calculation programs, taking into account fuel efficiency and low torque demands. During the design process, various parametric analyses and calculations were performed to obtain the ideal rotor profile. The prototypes were subjected to performance tests and the calculated torque values were compared with experimental data.

The results show that the calculated torque values show high agreement with the experimental data, and this agreement reveals the accuracy of the design and simulation processes. This result proved that the rotor

design was successful in achieving the efficiency and performance targets. [10]. In his study, Akhan achieved significant energy savings by using frequency inverter in variable flow fan and pump systems. In the study, thanks to the use of frequency inverter, the efficiency of the systems was optimized and energy consumption was reduced by 60% [11].

The highly efficient P/M internal gear pump rotors developed by Sasaki and his team are called Megaflod rotors and respond to the demands for fuel consumption reduction and hydraulic power increase in the automotive industry. These rotors are equipped with an innovative tooth profile and offer a discharge volume of 10% or more compared to conventional rotors of the same size. Thanks to these features, the pumps can be produced in smaller sizes and operate with lower torque, resulting in significant improvements in fuel efficiency. Megaflod rotors are widely used, especially in automotive engine oil pumps, contributing to energy efficiency targets in the industry [12]. In their study, Öztürk and Küçük developed a new gear pump design to optimize energy consumption. This design, obtained by using the Fundamental Motion Analysis method, aims to provide maximum flow rate with low energy consumption during fuel transfer. In the study, the effects of engine speed and gear design on energy consumption were investigated and it was determined that energy consumption was minimized especially in the 500-600 RPM range. In the experiments, it is predicted that 3506 kWh energy saving can be achieved annually with the newly developed spur gear pump design.[2]. In their study, Öztürk et al. present an experimental investigation on the optimization of energy consumption of internal gear pumps using Taguchi and Response Surface Method (RSM). In the study, the effects of the pump design parameters of tooth length and motor speed on flow rate, power consumption and specific energy consumption (SEC) were investigated. The optimum motor speed was determined as 700 RPM and tooth length as 85 mm, and energy consumption was reduced by 41% from 156.1 Wh/m³ to 92.0 Wh/m³ with the new pump design. The effect of flow rate change on energy consumption was found to be 83% [13]. Artificial Neural Networks, RSM, and Taguchi techniques are frequently used in various fields and diverse industrial applications due to their

robust sensing and optimization capability [14-17]. In a study conducted by the American Hydraulic Institute, 20% of the energy consumed in developed countries is consumed by pumps. It is explained that 30% of this energy can be saved with a good system design and selection of suitable pumps [18].

The need for energy in the world has emerged in four different areas: industry, transport, housing and trade. The highest energy consumption is realized in industry with 51% and in transport with 27% (Figure 1). Energy consumption in production worldwide has been increasing continuously for the last 20 years and it is predicted that it will be in a continuous increase for the next 20 years (Figure 2). The limited availability of energy resources has led to a continuous increase in energy costs [19].

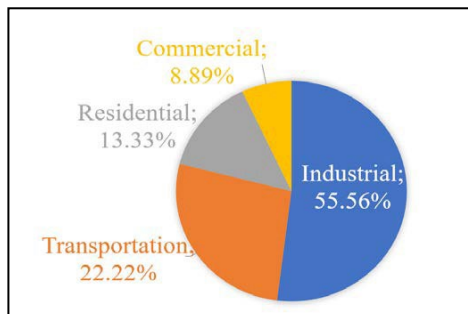


Figure 1. Energy consumption areas in the world [19].

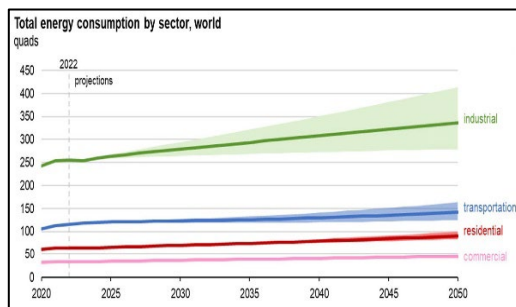


Figure 2. Total energy consumption by sector, World [19].

The concepts of sustainable production and energy efficiency are of great importance in modern engineering practice. Studies in these fields aim to save energy, optimize resource use and reduce environmental impacts in production processes. In particular, life cycle assessment and resource efficiency strategies in manufacturing processes are widely applied to increase environmental and economic sustainability in production [20-22].

Strategies to improve energy efficiency and optimise resource use increase production efficiency by reducing energy intensity in industrial processes. In this way, businesses reduce their carbon footprint while at the same time reducing costs [22].

Carbon footprint is one of the most widely used indicators to measure climate impacts today. Since its introduction in public relations, various stakeholders have continued their efforts to reduce their carbon footprint and communicate this to customers and other interested parties. Carbon footprinting is a component of life cycle assessment (LCA) that focuses solely on greenhouse gas emissions. LCA is guided by ISO 14040-44:2006 standards, while carbon footprint calculations are performed according to ISO 14067:2018 standard [23].

In this study, experimental design methods using RSM (Response Surface Method) will be applied for the design and optimization of energy consumption and energy efficiency. In this way, it is aimed to develop an ideal pump to increase sustainability.

2. MATERIAL AND METHOD

In the calculation of active power in 3-phase electric motors, it is calculated with parameters such as the energy load (I) measured with an ammeter and the voltage value (V) of the motor. For three-phase motors, this power consumption is calculated in kW using energy power conversion equations. The generally used equation is converted into kW power consumption with the equation (Equation 1). I =Energy load measured by ammeter (A), $\cos \sigma$ =Power Factor (Induction Motor; 0,85) [8, 24,25].

$$P_{total} = \sqrt{3} \cdot V \cdot I \cdot \cos \sigma \quad (1)$$

Carbon footprint is a measure of the total emissions of carbon dioxide (CO₂) and other greenhouse gases released directly or indirectly into the atmosphere by individuals, businesses or products. These emissions can come from a variety of sources, such as the burning of fossil fuels, deforestation and agricultural activities. The carbon footprint is usually expressed in terms of carbon dioxide equivalents (CO_{2e}), which provides a combined measure of the impacts of different greenhouse gases on the climate. According to a report published by

Defra, based on 2023 data, the emission factor for natural gas is 0.202 kg CO_{2e} per kilowatt-hour (kWh), while the emission factor for coal used in electricity generation is 0.33 kg CO_{2e} per kilowatt- hour. However, after taking into account all production types and related processes, the average emission factor is considered to be 0.48 kg CO_{2e} per kilowatt-hour (Equation 2) [26,27].

$$CF(t)(CO_2) = 0.48 \times \sum_{k=1}^{\Delta t} kWh \quad (2)$$

The Surface Method (RSM) has been used to determine the optimal machining conditions of extruded aluminum parts. Developed in 1951 by Box and Wilson, RSM provides fast and sequential results for the improvement, optimization and modelling of complex processes in industrial experiments [28]. This method designs a series of experiments with the aim of obtaining optimal results by analyzing the interactions between various independent variables and one or more response variables [29,30]. When the linear function of the independent variable closely matches the response of the system, the approximation is modelled using a first-order equation [31]. In this research study, the selection of the gear length and the number of revolutions required to provide the most ideal fuel oil transfer during this process while ensuring minimum energy consumption was carried out using the RSM method.

Table 1. RSM Experiment Design.

| RPM | Length (mm) | StdOrder | RunOrder | Blocks | PtType |
|-----|-------------|----------|----------|--------|--------|
| 100 | 100 | 1 | 1 | 1 | 1 |
| 200 | 100 | 2 | 2 | 1 | 1 |
| 300 | 100 | 3 | 3 | 1 | 1 |
| 400 | 100 | 4 | 4 | 1 | 1 |
| 500 | 100 | 5 | 5 | 1 | 1 |
| 600 | 100 | 6 | 6 | 1 | 1 |
| 700 | 100 | 7 | 7 | 1 | 1 |
| 100 | 90 | 8 | 8 | 1 | 1 |
| 200 | 90 | 9 | 9 | 1 | 1 |
| 300 | 90 | 10 | 10 | 1 | 1 |
| 400 | 90 | 11 | 11 | 1 | 1 |
| 500 | 90 | 12 | 12 | 1 | 1 |
| 600 | 90 | 13 | 13 | 1 | 1 |
| 700 | 90 | 14 | 14 | 1 | 1 |

While the speed change in the range of 100-700 RPM was determined as the parameter level, the gear length of 90-100 mm was selected as the second parameter. The pump body and gear

were manufactured by turning on a lathe according to the technical drawing dimensions. Table 1 shows the RSM experiment design. The thrust gear pump used in the experiments and the IPT Fuel Oil test system where the tests were performed are shown in Figure 3. Within the scope of university - industry cooperation, all experiments were carried out with the support of the R&D unit of the factory and all results were reported and then the necessary statistical analysis was carried out.



Figure 3. Pump efficiency test unit.



Figure 4. Internal gear pump

3. EXPERIMENTAL FINDINGS

All test results performed according to the experimental design are presented in Table 2.

Table 2. Experiment Results.

| Volume (Lt) | Power (W) | SEC (kW/lit) | SCF (CO ₂) |
|-------------|-----------|--------------|------------------------|
| 108 | 1140 | 94.74 | 45.5 |
| 226 | 1980 | 114.14 | 54.8 |
| 326 | 2620 | 124.43 | 59.7 |
| 440 | 3340 | 131.74 | 63.2 |
| 560 | 4220 | 132.70 | 63.7 |
| 600 | 5070 | 118.34 | 56.8 |
| 660 | 5700 | 115.79 | 55.6 |
| 89 | 865 | 102.89 | 49.4 |
| 188 | 1520 | 123.68 | 59.4 |
| 280 | 2150 | 130,23 | 62.5 |
| 390 | 2540 | 153.54 | 73.7 |
| 480 | 2880 | 166.67 | 80.0 |
| 560 | 3200 | 175.00 | 84.0 |
| 600 | 3600 | 166.67 | 80.0 |

Specific energy consumption values are considered as an important indicator in determining the ideal energy consumption. As a result of the analyses, it was observed that the ideal energy consumption value was reached at 600 RPM. In instantaneous current changes, it has been determined that a significant reduction in energy consumption is achieved by reducing the gear length. In particular, the instantaneous power consumption was reduced from 5.7 kW to 3.6 kW. The lowest CO₂ emission results were obtained in the 600-700 RPM ranges with the use of gears between 200-300 mm in length. Similar results were obtained in the studies conducted in the literature [32,33]. However, it is considered that these ranges may not always be a suitable choice due to the low amount of flow rate required at lowspeed ranges. Figure 5 shows the SCF (Stress Concentration Factor) and Figure 6 shows the Probability Plot graph showing the accuracy of the values obtained for the volume results. It can be stated that the results obtained are within the lower and upper limit value range and the experiments are completed within the desired confidence interval.

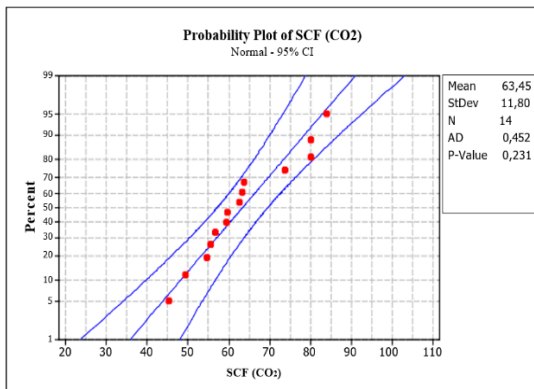


Figure 5. Probability Plot of SCF (CO₂) Results.

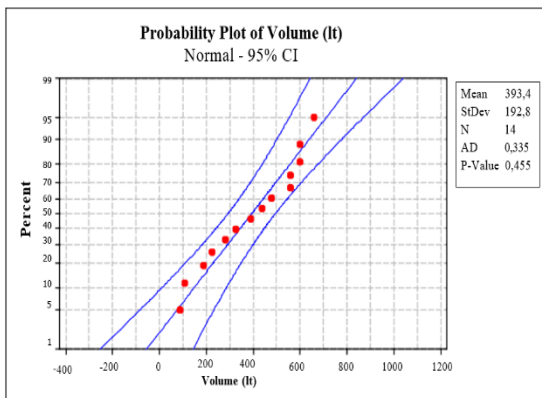


Figure 6. Probability Plot of Volume (Lt) Results.

Figures 7, 8 and 9 show the Surface Plot graphs generated using the Response Surface Methodology (RSM) method.

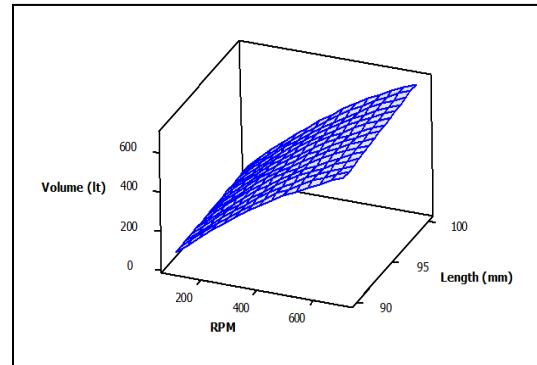


Figure 7. RSM surface plot of volume.

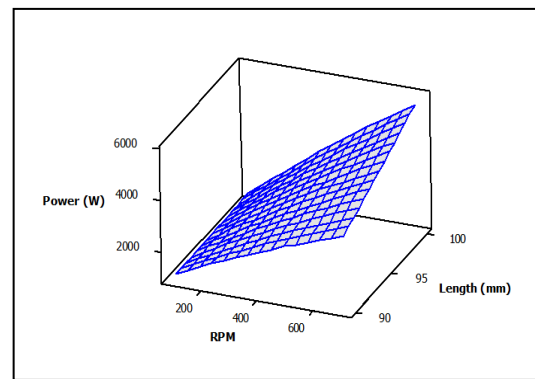


Figure 8. RSM surface plot of power.

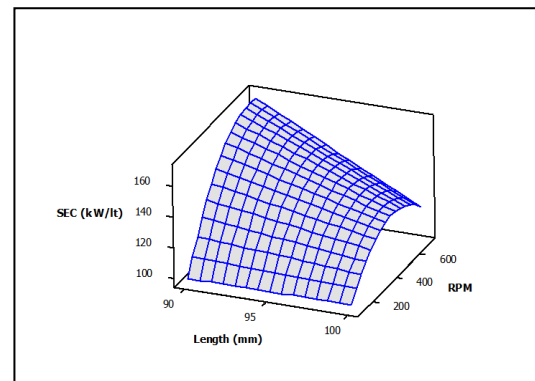


Figure 9. RSM surface plot of SEC.

These graphs provide a clear observation of the effects of level changes in the experimental parameters on the results. It was found that the increase in the number of revolutions has a direct effect on the volume change, but the gear length does not contribute much to this change. In terms of power index change, both gear length and speed change were found to be effective at approximately similar rates. SEC (Specific Energy Consumption) and SCF (Stress Concentration Factor) graphs showed

similar results and the maximum value of both parameters was obtained at 400 RPM. This shows the most critical range for both energy consumption and CO₂ emission of the pumps. However, the surface plot graphs for energy consumption and CO₂ emissions exhibit a parallel trend.

The RSM Optimizer results in Figure 10 allowed the determination of the ideal pump operating range. RSM Optimizer is able to evaluate the ideal values of the results according to the order of importance and thus enables the determination of optimum conditions. According to the analyses, it is predicted that maximum flow rate, minimum energy consumption and accordingly minimum CO₂ emission can be obtained by producing at a speed of 609 RPM and a gear length of 100 mm.

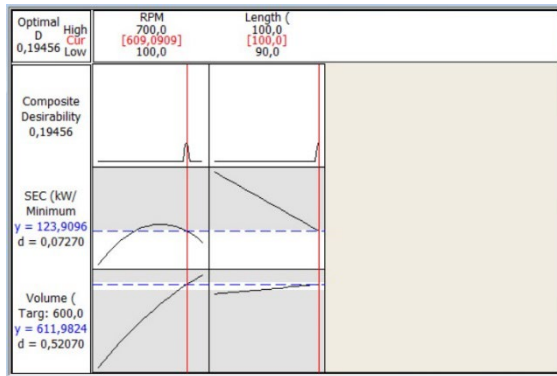


Figure 10. RSM Optimizer.

Table 3 shows the ANOVA results which provide information about the effect rates of the experimental design parameter on the results

Table 3. ANOVA results.

| | Source | DF | Seq SS | Adj SS | Adj MS | F | P | % Effect |
|------------------------|-------------|----|----------|----------|---------|--------|-------|----------|
| Volume (L) | RPM | 6 | 474353 | 474353 | 79059 | 435.24 | 0 | 98.1 |
| | Length (mm) | 1 | 7921 | 7921 | 7921 | 43.61 | 0.001 | 1.6 |
| | Error | 6 | 1090 | 1090 | 182 | | | |
| | Total | 13 | 483363 | 483363 | | | | |
| Power (W) | RPM | 6 | 20396496 | 20396496 | 3399416 | 12.72 | 0.003 | 47.1 |
| | Length (mm) | 1 | 3822088 | 3822088 | 3822088 | 14.3 | 0.009 | 52.9 |
| | Error | 6 | 1603225 | 1603225 | 267204 | | | |
| | Total | 13 | 25821809 | | | | | |
| SCF (CO ₂) | RPM | 6 | 931.06 | 931.06 | 155.18 | 3.07 | 0.099 | 21.3 |
| | Length (mm) | 1 | 574.3 | 574.3 | 574.3 | 11.36 | 0.015 | 78.7 |
| | Error | 6 | 303.39 | 303.39 | 50.57 | | | |
| | Total | 13 | 1808.76 | | | | | |

[34]. When these results are taken into consideration, volume changes are 98% related to the number of revolutions. In other words, a change in gear size for flow rate change does not have a significant effect. In the instantaneous power consumption, it can be said that a contribution of almost 50% - 50% is provided. In other words, it has been observed that reducing the gear size reduces energy consumption at a very high rate. According to these results, it is determined that the gear size is 78% effective in CO₂ emission reduction studies.

3.1 ANOVA Results and Evaluation

In Table 3, ANOVA (Analysis of Variance) results showing the effects of the experimental design parameters on the results are given.

According to these results, it is determined that 98% of the volume changes are related to the speed. This shows that a change in gear size does not have a significant effect in terms of flow rate change [35]. On the other hand, speed and gear size have an effect on instantaneous power consumption by approximately 50%-50%. This shows that reducing the gear size leads to a significant reduction in energy consumption. In CO₂ emission reduction studies, it has been determined that the gear size is 78% effective in line with these results. These findings show that optimizing the gear size is critical for energy efficiency and environmental impacts [36].

4. RESULTS

In this study, the effects of different engine speeds (100-700 RPM) and gear lengths (90-100 mm) on the flow rate and energy consumption of an industrial internal gear pump were investigated. According to the findings, it was found that the energy consumption reached ideal levels at 600 RPM engine speed and the lowest CO₂ emission was obtained in this speed range. The effect of gear length on energy consumption is remarkable and significant reductions in energy consumption are achieved with decreasing gear length. In particular, it was observed that the instantaneous power consumption was reduced from 5.7 kW to 3.6 kW. These findings indicate that gear size is a crucial parameter for optimizing the system in terms of energy efficiency.

In addition, according to the results of ANOVA analyses, it was determined that the flow rate variations were related to engine speed by 98% and gear length was effective in reducing CO₂ emissions by 78%. These results show that optimizing the engine speed and gear length provides significant contributions in terms of energy efficiency and environmental sustainability.

As a result of the experimental studies, maximum flow rate and minimum energy consumption were obtained at 609 RPM motor speed and 100 mm gear length. This study presents an innovative approach to improve energy efficiency and reduce carbon footprint in the design of internal gear pump systems. The findings of the study provide an important guide to save energy and minimize environmental impacts in industrial applications.

ACKNOWLEDGES

This study was conducted with the support of IPT Akaryakıt Malzemeleri Petrol Kimya Sanayi ve Ticaret Ltd. Şti. The authors would like to extend their sincere gratitude to the company for providing access to their R&D facilities and experimental setups. Their contributions significantly enhanced the quality and scope of this research.

REFERENCES

- 1 S. Chakraborty and K. Pandey, "Numerical Studies on Effects of Blade Number Variations on Performance of Centrifugal Pumps at 4000 RPM," *International Journal of Engineering and Technology*, Vol. 3, Issue 4, Pages 410, 2011.
- 2 B. Öztürk and Ö. Küçük, "Development of a New Pump Gear Using Basic Motion Analysis for Optimisation in Energy Consumption," **Bilecik Şeyh Edebali University Journal of Science and Technology*, Vol. 6, Issue 1, Pages 49-57, 2019.
- 3 İ. Düzdar Argun, B. Kantoğlu, and B. Öztürk, "A New Product Design After Benchmarking Analysis of Helix Gear Pumps and Optimisation in Energy Consumption," *Düzce University Science and Technology Journal**, Vol. 6, Issue 3, Pages 610-617, 2018.
- 4 N. Di Franco and M. Jorizzo, "Efficiency, Energy Saving, and Rational Use of Energy: Different Terms for Different Policies," *Innovation in Energy Systems-New Technologies for Changing Paradigms*, T.S. Ustun (Ed.), Pages 93-112, 2019.
- 5 M. Aydın, "The Role of Energy Efficiency in Sustainable Development: An Assessment of Turkey," *Journal of Management Sciences*, Vol. 14, Issue 28, Pages 409-441, 2016.
- 6 Z. Yumurtaci and A. Sarigul, "Energy Efficiency and Applications in Centrifugal Pumps," *Chamber of Mechanical Engineers Journal of Installation Engineering*, Pages 49-58, 2011.
- 7 M. Golcu, Y. Pancar, and Y. Sekmen, "Energy Saving in a Deep Well Pump with Splitter Blade," *Energy Conversion and Management*, Vol. 47, Issue 5, Pages 638-651, 2006.
- 8 D. Kaya, F. Çanka Kılıç, and H.H. Öztürk, "Energy Efficiency in Pumps," in *Energy Management and Energy Efficiency in Industry: Practical Examples*, Springer, Pages 329-374, 2021.
- 9 J.L. Pellegrino, N. Margolis, M. Justiniano, M. Miller, and A. Thedki, "Energy Use, Loss, and Opportunities Analysis for US Manufacturing and Mining," *Energetics Inc.*, Columbia, MD, USA, 2004.
- 10 J.-H. Bae and C. Kim, "Design of Rotor Profile of Internal Gear Pump for Improving Fuel Efficiency," *International Journal of Precision Engineering and Manufacturing*, Vol. 16, Pages 113-120, 2015.

- 11 H. Akhan, "Energy Management in Industry: Efficiency Increasing Applications in Pump and Fan Systems," *Trakya University Journal of Engineering Sciences*, Vol. 23, Issue 1, Pages 11-23, 2022.
- 12 H. Sasaki, N. Inui, Y. Shimada, and D. Ogata, "Development of High Efficiency P/M Internal Gear Pump Rotor (Megafloid Rotor)," *SEI Technical Review-English Edition*, Vol. 66, Pages 124, 2008.
- 13 B. Öztürk, Ş. Kaymak, and Ö. Küçük, "Taguchi and RSM Based Optimization of Energy Consumption on Internal Gear Pumps," *International Journal of 3D Printing Technologies and Digital Industry*, Vol. 6, Issue 1, Pages 164-175, 2022.
- 14 Y. O. Alpay, İ. Uygur, M. Kılınçel, and G. Samtaş, "Cure cycle optimization of infrared cured composites using Taguchi method," *Journal of Applied Polymer Science*, Vol. 140, Issue 22, Pages e53922, 2023.
- 15 I. Uygur, A. Cicek, E. Toklu, R. Kara, and S. Saridemir, "Fatigue life predictions of metal matrix composites using artificial neural networks," *Archives of Metallurgy and Materials*, Vol. 59, Issue 1, Pages 97-103, 2014.
- 16 Ç. V. Yıldırım, T. Kıvak, F. Erzincanlı, İ. Uygur, and M. Sarıkaya, "Optimization of MQL Parameters Using the Taguchi Method in Milling of Waspaloy," *Gazi University Journal of Science*, Vol. 30, Issue 2, Pages 173-186, 2017.
- 17 Oktem, H., Uygur, I., Sarı, E. S., & Shinde, D. "The hybrid approach of genetic algorithm and particle swarm optimization on reduced weld line defect in plastic injection molding." *Progress in Rubber, Plastics and Recycling Technology*, 2024.
- 18 A.Ö. Ertöz, "Energy Efficiency in Pumps," *Tesisat Journal*, Vol. 95, Pages 192, 2003.
- 19 U.S. Energy Information Administration, "International Energy Outlook 2023 with Projections to 2050," IEO2023 Release, CSIS, Available: <https://www.eia.gov/outlooks/ieo/October 11, 2023>.
- 20 S.A. Blume, "Resource Efficiency in Manufacturing Value Chains," Springer International Publishing, Pages 9-40 Springer, 2020.
- 21 C. Hermann and S. Kara, "Sustainable Production, Life Cycle Engineering and Management," Springer International Publishing, 2012.
- 22 J. Dufloy, K. Kellens, and W. Dewulf, "Unit Process Impact Assessment for Discrete Part Manufacturing: A State of the Art," *CIRP Journal of Manufacturing Science and Technology*, Vol. 4, Issue 2, Pages 129-135, 2011.
- 23 T.V. Uimonen, "Development of Climate Responsible Actions for a Pump Manufacturer," Master's Thesis, Lappeenranta-Lahti University of Technology, 2022.
- 24 B. Öztürk and Ö. Küçük, "Special Energy Consumption Model for Two Different Types of Production of Pipe Fittings Reinforced with Copper and Brass Filings (SEC)," *Polytechnic Journal*, 2019.
- 25 B. Öztürk, "Optimization in Mass Production Energy Consumption of Solid Brass Pipe Fitting," *Technological Applied Sciences*, Vol. 14, Issue 3, Pages 68-79, 2019.
- 26 İ. Alagöz, E. Coşkun, S. Babaoğlu, R. Kaykaç, and A. Cıdacı, "Calculating the Carbon Footprint of EÜAŞ Central Campus 2021," *Environment Climate and Sustainability*, Vol. 23, Issue 2, Pages 161-166, 2022.
- 27 W. Lin et al., "A Multi-Objective Teaching-Learning-Based Optimization Algorithm to Scheduling in Turning Processes for Minimizing Makespan and Carbon Footprint," *Journal of Cleaner Production*, Vol. 101, Pages 337-347, 2015.
- 28 M. Jenarathanan and N. Neeli, "Mathematical Modelling of Delamination Factor on Drilling of ARALL Composites through RSM," *Multidiscipline Modelling in Materials and Structures*, Vol. 13, Issue 4, Pages 578-589, 2017.
- 29 B. Öztürk, "Investigation of Effects of Inverter Frequency Changes on the Specific Energy Consumption of Pipe Threading Using Response Surface Methodology," *Measurement*, Vol. 152, Pages 107296, 2020.
- 30 E. Nas, "Analysis of the electrical discharge machining (EDM) performance on Ramor 550 armor steel," *Materials Testing*, Vol. 62, Issue 5 Pages 481-491, 2020.
- 31 K. Panneerselvam and K. Lenin, "Parameters Optimization in FSW of Polypropylene Based on RSM," *Multidiscipline Modelling in Materials and Structures*, Vol. 11, Issue 1, Pages 32-42, 2015.
- 32 B. Öztürk and Ö. Küçük, "Enerji Tüketiminde Optimizasyon İçin Temel Hareket Analizi Kullanılarak Yeni Bir Pompa Dişlisinin Geliştirilmesi, Bilecik Şeyh Edebali Üniversitesi Fen Bilimleri Dergisi," Vol. 6, Issue 1, Pages 49-57, 2019.

33 Öztürk, B., Endüstriyel Bir İçten Dişli Pompanın Debi Ve Enerji Tüketim Değişimlerinin İncelenmesi. 4th International Congress On 3d Printing (Additive Manufacturing) Technologies and Digital Industry, Antalya /Turkey 2019

34 E. Nas, B. Öztürk, "Optimization of surface roughness via the Taguchi method and investigation of energy consumption when milling spheroidal graphite cast iron materials," Materials Testing, Vol. 60 Issue 5, Pages 519-525, 2018.

35 Yalçın, E., Oral, O., & Devecili, A. O. Dişli Pompaların Mekanik Veriminin Artırılması. Bilecik Şeyh Edebali Üniversitesi Fen Bilimleri Dergisi, Vol. 8, Issue 2, Pages 553-566. 2021.

36 Demir, Yıldırım, Şakir İşleyen, and Kerem Özen. "Seçili Enerji Tüketimlerinin Karbondioksit Emisyonu Üzerindeki Etkisinin ARDL Sınır Testi ile Belirlenmesi." Yüzüncü Yıl Üniversitesi Sosyal Bilimler Enstitüsü Dergisi, Vol. 59, Pages 80-107. 2023



ULUSLARARASI 3B YAZICI TEKNOLOJİLERİ
VE DİJİTAL ENDÜSTRİ DERGİSİ

INTERNATIONAL JOURNAL OF 3D PRINTING
TECHNOLOGIES AND DIGITAL INDUSTRY

ISSN:2602-3350 (Online)

URL: <https://dergipark.org.tr/ij3dptdi>

OPTIMIZATION OF ENERGY CONSUMPTION IN CNC MARBLE PROCESSING: STATISTICAL AND MACHINE LEARNING APPROACHES

Yazarlar (Authors): Gencay Sarıışık^{id*}, Ahmet Sabri Öğütlü^{id}

Bu makaleye şu şekilde atıfta bulunabilirsiniz (To cite to this article): Sarıışık G., Öğütlü A. S., "Optimization of Energy Consumption in CNC Marble Processing: Statistical and Machine Learning Approaches" *Int. J. of 3D Printing Tech. Dig. Ind.*, 8(3): 437-450, (2024).

DOI: 10.46519/ij3dptdi.1564924

Araştırma Makale/ Research Article

Erişim Linki: (To link to this article): <https://dergipark.org.tr/en/pub/ij3dptdi/archive>

OPTIMIZATION OF ENERGY CONSUMPTION IN CNC MARBLE PROCESSING: STATISTICAL AND MACHINE LEARNING APPROACHES

Gencay Sarıışık^a , Ahmet Sabri Öğütlü^a 

^a Harran University, Engineering Faculty, Industrial Engineering Department, TÜRKİYE

* Corresponding Author: gsariisik@gmail.com

(Received: 10.10.2024; Revised: 26.11.2024; Accepted: 03.12.2024)

ABSTRACT

This study aims to evaluate the specific energy consumption during marble processing on CNC machines both by traditional statistical methods and machine learning models. It presents an analytical framework that examines the effects of process parameters to improve energy efficiency in CNC machining processes. In the experimental part, a data set of 5400 observations was obtained considering different machining types, depths of cut and feed rates. Analysis of Variance (ANOVA) and regression models confirmed the decisive role of material removal rate (MRR) on specific energy consumption. The study comprehensively analyzed the performance of four different machine learning models (Gradient Boosting, Random Forest, XGBoost, LightGBM) to predict the specific energy consumption during marble processing on CNC machines. The findings show that specific energy consumption is an important parameter for energy efficiency and cost reduction. The accuracy of the models was evaluated with metrics such as R^2 , RMSE and MAE, and as a result, it was found that Gradient Boosting and XGBoost models outperformed the others in the Spiral machining type. These findings provide a solid basis for developing strategies to improve energy efficiency in marble processing on CNC machines. The study provides important information that can help make strategic decisions to save energy and improve environmental sustainability. Providing valuable guidance for future research, this study demonstrates the potential use of machine learning models to improve energy efficiency in the natural stone industry.

Keywords: Marble, Energy Consumption, Specific Energy, CNC Machines, Machine Learning.

1. INTRODUCTION

Natural stones are frequently preferred by architects in modern building designs due to their aesthetic properties, durability and sustainability. These stones are especially suitable for indoor and outdoor use with their variety of colors, patterns and natural textures. With the impact of technological developments, two-dimensional (2D) and three-dimensional (3D) designs are processed in line with higher precision and quality requirements, and these processes are usually carried out with Computer Aided Control (CNC) machines. CNC machines play a critical role in responding to the increasing design demands and quality expectations in the natural stone industry. In particular, vertical machining centers are

preferred in the production of architectural decorative products (sculptures, column capitals, reliefs, carvings, frescoes, etc.), and with these machines, precise and detailed 3D machining becomes possible. CNC technology enables the production of high quality products by offering small depth cutting and fine detailed machining in the x, y, z axes. This gives companies the opportunity to produce high value-added products and gain a competitive advantage in the global market. Nowadays, research on the determination of optimum machining parameters in CNC machines to achieve more efficient production in natural stone processing processes is increasing [1-2]. Studies on the cutting process of natural stones and the performance of CNC machines make important contributions both to increase

productivity in the stone processing industry and to obtain quality products. In these studies, many parameters affecting the cutting process and the performance of CNC machines have been analyzed. These parameters include the geometry of cutting tools, cutting speeds, feed rates and the use of coolants. Modeling the forces generated during the cutting process in CNC machines is of great importance for the optimization of the cutting process. Mathematical and simulation-based models are frequently used to calculate cutting forces and energy consumption. Especially recent studies have investigated in detail the effects of parameters such as cutting forces and specific cutting energy on both energy efficiency and surface quality [3-14].

The wear of the tools used during the cutting process and its effect on the machining quality is also of great importance. The hardness and durability properties of natural stones can cause rapid tool wear, which can adversely affect surface quality. Research to minimize tool wear has focused on the development of new tool materials and coatings. However, elastic and plastic deformations that occur during the cutting of stones are also among the factors that determine the process quality. Plastic deformations, especially in hard stones, can increase the forces used during the cutting process and increase energy consumption. Therefore, the correct selection of machining parameters minimizes both tool wear and deformations, resulting in more efficient and high quality cutting operations [15-19].

Recent research shows that process efficiency can be improved by customizing CNC technologies in natural stone machining processes. The performance of diamond and carbide tools has been studied along with their effects on cutting parameters. While diamond tools are preferred for machining hard stones due to their high hardness and wear resistance, the optimum cutting parameters were determined by cooled cutting experiments. Low cutting speed and feed rate were found to improve machinability for diamond tools. The relationship between cutting forces and energy consumption was also investigated and the optimum process parameters were determined. It has been observed that diamond tools improve the surface quality, while carbide tools

may lead to loss of efficiency in hard stones [20-26].

In recent years, Machine Learning (ML) applications in CNC machine tools have been investigated with increasing interest and future research areas have been identified [27-31]. ML is an important revolution in computer science and enables the optimization of various manufacturing processes in CNC machines. Especially in areas such as cutting forces, cutting tool wear prediction and optimization of machining parameters, the use of ML algorithms can significantly increase production efficiency. In addition, advanced machine learning systems are also used to improve the surface quality of machined parts and to predict and prevent errors that may occur during production. It has been emphasized that the use of ML algorithms in CNC machines contributes to energy efficiency and cost savings by predicting cutting forces and extending tool life [32-33]. It is predicted that such technologies will contribute to the development of autonomous production processes and the achievement of industry 4.0 targets in the future.

Electrical energy is a fundamental element of social and economic development and an integral part of industrial production. Accurate forecasting of electricity generation is critical for energy planning and efficient use; in this context, machine learning (ML) algorithms have become prominent in the energy sector thanks to their ability to analyze complex relationships and make accurate forecasts [34]. Similarly, ML algorithms are also effective for optimizing resource utilization in logistics and manufacturing processes [35]. Environmental sustainability has become an increasing focus in the manufacturing sector. Especially in energy-intensive systems such as CNC machines, comprehensive approaches such as accurate estimation of energy consumption, waste reduction strategies and regular maintenance are important to reduce the carbon footprint. With these strategies, 23% energy savings and 14% waste reduction can be achieved, while practices such as regular maintenance and operator training contribute to energy efficiency by extending machine life [36-38]. These studies demonstrate the potential of ML algorithms and sustainability-oriented

approaches to increase efficiency in energy and resource management.

Evaluating the performance of machine learning models is critical to understanding and optimizing their effectiveness. This paper comprehensively analyzes the performance of different machine learning models in predicting energy consumption. Using the Python programming language, the actual specific energy values are compared with the values predicted by the models, and an objective evaluation is performed using performance metrics such as coefficient of determination (R^2), mean absolute error (MAE) and root mean squared error (RMSE) of each model. By examining the outputs of the XGBoost model, the analysis revealed that the material removal rate (MRR) is the most critical factor and accordingly, the performance of different prediction models such as XGBoost, Gradient Boosting, Random Forest and LightGBM based on MRR were compared. All models were found to perform with high accuracy, with XGBoost in particular standing out with the highest coefficient of determination (R^2). These findings provide important strategies to improve energy efficiency and reduce costs and highlight the potential of machine learning methods to optimize energy consumption in CNC machines. The findings of the study provide important insights into how machine learning methods can be used to improve energy efficiency, providing a valuable foundation for future research.

2. MATERIALS AND METHODS

2.1. Methodology

CNC machines have undergone significant advancements in recent years, particularly through the integration of artificial intelligence (AI), which has greatly enhanced the optimization of machining performance, reduced errors, and improved efficiency [40]. In addition, the adoption of cloud-based platforms has enabled faster and more reliable access to production processes, thus fostering greater collaboration among teams [41]. The integration of robotic technologies, particularly collaborative robots, with CNC machines has not only increased production speeds but also enhanced workplace safety [42]. Furthermore, the application of Internet of Things (IoT) technologies in CNC systems has allowed for inter-machine communication, enabling predictive maintenance and the optimization of production schedules [43]. These technological advancements have contributed to making CNC machines more intelligent, precise, and adaptive, improving production efficiency across industries such as aerospace, automotive, and medical sectors. As these innovations continue to evolve, CNC machines are expected to offer even more advanced solutions and further enhance industrial production quality.

In this study, experiments were carried out on CNC machines using different machining parameters on marble and the effects of these parameters on material machining performance were investigated. A load cell tester fixed to the CNC machine table was used to measure the forces generated during the experiment. The general methodology followed during the experimental study is shown in Figure 1.

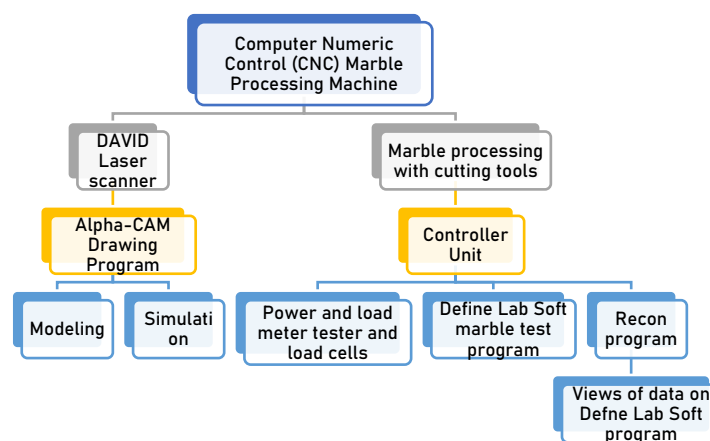


Figure 1. Methodology followed during the experimental study phase [1]

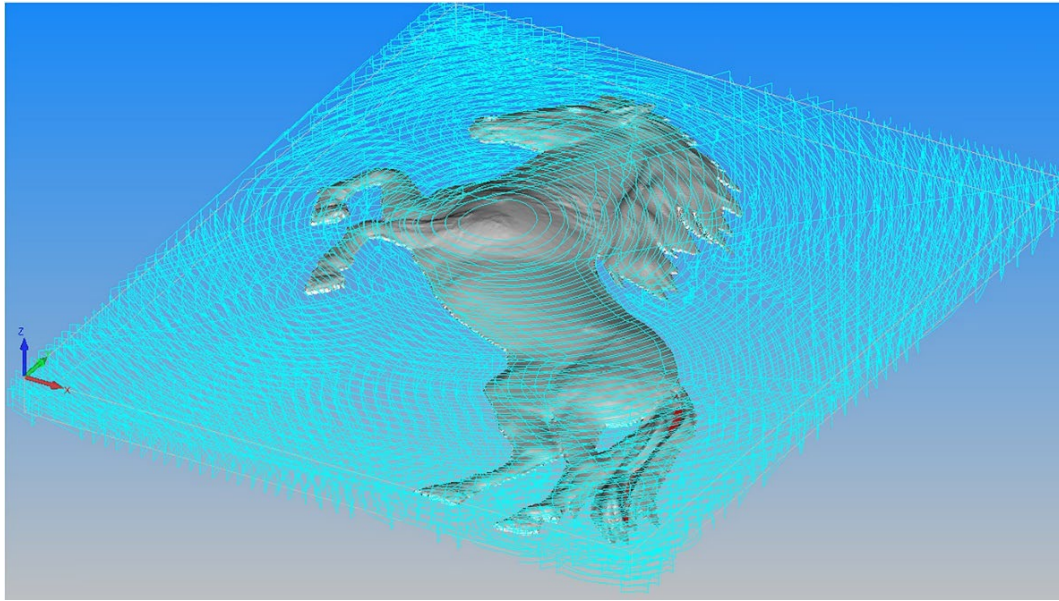


Figure 2. 3D product design in Alpha-CAM software [1]

The modeling of a horse figure was scanned using a 3D laser scanner and the resulting STL file was imported into Alpha-CAM design software (Figure 2).

The laser scanner used was DAVID Professional Version-3 software, known for its high scanning speed and resolution. Alpha-CAM software, which has 3D surface processing and simulation features, was preferred because it allows the drawings to be compatible with different programs. The specimens used in the experiments were modeled in Alpha-CAM software with dimensions of 125x100 mm. Different cutting parameters were determined for each figure and the experiments were tested with simulations beforehand.

The load meter tester consists of load cells, measurement and control units and is integrated with Defne Lab-Soft software. Before the experiments, the specimens were fixed to the device with a quick-clamping apparatus. There are a total of eight load cells in the system, four of which are used for force measurement in the Z axis and the other four are used for force measurement in the X and Y axes. Defne Lab-Soft software allowed the input of parameters such as specimen type, size, diameter, weight, machining type, depth of cut, spindle speed, cutting speed, feed rate, tool sinking speed and water content.

For each experiment, the Numerical Control (NC) codes generated in Alpha-CAM software were transferred to the CNC machine control unit via RSP (Recon Software Program). For each measurement, 100 data were collected per second from each 60x60 mm square for a period of 60 seconds, totaling 600 data. This high-resolution data collection method provided the precision needed to analyze in detail the effects of machining parameters on marble cutting performance.

2.2. Process Parameters

In this study, cutting forces (F_c), depth of cut (F_t) and energy consumption (E_c) were used as effective cutting parameters to monitor the performance of cutting tools for optimization of marble processing. Experimental models were used to determine the process conditions. The process parameters and values used in the experimental studies are presented in Table 1.

Table 1. Process parameters used in the experiments

| Process Parameters | SI | Values |
|----------------------|--------|------------------------|
| Milled Tool Diameter | mm | 4.0 |
| Spindle Speed | d/min | 10,000 |
| Plunge Speed | d/min | 1000 |
| Cutting Speed | m/min | 125.6 |
| Cutting Width | mm | 2.0 |
| Depth of Cut | mm | 1.0-1.5- 2.0 |
| Feed Speed | mm/min | 2000- 2500- 3000 |

The machining parameters are defined by variables such as cutting speed (V_c), feed rate (V_a), equivalent depth of cut (h_{eq}) and material removal rate (MRR). The cutting parameters F_c , F_t and E_c were calculated with the equations (Equations 1 to 4) proposed by Sarışık and

Özkan (2018)[2]. Furthermore, the equations presented by Polini and Turchetta (2004) and Teale (1965) (Equations 5 to 16 and 17 to 18) were also used to calculate the parameters of the machining process[19,33] (Table 2).

Table 2. Equations and explanations of processing parameters

| No | Equation | Description |
|----|--|---|
| 1 | $F_x = F_{x1} + F_{x2} $ | F_x cutting force |
| 2 | $F_y = F_{y1} + F_{y2} $ | F_y cutting force |
| 3 | $R = \sqrt{F_x^2 + F_y^2}$ | Resultant force $R(N)$, the sum of the cutting forces F_x and F_y |
| 4 | $\beta = \tan^{-1}\left(\frac{F_y}{F_x}\right)$ | Beta angle, inverse tangent of the ratio of the cutting forces F_y and F_x |
| 5 | $\theta = \cos^{-1}\left(1 - \frac{2d_p}{d}\right)$ | Contact angle between cutting tool and material θ |
| 6 | $F_c = R \sin \delta$ | Tangential force $F_c(N)$ is calculated with resultant force R and angle δ |
| 7 | $F_t = R \cos \delta$ | The radial force $F_t(N)$ is calculated by the resultant force R and angle δ |
| 8 | $\delta = \beta - Z\theta$ | Angle δ is the difference of beta angle and $Z\theta$ angle |
| 9 | $Z = \frac{AB}{AC}$ | Parameter Z determines the position of the application point of the resultant force in the contact spring |
| 10 | $h_{eq} = \frac{d_p \times V_a}{V_t}$ | Equivalent depth of cut h_{eq} (mm) is calculated by depth of cut d_p and feed rate V_a |
| 11 | $V_t = \frac{\pi \times D \times n}{1000}$ | Cutting speed V_t (m/min) is calculated with spindle speed n and cutter diameter D |
| 12 | $V_a = f_z \times z \times n \times f_2$ | Calculated with feed rate V_a (mm/min), feed per tooth f_z , number of inserts z , spindle speed n and correction factor f_2 |
| 13 | $E_c = \frac{F_c \times V_t}{V_a \times d_p \times b}$ | Energy consumption E_c (J) is calculated by tangential force F_c , cutting speed V_t , feed speed V_a , depth of cut d_p and width of cut b |
| 14 | $MRR = V_a \cdot d_p \cdot b$ | Material removal rate MRR (mm ³ /min) is calculated by feed rate V_a , depth of cut d_p and width of cut b |
| 15 | $MRR = h_{eq} \cdot V_t \cdot b$ | Material removal rate MRR (mm ³ /min) is calculated by equivalent depth of cut h_{eq} , cutting speed V_t and cutting width b |
| 16 | $h_{eq} = \frac{MRR}{V_t \cdot b}$ | Equivalent depth of cut h_{eq} (mm) is calculated by material removal rate MRR , cutting speed V_t and cutting width b |
| 17 | $Q_w = b \times l \times d_p$ | Chip volume (mm ³) is calculated. |
| 18 | $S_e = \frac{\sum_{j=1}^n p_j}{n} \times \sum_{j=1}^n t_j$ | The total specific energy (J/mm ³) is calculated. |

These equations allow us to analyze the efficiency and energy consumption of cutting tools in the marble processing process, contributing to the determination of optimal processing conditions. This data will help to

develop strategies to improve the machinability of marble.

2.3. Machine Learning

Machine learning includes various algorithms used to analyze data and identify patterns and offers various approaches to solve different problems such as regression and classification. In this study, popular machine learning models such as XGBoost, Gradient Boosting, Random Forest and LightGBM will be used to evaluate energy consumption.

The XGBoost model is an optimized version of the Gradient Boosting algorithm. It uses quadratic functions for calculating the loss function, allowing for a faster and more optimized training process compared to standard methods [43-46]. Gradient Boosting, on the other hand, is a decision-tree-based learning algorithm that converts weak learners into strong learners through gradient boosting, offering a transparent and comprehensible framework [44-45,47]. Random Forest, is widely used for both regression and classification tasks. It performs well by reducing variance without the need for complex hyperparameter tuning [44,48-49]. LightGBM is a machine learning algorithm based on histograms, which discretizes continuous variables to minimize computational costs. Its leaf-oriented growth strategy accelerates the learning process [50-51].

In evaluating each model's performance, the dataset was partitioned into a 70% training set and 30% test set, enabling reliable model validation and comparison. Key metrics such as Mean Squared Error (MSE) and R-squared (R^2) were used to assess predictive accuracy,

ensuring each model's effectiveness in estimating energy consumption under varied machining conditions. Cross-validation techniques, particularly k-fold cross-validation, were applied to reinforce model robustness and reduce overfitting risks, thereby enhancing generalizability. Each model's predictive capacity was rigorously validated through cross-validation to produce robust and consistent findings. This systematic evaluation process highlighted the predictive strengths and limitations of each model, establishing a clear understanding of how different algorithms respond to machining conditions and contributing substantially to the optimization of CNC processes.

3. RESULTS

3.1. Experimental Study and Energy Consumption Analysis

In the experimental study, data were obtained from power consumption (W) measurements depending on the processing time of the marble. Three different feed rates and three different depths of cut were used in the processing of three-dimensional products. In total, a data set of 5400 observations was used in the experiments (3 processing types x 3 depth of cut x 3 feed rate x 600 data points). For specific energy, the MRR process parameters were analyzed statistically using ANOVA in the different experiments of marble (Table 3). In this context, it was observed that MRR was effective on the specific energy values of three-dimensional marble products in all experiments ($p < 0.001$).

Table 3: ANOVA table for linear regression between mrr and specific energy

| Process Type | Dependent variable | Model | Sum of Squares | df | Mean Square | F | Sig. |
|----------------|--------------------|------------|----------------|------|-------------|----------|-------|
| External lines | MRR | Regression | 6902,923 | 1 | 6902,923 | 32220,88 | 0,001 |
| | | Residual | 320,928 | 1498 | 0,214 | | |
| | | Total | 7223,851 | 1499 | | | |
| Linear | MRR | Regression | 4800,926 | 1 | 4800,926 | 8698,315 | 0,001 |
| | | Residual | 826,802 | 1498 | 0,552 | | |
| | | Total | 5627,729 | 1499 | | | |
| Sprial | MRR | Regression | 1682,361 | 1 | 1682,361 | 21115,84 | 0,001 |
| | | Residual | 119,350 | 1498 | 0,080 | | |
| | | Total | 1801,711 | 1499 | | | |

In Figure 3, the effect of MRR (Material Removal Rate) parameter on specific energy according to the processing type is analyzed in

detail. In this analysis, linear regression analysis was performed to determine the relationship between MRR and specific energy for each

processing type. According to the results, the coefficient of determination (R^2) for contour machining was 0.956, which indicates that 95.6% of the variance in specific energy values is explained by MRR. The R^2 value for linear processing was 0.853, indicating that 85.3% of the variance in specific energy in this type of processing was explained by MRR. For spiral processing, the R^2 value was calculated as 0.934, indicating that 93.4% of the specific energy variance was explained by MRR. These results provide important findings for understanding the impact of MRR on specific energy in different processing types. The highest R^2 value was achieved in outline machining, indicating that the specific energy in this type of machining is largely influenced by MRR. Linear and spiral processes also show a significant effect of MRR on specific energy with high R^2 values.

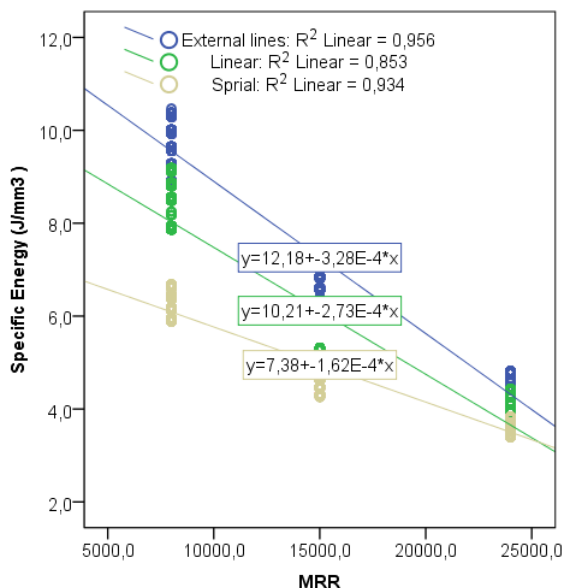


Figure 3. Regression plot showing the relationship between specific energy and MRR parameters by processing type

This research presents a comprehensive analysis using ANOVA to evaluate the specific energy consumption during marble processing on CNC machine. The ANOVA results revealed significant differences between the processing types. However, considering the complexity of

the available dataset and the non-linear relationships between variables, it is also proposed to apply machine learning models to gain a deeper understanding. In this context, the use of machine learning methods can be important to more accurately estimate specific energy consumption and enable optimization of processing parameters. For example, advanced regression models such as Gradient Boosting, Random Forests, LightGBM and XGBoost can provide higher accuracy predictions by better capturing non-linear relationships and interactions. The application of these models will allow the development of potential strategies to improve energy efficiency and reduce costs in CNC machines. In conclusion, this study provides important insights for improving energy efficiency in CNC marble machining processes by evaluating the effects of MRR on specific energy according to machining types. This approach, supported by advanced analysis methods, will provide a valuable basis for future studies.

3.2. Machine Learning Model Analysis and Performance Evaluation

In this section, the performance of the previously introduced machine learning models on the specific energy dataset is analyzed in detail. During the evaluation process, comparisons were made between the actual specific energy values and those predicted by the machine learning algorithms. To assess the effectiveness and accuracy of each model, performance metrics such as the coefficient of determination (R^2), Mean Absolute Error (MAE), and Root Mean Square Error (RMSE) were used. These metrics help evaluate how successful the machine learning models are in predicting specific energy and provide important insights into the reliability of the models.

In Figure 4, the outputs of the XGBoost model are analyzed, and the effect of the input features on the model is discussed in detail.

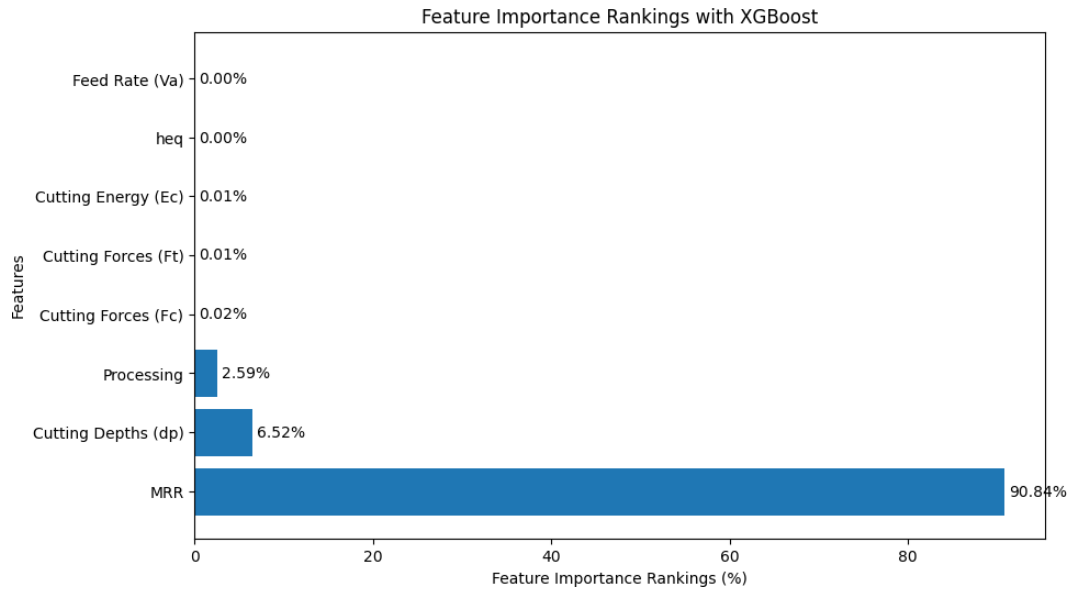


Figure 4. Importance ranking of the parameters affecting specific energy

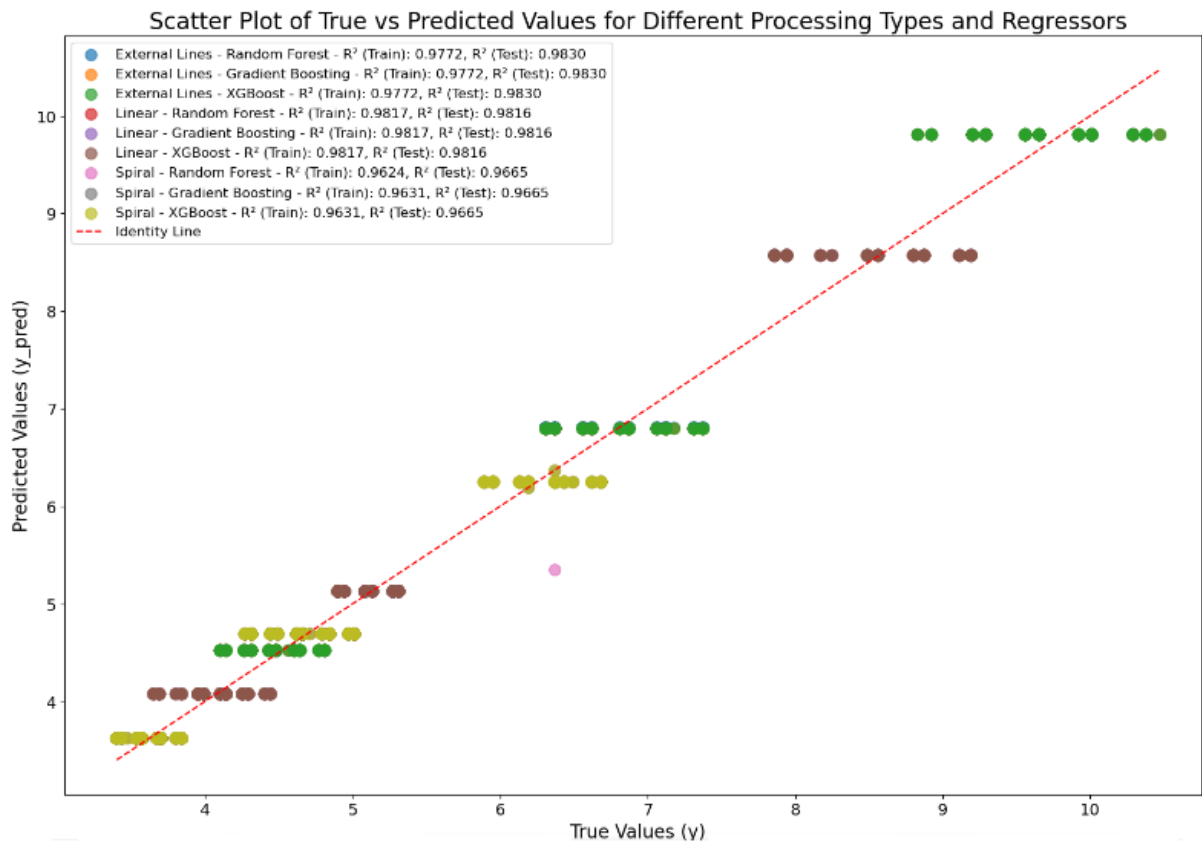


Figure 5. Prediction models according to the effect of specific energy on material lift ratio

This analysis provides an important perspective on the contribution of each input feature to the prediction results. For specific energy, the Material Removal Rate (MRR) is found to be the most influential factor, affecting the model output by 90.84%. This finding highlights the critical role of MRR in the model's prediction of specific energy. This information helps us understand the model's sensitivity to certain

input features and serves as an important resource for optimizing predictions and enhancing the model's reliability. This analysis is highly valuable for professionals in the natural stone industry and researchers working to improve energy consumption predictions in CNC machine operations.

In Figure 5, the effect of mmr on specific energy is analyzed by using four different prediction models and the prediction results are obtained. This analysis aims to evaluate how accurate the different models are in predicting specific energy. The models are specifically designed to analyze various input characteristics in specific energy forecasts. The coefficient of determination (R^2) obtained in the training set was 0.9817 and 0.9816 in the test set. This comprehensive comparison helps us to understand how accurately each model predicts the impact of MRR in specific energy forecasts.

According to the model performance comparison results, the XGBoost model has the highest accuracy in specific energy estimation with MRR, with an R^2 value of 0.9817, indicating that 98.17% of the specific energy variance is explained by MRR. The Gradient

Boosting model, which has the second highest accuracy, has an $R^2 = 0.9816$ and explains 98.16% of the specific energy variance. The coefficient of determination of the Random Forest model was also found to be 0.9817, revealing that 98.17% of the specific energy variance is due to MRR. The LightGBM model successfully analyzed the relationship between energy consumption and MRR. The results confirm that MRR is an important factor in specific energy predictions in all models. These findings provide important insights to improve energy efficiency and reduce costs in CNC marble machining processes. The use of machine learning methods offers significant contributions to more accurately predict specific energy consumption and optimize machining parameters.

Table 4. Performance comparison of prediction models for different processing types

| Processing | Model | R^2 | | MAE | | RMSE | |
|----------------|-------------------|--------|--------|--------|--------|--------|--------|
| | | Train | Test | Train | Test | Train | Test |
| External lines | Gradient Boosting | 0,9772 | 0,9830 | 0,2732 | 0,2501 | 0,3280 | 0,2976 |
| | Random Forest | 0,9772 | 0,9830 | 0,2729 | 0,2500 | 0,3281 | 0,2976 |
| | XGBoost | 0,9772 | 0,9830 | 0,2732 | 0,2501 | 0,3280 | 0,2976 |
| | LightGBM | 0,9772 | 0,9830 | 0,2732 | 0,2501 | 0,3280 | 0,2976 |
| | | | | | | | |
| Linear | Gradient Boosting | 0,9817 | 0,9816 | 0,1930 | 0,1948 | 0,2600 | 0,2687 |
| | Random Forest | 0,9817 | 0,9816 | 0,1931 | 0,1949 | 0,2600 | 0,2687 |
| | XGBoost | 0,9817 | 0,9816 | 0,1930 | 0,1948 | 0,2600 | 0,2687 |
| | LightGBM | 0,9817 | 0,9816 | 0,1930 | 0,1948 | 0,2600 | 0,2687 |
| | | | | | | | |
| Spiral | Gradient Boosting | 0,9631 | 0,9665 | 0,1727 | 0,1666 | 0,2094 | 0,2045 |
| | Random Forest | 0,9624 | 0,9665 | 0,1735 | 0,1665 | 0,2115 | 0,2044 |
| | XGBoost | 0,9631 | 0,9665 | 0,1727 | 0,1666 | 0,2094 | 0,2045 |
| | LightGBM | 0,9578 | 0,9664 | 0,1751 | 0,1670 | 0,2239 | 0,2047 |
| | | | | | | | |

Table 4 compares the performance of four different machine learning models (Gradient Boosting, Random Forest, XGBoost, LightGBM) for three different processing types (Outline, Linear and Spiral). Performance measures such as coefficient of determination (R^2), Mean Absolute Error (MAE) and Root Mean Square Error (RMSE) are presented for both training and test sets. The R^2 values of all the models in the external lines processing type were found to be very high, 0.9772 in the

training set and 0.9830 in the test set, indicating a good fit of the models to the data. The MAE values were approximately 0.2732 in the training set and 0.2501 in the test set, indicating that the prediction errors were quite low and accurate predictions were made. The RMSE values are around 0.3280 for the training set and 0.2976 for the test set, which indicate that no large errors were made. In the linear processing type, the R^2 values are 0.9817 in the training set and 0.9816 in the test set, indicating that the

models continue to fit the data. The MAE values remained at a low level, approximately 0.1930 in the training set and 0.1948 in the test set, indicating that the predictions are close to reality. The RMSE values were approximately 0.2600 in the training set and 0.2687 in the test set, indicating that no large errors were made. In the Spiral processing type, R^2 values are slightly lower than the other processing types, 0.9631 in the training set and 0.9665 in the test set for the Gradient Boosting and XGBoost models; Random Forest and LightGBM show similar high performance. For the Spiral type, the MAE values are about 0.1727 in the training set and 0.1666 in the test set, which are also low. The RMSE values are approximately 0.2094 in the training set and 0.2045 in the test set, which are similarly low compared to the other processing types, confirming that the models do not make large errors.

The results obtained show that all models make efficient predictions with high R^2 values and low MAE and RMSE values. While there is no significant performance difference between the models for Outline and Linear machining, Gradient Boosting and XGBoost models give slightly better results for Spiral machining. Overall, the Gradient Boosting model, with its high accuracy and low error rates, was identified as the most suitable model for predicting the specific energy consumption during marble processing on CNC machines. These findings show that machine learning techniques can be effectively used in specific energy estimation.

This study presents valuable insights into the analysis and prediction of specific energy consumption in marble processing processes on CNC machines, while also providing several critical recommendations for advancing research and enhancing energy efficiency in this domain. First, it is recommended that deep learning techniques, such as artificial neural networks, be employed to more effectively model nonlinear relationships, which could further enhance the accuracy of the model. Additionally, incorporating other influencing parameters, such as machine maintenance and environmental conditions, into the model could improve prediction accuracy and overall energy efficiency. Expanding the dataset to include a broader range of processing parameters would enhance the model's generalization ability,

particularly by considering different types of marble and processing methods. The investigation of hybrid models, which combine multiple machine learning algorithms, is also suggested, as these could offer higher accuracy and improved overall performance. Finally, in pursuit of energy conservation and sustainability, the development of strategies aimed at reducing energy consumption through machine learning-based optimization techniques is proposed. These recommendations serve as a guide for future research focused on improving energy efficiency and reducing costs in CNC machine operations.

4. DISCUSSION

Nowadays, machine learning (ML) methods play an important role in optimizing complex processes such as marble machining on CNC machines. This paper comprehensively investigates the performance of four different ML models such as Gradient Boosting, Random Forest, XGBoost and LightGBM to predict the specific energy consumption during marble processing. Specific energy consumption is a critical parameter to improve energy efficiency and reduce costs. The analysis is carried out using metrics such as R^2 , RMSE and MAPE, which provide important data to evaluate the effectiveness and reliability of the models. Previous studies have analyzed cutting forces and energy consumption in a similar framework; researchers have studied the physical and mechanical properties of natural stones, focusing on parameters such as cutting forces, specific energy and cutting energy. Our current study aims to evaluate the specific energy consumption during marble processing on a CNC machine, both with traditional statistical methods and machine learning models. This provides a more advanced and comprehensive approach to energy consumption estimation, unlike previous studies [1-2]. It also examines the application of machine learning and artificial intelligence techniques, focusing on issues such as energy consumption, cutting forces, and cutting tool wear in CNC machines, while providing recommendations to improve energy efficiency [32-33]. In this context, both studies point to important contributions in the field of CNC machines.

In our study, each machine learning model is analyzed for different processing types (external lines, linear and spiral). In particular, the accuracy and error rates of the models were evaluated using performance metrics such as coefficient of determination (R^2), mean absolute error (MAE) and root mean square error (RMSE). The results show that, in general, all four models perform well and the performance differences between them are quite small. However, in the case of spiral processing, Gradient Boosting and XGBoost perform better than the other models. This finding is due to the ability of these models to better capture complex and non-linear relationships.

These analyses provide critical data for understanding the effectiveness and reliability of machine learning models in various classification tasks. In conclusion, the use of machine learning methods for specific energy consumption prediction in CNC machines offers a strategic approach to improve energy efficiency and reduce costs. The current findings provide important insights to improve the performance of machine learning models and optimize their effectiveness in specific tasks. Future studies can conduct more in-depth analyses to evaluate model performance on more complex and dynamic datasets and contribute to developing more robust and reliable models for real-world applications. Research in this area has the potential to optimize energy consumption and improve efficiency in manufacturing processes.

5. CONCLUSION

This study provides a comprehensive analysis of the factors affecting specific energy consumption during marble processing on CNC machines, providing important information for improving energy efficiency. Based on three different feed rates and depths of cut used in the marble processing process, the analysis of 5,400 data points showed that Material Removal Rate (MRR) plays a critical role in determining specific energy consumption.

ANOVA on the experimental data revealed a significant effect of MRR on specific energy consumption ($p < 0.001$). The R^2 values determined for each processing type by regression analyses show that a large part of the specific energy variance is explained by MRR. The R^2 values were 0.956, 0.853 and 0.934 for

outline, linear and spiral machining, respectively, confirming the strong influence of MRR on specific energy. These high coefficients of determination emphasize how significant the impact of MRR on energy consumption in marble processing is.

Forecasting specific energy consumption using machine learning models has provided a better understanding of non-linear relationships and interactions between variables. Advanced regression models such as Gradient Boosting, Random Forest, LightGBM and XGBoost were analyzed for their prediction performance on the dataset. All models gave successful results with high accuracy and low error rates. The values of $R^2=0.9817$ in the training set and $R^2=0.9816$ in the test set indicate that the models are compatible with the data and have high generalization capabilities.

When the outputs of the XGBoost model are analyzed, it is seen that MRR has the most significant impact on the model (impact rate 90.84%) and this finding is a critical factor in specific energy forecasts. Analyses showing the ranking of the importance of model features provide important information for optimizing predictions and improving model reliability. In terms of performance metrics for different processing types, it was observed that the Gradient Boosting and XGBoost models performed slightly better, especially in the spiral processing type. However, all models perform well in the outline and linear processing types. The similar performances in the training and test sets suggest that the models are not overfitting and have good generalization capabilities. Based on these evaluations, the Gradient Boosting model was identified as the best model due to its overall performance and superiority in specific processing types.

The findings of this study provide a valuable basis for developing important strategies to improve energy efficiency in marble processing processes on CNC machines. Future work can extend and deepen these analyses using more data and advanced algorithms. In particular, improving the performance of machine learning models and using these models in real-world applications to optimize energy consumption will lead to efficiency and cost effectiveness in industrial applications.

In conclusion, this research provides important insights for optimizing energy consumption in CNC marble machining processes by comprehensively evaluating the factors affecting specific energy consumption and their impact on energy efficiency. The use of machine learning models improves prediction accuracy, allowing the development of potential strategies to improve energy efficiency. These findings provide valuable guidance for natural stone industry professionals and researchers.

This study offers significant contributions to the natural stone industry, particularly in improving energy efficiency during CNC marble processing. By identifying Material Removal Rate (MRR) as the primary factor influencing energy consumption, this research provides a foundation for optimizing processing parameters to reduce energy costs. The application of machine learning models, including Gradient Boosting and XGBoost, demonstrates high accuracy in predicting specific energy consumption, offering valuable insights for real-world energy management strategies. Future work should focus on incorporating additional variables, such as machine maintenance and environmental conditions, to further enhance model accuracy and applicability. Additionally, exploring hybrid machine learning models and real-time optimization techniques can drive further advancements in energy conservation, helping the industry adopt more sustainable practices while lowering operational costs.

REFERENCES

1. Sarıışık, G., "Investigation on cutting parameter models and processability index in 3D marble products with milled tools," *Arabian Journal of Geosciences*, Vol. 14, Issue 18, Pages 1854, 2021.
2. Sarıışık, G. and Özkan, E., "Effects of natural rock properties on cutting forces, specific energy and specific cutting energy by four-axis machine," *Arabian Journal of Geosciences*, Vol. 11, Pages 1-19, 2018.
3. Turchetta, S., "Cutting force and diamond tool wear in stone machining," *The International Journal of Advanced Manufacturing Technology*, Vol. 61, Pages 441-448, 2012.
4. Mishra, V.K. and Salonitis, K., "Empirical estimation of grinding specific forces and energy based on a modified Werner grinding model," *Procedia CIRP*, Vol. 8, Issue 1, Pages 287-292, 2013.
5. Salonitis, K., Stavropoulos, P., and Kolios, A., "External grind-hardening forces modelling and experimentation," *International Journal of Advanced Manufacturing Technology*, Vol. 70, Issues 1-4, Pages 523-530, 2014.
6. Yurdakul, M., Gopalakrishnan, K., and Akdas, H., "Prediction of specific cutting energy in natural stone cutting processes using the neuro-fuzzy methodology," *International Journal of Rock Mechanics and Mining Sciences*, Vol. 67, Pages 127-135, 2014.
7. Zhang, H., Zhang, J., Wang, Z., Sun, Q., and Fang, J., "A new frame saw machine by diamond segmented blade for cutting granite," *Diamond and Related Materials*, Vol. 69, Pages 40-48, 2016.
8. Polini, W. and Corrado, A., "Digital twin of stone sawing processes," *The International Journal of Advanced Manufacturing Technology*, Vol. 112, Issue 1, Pages 121-131, 2021.
9. Breidenstein, B., Denkena, B., Bergmann, B., Picker, T., and Wolters, P., "Tool wear when using natural rocks as cutting material for the turning of aluminum alloys and plastics," *Production Engineering*, Vol. 17, Issue 3, Pages 425-435, 2023.
10. Wang, K., Zhang, J., and Zhang, H., "An analytical dynamic force model for sawing force prediction considering the material removal mode," *Journal of Manufacturing Processes*, Vol. 106, Pages 494-505, 2023.
11. Dong, P., Zhang, J., and Zhang, H., "Wear performance of diamond tools during sawing with reciprocating swing frame saw," *Diamond and Related Materials*, Pages 110890, 2024.
12. Turchetta, S. and Sorrentino, L., "Forces and wear in high-speed machining of granite by circular sawing," *Diamond and Related Materials*, Vol. 100, Page 107579, 2019.
13. Zhu, Z., Buck, D., Guo, X., Xiong, X., Xu, W., and Cao, P., "Energy efficiency optimization for machining of wood plastic composite," *Machines*, Vol. 10, Issue 2, Page 104, 2022.
14. Inal, S., Erkan, I., and Aydinler, K., "Determination of the wear performance of diamond saw blades using inductively coupled plasma," *Sādhanā*, Vol. 44, Issue 5, Page 127, 2019.
15. Wang, F., Liu, S., Guo, Z., and Cao, L., "Analysis of cutting forces and chip formation in

- milling of marble,” *International Journal of Advanced Manufacturing Technology*, Vol. 108, Issue 9, Pages 2907–2916, 2020.
16. Wang, K., Zhang, J., and Zhang, H., “An analytical dynamic force model for sawing force prediction considering the material removal mode,” *Journal of Manufacturing Processes*, Vol. 106, Pages 494-505, 2023.
17. Breidenstein, B., Denkena, B., Bergmann, B., Picker, T., and Wolters, P., “Tool wear when using natural rocks as cutting material for the turning of aluminum alloys and plastics,” *Production Engineering*, Vol. 17, Issue 3, Pages 425-435, 2023.
18. Zhu, Z., Buck, D., Guo, X., Ekevad, M., and Cao, P., “Effect of cutting speed on machinability of stone-plastic composite material,” *Science of Advanced Materials*, Vol. 11, Issue 6, Pages 884-892, 2019.
19. Polini, W. and Turchetta, S., “Force and specific energy in stone cutting by diamond mill,” *International Journal of Machine Tools and Manufacture*, Vol. 44, Issue 11, Pages 1189-1196, 2004.
20. Sarıışık, G. and Özkan, E., “Mermerlerin CNC makinesi ile işlenmesinde kesme kuvvetleri ve spesifik kesme enerjisinin istatistiksel analizi,” *Dokuz Eylül Üniversitesi Mühendislik Fakültesi Fen ve Mühendislik Dergisi*, Vol. 19, Issue 55, Pages 178-193, 2017.
21. Sarıışık, G. “Force and Specific Energy in Natural Rocks Cutting by Four-Axis Machine.” In *Earth Crust*. IntechOpen, 2019.
22. Klaić, M., Brezak, D., Staroveški, T., and Murat, Z. “On-line Workpiece Hardness Monitoring in Stone Machining.” *Transactions of FAMENA*, Vol. 43, Issue 4, Pages 43-53, 2019.
23. Bai, S., Qiu, H., Rabe, L., Jia, S., Elwert, T., Wang, Q. Y., and Sun, Y. “A Study on Energy-saving Optimization Strategy for the Stone Processing Industry—An Improved Method for Modeling Cutting Power and Energy Consumption: A Case Study of Block Sawing Process.” *Journal of Cleaner Production*, Vol. 300, Page 126922, 2021.
24. Gupta, R. K., and Pratap, B. “Diamond Tools Processing for Marble and Granite: Cutting & Wear.” *Materials Today: Proceedings*, Vol. 46, Pages 2135-2140, 2021.
25. Özkan, E., and Öz, O. “Determination of Appropriate Cutting Parameters Depending on Surface Roughness by Taguchi Method in Milling of Marbles.” *Arabian Journal of Geosciences*, Vol. 13, Issue 13, Pages 532, 2020.
26. Nallusamy, S. “Enhancement of Productivity and Efficiency of CNC Machines in a Small Scale Industry Using Total Productive Maintenance.” *International Journal of Engineering Research in Africa*, Vol. 25, Pages 119-126, 2016.
27. Moreira, L. C., Li, W. D., Lu, X., and Fitzpatrick, M. E. “Supervision Controller for Real-time Surface Quality Assurance in CNC Machining Using Artificial Intelligence.” *Computers & Industrial Engineering*, Vol. 127, Pages 158-168, 2019.
28. Fertig, A., Weigold, M., and Chen, Y. “Machine Learning Based Quality Prediction for Milling Processes Using Internal Machine Tool Data.” *Advances in Industrial and Manufacturing Engineering*, Vol. 4, Page 100074, 2022.
29. Yang, Y., Hu, T., Ye, Y., Gao, W., and Zhang, C. “A Knowledge Generation Mechanism of Machining Process Planning Using Cloud Technology.” *Journal of Ambient Intelligence and Humanized Computing*, Vol. 10, Pages 1081-1092, 2019.
30. Jamwal, A., Agrawal, R., Sharma, M., Kumar, A., Kumar, V., and Garza-Reyes, J. A. A. “Machine Learning Applications for Sustainable Manufacturing: A Bibliometric-based Review for Future Research.” *Journal of Enterprise Information Management*, Vol. 35, Issue 2, Pages 566-596, 2021.
31. Rajesh, A. S., Prabhuswamy, M. S., and Satish, H. S. “Smart Manufacturing Through Machine Learning: A Review, Perspective and Future Directions to Machining Industry.” In *AIP Conference Proceedings*, Vol. 2399, Issue 1, 2023.
32. Soori, M., Jough, F. K. G., Dastres, R., and Arezoo, B. “Sustainable CNC Machining Operations, A Review.” *Sustainable Operations and Computers*, Vol. 5, Pages 73-87, 2024.
33. Teale, R. “The Concept of Specific Energy in Rock Drilling.” *International Journal of Rock Mechanics and Mining Sciences*, Vol. 2, Issue 1, Pages 57-73, 1965.
34. Özdemir, M. H., Aylak, B. L., İnce, M., and Oral, O. “Predicting world electricity generation by sources using different machine learning algorithms.” *International Journal of Oil, Gas and Coal Technology*, Vol. 35, Issue 1, Pages 98-115, 2024.

35. Aylak, B. L., İnce, M., Oral, O., Süer, G., Almasarwah, N., Singh, M., and Salah, B. "Application of machine learning methods for pallet loading problem." *Applied Sciences*, Vol. 11, Issue 18, Pages 8304, 2021.
36. Li, C., Tang, Y., Cui, L., Li, P., "A quantitative approach to analyze carbon emissions of CNC-based machining systems," *Journal of Intelligent Manufacturing*, Vol. 26, 2013.
37. Zhang, C., Jiang, P., "Sustainability Evaluation of Process Planning for Single CNC Machine Tool under the Consideration of Energy-Efficient Control Strategies Using Random Forests," *Sustainability*, Vol. 11, 2019.
38. Feng, Z., Zhang, H., Li, W., Yu, Y., Guan, Y., Ding, X., "Exergy Loss Assessment Method for CNC Milling System Considering the Energy Consumption of the Operator," *Processes*, Vol. 11, Issue 2702, 2023.
39. Soori, M., Arezoo, B., and Dastres, R. "Machine Learning and Artificial Intelligence in CNC Machine Tools, A Review." *Sustainable Manufacturing and Service Economics*, Vol. 2, Page 100009, 2023.
40. Martinov, G. M., Ljubimov, A. B., and Martinova, L. I., "From classic CNC systems to cloud-based technology and back," *Robotics and Computer-Integrated Manufacturing*, Vol. 63, 101927, 2020.
41. Soori, M., Jough, F. K. G., Arezoo, B., and Dastres, R., "Robotical automation in CNC machine tools: a review," *Acta Mechanica et Automatica*, Vol. 18, Pages 434-450, 2024.
42. Aebersold, S. A., Akinsolu, M. O., Monir, S., and Jones, M. L., "Ubiquitous control of a CNC machine: Proof of concept for industrial IoT applications," *Information*, Vol. 12, Issue 12, 529, 2021.
43. Re, M., and Valentini, G. "Ensemble Methods: A Review in Advances in Machine Learning and Data Mining for Astronomy." In Kumar, V. (Ed.), Pages 563-594, 2012.
44. Xu, P., Ji, X., Li, M., and Lu, W. "Small Data Machine Learning in Materials Science." *npj Computational Materials*, Vol. 9, Issue 1, Page 42, 2023.
45. Sharma, S., Gupta, V., Mudgal, D., and Srivastava, V. "Machine Learning for Forecasting the Biomechanical Behavior of Orthopedic Bone Plates Fabricated by Fused Deposition Modeling." *Rapid Prototyping Journal*, Vol. 30, Issue 3, Pages 441-459, 2024.
46. Chen, T., and Guestrin, C. "Xgboost: A Scalable Tree Boosting System." In *Proceedings of the 22nd ACM SIGKDD International Conference on Knowledge Discovery and Data Mining*, Pages 785-794, 2016.
47. Friedman, J. H. "Greedy Function Approximation: A Gradient Boosting Machine." *Annals of Statistics*, Pages 1189-1232, 2001.
48. Sharma, S., Gupta, V., and Mudgal, D. "Response Surface Methodology and Machine Learning Based Tensile Strength Prediction in Ultrasonic Assisted Coating of Poly Lactic Acid Bone Plates Manufactured Using Fused Deposition Modeling." *Ultrasonics*, Vol. 137, Page 107204, 2024.
49. Breiman, L. "Random Forests." *Machine Learning*, Vol. 45, Pages 5-32, 2001.
50. Ke, G., Meng, Q., Finley, T., Wang, T., Chen, W., Ma, W., and Liu, T. Y. "Lightgbm: A Highly Efficient Gradient Boosting Decision Tree." *Advances in Neural Information Processing Systems*, Vol. 30, 2017.
51. Zhou, Y., Wang, W., Wang, K., and Song, J. "Application of LightGBM Algorithm in the Initial Design of a Library in the Cold Area of China Based on Comprehensive Performance." *Buildings*, Vol. 12, Page 1309, 2022.



ULUSLARARASI 3B YAZICI TEKNOLOJİLERİ
VE DİJİTAL ENDÜSTRİ DERGİSİ

INTERNATIONAL JOURNAL OF 3D PRINTING
TECHNOLOGIES AND DIGITAL INDUSTRY

ISSN:2602-3350 (Online)

URL: <https://dergipark.org.tr/ij3dptdi>

CONTROL OF SEAT BELTS OF VEHICLE DRIVERS WHILE DRIVING WITH AN UNMANNED AERIAL VEHICLE WITH ARTIFICIAL INTELLIGENCE

Yazarlar (Authors): Mustafa Melikşah ÖZMEN^{ID}, Muzaffer EYLENCE^{ID}, Bekir AKSOY^{ID*}

Bu makaleye şu şekilde atıfta bulunabilirsiniz (To cite to this article): Özmen M. M., Eylence M., Aksoy B., "Control of Seat Belts of Vehicle Drivers While Driving with An Unmanned Aerial Vehicle with Artificial Intelligence" *Int. J. of 3D Printing Tech. Dig. Ind.*, 8(3): 451-458, (2024).

DOI: 10.46519/ij3dptdi.1568029

Araştırma Makale/ Research Article

Erişim Linki: (To link to this article): <https://dergipark.org.tr/en/pub/ij3dptdi/archive>

CONTROL OF SEAT BELTS OF VEHICLE DRIVERS WHILE DRIVING WITH AN UNMANNED AERIAL VEHICLE WITH ARTIFICIAL INTELLIGENCE

Mustafa Melikşah ÖZMEN^a , Muzaffer EYLENCE^a , Bekir AKSOY^a *

^a Isparta University of Applied Sciences, Faculty of Technology, Mechatronics engineering, TURKEY

* Corresponding Author: bekiraksoy@isparta.edu.tr

(Received: 16.10.2024; Revised: 11.11.2024; Accepted: 13.12.2024)

ABSTRACT

Today, with the rapid development of technology, the areas of use of artificial intelligence technologies are also rapidly increasing. Artificial intelligence applications are frequently used in many fields such as education, engineering and health. One of the important areas of use of artificial intelligence systems is mechatronic engineering. Artificial intelligence methods are frequently used especially in robotics and unmanned aerial vehicle applications. In the study, an artificial intelligence model developed to detect seat belt use by drivers using unmanned aerial vehicles is introduced. Seat belts play an important role in reducing injuries and deaths in traffic accidents, but current examination methods are time-consuming and limited. In this study, image processing techniques were used to determine whether drivers are wearing seat belts. For this purpose, a dataset consisting of in-car images taken under different driving conditions was created and Gaussian filters were applied to these images to remove noise and interference. Convolutional neural network architecture was used for model training and the results were compared with common models such as ResNet-18 and AlexNet. The model developed as a result of training has an accuracy rate of 94.55%. Test results showed that the developed special convolutional neural network model is superior to other models in terms of accuracy and performance. The study revealed that artificial intelligence and image processing techniques can increase traffic safety by monitoring seat belt use more effectively.

Keywords: Image processing, Unmanned Aerial Vehicle, Deep Learning.

1. INTRODUCTION

Fatal and injury incidents that occur after traffic accidents are considered one of the most important public health problems in the world [1]. In such accidents, the use of seat belts, which is one of the simplest and most effective precautions, is of great importance. According to research, seat belt use reduces the risk of fatal accidents by 40-65% and the risk of injury accidents by 40-50% [1].

A simple safety measure, the seat belt is one of the most effective methods of saving lives in traffic accidents [3]. Drivers and passengers who are wearing seat belts in a vehicle are protected from serious injuries by remaining stable in the vehicle during an accident and preventing them from being thrown. According to scientific research, seat belts have been

shown to significantly reduce head, neck and chest injuries by keeping the body in a safe position during a collision [3]. In addition, with the developing technology, other safety measures in modern vehicles must be worn in order for them to work actively and correctly. For example; airbags perform best when seat belts are worn.

Injuries and deaths resulting from not wearing a seat belt clearly show how serious the consequences of neglecting this simple safety precaution can be. For example, in the United States, approximately 7,000 people die and more than 100,000 people are reported to be injured each year due to not wearing a seat belt [2]. In such accidents, passengers who are not wearing a seat belt are at a very high risk of being thrown from the vehicle, which often

leads to fatal consequences. According to a study conducted by the General Directorate of Security Traffic Research Center, it was determined that passengers who are not wearing a seat belt have a 75% lower chance of survival after an accident than those who are.

Seat belt use, which is of such importance, was determined to be an average of 45-65% among drivers as a result of intercity checks and inspections carried out around Ankara in 2000. It was observed that this rate was even lower in urban use [1].

Traditional methods such as police checks used in seat belt inspections do not provide a sufficiently effective deterrent as they are time-consuming and usually carried out in limited areas. Therefore, with the advancement of technology, the use of artificial intelligence and image processing techniques in these checks offers the opportunity to monitor and control seat belt use more effectively and comprehensively [4].

By using artificial intelligence and image processing technology, it provides the opportunity to monitor and control seat belt use more effectively and comprehensively [5]. In the study, a comprehensive original data set including different driving conditions and in-car images taken from various angles was created with the data set we created in order to detect those not wearing seat belts. Drivers and passengers with and without seat belts will be manually labeled in the data set. Convolutional Neural Network (CNN) architecture will be used for model training. CNN is a deep learning algorithm that shows superior performance in image processing tasks and in this study, it will be optimized to detect whether seat belts are worn in in-car images. During the training process, Gaussian filter and normalization processes were applied to reduce noise and interference on the collected images in order to increase the accuracy and overall performance of the model. After the training of the model is completed, different tests will be performed on the test data set to evaluate the accuracy and effectiveness of the model. The test results will be used to determine the extent to which the model correctly detects seat belt use in different conditions and angles. The data will reveal the potential of artificial intelligence-based image

processing systems in controlling seat belt use and increasing traffic safety.

The study aims to show how artificial intelligence and image processing technologies offer innovative solutions in the field of traffic safety and how they can contribute to increasing seat belt use. The study, which will be carried out with the data set and artificial intelligence model prepared specifically for the study, will be an important step towards identifying drivers and passengers who do not wear seat belts and thus reducing traffic accidents and related injuries and deaths.

2. MATERIAL AND METHODS

2.1. Material

In the material section of the study, the data set used in the study, the artificial intelligence algorithms and the performance evaluation metrics used in evaluating the results obtained from the artificial intelligence algorithms are discussed in detail under the following subheadings.

2.1.1. Dataset

In the study, an original dataset was created using unmanned aerial vehicles to determine whether the drivers of moving vehicles have their seat belts fastened. The images in the dataset were taken while the drivers were wearing or not wearing their seat belts. The images in the dataset were recorded in color at 240x240 dimensions. The collected images were subjected to Gaussian filtering and normalization processes in order to reduce noise and interference on them. The dataset, which consists of a total of 1000 images, consists of 600 drivers wearing seat belts and 400 drivers not wearing seat belts. A sample image taken from the dataset prepared specifically for the study is shown in Figure 1.

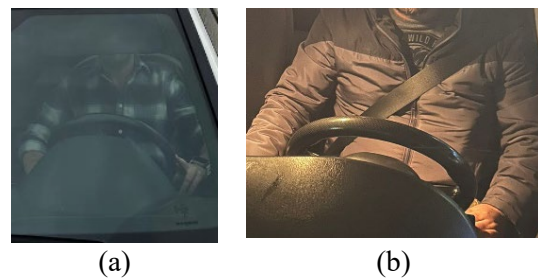


Figure 1. Example image of a person (a) not wearing a seat belt (b) wearing a seat belt for the dataset

2.1.2. Convolutional neural network

CNN is a deep learning method frequently used in image processing and computer vision applications. Studies conducted in 2023 focused on improving the performance of CNNs. For example, the integration of attention mechanisms into CNNs has been proposed to increase the accuracy of deep learning models [6]. In addition, studies have been conducted on reducing the training time and improving the performance of CNNs using transfer learning methods [7]. In the field of biomedical image processing, CNNs have provided high accuracy, especially in COVID-19 diagnosis [8]. In autonomous systems, CNNs have shown reliable performance for autonomous vehicles despite harsh environmental conditions [9]. Finally, studies to increase the scalability of CNNs on large data sets are also attracting attention as of 2023 [10].

2.1.3. Resnet 18

ResNet-18 is an architecture among deep neural networks that can learn more complex features by increasing the number of layers. However, residual connections were used to solve the "gradient extinction" problem that occurs with increasing the number of layers [10]. A study conducted in 2023 showed that ResNet-18 provides more efficient and faster results compared to deeper models on various datasets [11]. In particular, ResNet-18's ability to run with low latency on devices with limited resources has widespread its use in areas such as autonomous systems and mobile applications [12]. In addition, studies on optimizing ResNet-18 with transfer learning have highlighted the flexible structure of this model that can easily adapt to different areas [13].

2.1.4. AlexNet

AlexNet is known as one of the first architectures that revolutionized the field of deep learning and attracted attention especially with its success in the ImageNet competition in 2012. Studies conducted in 2023 show that AlexNet is still frequently preferred in applications with low hardware requirements because it is smaller and faster compared to more modern networks [14]. In one study, it was emphasized that the simple structure of AlexNet is ideal for mobile devices and low-cost systems, and it was stated that it achieved high accuracy results especially in image classification tasks [15]. In addition, studies

have been conducted to increase the applicability of AlexNet to more complex data sets with transfer learning techniques [16]. Thus, today, AlexNet still provides an effective solution in many different areas, especially in systems with limited resources [17].

2.1.5. Performance evaluation metrics

Performance evaluation metrics are critical in evaluating the success of a model. Accuracy, recall, precision, and F1 score are commonly used metrics, especially in classification problems. Accuracy is the ratio of the examples correctly classified by the model to the total number of examples and is calculated using the mathematical expression given in equation 1 [18].

$$Accuracy = \frac{TP+TN}{TP+TN+FP+FN} \quad (1)$$

In the equation, TP (True Positive), TN (True Negative), FP (False Positive), and FN (False Negative) represent the classification results [18]. The accuracy metric is useful in cases where the classes in the dataset are balanced; however, it can be misleading in imbalanced datasets.

Recall indicates how many of the true positives were classified correctly and is calculated using the mathematical expression given in equation 2. [19].

$$Recall = \frac{TP}{TP+FN} \quad (2)$$

This metric is especially preferred in cases where under classification is important. High recall indicates that the model performs well without skipping positive classes [19].

Precision measures how many of the model's positive predictions are correct and is calculated using the mathematical expression given in equation 3 [20].

$$Precision = \frac{TP}{TP+FP} \quad (3)$$

Sensitivity is often used, especially in cases where false positive results are costly. High sensitivity indicates that the model is consistent in its positive predictions [20].

F1 Score is the harmonic mean of precision and recall and is used to evaluate the performance in imbalanced classes in a more balanced manner and is calculated using the mathematical expression given in equation 4 [21]

$$F1\ Score = 2 \times \frac{Precision \times Recall}{Precision + Recall} \quad (4)$$

F1 score is an ideal solution metric for situations where both precision and recall are important [21].

2.2. Method

The workflow process followed in the study is presented in Figure 2. In this study, we used an image classification approach to detect seat belt usage in moving vehicles using three different models: Custom CNN, ResNet-18, and AlexNet. The methodology involved multiple stages, which are detailed below:

Dataset Preparation:

The dataset consisted of 1000 images captured using an unmanned aerial vehicle (UAV) under various driving conditions. Each image was manually labeled to indicate whether a seat belt was worn. The images were recorded at a resolution of 240x240 pixels and included diverse lighting and weather scenarios to ensure robustness.

Data Preprocessing:

Preprocessing played a critical role in improving model performance. Gaussian filtering was applied to the images to remove noise and interference, which is crucial in reducing false positive and false negative results. This step ensured the images were clear and consistent, facilitating effective feature extraction. Additionally, normalization was performed to scale pixel values between 0 and 1, standardizing the dataset and improving the training convergence of the models.

Custom CNN: A convolutional neural network (CNN) designed specifically for this task. It included multiple convolutional layers, pooling layers, and dense layers optimized for the dataset.

ResNet-18: A deep residual network known for its efficiency in handling complex image processing tasks.

AlexNet: A simpler architecture that demonstrated strong performance in earlier

image classification challenges, chosen for comparison.

Training Process:

All models were trained for 100 epochs using the same dataset and hyperparameters. The learning rate was set to 0.0001, and cross-entropy loss was used as the optimization criterion. During training, techniques such as data augmentation and early stopping were employed to enhance generalization and prevent overfitting.

Performance Evaluation:

The models were evaluated using metrics such as accuracy, recall, precision, and F1 score. These metrics were calculated based on the confusion matrices generated from the classification results. The training process also involved monitoring loss values to assess the models' learning efficiency over time.

Implementation Tools:

The models were implemented using Python and TensorFlow libraries. GPU acceleration was utilized to expedite the training process. The results were visualized using matplotlib to better interpret model performance trends.

By elaborating on these methodological details, we aimed to ensure clarity and reproducibility of the study. The comprehensive workflow allows future researchers to replicate and build upon our findings.

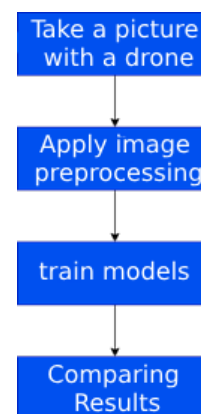


Figure 2. Workflow diagram

In the study, a system was developed that aims to detect whether the drivers of the vehicles are wearing seat belts while driving, using images collected using an unmanned aerial vehicle (UAV). In this context, a Convolutional Neural Network (CNN) based model was created and this model was trained with ResNet-18 and

AlexNet architectures in order to make a performance comparison. The dataset used in the study consists of images obtained with the UAV and this dataset was subjected to a series of pre-processing stages before training.

First, a Gaussian filter was applied to remove noise and interference from the images. This process made the images clearer and cleaner, thus contributing to the model producing more reliable results. Removing the noise is a critical step to reduce the possibility of the model giving false positive or false negative results. After the Gaussian filter, the normalization process was applied to the images in the dataset. Normalization shortened the training time of the model by scaling the pixel values in each image within a certain range and also increased the learning ability of the model. This process also helped the model to perform more generally under different lighting and contrast conditions.

A specific set of hyperparameters was used for training the models. Both models were trained for 100 epochs, and the learning rate was set to 0.0001. In this process, appropriate training strategies were adopted to prevent the model from overfitting. During training, both ResNet-18 and AlexNet models were trained with the same dataset and parameters, thus comparing the performances of the two models. During the training process, different metrics were used to monitor accuracy, loss values, and model performance during training.

3. RESULTS

In this study, the performance evaluations and obtained results of the CNN-based model developed to detect whether the drivers of moving vehicles are wearing seat belts are presented. In our study, the findings obtained in terms of accuracy, training time and overall performance of the model as a result of the trainings performed using ResNet-18, AlexNet and the CNN model we specially developed were discussed in detail. During the experimental process, the training accuracies of the models and their performances in the test phase were compared and presented, and it was discussed which model gave more effective results in this direction. Model training results are given in Table 1.

Table 1. Model Performance Metrics

| Model | Accuracy (%) | Precision (%) | Recall (%) | F1 Score (%) |
|-----------|--------------|---------------|------------|--------------|
| CNN Model | 94.55 | 95 | 93.8 | 94.4 |
| Resnet18 | 89.54 | 90 | 89.1 | 89.55 |
| AlexNet | 88.33 | 88.5 | 88.2 | 88.35 |

The accuracy graph shown in Figure 3 shows the accuracy values obtained by the models during the training process for 50 epochs. The graph was created to compare the accuracy performances of three different models (custom CNN model, ResNet-18 and AlexNet). As can be seen from the figure and the graph, the initial accuracy levels of the models were quite low, and all three models exhibited similar performance during the first 5 epochs. In this phase, the accuracy rates of all models changed around 10-15%.

As the number of epochs increases, especially after the 15th epoch, a significant increase in the accuracy rates was observed in all three models. It is seen that the specially developed CNN model reached a higher accuracy rate than the other two models as of the 20th epoch and this superiority continued throughout the training process. ResNet-18 and AlexNet models showed similar performance, but it was determined that the AlexNet model sometimes had lower accuracy rates than ResNet-18. After the 35th epoch, both models reached a stable point in terms of accuracy and settled at approximately 85% levels.

On the other hand, the special CNN model continued to increase the accuracy rate until the last epoch and reached approximately 95%. This shows that the model is more successful in seat belt detection than the other two models. It is thought that the deep learning model developed specifically for the study, which consistently obtained higher accuracy values throughout the training process, may have been positively affected by preprocessing steps such as denoising and normalization. The results obtained reveal that the CNN model developed specifically for the study provides a more effective solution to seat belt classification problems.

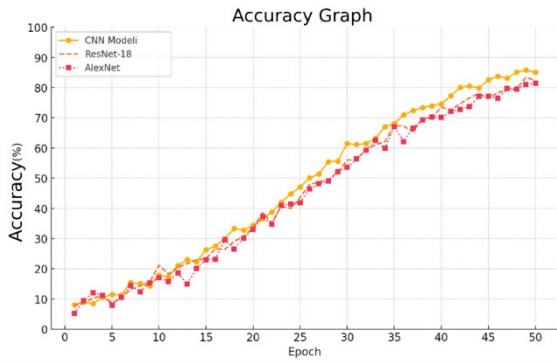


Figure 3. Accuracy graph

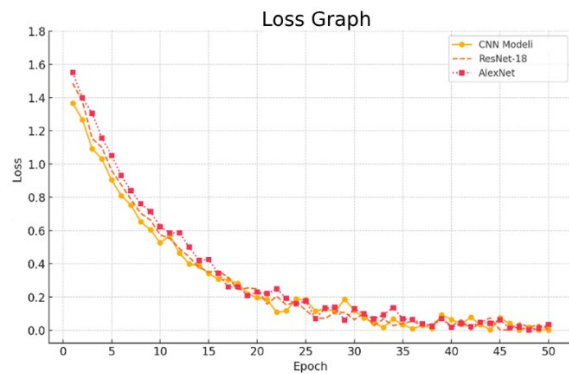


Figure 4. Loss graph

The loss graph given in Figure 4 shows the CNN model, ResNet-18 and AlexNet deep learning models used in the study, and the loss values they encountered during the training process. The loss value represents a metric used to measure the accuracy of the results predicted by the model. Therefore, a lower loss value means that the model performs better.

When the graph is examined, it is observed that all three models start with very high loss values at the beginning of the training process. In the beginning, especially during the first few epochs, the loss values are at the level of 1.6. However, as the number of epochs increases, a rapid decrease is observed in the loss values of all three models. This decrease shows that the models start to learn the dataset better and their prediction performance improves.

The loss value of the special CNN model started to be lower than the other two models starting from the 10th epoch. This shows that the model has a faster learning capacity and is better suited to the dataset. ResNet-18 and AlexNet models showed approximately similar loss values, but it was observed that the AlexNet model had slightly higher loss values than ResNet-18 at certain points. Starting from the 20th epoch, the rate of decrease in the loss values of all three

models slowed down and after the 30th epoch, the loss values decreased below 0.2 and continued to be stable. Especially as of the 35th epoch, the loss value of the CNN model developed specifically for the study decreased below 0.1 and achieved the lowest loss value during the training period. ResNet-18 and AlexNet models completed the process with loss values at the level of 0.2. In general, the success of the special CNN model in the loss graph shows that the model has a better generalization ability on the dataset and makes fewer errors. ResNet-18 and AlexNet models exhibited similar performances, but they completed the training with slightly higher loss values compared to the CNN model developed specifically for the study. This suggests that the CNN model developed specifically for the study may be suitable for classifying images of seat belt fastening/not fastening.

The performance of the models developed and compared in this study—Custom CNN, ResNet-18, and AlexNet—was assessed using confusion matrices Table 2. These matrices summarize the classification results, providing insights into each model's ability to correctly identify seat belt usage.

Table 2. Model Confusion Matrices

| | Custom CNN | ResNet-18 | AlexNet |
|----|------------|-----------|---------|
| TP | 938 | 890 | 882 |
| FP | 46 | 89 | 101 |
| FN | 7 | 15 | 15 |
| TN | 7 | 4 | 1 |

The confusion matrices highlight that the Custom CNN model outperforms the other two models in terms of both sensitivity (true positive rate) and specificity. The Custom CNN achieves a significantly higher number of true positives (938) while maintaining a lower false positive (46) and false negative (7) count compared to ResNet-18 and AlexNet. In contrast, AlexNet, while having a slightly lower number of true positives (882), exhibits the highest number of false positives (101) and a minimal count of true negatives (1), indicating challenges in distinguishing negative instances. The ResNet-18 model performs moderately, with true positives and false positives falling between those of Custom CNN and AlexNet. However, its higher false negative count (15) compared to the Custom CNN suggests

potential room for improvement in recall. These findings underscore the superiority of the Custom CNN model for the classification task, reflecting its robustness and reliability in detecting seat belt usage under varying conditions.

In the new studies to be carried out, the use of advanced and up-to-date models and performance comparison in real-time applications will be made. In addition, the visuals in the data set will be diversified and the performance in different weather conditions will be improved.

ETHICAL APPROVALS

The study was carried out by the Scientific Research and Publication Ethics Committee of Isparta University of Applied Sciences with the decision of the ethics committee numbered 202/01.

ACKNOWLEDGES

This work was presented as an abstract at the 6th International Conference on Artificial Intelligence and Applied Mathematics in Engineering (ICAIAME 2024).

REFERENCES

- Boztaş, G., and Özcebe, H., "Secondary protection in traffic accident injuries: Seat belt", *Journal of Continuing Medical Education*, Vol. 14, Issue 5, Pages 94-97, 2005.
- Bektaş, S., and Hıms, M.A., "Prediction model of factors affecting seat belt usage for automobile drivers", *Erciyes University, Institute of Science, Journal of Science*, Vol. 25, Issue 1, Pages 208-222, 2009.
- Usman, B. A., and Adebosin, T., "Seat belt use and perceptions among Inter-Urban commercial vehicle drivers in Ilorin, Nigeria", *Journal of Road Safety*, Vol. 35, Issue 3, Pages 32-43, 2024.
- Delice, M., and Demir, I., "Investigation of the relationship between seat belt wearing rates and traffic accidents death rates in countries", *Hitit University Social Sciences Institute Journal*, Vol. 8, Issue 2, 2015.
- Sengupta, S., "Artificial intelligence and image processing", pages 51-60., Chapman and Hall/CRC, 2021.
- Smith, J., and Brown, A., "Enhancing CNN accuracy with attention mechanisms", *Journal of Machine Learning Research*, Vol. 24, Issue 5, Pages 102-119, 2023.
- Patel, R., and Liu, Z., "Transfer learning strategies for CNNs", *IEEE Transactions on Neural Networks and Learning Systems*, Vol. 34, Issue 2, Pages 432-445, 2023.
- Rahman, M., and Singh, P., "CNN-based COVID-19 detection from medical images", *Computers in Biology and Medicine*, Vol. 155, 106631, 2023.
- Wang, H., and Zhang, X., "Reliable performance of CNNs in autonomous driving", *ACM Computing Surveys*, Vol. 56, Issue 1, Pages 88-104, 2023.
- Chen, L., and Kim, D., "Scaling CNNs for big data applications", *Artificial Intelligence Review*, Vol. 56, Issue 7, Pages 1467-1485, 2023.
- Zhang, Y., and Lee, K., "ResNet-18 performance in low-Resource Environments", *IEEE Transactions on Neural Networks and Learning Systems*, Vol. 34, Issue 2, Pages 532-549, 2023.
- Liu, W., and Wang, X., "Optimizing ResNet-18 for edge computing", *ACM Transactions on Intelligent Systems and Technology*, Vol. 14, Issue 3, Pages 99-112, 2023.
- Patel, R., and Liu, Z., "Transfer learning strategies for CNNs", *IEEE Transactions on Neural Networks and Learning Systems*, Vol. 34, Issue 2, Pages 432-445, 2023.
- Smith, J., and Brown, A., "Enhancing CNN accuracy with attention mechanisms", *Journal of Machine Learning Research*, Vol. 24, Issue 5, Pages 102-119, 2023.
- Liu, W., and Zhang, Y., "AlexNet in resource-constrained environments", *IEEE Transactions on Neural Networks and Learning Systems*, Vol. 34, Issue 3, Pages 678-692, 2023.
- Patel, R., and Liu, Z., "Transfer learning strategies for CNNs", *IEEE Transactions on Neural Networks and Learning Systems*, Vol. 34, Issue 2, Pages 432-445, 2023.
- Chen, L., and Kim, D., "Scaling CNNs for big data applications", *Artificial Intelligence Review*, Vol. 56, Issue 7, Pages 1467-1485, 2023.
- Zhang, Y., and Lee, K., "ResNet-18 performance in low-resource environments", *IEEE Transactions on Neural Networks and Learning Systems*, Vol. 34, Issue 2, Pages 532-549, 2023.

19. Liu, W., and Wang, X., "Optimizing ResNet-18 for edge computing", *ACM Transactions on Intelligent Systems and Technology*, Vol. 14, Issue 3, Pages 99-112, 2023.

20. Patel, R., and Liu, Z., "Transfer learning strategies for CNNs", *IEEE Transactions on Neural*

Networks and Learning Systems, Vol. 34, Issue 2, Pages 432-445, 2023.

21. Chen, L., and Kim, D., "Scaling CNNs for big data applications", *Artificial Intelligence Review*, Vol. 56, Issue 7, Pages 1467-1485, 2023.



ULUSLARARASI 3B YAZICI TEKNOLOJİLERİ
VE DİJİTAL ENDÜSTRİ DERGİSİ

INTERNATIONAL JOURNAL OF 3D PRINTING
TECHNOLOGIES AND DIGITAL INDUSTRY

ISSN:2602-3350 (Online)

URL: <https://dergipark.org.tr/ij3dptdi>

EKLEMELİ İMALAT İLE DEMİR KATKILI FİLAMAN ÜRETİMİ İÇİN EKSTRÜZYON CİHAZININ TASARIMI, İMALATI VE CİHAZIN TERMAL ANALİZİ

DESIGN, MANUFACTURING AND THERMAL
ANALYSIS OF EXTRUSION DEVICE FOR IRON-
INCLUSION FILAMENT PRODUCTION BY ADDITIVE
MANUFACTURING

Yazarlar (Authors): Barış Güneç^{id*}, Ertuğrul Durak^{id}

Bu makaleye şu şekilde atıfta bulunabilirsiniz (To cite to this article): Güneç B., Durak E., "Eklemeli İmalat ile Demir Katkılı Filaman Üretimi İçin Ekstrüzyon Cihazının Tasarımı, İmalatı Ve Cihazın Termal Analizi" *Int. J. of 3D Printing Tech. Dig. Ind.*, 8(3): 459-467, (2024).

DOI: 10.46519/ij3dptdi.1571711

Araştırma Makale/ Research Article

Erişim Linki: (To link to this article): <https://dergipark.org.tr/en/pub/ij3dptdi/archive>

EKLEMELİ İMALAT İLE DEMİR KATKILI FİLAMAN ÜRETİMİ İÇİN EKSTRÜZYON CİHAZININ TASARIMI, İMALATI VE CİHAZIN TERMAL ANALİZİ

Barış Güneç^a , Ertutuğrul Durak^a 

^a Süleyman Demirel Üniversitesi, Mühendislik Fakültesi, Makine Mühendisliği Bölümü, TÜRKİYE

* Sorumlu Yazar: gunenbaris@gmail.com

(Geliş/Received: 11.09.24; Düzeltme/Revised: 09.11.24; Kabul/Accepted: 09.12.24)

ÖZ

Eklemeli imalat, malzeme ve imalat teknolojilerinin ilerlemesiyle her geçen gün farklı özellikte makine parçalarının üretilmesine olanak tanımaktadır. Farklı katkı maddelerini içeren yazıcı filamanları ile imal edilen parçaların mekanik, termal, kimyasal ve manyetik vb. özelliklerinde iyileşmeler elde edilmektedir. Bu çalışmada, katkılı filaman üretimine uygun ekstrüderlerin özelliklerinin daha iyi tanımlanabilmesi ve bu konuda yapılacak bilimsel çalışmalara kaynak oluşturabilmesi amacıyla, üç boyutlu yazıcılarda kullanılmaya uygun, katkılı filaman ekstrüzyonu yapabilecek bir ekstrüder tasarımı gerçekleştirilmektedir. Çalışmanın kapsamı; ekstrüder milinin seçimi, tahrik iletim ve yataklama elemanlarının belirlenmesi, kovan ve nozul sistemine ısıtıcı bantların yerleştirilmesi, PID kontrol sistemiyle istenen sıcak değerlerinin yönetilmesi, Solidworks programı kullanılarak termal simülasyonunun yapılması ve termal görüntüleme kamerası yardımıyla gerçek değerlerin simülasyon sonuçlarıyla kıyaslanması gibi adımları içermektedir. Kurulan deney düzeneğinde bulunan kovan gövdesindeki ısıtma bölgelerinin zamana bağlı sıcaklık değişim grafikleri oluşturulmakta ve incelenmektedir. Yapılan çalışmada cihazın iyileştirilebilmesi amacıyla kovan yüzeyine uygulanan taş yünü ceket sayesinde, hedef sıcaklık değerine ulaşmak için ısıtıcı bantların enerji tüketiminde %32,88 oranında iyileşme sağlandığı görülmektedir. Ayrıca, her bölge için zamana bağlı sıcaklık değişim grafikleri ayrı ayrı oluşturulmakta ve izolasyonun, orta kısımda hedef sıcaklığın aynı süre içinde 12 °C üzerine çıkmasına neden olduğu tespit edilmektedir.

Anahtar Kelimeler: Eklemeli İmalat, Demir Katkılı Filaman, Filaman Ekstrüzyonu, PLA, Termal Simülasyon.

DESIGN, MANUFACTURING AND THERMAL ANALYSIS OF EXTRUSION DEVICE FOR IRON- INCLUSION FILAMENT PRODUCTION BY ADDITIVE MANUFACTURING

ABSTRACT

Advancements in materials and manufacturing technologies are enabling the production of machine parts with diverse characteristics through additive manufacturing. Significant improvements in mechanical, thermal, chemical, and magnetic properties, among others, are being achieved with 3D printer filaments that contain different additives. To better define the characteristics of extruders suitable for the production of filaments with additives, and to serve as a resource for studies in this area, an extruder capable of producing additive-containing filaments for use in 3D printers has been designed. The scope of the study includes the selection of the extruder screw, the drive transmission and bearing components, the barrel and nozzle system, the placement of barrel heaters within the setup, the control of the desired temperature values using a PID control system, conducting thermal simulations with the help of SolidWorks, and comparing the actual values with the simulation results using a thermal imaging camera. Time-dependent temperature change graphs for the heating zones of the barrel body in the established system were created and examined. The study found that by improving the device, the effect

of heater bands on the power required to reach the target temperature was improved by 32,88% with the application of a rock wool jacket to the barrel surface. Additionally, separate time-dependent graphs for each zone were created, revealing that the insulation increased the temperature by 12°C above the target in the middle section of the barrel body within the same time frame.

Keywords: Additive Manufacturing, Iron-infused Filament, Filament Extrusion, PLA, Thermal Simulation.

1. GİRİŞ

Ekstrüzyon işlemi, termoplastik malzemelerin kontrollü bir şekilde eritilerek, belli bir geometrik şekle sahip bir kalıptan geçirilmesi suretiyle sürekli bir ürün elde edilmesi işlemidir. Bu yöntem, üç boyutlu (3D) baskı teknolojisinde yaygın bir şekilde kullanılmaktadır. Eritilmiş biriktirme modellemesi (FDM, Fused Deposition Modeling) ya da Erimiş Filaman Üretimi (FFF, Fused Filament Fabrication) gibi süreçlerin temelini oluşturmaktadır. Ekstrüzyon işlemi, polimer malzemelerin istenilen formlarda üretimini sağlarken, üretim sürecinde hız, hassasiyet ve maliyet avantajları sunmaktadır. Demir katkılı filaman üretiminde ekstrüder, yalnızca bir polimeri eritmeyi değil, aynı zamanda demir partikülleriyle homojen bir karışım sağlamayı da amaçlamaktadır [1-2].

Demir partiküllerinin polimer matrisi içinde eşit şekilde dağılması için özel bir vida tasarımı ve karıştırma mekanizması gereklidir. Aksi takdirde, demir partikülleri filamanın belirli bölgelerinde yoğunlaşabilir ve bu heterojen yapı ise filamanın mekanik ve manyetik özelliklerini olumsuz yönde etkileyebilmektedir. Ayrıca demir partikülleri, ekstrüderde aşındırıcı etki yaratabilmektedir. Bu nedenle, ekstrüderin iç yüzeyinde aşınmaya dayanıklı malzemeler kullanılmalı ve vida sistemi bu malzemelerin zarar görmesini önleyecek şekilde tasarlanmalıdır [3].

Demir katkılı polimerlerde hem polimerin erime noktası hem de demir partiküllerinin sıcaklıkla olan etkileşimi dikkate alınmalıdır. Özellikle yüksek demir içeriği, ısıl iletkenlik özelliklerini değiştirebilir ve polimerin dengesiz bir şekilde soğumasına neden olabilmektedir. Demir katkılı filamanlar, metalik özelliklere sahip olmasının yanı sıra manyetik özellikleri sayesinde de çeşitli endüstriyel uygulamalarda kullanılabilmektedir. Örneğin, manyetik sensörlerin üretiminde, elektromanyetik kalkan

oluşturabilmek amacıyla ve hatta dekoratif ürünlerde kullanılabilmektedir. Bu tür filamanların üretiminde ekstrüderin uygun tasarımı, sadece homojen bir karışım elde edilmesini sağlamakla kalmaz, aynı zamanda üretilen filamanın kalitesini ve performansını da doğrudan etkilemektedir [4-5].

Demir katkılı filamanlar, geleneksel plastik filamanların yanı sıra metalin özelliklerini de taşıyan yenilikçi bir malzeme kategorisidir. Bu filamanlar, plastik polimer matrisi içinde demir partiküllerinin homojen dağılımıyla üretilmektedir. Metalik katkı sayesinde üretilen parçaların mekanik, manyetik ve elektriksel performansının artırılmasına imkan sağlamaktadır. Demir katkılı filamanlar, özellikleri itibarıyla geniş bir uygulama yelpazesine sahip olup, özellikle dayanıklılık, manyetik etkileşimler ve elektriksel iletkenlik gibi avantajlar sunmaktadır [6].

Yapılan literatür araştırmalarında demir katkılı filaman imalatına uygun ekstrüder tasarımına yönelik yeterli çalışmalara yer verilmediği gözlemlenmektedir. Sektörde bulunan ekstrüderlerin çok yüksek maliyetli, büyük boyutlu ve filaman imalatına uygun olmaması nedeniyle bu çalışmada ekonomik, kompakt ve demir katkılı filaman imalatına uygun bir ekstrüder tasarımı yapılmaktadır. Ayrıca tasarımı yapılan ekstrüderin 3 boyutlu termal analizi benzetim ortamında gerçekleştirilmektedir.

2. KAYNAK ARAŞTIRMASI

Amirov vd. [7], yaptıkları çalışmada 3D yazıcı filamanını tedarik edilen bir ekstrüderle kendileri üretmeyi amaçlamaktadırlar. Yapılan çalışmada, kendi ürettikleri filamanın mekanik özelliklerinin karakterizasyonu ve ekstrüzyon parametrelerinin iyileştirilmesi için çalışmalar yer almaktadır. Çalışmada elde ettikleri filamanların, tedarik edilen filamanlara nazaran daha ekonomik olduğu ve zaman tasarrufu sağladığı düşünülmektedir. PLA malzemelerin

ekstrüzyon temelli eklemeli imalatla en fazla kullanılan malzemelerden biri olmasının temel sebeplerinden biri biyolojik temelli olduğundan biyolojik olarak parçalanabilen malzeme olmasıdır. PLA malzemelerin geri dönüştürülmesinde polimer yapı kalitesinin azalması nedeniyle bir co-ekstrüzyon düzeneği ve özel bir nozul kullanılarak geri dönüştürülmüş PLA filamanın belirli miktarını yeniden kazandırılmaya çalışılmaktadır [8].

İyi bir filaman üretimi için sıcaklık ve ekstrüzyon hızının doğru ayarlanması gerekmektedir. Ekstrüzyon hızının artması ham plastiğin düzgün erimemesine, kabarcık oluşumuna ve filamanda pürüzlü bir yüzeyli olmasına sebep olabilmektedir. Filamanın nihai çapının nozul çapı ve filamanın çekme hızına bağlı olduğu incelenmiş ve çalışmada kullanılan ekonomik bir filaman cihazı imalatı gerçekleştirilmiştir. Çalışmadaki filaman ekstrüderi, tek bölgede bir ısıtma bandı içermekte olup optimum sıcaklık dağılımı ise yalnızca gözlemsel sonuçlar üzerinden incelenmektedir. Polimer ekstrüzyonunda sistemin optimize edilmemiş parametrelerle kullanılması %15-20 oranlarına varan enerji kayıplarına sebep olabilmektedir. Ürün kalitesi; erimiş polimer akış kontrolü, erime sıcaklığı, vida hızı gibi parametrelerin doğru ayarlanması ile mümkün olabilmektedir. Bu çalışmada tek vidalı bir ekstrüder parametrelerinin doğru ayarlanabilmesi amacıyla bulanık mantık denetleyicisi geliştirilmektedir. Çalışmada açık döngülü bir sistem ile kıyaslama yapılarak ekstrüderin enerji verimliliğinin sağlanabileceği gösterilmektedir [9-10]. Demir partiküllerinin varlığı filamanın manyetik özellikler kazanmasını sağlayabilmektedir. Demir katkı filamanlar, manyetik alanlarla etkileşime girebilmektedir. Bu özellik, manyetik sensörler, elektromanyetik kalkan ve diğer manyetizma temelli uygulamalarda, endüstriyel robotik veya manyetik bağlantı gerektiren uygulamalarda, büyük bir avantaj sağlamaktadır. Manyetik özellikleri demir katkı filamanların, elektronik, otomotiv ve mühendislik uygulamalarında kullanılmalarına olanak vermektedir. Saf polimerler tipik olarak elektriksel iletkenlik sağlamazken, demir katkı filamanlar bir dereceye kadar elektriksel iletkenlik sağlayabilmektedir. Demir partiküllerinin malzeme içinde varlığı, özellikle düşük akım gerektiren uygulamalarda elektrik iletimi sağlamaktadır. Bu özellikler, demir

katkılı filamanların sensörler, devre elemanları ve elektromanyetik girişim (EMI) koruma uygulamalarında kullanılmasını kolaylaştırmaktadır. Demir katkısı filamanlara, görsel olarak metalik bir görünüm sunmaktadır. Bu, endüstriyel tasarımlarda dekoratif unsurların yaratılmasında, metal hissi veren hafif parçalar üretmek için uygun bir yöntem olarak kullanılabilmesine olanak vermektedir. Ek olarak, demir içeriği filamanın ağırlığını artırır, bu da bazı uygulamalarda ürünün el ile temasında daha sağlam hissedilmesini sağlamaktadır [7-11]. Bu sebeple ekonomik ve demir katkı filaman imalatına uygun bir ekstrüderin tasarımı için, termal simülasyon ve analizinin yapılması gerekli olup, enerji verimliliği için de termal izolasyonun etkisinin incelenmesi önemlidir.

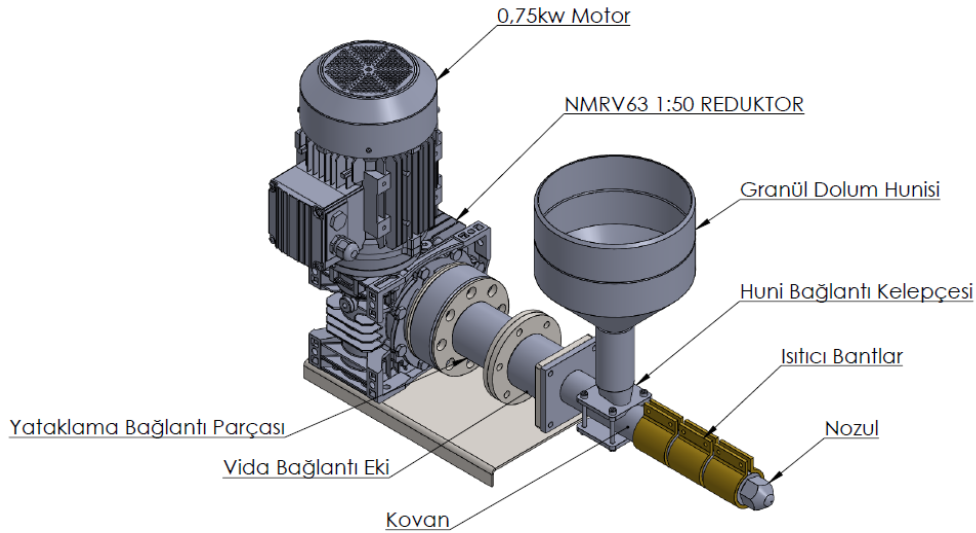
3. MATERYAL VE YÖNTEM

Demir katkı filamanların üretimine olanak sağlayacak bir ekstrüder kovanı; besleme, erime ve şekillendirme olmak üzere üç temel bölümden oluşmaktadır. Ekstrüderde polimer, granül veya toz formunda cihazın huni kısmına yerleştirilmektedir. Bu aşamada vida sistemi, malzemeyi ileriye doğru taşımakta ve polimer sıcaklık etkisiyle sıvı hale gelmektedir. Erimiş polimer, belirli bir nozul çapından geçirilerek istenen kalınlık ve şekle sahip filaman üretilmektedir. Üretilen filaman, bir soğutma hattına alınarak katılaşmakta ve bobin haline getirilmektedir. Bu filaman daha sonra 3 boyutlu baskı makinelerinde kullanılabilir [11]. L/D oranı, vida tasarımında "uzunluk/çap oranı" anlamına gelmekte olup, vida uzunluğunun çapına oranı olarak hesaplanmaktadır. Ekstrüder tasarımında, vida helis açısı ve kanal boşluk yüksekliği arttıkça enerji verimliliği artış göstermekte; ancak, L/D oranının artması enerji verimliliği üzerinde olumsuz etki yaratmaktadır. Vida hızının azaltılması ve sıkıştırma oranının artırılması ise vida verimliliğini ve dolayısıyla enerji verimliliğini yükseltmektedir [13]. Bu çalışmada kullanılan vida, 15:1 L/D oranına ve 2.8 sıkıştırma oranına sahip olarak belirlenmektedir. Yapılan çalışmada 20 mm çapında vida kullanılmaktadır. Kovan ve nozul malzemeleri olarak 38CrMoA1A tercih edilmektedir. Vida doğrusallığı 0.015 mm olup, nitrasyon derinliği 0.5-0.8 mm arasında değişmekte ve yüzey sertliği 900 – 1000 HV arasında yer almaktadır. Gövdenin ayakta durabilmesi amacıyla

tasarlanan yapı, St37-2 çelik levha malzemeden lazer kesimle imal edilmektedir. Bağlantı elemanları ise 1040 kalite çelikten üretilmektedir. Gövde üzerinde üç adet K tipi termokupl, REX-C100 ısı kontrol üniteleri ve yerli bir firmadan temin edilen üç adet 250 W ısıtma gücüne sahip rezistans kullanılmaktadır. Demir katkılı filaman üretiminde kullanılan ekstrüderlerin performansı, doğru bileşen seçimi ve tasarımıyla doğrudan ilişkilidir. Bu çalışmada, ekstrüzyon miline tahrik vermek amacıyla 0,75 kW gücünde asenkron motor tercih edilmektedir. Kullanılan motorun çıkış devri 1425 d/d olarak belirlenmiştir. Motor çıkış mili, NRW63 gövdeli bir sonsuz vidalı dişli kutusuna bağlıdır. Sonsuz dişli tahvil oranı 50 olarak belirlenmektedir. Motor için sürücü olarak “Vacon 0010-1L-0004-2” modeli kullanılmıştır.

(<https://www.vacondrives.com/>). Ekstrüzyon sürecinde malzemenin homojen bir şekilde karıştırılması, eritilmesi ve filaman haline getirilmesi için vida tasarımı, nozul çapı, sıcaklık kontrolü ve motor gücü gibi temel bileşenlerin her birinin kritik bir rol oynadığı bilinmektedir. Ekstrüderde kullanılan vida, polimer ve demir partiküllerinin etkili bir

şekilde karıştırılmasını ve erimesini sağlayan temel bileşen olarak görev yapmaktadır. Vida tasarımı, malzeme akışını düzenleyerek filaman üretim kalitesini doğrudan etkileyen en önemli unsurlardan biri tanesidir [10]. Tek bir vida ile polimer ve katkı maddeleri karıştırılmakta ve eritilebilmektedir. Kullanılan vida üç bölümden oluşmaktadır. Şekil 1.'de çalışmada tasarlanan sistem elemanları gösterilmektedir. Besleme bölgesi malzemenin vida içine alındığı ilk bölgedir. Bu bölgede demir katkılı polimerin etkili bir şekilde alınması ve aşağıya doğru taşınması önemlidir. Sıkıştırma bölgesinde vida, malzemeyi sıkıştırarak daha yoğun bir karışım sağlamakta ve erime işlemini hızlandırmaktadır. Bu kısımda malzemenin düzgün bir şekilde eritilmesi sağlanmaktadır. Karıştırma bölgesi malzemenin tamamen eridiği ve demir partiküllerinin polimer matrisi içinde homojen bir şekilde dağıtıldığı bölümdür. Karıştırma işlemi ne kadar etkili olursa, filamanın kalitesi o kadar artmaktadır. Tek vidalı ekstrüderler basit yapısı nedeniyle yaygın olarak sektörde kullanılmaktadır, ancak homojen karışım sağlamakta bazen yetersiz kalabileceği düşünülmektedir[3].



Şekil 1. Solidworks ile Tasarlanan Ekstrüder Düzenegi

Ekstrüderin çıkışında bulunan nozul, eritilmiş polimerin filaman haline dönüştüğü bileşen olmaktadır. Nozul çapı, filamanın çapını belirlemekte ve baskı kalitesi üzerinde doğrudan bir etkiye sahip olmaktadır. Filaman üretiminde yaygın olarak kullanılan çaplar 1,75

mm ve 2,85 mm'dir. Nozul çapı, ekstrüzyon işlemi sırasında malzemenin düzgün bir şekilde akmasını sağlamaktadır. Şekil 2.'de nozul, kovan ve mil gösterilmektedir. Daha küçük çaplı nozullar, daha ince ve hassas filaman üretimine olanak tanımaktadır. Bununla

birlikte, demir katkılı filamanlarda, partikül boyutuna bağlı olarak daha büyük çaplı nozullar tercih edilebilmektedir. Küçük çaplı nozulların kullanılması demir partiküllerinin nozul çıkışının tıkanmasına neden olabilmektedir. Bu nedenle, demir katkılı filaman üretiminde, partikül boyutu ile uyumlu bir nozul çapı seçimi önem taşımaktadır. Bu çalışmada, ekstrüder nozul çapı 1,75mm olarak belirlenmektedir.



Şekil 2. Ekstrüderde kullanılan vida, nozul ve kovan sistemi

3.1. Termal Analiz

Ekstrüderde sıcaklık kontrolü, polimerin düzgün bir şekilde erimesini ve homojen bir karışım elde edilmesini sağlamak için kritik öneme sahiptir. Demir katkılı filamanlarda, metal partiküllerin varlığı nedeniyle sıcaklık kontrolü daha hassas yapılmalıdır. Ekstrüder üzerinde üç adet PID ısı kontrol ünitesi REX-C100, K tipi termokupl, SSR-40 DA katı hal rölelerinden üçer adet kullanılmaktadır. Şekil 3.'te gösterilen sistemde kullanılan bileşenler 3 mm çelik levha malzemeden imal edilen bir ayak üzerine monte edilmektedir. Sistem besleme gerilimi olarak AC 220 V, 50 Hz. ve katı hal röleleri için DC 24V ile çalışmaktadır.



Şekil 3. Isı kontrol ve takip Ünitesi

Her bir kademe için, Şekil 4.'te gösterilen 250 W gücünde ısıtıcı bant rezistans kullanılmaktadır. Kullanılan rezistanslar, mika yalıtımlı ve pirinç gövdelidir. Rezistanslar $\varnothing 40 \times 50$ mm ölçülerinde olup, 220V AC elektrik ile kumanda edilmektedir. Sistemde sıcaklık ölçümü amacıyla, termokupl olarak K serisi 6 mm çapında termokupl kullanılmaktadır. Düzenekte bulunan PID kontrolcüler (REX-C100) Çizelge 1.'de belirtildiği şekilde ayarlanmaktadır. Kurulan düzenekte, ısıtıcı bantlara uygulanan gerilim, katı hal röleleri yardımıyla açılıp kapatılmaktadır. Devredeki ısıtıcıların açılıp kapanmasını yöneten PID devreleri, hedef sıcaklık ile mevcut sıcaklık arasındaki farka bağlı olarak çalışmaktadır.

Çizelge 1. PID kontrolcüsüne ait parametreler

| PID Parametresi | Değer |
|-----------------|-------|
| Ary | 0 |
| P | 30 |
| I | 240 |
| D | 60 |
| Ar | 100 |
| r | 2 |
| Sc | 0 |
| LcY | 0 |
| Aru | 0 |

Besleme bölgesinde (Bölge 1) polimer ve demir partikülleri hala katı halde bulunmaktadır. Bu nedenle sıcaklık, polimerin yumuşamadan beslenmesini sağlamak amacıyla düşük tutulmaktadır. Yüksek sıcaklığın besleme boğazında tıkanmalara yol açabileceği yapılan çalışmalarda gözlemlenmiştir. Bu çalışmada, hareket aktarım organları ve bağlantılar nedeniyle en geç sıcaklık hedef değerine ulaşan bölge olmuştur. Erime bölgesi (Bölge 2), polimerin eriyerek akışkan hale geçtiği bölgedir ve bu bölgede sıcaklık artırılmaktadır. Sıcaklık, kullanılan polimerin erime noktasına uygun olarak ayarlanmalıdır (örneğin; PLA için 180-210°C, ABS için 230-260°C). Karıştırma bölgesinde (Bölge 3) ise sıcaklık, malzemenin homojen bir şekilde karışmasını sağlayacak seviyede tutulmaktadır. Aynı zamanda, demir partiküllerinin polimer içinde düzgün bir şekilde dağılmasını sağlamak için belirlenen sıcaklık sınırının üzerine çıkılmaması gerekmektedir.



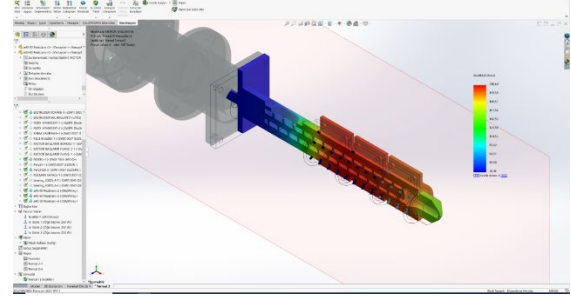
Şekil 4. Termokupl ve rezistansların yerleşimi

Metal partikülleri ısı iletkenliği arttırdığı için, ekstrüderin farklı bölgelerinde sıcaklık kontrolü daha hassas yapılmalıdır. Aksi takdirde, malzeme beklenenden daha hızlı soğuyabilmekte veya aşırı ısınarak polimerin bozulmasına neden olabilmektedir [6].

3.2. Termal Simülasyonun Modellenmesi

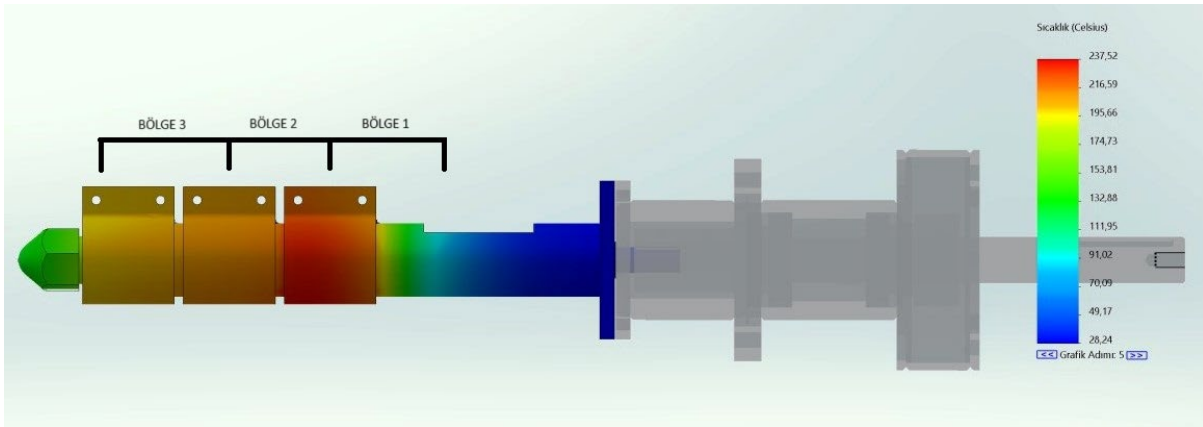
Ekstrüder tasarımındaki ısı dağılımını gözlemlemek amacıyla, Solidworks programında yer alan sonlu eleman çözümü kullanılmaktadır. Üç kademedan oluşan

ısıtıcılar ve termokupllar için, katı modelde belirlenen ölçüler dikkate alınmaktadır. Bu katı model parçaların montajında yer alan ısıtıcılar, Solidworks programında termal yük olarak belirlenen noktalarda her üç bölge için belirlenen noktalarda tanımlanmaktadır. Sistemin kesit görüntüsünde termal yüklerin dağılımı Şekil 5.'te gösterilmektedir. Termal yük olarak gerçek değer olan 250 W değeri kullanılmaktadır.



Şekil 5. Termal yükler ve sensorların dağılımı

Kurulan düzeneğin program içerisindeki görüntüsü Şekil 6.'da gösterilmektedir. Sistemde yer alan tüm elemanlar katı model olarak tasarlanmakta ve montajı yapılmaktadır.



Şekil 6. Simülasyon sonucunda sıcaklık dağılımı

Sistemde bulunan kovan üzerindeki ısıtıcı bantlar, kovan sıcaklık değerini sabit tutmak amacıyla yüzeylerine kelepçelenmektedir. Kovan gövdesinden konveksiyon ve radyasyonla ortama aktarılan kayıp ısı enerjisini azaltmak için, kovanın etrafına 30 mm kalınlığında taş yünlü bir ceket sarılmaktadır. Bu taş yünü ceket, ısıtıcı bant, kovan ve termokuplları sararak kovandan kaybedilen ısı enerjisini korunmasına yardımcı olmaktadır. Yapılan çalışmada hem izolasyonlu hem de izolasyonsuz durumda ortam ve ekstrüder sıcaklığı 22°C, bağıl nem ise %45 civarında

olacak şekilde deneye başlanmaktadır. Burada PID devreleri için eşik değeri 170°C olarak belirlenmektedir. Her üç bölgede eşik değeri olan 170°C aşıldığında deney sonlandırılmaktadır. Çalışmada, her 10 saniyede bir üç bölgeye bağlı termokupllardan gelen veriler kaydedilerek Excel dosyasına aktarılmaktadır. Excel'de elde edilen değerler bir grafik haline getirilebilmektedir. Düzenekte yer alan ısıtıcı bantların yakınında bulunan termokupllar hedef ısı değerlerini aştığı anda, sistemin enerji tüketim miktarlarını ölçmek amacıyla, ısıtıcıların bağlı olduğu devreye priz

tipi bir wattmetre (<https://s-line.com.tr/sline-web/>) yerleştirilmektedir. Böylece çalışmada, hedef sıcaklık değerinin aşılması anında ve eşit süre içerisinde ısıtıcı bantların tüketim miktarlarındaki değişimler gözlemlenmektedir.

4. DENEYSEL SONUÇLAR

Yapılan çalışmada ekonomik, kompakt bir ekstrüder düzeneği oluşturulmaktadır. Şekil 7.'de tasarımı ve imalatı gerçekleştirilen düzenek yer almaktadır. Ekstrüderin katı modeli Solidworks yazılımıyla yapılmakta ve termal yükler programa tanımlanmaktadır. Simülasyonu yapılan kovandaki ısı dağılımları incelenmektedir. Şekil 8.'de yer alan termal kamera görüntüsü ile simülasyon sonuçları kıyaslandığında, sıcaklık dağılımının tutarlı bir benzerlik gösterdiği gözlemlenmektedir.

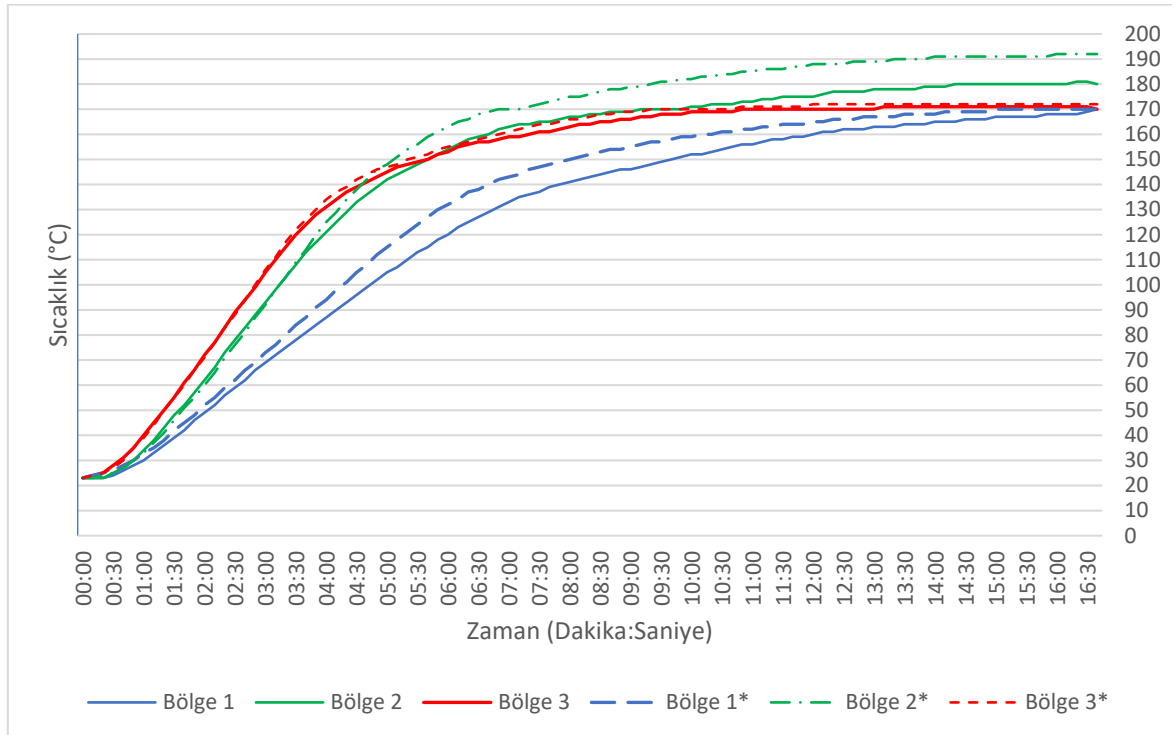


Şekil 7. Termal kamera ile alınan fotoğraf örneği



Şekil 8. Termal kamera ile görüntülenmiş kovanın sıcaklık dağılımı

Ekstrüder üzerindeki üç bölge için alınan değerlerde, izolasyon yapılmış bölgelerde daha hızlı yükselen bir sıcaklık grafiği elde edilmektedir. Hedef süre sonunda elde edilen bir diğer bulgu, izolasyonsuz durumda olan Bölge 2'nin maksimum sıcaklık değerinin 180°C'ye ulaştığı, izolasyon yapılan düzenekte Bölge 2*'nin maksimum sıcaklığının 192°C olduğu gözlemlenmektedir. Elde edilen bu değerler, Şekil 9'da "Bölge (1 - 2 - 3)" izolasyonsuz, "Bölge (1* - 2* - 3*)" izolasyonlu olarak gösterilmektedir. Deneyde kullanılan şebeke gerilimi AC 220.9V ve frekans 50Hz olarak ölçülmektedir.



Şekil 9. Kovan Bölgelerinin Zamana Bağlı Sıcaklık Değişimi

Yapılan ikinci gözlemede, bant ısıtıcıların izolasyonlu durumda çektiği maksimum anlık güç tüketimi 694.1W olarak ölçülmektedir. İzolasyon yapılmayan sistemde ise bu değer 697.6W olduğu tespit edilmektedir. Hedef sıcaklık olan 170°C 'ye ulaşmaya kadar, ekstrüder kovanın izolasyonlu ve izolasyonsuz durumda tükettiği toplam enerji miktarı Çizelge 2'de gösterilmektedir. İzolasyonlu kovan, hedef sıcaklığa 16 dakika 40 saniyede ulaşırken, izolasyonsuz kovan aynı sıcaklığa 19 dakika 12 saniyede ulaşabilmektedir.

Çizelge 2. İzolasyonun enerji tüketimine etkisi

| Özellik | Biri m | İzolasyonlu u | İzolasyonsuz z |
|---------------------------------|-----------|------------------|-------------------|
| Tüketilen Toplam Enerji Miktarı | kWh | 0,073 | 0,097 |
| Anlık Maksimum Enerji Miktarı | kW | 0,6941 | 0,6976 |

5. SONUÇ VE TARTIŞMA

Çalışma sonunda, simülasyonda takip edilen termal analizdeki ısı dağılımının, sistemin termal kamera ile gözlemlenmesi ile elde edilen görüntülerle büyük oranda örtüştüğü gözlemlenmektedir. İmalatı gerçekleştirilen makinede, PLA malzemeye göre yapılan optimizasyon sonucunda ortalama 3 m/dakika üretim hızında 1,75 mm çapında katkılı filaman üretimi gerçekleştirilmektedir. Çalışmada, filaman içerisine eklenen %98 saflıkta, 100 µm elekten geçirilmiş demir tozu kullanılmaktadır. Elde edilen filamandaki demir katkısının kütle oranı ortalama %10 olarak ölçülmektedir. Tasarlanan katı model ve bu modele ait simülasyon, ekstrüder üzerindeki ısı dağılımının termal kamera ile elde edilen görüntülerle uyumlu olduğunu ortaya koymaktadır. Bu sonuç, gelecekteki çalışmalarda simülasyon verileri üzerinden farklı analizlerin yapılmasına olanak tanıyacaktır. Kovan bölgelerinin hedef sıcaklığa ulaşması sırasında, özellikle orta bölgenin (Bölge 2), uç (Bölge 3) ve dip kısımdaki (Bölge 1) sıcaklıklarına kıyasla daha yüksek sıcaklığa ulaştığı gözlemlenmektedir. Orta bölümün her iki yanında bulunan ısıtıcı bantların etkisi nedeniyle bu bölgedeki sıcaklık artışının daha yüksek olduğu düşünülmektedir. Bölge 1'de ise

bu durumun tam tersi bir durum tespit edilmiştir. Kovan bağlantı elemanları, vidalı mil yataklaması ve hareket aktarım elemanlarının bu kısma bağlı olmasının, sıcaklık artış hızını fark edilebilir ölçüde azalttığı görülmektedir. Güç tüketimi incelendiğinde, zamana ve sıcaklık sınırına bağlı gözlemlerde anlık maksimum çekilen gücün, izolasyon bulunmadığında 3.5 W daha yüksek olduğu tespit edilmektedir. Bu farkın oluşmasındaki temel nedenin şebeke gerilimindeki dalgalanmalar olabileceği düşünülmektedir. Ayrıca, izole edilen kovanda, özellikle uç (Bölge 3*) ve orta kısımda (Bölge 2*) sıcaklığın daha hızlı yükselmesi sebebiyle PID kontrolcüsünün, sıcaklık farkına göre bantlardaki çalışma sürelerini daha uzun tutmasının da sebep olabileceği düşünülmektedir. Bu konu, gelecekte yapılacak başka bir çalışmada değerlendirilebilir. Aynı süre içerisinde yapılan gözlemlerde, izolasyon yapılmamış sistemin hedef sıcaklığa ulaştırılabilmesi için gereken güç miktarı 0,097 kWh olarak ölçülürken, izolasyon yapılmış düzenekte bu değer 0,073 kWh olarak ölçülmektedir. İzolasyonun, kurulan sistemde %32,88 oranında enerji tasarrufu sağladığı tespit edilmektedir.

Daha uzun süreli çalışmalarda, kovan yüzeyine uygulanan izolasyon yardımıyla sistemdeki enerji kayıplarının önlenilebileceği düşünülmektedir. Bu durum, sistemin enerji kayıplarını önlemede kovan üzerine uygulanan termal izolasyonun önemini göstermektedir. Demir katkılı filaman üretiminde enerji verimliliğinin önemi hem maliyetlerin azaltılması hem de sürdürülebilir üretim süreçlerinin geliştirilmesi açısından büyük bir önem taşımaktadır. Metal katkılı filaman üretimi, yüksek enerji gereksinimi olan bir süreç olduğundan, enerji verimliliği sağlanması, üretim maliyetlerini düşürmenin yanı sıra sistem ömrünü uzatmak ve çevresel etkileri azaltmak için kritik bir faktördür. Bu nedenle, ekstrüzyon sürecinde sıcaklık kontrolü, termal izolasyon gibi enerji verimliliğini artıracak önlemlerin uygulanması, demir katkılı filaman üretiminde hem ekonomik hem de çevresel sürdürülebilirlik açısından önemli bir katkı sunmaktadır.

KAYNAKLAR

1. F. Cerejo, D. Gatões ve M. T. Vieira, “Optimization of metallic powder filaments for additive manufacturing extrusion (MEX)”, *Int. J. Adv. Manuf. Technol.*, Vol. 115, Issue 7, Pages 2449-2464, 2021.
2. E. H. Tümer ve H. Y. Erbil, “Extrusion-Based 3D Printing Applications of PLA Composites: A Review”, *Coatings*, Cilt 11, Sayı 4, Sayfa 4, 2021.
3. V. S. Vakharia, L. Kuentz, A. Salem, M. C. Halbig, J. A. Salem ve M. Singh, “Additive Manufacturing and Characterization of Metal Particulate Reinforced Polylactic Acid (PLA) Polymer Composites”, *Polymers*, Vol. 13, Issue 20, Page 3545, 2021.
4. S. Akkurt, “Plastik malzeme bilimi, teknolojisi ve kalıp tasarımı”, Sayfa 50-51, Birsen Yayınevi, İstanbul, 2007.
5. S. Levy, “Plastics Extrusion Technology Handbook”, Pages 83-96, Industrial Press Inc., South Norwalk, 1989.
6. K. Doungkeaw ve J. Tungtrongpaioj, “Printability and Mechanical Properties of PLA/Iron Composites for FDM 3D Printing”, *Key Eng. Mater.*, Vol. 978, Pages 47-51, 2024.
7. A. Amirov vd., “3D printing of PLA/magnetic ferrite composites: effect of filler particles on magnetic properties of filament”, *Processes*, Vol. 10, Issue 11, Pages 2412, 2022.
8. J. Sasse, L. Pelzer, M. Schön, T. Ghaddar, ve C. Hopmann, “Investigation of Recycled and Coextruded PLA Filament for Additive Manufacturing”, *Polymers*, Vol. 14, Issue 12, Pages 12, 2022.
9. J. Deng vd., “Energy monitoring and quality control of a single screw extruder”, *Appl. Energy*, Vol. 113, Pages 1775-1785, 2014.
10. M. Nassar, M. El Farahaty, S. Ibrahim, ve Y. Hassan, “Design of 3D filament extruder for Fused Deposition Modeling (FDM) additive manufacturing”, *Int. Des. J.*, Vol. 9, Issue 4, Pages 55-62, 2019.
11. N. D. Watson ve P. Von Lockette, “Deposition Controlled Magnetic Alignment in Iron-PLA Composites”, <https://hdl.handle.net/2152/90192>, Kasım 22, 2023.
12. D. V. Rosato, *Extruding Plastics: A practical processing handbook*, Pages 208–213, Springer Science & Business Media, 2013.
13. S. Y. Kim, S. P. Hersh ve P. L. Grady, “Factors affecting the energy efficiency of single screw extruders”, *Fibre Sci. Technol.*, Vol. 17, Issue 1, Pages 41-61, 1982.